

**Structure-Composition Relationships and Their Influence on Long Luminescent
Lifetimes in Persistent Luminescent Phosphors**

A Dissertation Presented to

The Faculty of the Department of Chemistry

University of Houston

In Partial Fulfillment

Of the Requirements for the Degree

Doctor of Philosophy

By

Erin Elizabeth Finley

May 2019

**Structure-Composition Relationships and Their Influence on Long Luminescent
Lifetimes in Persistent Luminescent Phosphors**

Erin Elizabeth Finley

APPROVED:

Dr. Jakoah Brgoch, Chairperson

Dr. P. Shiv Halasyamani

Dr. Thomas Teets

Dr. Shoujun Xu

Dr. Jiming Bao

Dr. Dan E. Wells, Dean College of Natural Sciences and
Mathematics

Acknowledgements

On a dreary, rainy May evening in 2008 I walked into the apartment of my oldest friend. Together we hatched a plan for me to do what I was always meant to do: go to school and become a doctor. Thank you Rachel Burkhart, for this night and always being a place I know I can go.

After a sleepless night I found myself walking into another home, that of my parents. It was early and the weather was no better than the previous night when the plan was finalized. I sat them down and told them the plan. I told them this meant I would be forgoing a family of my own and asked for their support. Five and half years later they watched me walk across a stage with a B.S. in hand. From that very same stage I looked out to see the two most important professors I have had the privilege of knowing. They clapped with vigor and pride. Dave Aurentz Ph.D and Ike Shibley Ph.D. are the ones who knew before I did that I could do great, important things in science. They believed in me and my ability. Seeing them from that stage I was honored, humbled, and grateful for all they had done. I knew I was making the right choice. I knew embarking on a Ph.D. of my own was the only right choice. I thank them from the deepest part of my soul for their encouragement and belief in me.

Graduate school is not for the weak of heart. It is for the determined, the persistent, and the stubborn. Sitting across from my soon to be graduate advisor, he said to me: "The best graduate students are the ones who don't quit. The ones who are the most persistent." (The irony of my research subject and this statement is not lost on me.) I again knew I would be making the right choice. The importance of your research group and advisor cannot be overstated. My gratitude to Jakoah Brgoch Ph.D. and my fellow

group members is more than words can describe. Thank you Jakoah for having faith in me when I didn't have faith in myself, for pushing me, and for making me fight every single day of this journey. Thank you Anna Duke Ph.D. for being my lab sister and all that that means. Thank you Aria Manaouri Tehrani for sitting next to me every single day and all that that has meant. Thank you Andrew Paterson Ph.D. for being the one to bring this research to me, for being my friend, and for being a mentor.

To my family: Mom, Don, Kate, Gresh, G.K., and Rory. Your love and support has been my driving force. It has been the thing that got me through the hardest days. For ten years you have stood behind me at every stage and I honor you with this degree, for without you I would not be here today.

Lastly, thank you Russell, for being the one complete constant in my life every single day.

**Structure-Composition Relationships and Their Influence on Long Luminescent
Lifetimes in Persistent Luminescent Phosphors**

An Abstract of a Dissertation

Presented to

The Faculty of the Department of Chemistry

University of Houston

In Partial Fulfillment

Of the Requirements for the Degree

Doctor of Philosophy

By

Erin Elizabeth Finley

May 2019

Abstract

Persistent luminescence (PersL) is an optical phenomenon found in inorganic materials, where a luminescent center, e.g., Eu^{2+} or Cr^{3+} , is substituted into a host inorganic crystal structure, producing visible light on the order of minutes to hours. The mechanism driving PersL is generally agreed to arise from a relationship between the host structure's bandgap and any lattice defects stemming from anion vacancies, anti-site defects, and co-dopants, e.g., Dy^{3+} , that form electron traps. Research has primarily focused on establishing methods to improve the long luminescent lifetimes of known persistent luminescent phosphors (PLPs) and the extension of these materials into medical diagnostic applications. However, the PLPs available today have a limited range of emission wavelengths, low efficiency, and lack chemical stability. Developing novel PLPs requires a fundamental understanding of the relationship between the crystal structures and chemical compositions that bring about these distinctive optical properties. Until recently, it was thought that the $5d$ -orbitals present from a co-dopant were mainly responsible for creating electron traps; yet, thermoluminescence experiments proved a co-dopant was not necessary to observe PersL. This supports the notion that lattice defects are the main electron traps driving PersL.

The work presented herein addresses this question using a combination of experimental and computational chemistry tools to identify the intrinsic nature of the electron traps and their relationship to the optical properties. Detailed structural studies were first employed using high resolution synchrotron X-ray diffraction to show compositional control in a solid solution, while X-ray absorption spectroscopy revealed distortions around the luminescent center are linked to anti-site defects. Next, thermoluminescence spectroscopy and computational modeling provided the link between chemical

composition and presence of lattice defects to the efficiency of PersL. Finally, a novel synthesis approach to particle size reduction demonstrated an improvement to PersL by inducing surface defects while maintaining chemical composition. The results highlight the importance of investigating the connection between lattice defects, structural properties, *e.g.*, local polyhedral distortion, and optical properties such as PersL. Together, a stronger fundamental understanding of crystal structures and compositions of PLPs will advance the discovery of novel materials.

TABLE OF CONTENTS

CHAPTER 1. Introduction.....	1
1.1 Persistent Luminescent Phosphors.....	1
1.2 Overview of Significant Persistent Luminescent Phosphors.....	3
1.3 Mechanism of Persistent Luminescence.....	10
1.3.1 Photoluminescence of Eu ²⁺ Substituted Persistent Luminescent Phosphors.....	10
1.3.1.1 The Matsuzawa Model.....	11
1.3.1.2 The Dorenbos Model.....	13
1.3.1.3 The Clabau Model.....	15
1.3.1.4 <i>Ab Initio</i> Model from Density Functional Theory.....	17
1.3.2 Photoluminescence of Cr ³⁺ Substituted Persistent Luminescent Phosphors.....	19
1.3.2.1 Persistent Luminescent Mechanism of Cr ³⁺	20
1.4 Trap States.....	22
1.4.1 Types of Trap States Giving Rise to Persistent Luminescence.....	22
1.4.2 Thermoluminescence and Quantifying Trap States.....	25
1.5 Research Goals.....	28
1.6 Organization of the Thesis.....	29
1.7 References.....	30
CHAPTER 2. Experimental and Computational Methods.....	37
2.1 Experimental Synthesis.....	37
2.1.1 Starting Reagents.....	37
2.1.2 All Solid-State Method.....	38
2.1.3 Reverse Micelle Method.....	39
2.1.4 Tube Furnaces.....	40

2.1.4 Microwave Heating.....	41
2.2 Characterization	42
2.2.1 X-ray Powder Diffraction	42
2.2.2 Inductively Coupled Plasma-Optical Emission Spectroscopy	43
2.2.3 Scanning Electron Microscopy and Energy Dispersive X-ray Spectroscopy	43
2.2.4 Particle Size Measurements.....	43
2.2.5 Photoluminescence and Long Luminescent Lifetimes.....	44
2.2.6 Thermoluminescence.....	46
2.2.7 Diffuse Reflectance.....	48
2.2.8 X-ray Absorption Spectroscopy.....	49
2.3 Density Functional Theory Calculations.....	51
2.3.1 The Vienna <i>ab initio</i> Simulation Package (VASP).....	51
2.3.2 Formation Energy Calculations of Point Defects.....	52
2.4 References	54
CHAPTER 3. Optimizing Blue Persistent Luminescence	57
in $(\text{Sr}_{1-\delta}\text{Ba}_\delta)_2\text{MgSi}_2\text{O}_7:\text{Eu}^{2+},\text{Dy}^{3+}$ via Solid Solution in Point-of-Care Diagnostics	
3.1 Introduction.....	57
3.2 Experimental.....	59
3.2.1 Sample Preparation.....	59
3.2.2 X-ray Diffraction.....	60
3.2.3 Optical Characterization.....	60
3.2.4 Time-gated Smartphone Imaging.....	61
3.3 Results and Discussion	61
3.3.1 Structure Solution for $(\text{Sr}_{1-\delta}\text{Ba}_\delta)_2\text{MgSi}_2\text{O}_7$ ($\delta = 0, 0.125, 0.25, 0.375$).....	61
3.3.2 Photoluminescence.....	65

3.3.3 Thermoluminescence.....	71
3.3.4 Smartphone-based Time-gated Imaging.....	74
3.4 Conclusion.....	78
3.5 Acknowledgements.....	79
3.6 References.....	79
3.7 Supporting Information.....	82
CHAPTER 4. Deciphering the Loss of Red Persistent Luminescence in ZnGa ₂ O ₄ :Cr ³⁺ Upon Al ³⁺ Substitution.....	87
4.1 Introduction.....	87
4.2 Experimental.....	90
4.2.1 Sample Preparation.....	90
4.2.2 X-ray Diffraction.....	91
4.2.3 Optical Characterization.....	91
4.3 Results and Discussion.....	92
4.3.1 Synthesis and Characterization of the Solid Solution Zn(Ga _{1-δ} Al _{δ}) ₂ O ₄ (δ = 0, 0.25, 0.50, 0.75, 1).....	92
4.3.2 Optical Properties.....	96
4.3.3 Relating Bandgap to Trap Depth.....	108
4.4 Conclusion.....	109
4.5 Acknowledgments.....	110
4.6 References.....	111
4.7 Supporting Information.....	115
CHAPTER 5. Exploring the Local Structure in Cr-Substituted Zn(Ga _{1-δ} Al _{δ}) ₂ O ₄ Persistent Luminescent Phosphors.....	119
5.1 Introduction.....	119
5.2 Experimental.....	123
5.2.1 Sample Preparation and Characterization.....	123

5.2.2 Density Functional Theory Calculations.....	124
5.2.3 X-ray Absorption Spectroscopy.....	124
5.3 Results and Discussion.....	125
5.3.1 XANES Spectra of the Cr <i>K</i> Edge.....	125
5.3.2 EXAFS Spectra of the Cr <i>K</i> Edge.....	128
5.4 Conclusion.....	135
5.5 Acknowledgements.....	136
5.6 References.....	136
CHAPTER 6. Intrinsic Defects Drive Persistent Luminescence in.....	141
Monoclinic SrAl ₂ O ₄ :Eu ²⁺	
6.1 Introduction.....	141
6.2 Computational Details.....	143
6.3 Results and Discussion.....	146
6.4 Conclusion.....	155
6.5 Acknowledgements.....	156
6.6 References.....	156
CHAPTER 7. Reducing Particle Size of Persistent Luminescent SrAl ₂ O ₄ :Eu ²⁺ ,Dy ³⁺ ...	159
<i>via</i> Microwave-Assisted, Reverse Micelle Synthesis	
7.1 Introduction.....	159
7.2 Experimental.....	161
7.2.1 Precursor Synthesis.....	161
7.2.1.1 Reverse Micelle Preparation.....	161
7.2.1.2 All Solid-State Preparation.....	163
7.2.2 Synthesis Procedure.....	163
7.2.2.1 Microwave-Assisted Heating.....	163
7.2.2.2 High-Temperature Furnace Heating.....	164

7.2.3 Characterization.....	164
7.2.4 Optical Properties.....	165
7.3 Results and Discussion.....	166
7.3.1 Microwave-Assisted, Reverse Micelle Synthesis Of Persistent Phosphors.....	166
7.3.2 Particle Size Analysis.....	174
7.3.3 Optical Characterization.....	176
7.4 Conclusion.....	183
7.5 Acknowledgements.....	184
7.6 References.....	184
7.7 Supporting Information.....	188
CHAPTER 8. Conclusions and Direction of Research.....	192

List of Figures

- Figure 1.1 (a) The structure of $\text{SrAl}_2\text{O}_4:\text{Eu}^{2+}$ contains a three-dimensional network of corner-connecting tetrahedra with two independent Sr^{2+} sites sitting in the interstitials. (b) Photoluminescence spectra of $\text{SrAl}_2\text{O}_4:\text{Eu}^{2+}$ depicting a broad excitation spectrum (dashed line) that emits two peaks due to the two Sr^{2+} sites, $\lambda_{\text{em}} \approx 450$ nm and $\lambda_{\text{em}} \approx 520$ nm (solid line collected at 80K). 5
- Figure 1.2 (a) The structure of $\text{Sr}_2\text{MgSi}_2\text{O}_7:\text{Eu}^{2+}$ contains five-membered rings of alternating corner-connecting tetrahedra of $[\text{SiO}_4]$ and $[\text{MgO}_4]$. Sr^{2+} occupies one crystallographic site that sits in the middle of the five-membered rings. (b) Photoluminescence spectra depict a broad excitation peak (dashed line) that produces a single emission peak at $\lambda_{\text{em}} \approx 470$ nm (solid line). 7
- Figure 1.3 (a) The structure of $\text{ZnGa}_2\text{O}_4:\text{Cr}^{3+}$ is a cubic closed packed system with edge-sharing octahedra and corner-connected tetrahedra. (b) Photoexcitation spectra from Cr^{3+} results in two peaks, $\lambda_{\text{ex}} \approx 400$ nm and 550 nm (dashed line) and an emission spectra (solid line) in the NIR with several distinct peaks. 9
- Figure 1.4. Modified Jablonski diagram illustrating the luminescence mechanism of Eu^{2+} . 10
- Figure 1.5 Persistent luminescent mechanism of $\text{SrAl}_2\text{O}_4:\text{Eu}^{2+}, \text{Dy}^{3+}$ as proposed by Matsuzawa *et al.* An electron in Eu^{2+} is excited from the $4f$ -orbital to $5d$ -orbital. Its electron-hole is conducted through the VB and is trapped by the $4f$ -orbital of Dy^{3+} . Thermal energy (kT) releases the electron-hole and it is recombined with the relaxed electron to produce a photon. Excitation and trapping are black lines, thermal release and relaxation are red. Electron filled black circle, electron-hole is open circle. 12
- Figure 1.6 Energy schemes of rare earth $4f$ -orbitals (RE^{2+} black triangles and RE^{3+} blue triangles) ions required to promote an electron into the conduction band (E_{vc}). n is the number of electrons, E^{ex} is the energy required to produce an electron-hole pair, and E_{v} is the top of the valence band. 14
- Figure 1.7 Persistent luminescent mechanisms as proposed by Dorenbos. An electron in Eu^{2+} is excited from the $4f$ -orbital to $5d$ -orbital and is photoionized into the CB. The electron is trapped in the $5d$ -orbital of a RE co-dopant. The electron-hole remains in the $4f$ -orbital. Thermal energy (kT) releases the electron and it is recombined with its electron-hole to produce a photon. Excitation and trapping are black lines; thermal release and relaxation are red. Electron filled black circle, electron-hole is open circle. 15

Figure 1.8 Persistent luminescent mechanism as proposed by Clabau *et al.* An electron in Eu^{2+} is excited from the $4f$ -orbital to $5d$ -orbital is trapped in a anion vacancy (V_{O}). The electron-hole remains in the $4f$ -orbital. Thermal energy (kT) releases the electron and it is recombined with its electron-hole to produce a photon. Another electron from Eu^{3+} is excited via CT and its electron-hole is trapped in a cation vacancy (V_{Sr}). CT releases the electron-hole and it recombines to produce a photon. Excitation and trapping are black lines; thermal release and relaxation are red. Electron filled black circle, electron-hole is open circle. 16

Figure 1.9 Persistent luminescence model proposed by Qu *et al.* An electron in Eu^{2+} is excited from the $4f$ -orbital to $5d$ -orbital and is photoionized into the CB. The electron is trapped in the either an anion vacancy (V_{O}^{2+}) or the $5d$ -orbital of Nd^{3+} . The electron-hole remains in the $4f$ -orbital. Thermal energy (kT) releases the electron and it is recombined with its electron-hole to produce a photon. Cation vacancies (V_{Ca} and $\text{Eu}_{\text{Ca}} + V_{\text{Ca}}$) lie close to the top of the VB do participate in the mechanism. Excitation and trapping are black lines, thermal release and relaxation are red. Electron filled black circle, electron-hole is open circle. 18

Figure 1.10 Tanabe-Sugano diagrams for a $3d^3$ transition metal in O_h coordination. The $5d$ -orbitals are split into double degeneracy (e_g) and triple degeneracy (t_{2g}). (a) is the spin-allowed transition from the ground state to the first excited state: ${}^4A_2 \rightarrow {}^4T_1$ (4F) (purple arrow) and ${}^4A_2 \rightarrow {}^4T_2$ (4F) (green arrow) and electron (half arrow) is excited to an e_g orbital. (b) The spin-forbidden relaxation of an electron from the first excited state, ${}^2E \rightarrow {}^4A_2$ (red arrow) and all electrons lie in t_{2g} orbitals. 20

Figure 1.11 A general proposed model of the persistent luminescent mechanism of $\text{ZnGa}_2\text{O}_4:\text{Cr}^{3+}$. An electron is excited from ${}^4A_2 \rightarrow {}^4T_1$ (4F), it is trapped in a trap state, thermal energy (kT) releases it, and the ${}^2E \rightarrow {}^4A_2$ transition releases a photon. Excitation and trapping black arrows, relaxation and detrapping are red arrows. 21

Figure 1.12 A proposed secondary model of the persistent luminescence mechanism in $\text{ZnGa}_2\text{O}_4:\text{Cr}^{3+}$. An electron is excited from ${}^4A_2 \rightarrow {}^4T_2$ (4F), it is trapped in a trap state, and the ${}^2E \rightarrow {}^4A_2$ transition releases a photon. Excitation and trapping black arrows, relaxation and detrapping are red arrows. 22

Figure 1.13 Energy scheme of $\text{Sr}_2\text{MgSi}_2\text{O}_7:\text{Eu}^{2+}, \text{RE}^{3+}$ depicting the relationship between defect driven trap states (solid blue dashed) and the rare earth ions (RE^{2+} red circles and RE^{3+} blue circles) in their ground states ($4f$ -orbitals). Defect and RE^{2+} energy levels are with respect to the bottom of the CB. RE^{3+} energy levels are with respect to the top of the VB. 25

Figure 2.1 Calculated trap depths as a function of T_m of $\text{SrAl}_2\text{O}_4:\text{Eu}^{2+}$ from varying ramp rates resulting from TL. 48

Figure 3.1. (a) Synchrotron X-ray powder diffraction data $(\text{Sr}_{1-\delta}\text{Ba}_\delta)_2\text{MgSi}_2\text{O}_7$ ($\delta = 0, 0.125, 0.250, 0.375$) shows the solid solution can be prepared phase pure. The calculated pattern was determined from [16]. (b) Rietveld refinement shown for $\delta = 0$. Experimental data is black, refinement is orange, and the difference is blue. The rare-earth ions were excluded in the refinement due to their low substitution concentration. 62

Figure 3.2. Crystal structure of $(\text{Sr}_{1-\delta}\text{Ba}_\delta)_2\text{MgSi}_2\text{O}_7$ by Rietveld refinement with $[\text{SiO}_4]$ tetrahedra highlighted. 64

Figure 3.3. (a) Unit cell volume and (b) polyhedral volume increase linearly with in Ba^{2+} concentration. The (Sr/Ba)-O coordination environment is shown. 65

Figure 3.4. The (a) excitation, (b) emission spectra for $(\text{Sr}_{1-\delta}\text{Ba}_\delta)_{2-x}\text{MgSi}_2\text{O}_7:\text{Eu}^{2+}$ ($\delta = 0, 0.125, 0.250, 0.375$). Emission spectra were collected at $\lambda = 365$ nm and the excitation spectra were collected at the λ_{max} of emission spectrum for each sample. The Gaussian fit is solid gray (c) CIE diagram showing blue shift and reduction in green emission. 67

Figure 3.5. PersL of $(\text{Sr}_{1-\delta}\text{Ba}_\delta)_2\text{MgSi}_2\text{O}_7:\text{Eu}^{2+}$ ($\delta = 0, 0.125, 0.250, 0.375$) fit to a triple exponential. Circles indicate raw data and solid gray line is the fit. 68

Figure 3.6. (a) excitation, (b) emission spectra for $(\text{Sr}_{1-\delta}\text{Ba}_\delta)_2\text{MgSi}_2\text{O}_7:\text{Eu}^{2+}, \text{Dy}^{3+}$ ($\delta = 0, 0.125, 0.250, 0.375$) Emission spectra were collected at $\lambda = 365$ nm and the excitation spectra were collected at the λ_{max} of emission spectrum for each sample. The Gaussian fit is solid gray. (c) CIE diagram showing blue shift across the solid solution. 70

Figure 3.7 . PersL of $(\text{Sr}_{1-\delta}\text{Ba}_\delta)_{2-x}\text{MgSi}_2\text{O}_7:\text{Eu}_x^{2+}$ ($\delta = 0, 0.125, 0.250, 0.375$) fit to a triple exponential. Circles indicate raw data and solid gray line is the fit. 71

Figure 3.8. Thermoluminescence peaks and the corresponding temperatures for $(\text{Sr}_{1-\delta}\text{Ba}_\delta)_{2-x}\text{MgSi}_2\text{O}_7$ ($\delta = 0, 0.125, 0.250, 0.375$). Eu^{2+} only is shown for plots a, c, e, and g while $\text{Eu}^{2+}, \text{Dy}^{3+}$ is shown as plots b, d, f, and h. 73

Figure 3.9. Time-gated luminescence imaging acquired with a smartphone-based bio-sensing platform and intensity profile scan. (a) $\text{Sr}_{1-\delta}\text{Ba}_\delta)_{2-x}\text{MgSi}_2\text{O}_7:\text{Eu}^{2+}$ and (b) $\text{Sr}_{1-\delta}\text{Ba}_\delta)_{2-x}\text{MgSi}_2\text{O}_7:\text{Eu}^{2+}, \text{Dy}^{3+}$. Blue line represents the blue channel intensity and green line is the green channel intensity. 76

Figure 3.10. Comparison of spectral response between $\text{SrAl}_2\text{O}_4:\text{Eu}^{2+}, \text{Dy}^{3+}$ and (a) $(\text{Sr}_{1-\delta}\text{Ba}_\delta)_2\text{MgSi}_2\text{O}_7:\text{Eu}^{2+}$ and (b) $(\text{Sr}_{1-\delta}\text{Ba}_\delta)_2\text{MgSi}_2\text{O}_7:\text{Eu}^{2+}, \text{Dy}^{3+}$ using time-gated luminescence. The images were acquired with a smartphone-based bio-sensing platform. 77

Figure 3.S1. Rietveld refinement shown for $\delta = 0.125, 0.25, 0.375$ Experimental data is black, refinement is orange, and the difference is blue. All are in excellent agreement with the calculated pattern. 82

- Figure 3.S2. Thermoluminescence spectra showing the deconvolution of the trap states ($\text{Sr}_{1-\delta}\text{Ba}_\delta$)_{2-x}MgSi₂O₇ ($\delta = 0, 0.125, 0.250, 0.375$). Eu^{2+} only is shown for plots a, c, e, and g while $\text{Eu}^{2+}, \text{Dy}^{3+}$ is shown as plots b, d, f, and h. 85
- Figure 4.1. (a) Rietveld refinement of synchrotron X-ray powder diffraction data for the solid solution $\text{Zn}(\text{Ga}_{1-\delta}\text{Al}_\delta)_2\text{O}_4$ ($\delta = 0, 0.25, 0.50, 0.75, 1$) the solid line is the fit, and the circles are the observed data. A decreasing linear regression of the (b) unit cell volume and (c) $[\text{GaO}_6/\text{AlO}_6]$ polyhedron volume is shown as a function of Al^{3+} . 94
- Figure 4.2. The crystal structure for (a) ZnGa_2O_4 and (b) ZnAl_2O_4 as determined by Rietveld refinement with either Ga or Al octahedral sites highlighted. 96
- Figure 4.3. Diffuse reflectance of the optical bandgap (E_g) for $\text{Zn}(\text{Ga}_{1-\delta}\text{Al}_\delta)_2\text{O}_4$ ($\delta = 0 - 0.75$) $n = 2$ black dashed lines and black y-axis and ZnAl_2O_4 $n = 1/2$ blue dashed line and blue y-axis. 97
- Figure 4.4. (a) Excitation spectra of the solid solution $\text{Zn}(\text{Ga}_{1-\delta}\text{Al}_\delta)_2\text{O}_4:\text{Cr}^{3+}$; $\delta = 0$ gray, $\delta = 0.25$ orange, $\delta = 0.50$ green, $\delta = 0.75$ purple, $\delta = 1$ yellow. The deconvoluted peaks are the filled excitation curves for $\delta = 0$. (b) Linear trend of the deconvoluted peaks with increasing Al^{3+} concentration showing a decrease in energy for ${}^4\text{A}_2 \rightarrow {}^4\text{T}_1$ (c) Linear trend for ${}^4\text{A}_2 \rightarrow {}^4\text{T}_2$. 99
- Figure 4.5. Emission spectra of $\text{Zn}(\text{Ga}_{1-\delta}\text{Al}_\delta)_2\text{O}_4:\text{Cr}^{3+}$ ($\delta = 0, 0.25, 0.50, 0.75, 1$) with an excitation wavelength of $\lambda_{\text{ex}} = 400$ nm. R-lines are highlighted and are assigned to the spin-forbidden transition of ${}^2\text{E} \rightarrow {}^4\text{A}_2$, and the N is highlighted and is responsible for long luminescent lifetimes. 102
- Figure 4.6 Samples were excited by $\lambda_{\text{ex}} = 254$ nm for 10 min. Circles are the observed data, and the black lines are the fit. 104
- Figure 4.7. Thermoluminescence (TL) spectra of peaks contributing the long lifetimes for $\text{Zn}(\text{Ga}_{1-\delta}\text{Al}_\delta)_2\text{O}_4:\text{Cr}^{3+}$ (a) $\delta = 0$, (b) $\delta = 0.25$, and (c) $\delta = 0.50$. 107
- Figure 4.8. Trap depths that are participating in persistent luminescence with respect to the bottom of the conduction band for $\delta = 0, 0.25$ and 0.50 . 108
- Figure 4.S1. Rietveld refinement shown for (a) $\delta = 0$, (b) $\delta = 0.25$, (c) $\delta = 0.50$, (d) $\delta = 0.75$, and (f) $\delta = 1$ Experimental data is indicated by black circles, refinement is the solid color, and the difference is gray. Each refinement is in good agreement with the calculated pattern. 115
- Figure 4.S2. Thermoluminescence spectra showing the deconvolution of the trap states for $\text{Zn}(\text{Ga}_{1-\delta}\text{Al}_\delta)_2\text{O}_4:\text{Cr}^{3+}$ (a) $\delta = 0$, (b) $\delta = 0.25$, and (c) $\delta = 0.50$. 118
- Figure 5.1 Powder X-ray diffraction of $\text{Zn}(\text{Ga}_{1-\delta}\text{Al}_\delta)_2\text{O}_4:\text{Cr}^{3+}$ ($\delta = 0 - 1$). The whole solid solution forms in the space group $Fd\bar{3}m$ (no. 227) in agreement with the calculated pattern.³⁸ Shift of peaks to higher angle indicate smaller unit cell 124

parameters confirming incorporation of Al^{3+} into the system.

Figure 5.2 Cr K edge XANES spectra for $\text{Zn}(\text{Ga}_{1-\delta}\text{Al}_\delta)_2\text{O}_4:\text{Cr}^{3+}$ ($\delta = 0 - 1$). Dashed lines indicate four prominent features A-B is the $1s \rightarrow 3d$ transition, PC 1s-to-continuum, D is the first constructive interference. Lorentzian fitted peaks are grey. 126

Figure 5.3 EXAFS spectra across the solid solution $\text{Zn}(\text{Ga}_{1-\delta}\text{Al}_\delta)_2\text{O}_4:\text{Cr}^{3+}$ ($\delta = 0 - 1$) with k^3 -weighted Fourier transform of the magnitude. 129

Figure 5.4 Unit cells of the solid-solution from DFT calculations [GaO_6] (green) and [AlO_6] (blue) octahedron are highlighted, Zn^{2+} (black), and O^{2-} (orange). (a) ZnGa_2O_4 (b) $\text{Zn}(\text{Ga}_{0.75}\text{Al}_{0.25})_2\text{O}_4$ (c) $\text{Zn}(\text{Ga}_{0.50}\text{Al}_{0.50})_2\text{O}_4$ (d) $\text{Zn}(\text{Ga}_{0.25}\text{Al}_{0.75})_2\text{O}_4$ and (e) ZnAl_2O_4 . 131

Figure 5.5 Cr K edge EXAFS of for in Fourier transform k^2 -weighted R -space of (a) magnitude and (b) real. Black circles are the observed data, solid line is the fit. Dashed line is a guide for the eye to show the peak shift. 133

Figure 5.6 (a) Radial distance (R) of Cr–O as a function of δ in $\text{Zn}(\text{Ga}_{1-\delta}\text{Al}_\delta)_2\text{O}_4:\text{Cr}^{3+}$ ($\delta = 0 - 1$). (b) Difference in the calculated distance and the fit as a function of δ . 134

Figure 6.1. (a) Optimized $2 \times 1 \times 1$ supercell showing the two independent crystallographic sites for Sr^{2+} (blue) and the [AlO_4] tetrahedra highlighted in gray. (b) Total density of states (DOS) without Eu^{2+} and (c) total DOS with Eu^{2+} f -orbitals outlined in red, as determined by HSE06 with a calculated $E_g = 6.02$ eV. 144

Figure 6.2. Chemical stability regime of Sr-O-Al phase space. The chemical potential ($\mu_{\text{O}_2(\text{g})}$) is set to zero. Stability regime of SrAl_2O_4 is highlighted in green with the oxygen rich and poor limits indicated by black dots. 146

Figure 6.3. Thermodynamic transition levels, $\epsilon(q/q')$, of energetically favorable vacancies. The strontium vacancies (V_{Sr}) form at $E_F < 1$ eV and oxygen (V_{O}) from at $E_F > 2$ eV. 149

Figure 6.4. Formation energies of (a) $V_{\text{O}(1)}$, (b) $V_{\text{O}(2)}$, (c) $V_{\text{O}(3)}$, and (d) $V_{\text{O}(4)}$ in SrAl_2O_4 charged point defects at the oxygen-poor bounds. The solid lines show point charge that is favorable at a given E_F within E_g . Dashed lines show unfavorable point charge. 152

Figure 6.5. The thermodynamic transition levels, $\epsilon(q/q')$, for each vacancy does increase, placing $\epsilon(0/2+)$ in an ideal location to be a trap state participating in Persistent luminescence. 153

Figure 6.6. Formation energies of (a) $V_{\text{O}(1)}$, (b) $V_{\text{O}(2)}$, (c) $V_{\text{O}(3)}$, and (d) $V_{\text{O}(4)}$ in $\text{SrAl}_2\text{O}_4:\text{Eu}^{2+}$ charged point defects at the oxygen-poor bounds. The solid lines show point charge that is favorable at a given E_F within E_g . Dashed lines show unfavorable point charge. 154

- Figure 7.1. XRD patterns of microwave-assisted reverse micelle $\text{SrAl}_2\text{O}_4:\text{Eu}^{2+},\text{Dy}^{3+}$ 169 showing batch-to-batch consistency of the microwave heating process. Black is the calculated pattern.³⁹ “+” is an Al_2O_3 impurity.
- Figure 7.2. (a) Reverse micelle and (b) solid state synthesis Rietveld refinements 170 show the reverse micelle is comparable to the traditional solid state synthesis. Black circles are for observed data, solid lines are the refined pattern, and “+” is the Al_2O_3 impurity.
- Figure 7.3. The 2 independent polyhedra (a) $[\text{Sr}(1)\text{O}_7]$ and (b) $[\text{Sr}(2)\text{O}_7]$ are shown 174 to the left of the unit cell (c) of SrAl_2O_4 in the monoclinic space group $P2_1$ with the $[\text{AlO}_4]$ tetrahedra highlighted.
- Figure 7.4. SEM with a 200x magnification and the scale bar is 50 μm . (a) Reverse 175 micelle synthesis visualizes the overall particle sizes are much smaller than the (b) solid state synthesis. Both starting materials were reacted using microwave-assisted heating.
- Figure 7.5. Particle size analysis of the (a) reverse micelle synthesis showing that 176 50% of the equivalent sphere diameters ($d_{0.5}$) are 4.2 μm or smaller and (b) the all solid state synthesis gives a $d_{0.5} = 14.3 \mu\text{m}$.
- Figure 7.6. (a) Excitation and emission spectra of solid state (SS) and reverse 177 micelle (RM) showing $\lambda_{\text{em,max}} = 520 \text{ nm}$ for both synthesis pathways. (b) CIE diagram illustrating the calculated color coordinates have nearly identical visible emission.
- Figure 7.7. Temperature-dependent measurement of (a) RM and (b) SS emission 178 spectra (top) and the relative integrated intensity of the quenching temperature (T_{50}) of the combined emission peaks (bottom).
- Figure 7.8. Temperature-dependent luminescent decay of the (a) reverse micelle 180 and (b) solid state observed for 3600 seconds. The data fit to a tri-exponential (c) reverse micelle and (d) solid state show the reverse micelle has a longer lifetime than the all solid state sample.
- Figure 7.9. (a) TL emission curve cumulative fit of solid state (black) and reverse 181 micelle (red), grey is the observed data. Peaks determined by deconvolution for (b) reverse micelle and (c) solid state. Peaks with traps $< 0.4 \text{ eV}$ or $> 1 \text{ eV}$ are dashed lines and peaks between 0.4 eV and 1 eV are solid lines.
- Figure 7.S1. Powder X-ray diffraction of precursor material from reverse micelle 188 synthesis. Black is the observed data and blue is the calculated pattern from ICSD.
- Figure 7.S2. (a) Reverse micelle and (b) solid state synthesis performed by high- 189 temperature furnace heating of Rietveld refinements. Show the reverse micelle is again comparable to the solid state sample. Black circles are for observed data, solid lines are the refined pattern. And “+” is the Al_2O_3 impurity. An additional

unidentified impurity.

Figure 7.S3. Particle size analysis of samples prepared via high-temperature furnace heating (a) reverse micelle synthesis and (b) solid state synthesis have comparable particle sizes. 189

List of Tables

Table 1.1 Overview Of Significant Persistent Luminescent Phosphors Studied Over The Last Century	2
Table 2.1 Starting materials for all synthesis methods	38
Table 2.2 Fourier transform parameters. The first near neighbor was used for phase correction and $\epsilon(k) = 0$.	51
Table 3.1. Rietveld Refinement Data of $\text{Sr}_2\text{MgSi}_2\text{O}_7$ Using 11-BM Synchrotron Radiation. The rare-earth ions were excluded in the refinement due to their low substitution concentration.	63
Table 3.2. Atomic Coordinates and Isotropic Displacement Parameters of $\text{Sr}_2\text{MgSi}_2\text{O}_7:\text{Eu}^{2+}$ as Determined by Rietveld Refinement of 11-BM Synchrotron X-ray Diffraction Data. The rare-earth ions were excluded in the refinement due to their low substitution concentration.	63
Table 3.3. Average long lifetime decay times of $(\text{Sr}_{1-\delta}\text{Ba}_\delta)_2\text{MgSi}_2\text{O}_7:\text{Eu}^{2+}$.	69
Table 3.4. Average lifetime decay of $(\text{Sr}_{1-\delta}\text{Ba}_\delta)_{2-x}\text{MgSi}_2\text{O}_7:\text{Eu}^{2+}, \text{Dy}^{3+}$ ($\delta = 0, 0.125, 0.250, 0.375$) of each sample measured three times.	71
Table 3.5. TL peaks and their corresponding trap depths for $(\text{Sr}_{1-\delta}\text{Ba}_\delta)_{2-x}\text{MgSi}_2\text{O}_7$ ($\delta = 0, 0.125, 0.250, 0.375$). Eu^{2+} only is shown for plots a, c, e, and g, while $\text{Eu}^{2+}, \text{Dy}^{3+}$ is shown as plots b, d, f, and h.	74
Table 3.S1. Rietveld Refinement of $(\text{Sr}_{1-\delta}\text{Ba}_\delta)_2\text{MgSi}_2\text{O}_7$ ($\delta = 0.125, 0.25, 0.375$) Using Synchrotron Radiation.	83
Table 3.S2. Atomic Coordinates, Isotropic Displacement Parameters, and Occupancies as Determined by Rietveld Refinement of 11-BM Synchrotron X-ray Diffraction Data.	84
Table 4.1. Rietveld Refinement Data for the End Members of Solid Solution from 11-BM Synchrotron X-Ray Diffraction.	94
Table 4.2 (a) Crystallographic Data of ZnGa_2O_4 from Rietveld Refinement Resulting from 11-BM Synchrotron X-ray Diffraction Data, (b) Crystallographic Data of ZnAl_2O_4 from Rietveld Refinement Resulting from 11-BM Synchrotron X-ray Diffraction Data.	95
Table 4.3. Bandgap values across the solid solution determined from diffuse reflectance measurements.	98
Table 4.4. Calculated Racah Parameter (B) And Crystal Field Strength ($10Dq/B$) for $\text{Zn}(\text{Ga}_{1-\delta}\text{Al}_\delta)_2\text{O}_4$ ($\delta = 0, 0.25, 0.50, 0.75, 1$).	100

Table 4.5. The intensity ratio of the R and N-lines and the change in peak width of the N-line for $\text{Zn}(\text{Ga}_{1-\delta}\text{Al}_\delta)_2\text{O}_4$ ($\delta = 0, 0.25, 0.50, 0.75, 1$).	101
Table 4.6. Long Luminescent Lifetimes of $\text{Zn}(\text{Ga}_{1-\delta}\text{Al}_\delta)_2\text{O}_4:\text{Cr}^{3+}$ ($\delta = 0, 0.25, 0.50$). No long lifetimes were measured for $\delta = 0.75$ and $\delta = 1$.	105
Table 4.7. TL Peaks and Corresponding Trap Depths for $\text{Zn}(\text{Ga}_{1-\delta}\text{Al}_\delta)_2\text{O}_4:\text{Cr}^{3+}$ ($\delta = 0, 0.25, 0.50$).	107
Table 4.S1. Rietveld Refinement of $\text{Zn}(\text{Ga}_{1-\delta}\text{Al}_\delta)_2\text{O}_4$ ($\delta = 0.25, 0.50, 0.75$) from 11-BM Synchrotron X-Ray Diffraction.	116
Table 4.S2. Crystallographic Data of $\text{Zn}(\text{Ga}_{1-\delta}\text{Al}_\delta)_2\text{O}_4$ ($\delta = 0.25, 0.50, 0.75$) from Rietveld Refinement Resulting from 11-BM Synchrotron X-ray Diffraction Data.	117
Table 5.1. XANES peak fitting results for $\text{Zn}(\text{Ga}_{1-\delta}\text{Al}_\delta)_2\text{O}_4:\text{Cr}^{3+}$ ($\delta = 0 - 1$).	127
Table 5.2 Structural parameters around Cr^{3+} determined by fitting the Cr <i>K</i> edge EXAFS.	132
Table 6.1. Formation energies, ΔE_{vac} (eV) of potential vacancy sites in SrAl_2O_4 and $\text{SrAl}_2\text{O}_4:\text{Eu}^{2+}$ as determined by α -rich ($\alpha = \text{Sr}$ or O for the respective vacancy) conditions by PBE and PBE+U.	147
Table 6.2. Formation energies of potential vacancy sites in SrAl_2O_4 as determined by HSE06 at the μ_α limits.	148
Table 6.3. Formation energies of (a) $V_{\text{O}(1)}$, (b) $V_{\text{O}(2)}$, (c) $V_{\text{O}(3)}$, and (d) $V_{\text{O}(4)}$ in SrAl_2O_4 charged point defects at the oxygen-poor bounds. The solid lines show point charge that is favorable at a given E_F within E_g . Dashed lines show unfavorable point charge.	153
Table 7.1. ICP-OES of reverse micelle precursors establishing the amount of excess $\text{Sr}(\text{NO}_3)_2$ required to produce the desired stoichiometric ratios of Sr:Al.	168
Table 7.2. Rietveld refinement results for reverse micelle and solid state synthesis of $\text{SrAl}_2\text{O}_4:\text{Eu}^{2+}, \text{Dy}^{3+}$ using powder X-ray diffraction.	172
Table 7.3. Crystallographic results as determined by Rietveld refinement of powder X-ray diffraction.	173
Table 7.4. Calculated trap depths of reverse micelle and solid state synthesis from deconvolution of TL emission spectra.	182
Table 7.S1. Rietveld refinement results for reverse micelle and solid state synthesis of $\text{SrAl}_2\text{O}_4:\text{Eu}^{2+}, \text{Dy}^{3+}$ using powder X-ray diffraction of synthesis performed using a high-temperature furnace.	190

Table 7.S2. Crystallographic results as determined by Rietveld refinement of 191 powder X-ray diffraction. The samples were reacted using a high-temperature furnace.

Chapter 1

Introduction

1.1 Persistent Luminescent Phosphors

The phenomenon known as persistent luminescence (PersL) is a unique optical response whereupon the absorption of a photon the excited state slowly relaxes to the ground state on time scales far exceeding the expected length. This process, which is interchangeably referred to in the literature as phosphorescence, afterglow, or long-lasting phosphorescence, can occur for seconds, to as long as hours, or even days.^{1,2}

PersL is observed in crystalline inorganic semiconducting or insulating materials, called a host structure, that contain a luminescent center, which is an element generally a transition metals or rare-earth ion. The luminescent center undergoes electronic transitions that can be observed in the visible region of the electromagnetic spectrum. The resulting interaction between the host crystal structure and the luminescence center give rise to PersL and make up this class of persistent luminescent phosphors (PLPs).³

The discovery of PersL dates back at least one thousand years to the ancient Chinese; they mixed colors with a particular type of pearl shell or use in artwork and noticed the presence of visible light emitting from their paintings.⁴ The Bologna stone, also known as the Bologian Phosphor, found by Vincenzo Casariolo, is the first scientific example of a PLP reported in 1602.⁴ The naturally occurring afterglow that was observed was later attributed to impurities identified as BaS.⁵ However, the intentional incorporation of impurities, also known as “killers,” to induce long emission lifetimes was first introduced by substituting CaS with bismuth in 1866.^{4,6} Long luminescent lifetimes were significantly advanced by the discovery of Cu⁺ and Co²⁺ substituted ZnS in the early 20th century.^{4,6}

The long luminescent lifetime produced in $\text{ZnS}:\text{Cu}^+, \text{Co}^{2+}$ enabled the material to become commercially available in products such as luminous paints and watch dials ushering in an area of investigating new applications.^{3,6} Additional use in emergency signage and novelty items like children's toys have since been created with the discovery of the transformative PLP, green-emitting $\text{SrAl}_2\text{O}_4:\text{Eu}^{2+}, \text{Dy}^{3+}$, which was first reported in 1996.^{3,7} To date, there are now several commercially available PLPs with various emission colors, including blue emitting $\text{CaAl}_2\text{O}_4:\text{Eu}^{2+}, \text{Nd}^{3+}$ and $\text{Sr}_2\text{MgSi}_2\text{O}_7:\text{Eu}^{2+}, \text{Dy}^{3+}$, and red emitting $\text{Y}_2\text{O}_2\text{S}:\text{Eu}^{3+}, \text{Mg}^{2+}, \text{Ti}^{4+}$ (Table 1.1).⁸ In recent years, the use of PLPs has extended into bioanalytical applications that have been of great importance in the advancement of medical devices and imaging.⁹⁻¹³

Table 1.1 Overview Of Significant Persistent Luminescent Phosphors Studied Over The Last Century

Host material	Luminescent center	Co-dopant	$\lambda_{\text{em-max}}$ (nm)	Lifetime
ZnS^*	Cu^+	Co^{2+}	530	>3 h
CaS	Bi^{3+}	--	448	~20 min
CaGa_2S_4	Eu^{2+}	--	555	>30 min
$\text{Y}_2\text{O}_2\text{S}_2^*$	Eu^{3+}	$\text{Mg}^{2+}, \text{Ti}^{4+}$	570-710	~3 h
$\text{Ca}_2\text{Si}_5\text{N}_8^\dagger$	Eu^{2+}	Tm^{3+}	610	>1 h
$\text{SrAl}_2\text{O}_4^{*\dagger}$	Eu^{2+}	Dy^{3+}	520 nm	>30 h
CaAl_2O_4	Eu^{2+}	Nd^{3+}	440	>5 h
$\text{Sr}_4\text{Al}_{25}\text{O}_{14}^\dagger$	Eu^{2+}	Dy^{3+}	490	>20 h
$\text{Sr}_2\text{MgSi}_2\text{O}_7^*$	Eu^{2+}	Dy^{3+}	470	>10 h
$\text{ZnGa}_2\text{O}_4^\dagger$	Cr^{3+}	--	650-750	>1 h
MgGa_2O_4	Cr^{3+}	--	505	>15 min
$\text{Zn}_3\text{Ga}_2\text{Ge}_2\text{O}_{10}^\dagger$	Cr^{3+}	Pr^{3+}	696-713	>360

*indicates commercially available †indicates bioanalytical applications

Medical diagnostics, e.g., bioimaging or immunochromatographic lateral flow assays (LFAs), rely on photoluminescent labels, also called optical reporters or biomarkers, to provide diagnostic results relating to anatomical or physiological information in living systems as well as disease detection.^{8,13,14} Until recently, the optical reporters such as

quantum dots, organic fluorophores, and gold nanoparticles have been the most widely used source of photoluminescent labels. However, these materials have many drawbacks including autofluorescence, photobleaching, and tissue attenuation that can be overcome if the optical reporter is a PLP.¹³⁻¹⁵ PLPs as optical reporters have benefits for use in medical diagnostic tests stemming from the long lifetime, high emission intensity, and high signal-to-noise ratios they offer.⁸

Listed in Table 1.1 are PLPs that have been successfully used as *in vivo* and *in vitro* biomarkers due to their red ($\lambda_{em} \approx 610-700$ nm) to near-infrared (NIR) emission ($\lambda_{em} \geq 700$ nm) such as, $\text{Ca}_{0.2}\text{Zn}_{0.9}\text{Mg}_{0.9}\text{Si}_2\text{O}_6:\text{Eu}^{2+},\text{Dy}^{3+},\text{Mn}^{2+}$, $\text{Ca}_2\text{Si}_5\text{N}_8:\text{Eu}^{2+},\text{Tm}^{3+}$, $\text{ZnGa}_2\text{O}_4:\text{Cr}^{3+}$, and $\text{Zn}_3\text{Ga}_2\text{Ge}_2\text{O}_{10}:\text{Cr}^{3+}$.^{14,16-18} In light of the successful integration of PLPs in bioimaging, furthering the application to medical devices was achieved when $\text{SrAl}_2\text{O}_4:\text{Eu}^{2+},\text{Dy}^{3+}$ was reported as an optical reporter in a lateral flow immunoassay.¹³ Further expansion of the technology included the development of a medical device using smartphone time-gated imaging.¹² Moreover, $\text{SrAl}_2\text{O}_4:\text{Eu}^{2+},\text{Dy}^{3+}$ has also been shown to be a useful *in vivo* biomarker.^{19,20} Improvements in the synthesis of PLPs to produce particle sizes appropriate for bioanalytical applications and novel PLPs that tune emission wavelengths and lifetime decays has since become a major research focus.²¹⁻

25

1.2 Overview of Significant Persistent Luminescent Phosphors

For much of the early 20th century, $\text{ZnS}:\text{Cu}^+$ was the most well-known and studied PLP.²⁶ When co-doped with Co^{2+} , it produces a green emission, $\lambda_{em} \sim 530$ nm, and improved the long luminescent lifetime compared to the copper-only analog.^{3,6} The commercial production of $\text{ZnS}:\text{Cu}^+,\text{Co}^{2+}$ yield the first generation of “glow-in-the-dark” children’s toys,

watch dials, and luminous paints.^{6,7} However, ZnS:Cu⁺,Co²⁺ lacked efficient emission intensity and emission lifetime to further expand its applications. To overcome the shortcomings of emission intensity, radioisotopes, namely tritium (H³) and promethium (Pm¹⁴⁷) were added to applications such as luminous paint.⁷ Although successful in producing long luminescent lifetimes and brighter emission intensities in luminous paint, the isotopes proved to be environmentally toxic. As a result, there was an increasing demand for radioactive-free PLPs.^{7,26}

In the search for new PLPs, the alkaline earth aluminates $AEAl_2O_4:Eu^{2+}$ ($AE = Ca, Sr, Ba$) are among the most widely investigated.^{26,27} Out of the three compositions, $SrAl_2O_4:Eu^{2+}$ produces the most efficient and intense emission and the longest luminescent lifetime.^{1,26,27} The monoclinic phase of $SrAl_2O_4$ crystallizes in space group $P2_1$ (No. 4) containing a series of $[AlO_4]$ tetrahedra forming a three-dimensional corner connecting network with two independent crystallographic sites for the Sr atoms that form a six coordinated polyhedron, $[SrO_6]$ (Figure 1.1a).²⁸ Upon the substitution of Eu^{2+} onto the Sr^{2+} site, a broad photon emission corresponding to two peaks is produced due to Eu^{2+} occupying the two crystallographically independent sites of Sr^{2+} . Substitution on the Sr(2) site results in a blue emission, $\lambda_{em} \approx 450$ nm, which thermally quenches at 150 K, whereas substitution on the Sr(1) site generates a green emission, $\lambda_{em} \approx 520$ nm, Figure 1.1b.²⁹⁻³¹

$SrAl_2O_4:Eu^{2+}$ potential as a persistent luminescent phosphor was first realized in 1971 when photoconductivity and “glow curve” measurements were conducted. In this work the presence of lattice defects in the crystal structure were found to “trap” electron holes with continued excitation that were slowly released through thermal excitation generating long luminescent lifetimes of ≈ 70 min.³¹ The addition of Dy^{3+} as a co-dopant was

reported to not only improve the intensity of the emission but also extend the observable lifetime.⁷ In the decades since the discovery, $\text{SrAl}_2\text{O}_4:\text{Eu}^{2+},\text{Dy}^{3+}$ has gone on to become the most studied and commercially applicable PLP, quickly replacing $\text{ZnS}:\text{Cu}^+,\text{Co}^{2+}$.^{26,27}

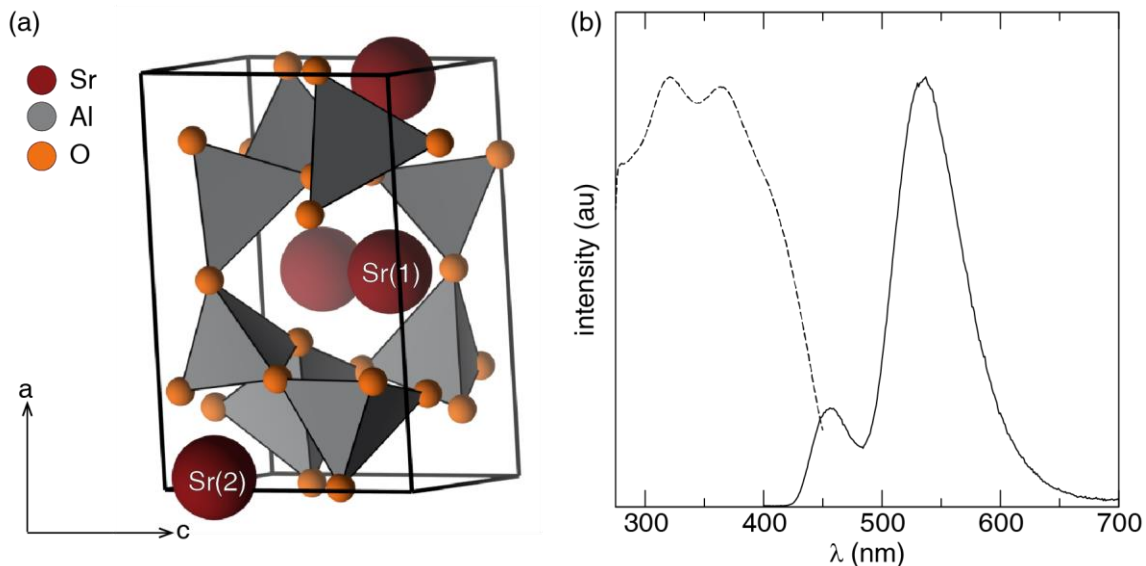


Figure 1.1 (a) The structure of $\text{SrAl}_2\text{O}_4:\text{Eu}^{2+}$ contains a three-dimensional network of corner-connecting tetrahedra with two independent Sr^{2+} sites sitting in the interstitials. (b) Photoluminescence spectra of $\text{SrAl}_2\text{O}_4:\text{Eu}^{2+}$ depicting a broad excitation spectrum (dashed line) that emits two peaks due to the two Sr^{2+} sites, $\lambda_{\text{em}} \approx 450$ nm and $\lambda_{\text{em}} \approx 520$ nm (solid line collected at 80K).

The exceptionally long luminescent lifetime of $\text{SrAl}_2\text{O}_4:\text{Eu}^{2+},\text{Dy}^{3+}$ coupled with its intense emission enables a vast range of applications for this PLP not only for emergency signage or novelty application, but there has also been significant interest in bioanalytical applications.^{8,27} However, this requires the preparation of high quality, pure PLPs with submicron sized particles. Researcher have turned to a variety of synthesis methods to achieve this goal including, but not limited to, sol-gel,^{32,33} combustion,^{34,35} hydrothermal,³⁶ and reverse micelle routes.²⁴ Although moderately successful, to produce a pure monoclinic phase of $\text{SrAl}_2\text{O}_4:\text{Eu}^{2+},\text{Dy}^{3+}$, reaction temperatures $\geq 1300^\circ\text{C}$

are required, which creates large agglomerated particles. The solution based methods investigated, often produce phase impurities that include the blue emitting polymorph $\text{Sr}_4\text{Al}_{14}\text{O}_{25}:\text{Eu}^{2+},\text{Dy}^{3+}$.^{24,27} Therefore, mechanical milling to physically reduce the particle have also been investigated, but found that milling caused oxidation of Eu^{2+} to Eu^{3+} , hindering the luminescence.^{37,38}

In light of the fact that $\text{SrAl}_2\text{O}_4:\text{Eu}^{2+},\text{Dy}^{3+}$ is the most well-known PLP due to its exceptional optical properties and array of subsequent applications, it has been the subject of extensive research into the mechanism that drives PersL.^{28,29,39} The focus of determining the PersL mechanism has generally centered on the role of the 5d-orbitals of the co-dopant, namely Dy^{3+} , and the oxidation state of Eu and Dy. While previously investigated via X-ray absorption spectroscopy (XAS),^{40,41} research has more recently turned to first principle calculations to investigate the presence of anion vacancies and their role in the mechanism in $\text{SrAl}_2\text{O}_4:\text{Eu}^{2+}$ and isostructural $\text{CaAl}_2\text{O}_4:\text{Eu}^{2+}$.^{42,43} Combining these efforts have provided valuable insight into what drives persistent luminescence in PLPs.

Another class of PLPs widely investigated is the alkaline earth Åkermanite structure type with the general formula $\text{AE}_2\text{MgSi}_2\text{O}_7:\text{Eu}^{2+}$ ($\text{AE} = \text{Ca}, \text{Sr}, \text{Ba}$).²⁶ Of these, $\text{Sr}_2\text{MgSi}_2\text{O}_7:\text{Eu}^{2+},\text{Dy}^{3+}$ generates the longest reported long luminescent lifetime out of the series.⁴⁴ The PLP crystallizes in the tetragonal space group $P\bar{4}2_1m$ (No. 113) and contains only one crystallographic site for Sr^{2+} , which occupies space between five-membered rings of alternating corner-connected $[\text{SiO}_4]$ and $[\text{MgO}_4]$ tetrahedra (Figure 1.2a).⁴⁵ Substituting Eu^{2+} on to the Sr^{2+} gives rise to a reported emission wavelength $\lambda_{\text{em}} \approx 470$ when excited by $\lambda_{\text{ex}} \approx 365$ nm, shown in Figure 1.2b, and a lifetime of >10 h.^{44,46}

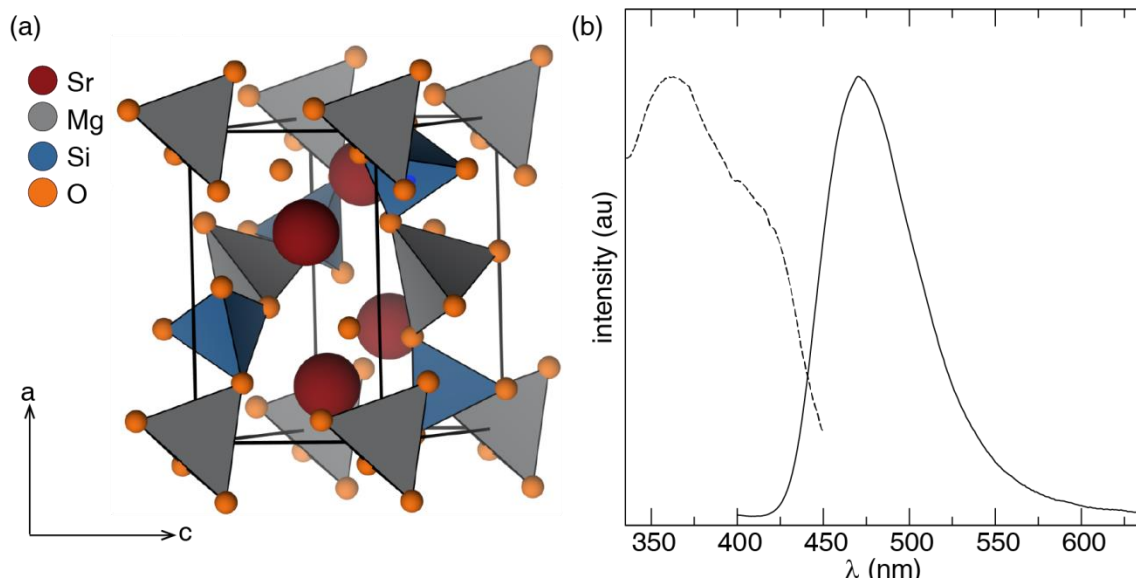


Figure 1.2 (a) The structure of $\text{Sr}_2\text{MgSi}_2\text{O}_7:\text{Eu}^{2+}$ contains five-membered rings of alternating corner-connecting tetrahedra of $[\text{SiO}_4]$ and $[\text{MgO}_4]$. Sr^{2+} occupies one crystallographic site that sits in the middle of the five-membered rings. (b) Photoluminescence spectra depict a broad excitation peak (dashed line) that produces a single emission peak at $\lambda_{\text{em}} \approx 470$ nm (solid line).

Due to the single crystallographic site for AE^{2+} in this structure type, there is an interesting opportunity to study the effects of crystal field splitting on long luminescent lifetimes, as well as, in depth analysis of the optically stimulated luminescence (OSL) of the trapping-detrapping-retrapping mechanism of electrons.^{25,47,48} Additionally, local structure investigation of the Eu^{2+} site via X-ray absorption spectroscopy (XAS) confirmed there is no Eu^+ or Dy^{4+} present in the system, providing valuable insight into the persistent luminescent mechanism.^{49,50} Also, extensive research into how co-dopants affect the performance and their contribution to the mechanism of persistent luminescence in $\text{Sr}_2\text{MgSi}_2\text{O}_7:\text{Eu}^{2+}$ has been completed.^{51,52} The wealth of information provided by studying this PLP has made it one of the valuable PLPs known from a fundamental science standpoint.

Even though Eu^{2+} substituted PLPs have been at the forefront of investigations, another class of PLPs that has proven to be of enormous value are the spinel-type crystal structures substituted with Cr^{3+} as the luminescent center. The most widely studied phase is $\text{ZnGa}_2\text{O}_4:\text{Cr}^{3+}$, which crystallizes in the cubic closed packed structure, space group $Fd\bar{3}m$ (No 227), with eight tetrahedrally coordinated Zn^{2+} sites and sixteen octahedrally coordinated Ga^{3+} sites per formula unit (Figure 1.3a).⁵³⁻⁵⁵ Substituting Cr^{3+} onto the Ga^{3+} site gives rise to a red emission, $\lambda_{\text{em-max}} \approx 695$ nm (solid line) when excited by $\lambda_{\text{ex}} \approx 400$ nm or 550 nm (dashed line), Figure 1.3b.⁵⁵⁻⁵⁷ Long luminescent lifetimes have been reported to be ≥ 1 h which can be enhanced by the addition of co-dopants such as Bi^{3+} .^{55,58,59} Interestingly, the NIR emission produced by the Cr^{3+} has led to applications such as *in vivo* imaging of tumors and grafted cells.^{11,60} Furthermore, $\text{ZnGa}_2\text{O}_4:\text{Cr}^{3+}$ has been successfully modified with substitution of Sn^{4+} and Ge^{4+} onto the Ga^{3+} site to produce novel PLPs such as $\text{Zn}_3\text{Ga}_2\text{Ge}_2\text{O}_{10}:\text{Cr}^{3+}$ which has a reported lifetime >360 h.^{59,61} These gallogermanates, when co-doped with Pr^{3+} , have also been shown to be effective for *in vivo* bioimaging.²²

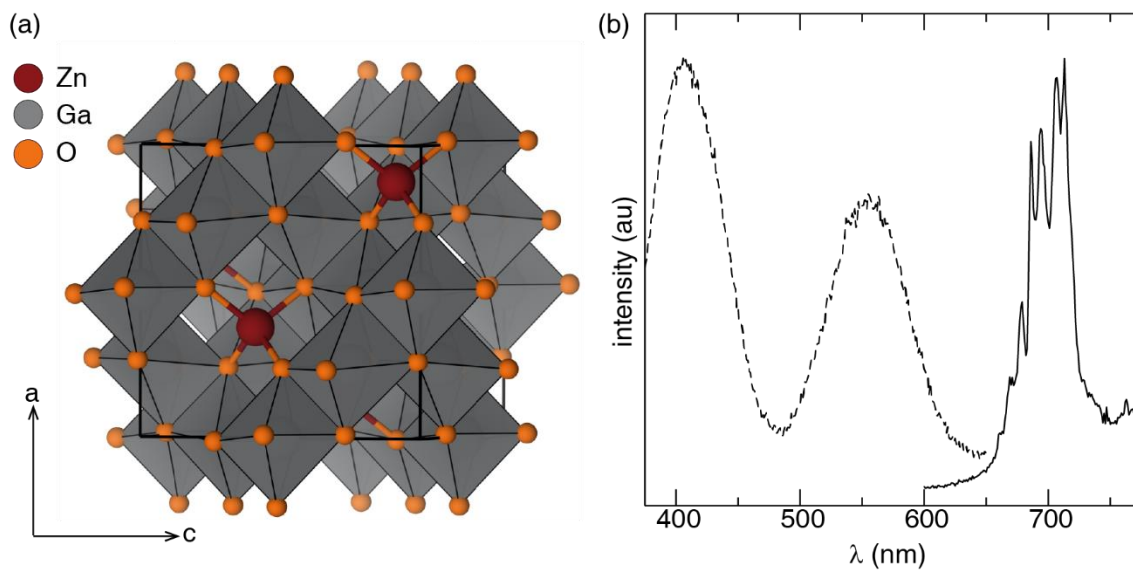


Figure 1.3 (a) The structure of $\text{ZnGa}_2\text{O}_4:\text{Cr}^{3+}$ is a cubic closed packed system with edge-sharing octahedra and corner-connected tetrahedra. (b) Photoexcitation spectra from Cr^{3+} results in two peaks, $\lambda_{\text{ex}} \approx 400 \text{ nm}$ and 550 nm (dashed line) and an emission spectra (solid line) in the NIR with several distinct peaks.

More importantly, the unique characteristic of the emission spectra and the relationship with the observed persistent luminescence in $\text{ZnGa}_2\text{O}_4:\text{Cr}^{3+}$ has spurred significant research into this material.⁵³ The consequence of lattice defects within the crystal structure has been investigated to the extent that the emission at $\lambda = 695 \text{ nm}$ has been identified as an anti-site defect responsible for the persistent luminescence.⁶² Further research into the local structure, which includes electron paramagnetic resonance (EPR), ¹⁷Ga NMR, and XAS have established the nature of the defects and their role in the trapping-detrapping of electrons.^{59,62-65} Although great strides in understanding the role of lattice defects in the persistent luminescence has been accomplished, more work in understanding their role is needed.

1.3 Mechanism of Persistent Luminescence

1.3.1 Photoluminescence of Eu^{2+} Substituted Persistent Luminescent Phosphors The photoluminescence of persistent luminescent phosphors (PLPs) follows a modified Jablonski diagram for Eu^{2+} substituted in a crystal structure, shown in Figure 1.4. Photoexcitation is achieved by exciting an electron in its 4*f*-orbitals (ground state) into the 5*d*-orbitals via an external energy source (typically ultraviolet-visible light). The electron in the excited state then relaxes via non-radiative relaxation to the lowest energy 5*d*-orbitals, where it will either continue to non-radiatively relax through internal conversion or a photon is emitted. If the material emits a photon, the emission lifetime is dependent on the spin-orbit coupled transition of the luminescent center.⁶⁶

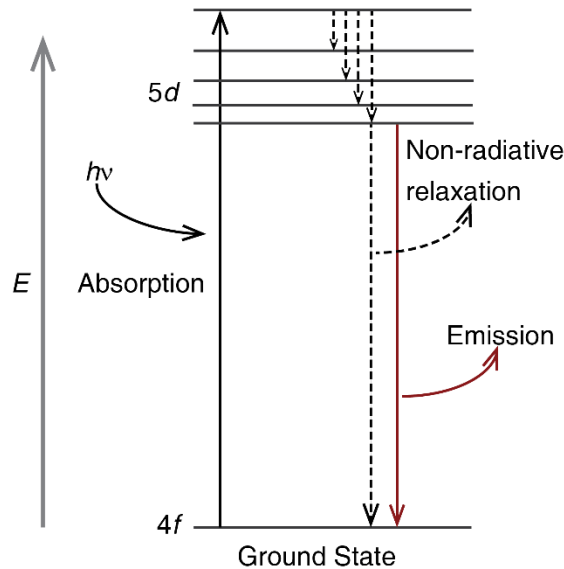


Figure 1.4. Modified Jablonski diagram illustrating the luminescence mechanism of Eu^{2+} .

Typically, the emission lifetime of Eu^{2+} is estimated to be $\approx 0.5 \mu\text{s} - 1 \mu\text{s}$ in the spin-orbit coupled transition from ${}^6P_j \rightarrow {}^8S_{7/2}$.^{67,68} However, in persistent luminescent phosphors,

emission lifetimes have been reported on the order of minutes and in some cases hours.¹ Early reports of PLPs, including ZnS and SrAl₂O₄:Eu²⁺, suggested that lattice defects in the crystal structures trapped charge carriers, e.g., electrons or holes upon excitation.^{6,31} The eventual thermal release of these electrons produced observable long emission lifetimes. The true mechanism that gives rise to persistent luminescence is still under debate; however, there is general agreement on the trapping-detrapping of an electron after it has been photoionized into the conduction band.¹

1.3.1.1 The Matsuzawa model The first suggested mechanism of persistent luminescence was reported for SrAl₂O₄:Eu²⁺ and considered that lattice defects act as the trap states and holes as the charge carriers.³¹ Photoconductivity measurements suggested the lattice defects arose from Sr²⁺ vacancies that acted as hole donors.⁷ Holes acting as the main charge carrier trapped by lattice defect was further supported using photoconductivity experiments when SrAl₂O₄:Eu²⁺ co-doped with Dy³⁺, as illustrated in Figure 1.5.⁷

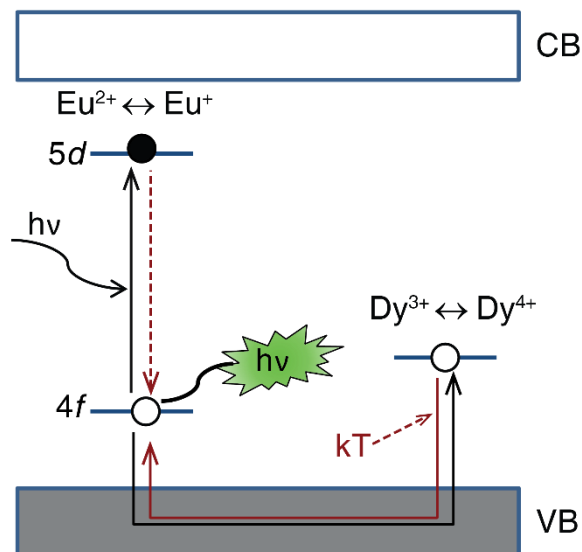


Figure 1.5 Persistent luminescent mechanism of $\text{SrAl}_2\text{O}_4:\text{Eu}^{2+}, \text{Dy}^{3+}$ as proposed by Matsuzawa *et al.* An electron in Eu^{2+} is excited from the $4f$ -orbital to $5d$ -orbital. Its hole is conducted through the VB and is trapped by the $4f$ -orbital of Dy^{3+} . Thermal energy (kT) releases the hole and it is recombined with the relaxed electron to produce a photon. Excitation and trapping are black lines, thermal release and relaxation are red. Electron filled black circle, hole is open circle.

When Dy^{3+} acts as a co-dopant, an electron from Eu^{2+} is promoted to the $5d$ -orbitals and is reduced to Eu^+ ; its hole is then carried through the valence band to the $4f$ -orbitals of Dy^{3+} oxidizing it to Dy^{4+} . Applying thermal energy (kT) to the trapped hole releases the electron that subsequently with Eu^+ to produce a photon and return to Eu^{2+} .⁷ The suggested oxidation of Dy^{3+} to Dy^{4+} was accepted because there was known stability of the tetravalent state of Nd in phosphors containing fluorine.⁶⁹ It was further supported because of the low transition energy of $4f \rightarrow 5d$ -orbitals and their high charge-transfer energies.⁷

This model was accepted for many years and subsequent experimental methods, such as thermoluminescence (TL),⁷⁰ photoconductivity,⁷¹ and EPR⁷² were used to validate the model. However, with a lack of experimental evidence to support it, further research was

conducted to explain how PLPs exhibit their extraordinary lifetimes. Nevertheless, in the years that followed, many new PLPs were discovered and this model was used to describe their persistent luminescent lifetimes.²⁶

1.3.1.2 The Dorenbos Model The continued investigation into the PersL mechanism was required because the Matsuzawa model could not explain the long luminescent lifetime of singly doped $\text{SrAl}_2\text{O}_4:\text{Eu}^{2+}$.²⁶ Further, reports disputing the reduction of Eu^{2+} to Eu^+ and the oxidation of Dy^{3+} to Dy^{4+} also called this model into question.⁴¹ In particular, theoretical calculations of the lanthanide energy levels in $\text{SrAl}_2\text{O}_4:\text{Eu}^{2+}$ as well as several other inorganic phosphors such as, $\text{YPO}_4:\text{Eu}^{3+}$ and $\text{CaGa}_2\text{S}_4:\text{Eu}^{2+}$, established localized energy levels of the rare earth luminescent center.⁴⁰ Figure 1.6 shows the energy scheme for SrAl_2O_4 where n is the number of electrons in the rare earth $4f$ -orbitals, E_{VC} is the energy required to promote an electron into the conduction band, E_{v} is the energy level of the top of the valance band, and E^{ex} is the energy of the creation of an electron-hole pair.⁴⁰ The energy scheme of the RE^{2+} ions show the $5d$ -orbitals (red line) lie within a favorable energy window, allowing an electron to be promoted into the conduction band via photoionization. Additionally, it revealed the $4f$ -orbitals of Eu^{2+} were not in an energy window favorable for an hole to act as a charge carrier. This was because for Dy^{3+} 's $4f$ -orbitals to act as a trap state, they needed to lie above the valence band; in reality, they lie just below it.

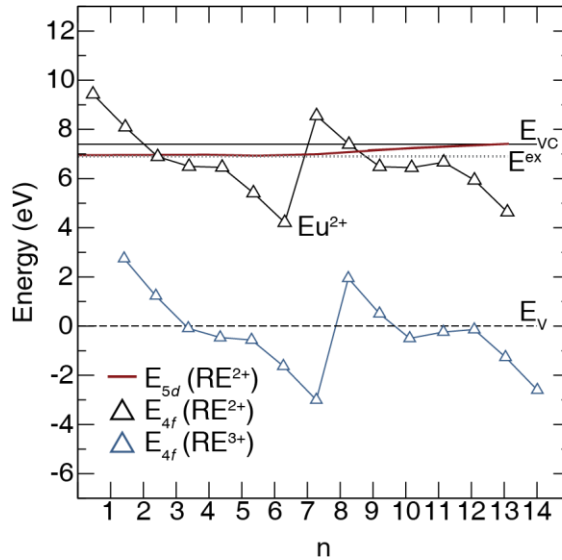


Figure 1.6 Energy schemes of rare earth 4f-orbitals (RE^{2+} black triangles and RE^{3+} blue triangles) ions required to promote an electron into the conduction band (E_{vc}). n is the number of electrons, E^{ex} is the energy required to produce an electron-hole pair, and E_v is the top of the valence band.

Based on this information the proposed Dorenbos model is presented in Figure 1.7. In this model it was shown that an electron upon continuous excitation would be photoionized through the 5d-orbitals into the conduction band. The electron would then be trapped by an additional rare earth (RE) co-dopant. In doing so, Eu^{2+} would become oxidized and the rare earth co-dopant would become reduced, which is contrary to the Matsuzawa model. Further, experimental evidence suggested that a trap state was present at approximately 0.95 eV when Dy^{3+} was used as a co-dopant in $SrAl_2O_4:Eu^{2+}$.⁷³ This was consistent with calculations of the energy levels of 5d-orbitals present in $Dy^{3+} \leftrightarrow Dy^{2+}$ by Dorenbos (Figure 1.6).⁴⁰ However, the Dorenbos model, similar to the Matsuzawa model, neglected the potential for trap states in the absence of a RE co-dopant.

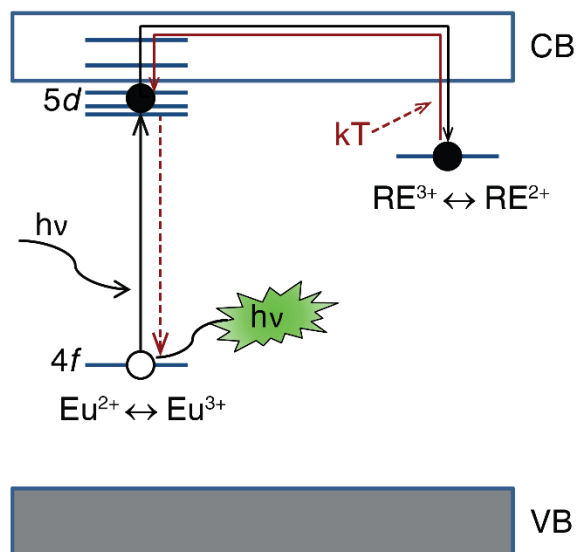


Figure 1.7 Persistent luminescent mechanisms as proposed by Dorenbos. An electron in Eu^{2+} is excited from the $4f$ -orbital to $5d$ -orbital and is photoionized into the CB. The electron is trapped in the $5d$ -orbital of a RE co-dopant. The hole remains in the $4f$ -orbital. Thermal energy (kT) releases the electron and it is recombined with its hole to produce a photon. Excitation and trapping are black lines, thermal release and relaxation are red. Electron filled black circle, hole is open circle.

1.3.1.3 The Clabau Model Although the Dorenbos model did not consider the presence of lattice defects in PLPs, the model did verify the location of the $5d$ -orbitals of Eu^{2+} , which was undoubtedly an important advancement in understanding the PersL mechanism. In an effort to consider the role of lattice defects, more specifically anion vacancies, EPR was conducted on $\text{SrAl}_2\text{O}_4:\text{Eu}^{2+}$ under excitation by UV light.^{28,74} In this study, a decrease in Eu^{2+} concentration was observed during excitation, followed by an increase upon termination of the UV light source. This suggested that Eu^{2+} was oxidized during excitation and was, therefore, participating in the electron trapping-detrapping process.^{26,28,74} The Clabau model was thus proposed and presented in Figure 1.8.

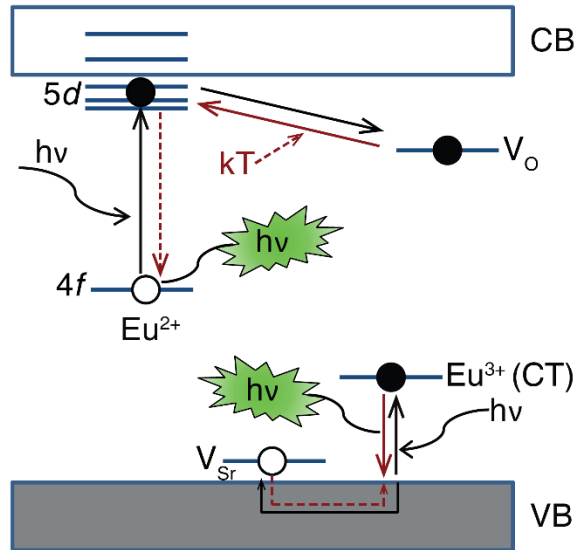


Figure 1.8 Persistent luminescent mechanism as proposed by Clabau *et al.* An electron in Eu^{2+} is excited from the 4f-orbital to 5d-orbital is trapped in a anion vacancy (V_o). The hole remains in the 4f-orbital. Thermal energy (kT) releases the electron and it is recombined with its hole to produce a photon. Another electron from Eu^{3+} is excited via CT and its hole is trapped in a cation vacancy (V_{Sr}). CT releases the hole and it recombines to produce a photon. Excitation and trapping are black lines; thermal release and relaxation are red. Electron filled black circle, hole is open circle.

Clabau *et al.* considered the persistent luminescence mechanism in the absence of a rare earth co-dopant; the 5d-orbitals of Eu^{2+} were placed close to the bottom of the conduction band, similar to the Dorenbos model. The Clabau model, however, differs in two critical ways: first an Eu^{2+} electron is excited but not photoionized into the conduction band, and secondly, the presence of Eu^{3+} in the structure, due to inefficient reduction of Eu^{2+} during synthesis, is considered to be participating in not only a trapping-detraping mechanism via charge transfer (CT), but also the emission of a photon. This model suggested that the second low temperature peak, at 450 nm, was produced by the recombination of a Eu^{3+} hole having been trapped by a cation vacancy, presumably Sr^{2+} . Simultaneously, an excited Eu^{2+} electron is trapped via direct transfer to anion vacancies, which is followed by the recombination of its hole and subsequent emission

of the room temperature photon observed at 520 nm. The flaw in this model is in the presence of an a second emission peak at low temperatures. Reports of thermal quenching of $\text{SrAl}_2\text{O}_4:\text{Eu}^{2+}$ and extensive crystallographic studies confirmed that the peak observed at 450 nm is due to $\text{SrAl}_2\text{O}_4:\text{Eu}^{2+}$ having two crystallographic sites for Sr^{2+} . When a luminescent center is substituted into this host structure, it can lie on either of the sites and the difference in polyhedron size of the two sites gives rise to the two observable peaks.²⁹ However, the Clabau model did successfully provide information in regards to the mechanism in the absence of a co-dopant by showing how lattice defects participate in the PersL mechanism.

1.3.1.4 Ab Initio Model from Density Functional Theory (DFT) Experimental efforts on other Eu^{2+} substituted phosphors, such as $\text{AE}_2\text{MgSi}_2\text{O}_7:\text{Eu}^{2+},\text{Dy}^{3+}$ ($\text{AE}=\text{Ca}$ and Sr) and $\text{CaAl}_2\text{O}_4:\text{Eu}^{2+},\text{Nd}^{3+}$, began to support a mechanism that combined the information gained from Dorenbos and Clabau. Moreover, investigation into the oxidation states of Eu^{2+} and Dy^{3+} using synchrotron X-ray absorption (XAS) and EPR established that there was no reduction of Eu^{2+} to Eu^+ and no oxidation of Dy^{3+} to Dy^{4+} .⁴⁹ The combination of these results allows one to confidently reject the mechanism suggested by Matsuwaza; however, the results of his photoconductivity experiments cannot be ignored. Recently, *ab initio* studies of $\text{CaAl}_2\text{O}_4:\text{Eu}^{2+},\text{Nd}^{3+}$ were conducted to verify the favorability of the vacancy formation in persistent luminescence and the impact of a trivalent rare earth co-dopant.⁴³ The results of these calculations confirmed the theory of combining the previous experimentally driven mechanisms. Figure 1.9 presents the suggested trapping mechanism calculated using DFT.

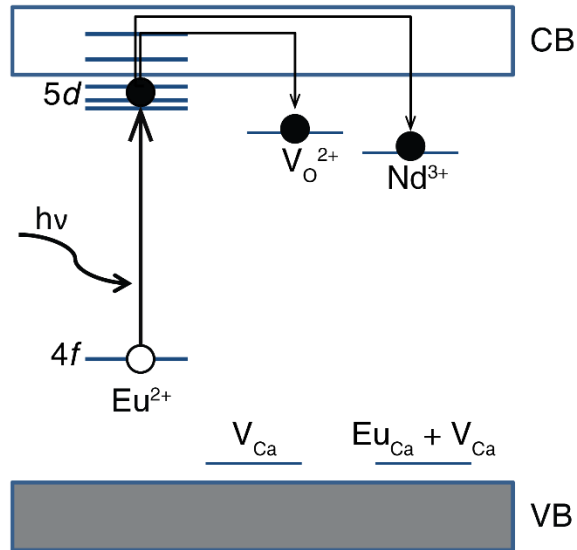


Figure 1.9 Persistent luminescence model proposed by Qu *et al.* An electron in Eu^{2+} is excited from the $4f$ -orbital to $5d$ -orbital and is photoionized into the CB. The electron is trapped in either an anion vacancy (V_O^{2+}) or the $5d$ -orbital of Nd^{3+} . The hole remains in the $4f$ -orbital. Thermal energy (kT) releases the electron and it is recombined with its hole to produce a photon. Cation vacancies (V_Ca and $\text{Eu}_\text{Ca} + \text{V}_\text{Ca}$) lie close to the top of the VB and do participate in the mechanism. Excitation and trapping are black lines; thermal release and relaxation are red. Electron filled black circle, hole is open circle.

Qu *et al.* were able to show that cation and anion vacancies form simultaneously, with the anion (V_O^{2+}) forming close to the bottom of the conduction band and the cation (V_Ca) forming close to the top of the valence band.⁴³ This finding validated both experimental EPR measurements, which suggest the formation of V_O acting as trap states, and the theoretical model of the presence of $5d$ -orbitals of the trivalent rare earth. More importantly, it shows that there are lattice defects, in this case combinations of two separate cation vacancies, lying close to the top of the valence band. The vacancy, $\text{Eu}_\text{Ca} + \text{V}_\text{Ca}$, is likely a similar vacancy observed in the $\text{SrAl}_2\text{O}_4:\text{Eu}^{2+}$, Dy^{3+} photoconductivity experiment that showed a trap state lying close to the valence band. The conclusion of the *ab initio* calculations seemed to confirm both V_O and $5d$ -orbitals of

a co-dopant will form in energetically favorable windows from the bottom of the conduction band to act as electron trap states in PLPs. However, the V_{Ca} do not act as trap states and instead act to stabilize the V_O^{2+} , while Nd^{3+} can both trap electrons and act as an electron donor.

1.3.2 Photoluminescence of Cr^{3+} Substituted Persistent Luminescent Phosphors When

Cr^{3+} acts as a luminescent center, the excitation and emission of a photon occurs within the $3d$ -orbitals, whereas in Eu^{2+} excitation and emission is a $4f \leftrightarrow 5d$ transition. Typically, Cr^{3+} is substituted onto octahedrally coordinated polyhedra, and therefore, can be best described using a Tanabe-Suagno diagram for a $3d^3$ transition metal in an octahedron (O_h). Visualized in Figure 1.10, is the spin-allowed transitions of an excited electron in this coordination environment, ${}^4A_2 \rightarrow {}^4T_1$ (4F) and ${}^4A_2 \rightarrow {}^4T_2$ (4F). Figure 1.10b illustrates the spin-forbidden transition of the emission, ${}^2E \rightarrow {}^4A_2$, in an octahedral environment and results in a near-infrared (NIR) phosphorescent emission. It is worth noting the $5d \rightarrow 4f$ (${}^6P_j \rightarrow {}^8S_{7/2}$) spin-allowed transition of Eu^{2+} is considered as a fluorescence transition because the electron that relaxes to the ground state is in a singlet state when in the $5d$ -orbitals. This is contrary to Cr^{3+} , which undergoes an intersystem crossing and the excited electron thus relaxes from a triplet (2E) state to a singlet state (4A_2). Therefore, terminology becomes critical: photon emission in the absence of an intersystem crossing is a fluorescence mechanism and leads to emission lifetimes of $<10^{-10}$ to 10^{-7} sec whereas an intersystem crossing produces a phosphorescent mechanism with emission lifetimes of 10^{-5} to 10^{+3} sec. Nevertheless, due to the persistent luminescence mechanism, both fluorescent and phosphorescent materials can generate emission lifetimes on the order of minutes.

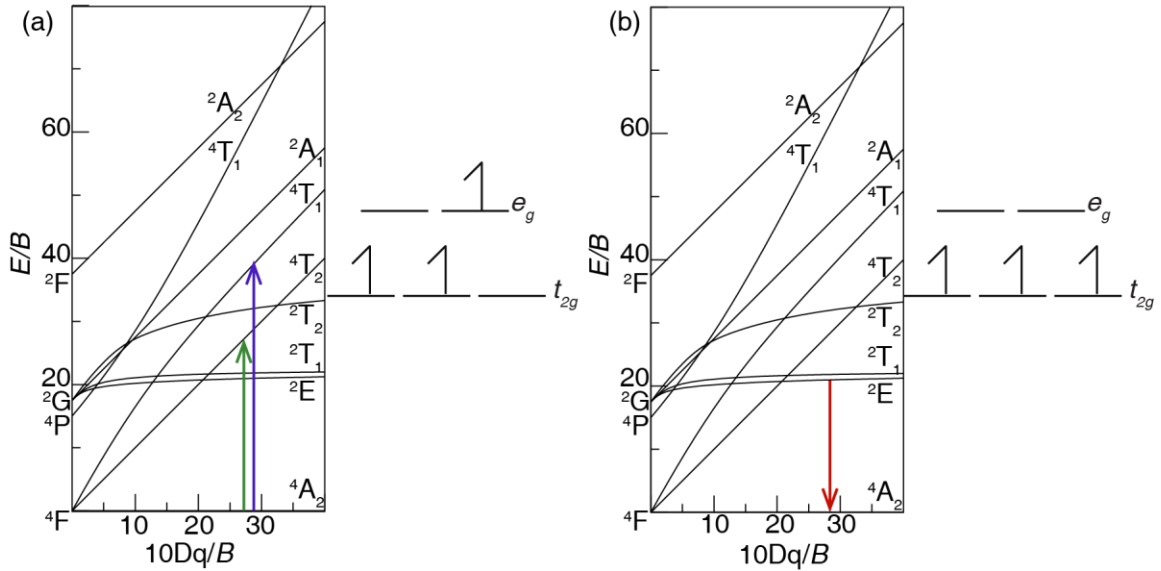


Figure 1.10 Tanabe-Sugano diagrams for a $3d^3$ transition metal in O_h coordination. The $3d$ -orbitals are split into double degeneracy (e_g) and triple degeneracy (t_{2g}). (a) is the spin-allowed transition from the ground state to the first excited state: $4A_2 \rightarrow 4T_1$ ($4F$) (purple arrow) and $4A_2 \rightarrow 4T_2$ ($4F$) (green arrow) and electron (half arrow) is excited to an e_g orbital. (b) The spin-forbidden relaxation of an electron from the first excited state, $2E \rightarrow 4A_2$ (red arrow) and all electrons lie in t_{2g} orbitals.

1.3.2.1 Persistent Luminescent Mechanism of Cr^{3+} Investigations into the Cr^{3+} PersL mechanism has largely revolved around experimental evidence such as XAS, EPR, and TL. The spinel-type structure of $ZnGa_2O_4:Cr^{3+}$ has been studied with these methods at great length.^{55,62-64,75} Crystallographic evidence based on powder X-ray diffraction (PXRD), coupled with Rietveld refinements and nuclear magnetic resonance (NMR) spectroscopy, has shown there is a slight inversion of the Zn and Ga sites.⁵⁹ This inversion is believed to be the origin of trap states found within the host structure.^{59,62,65} Figure 1.11 visualizes a generalized understanding of the PersL mechanism in $ZnGa_2O_4:Cr^{3+}$. In this case, an electron-hole pair in their ground state ($4A_2$), next to an anti-site defect ($[Cr^{3+}, Ga_{Zn}^+ + Zn_{Ga}^-]_{N2}$), are excited to $4T_1$ ($4F$) excited state. The pair is then trapped by the anti-site defect, or trap state. Thermal energy (kT) is applied to

release the electron-hole pair that relax to the 2E where a photon is emitted in the form of NIR light.^{62,65}

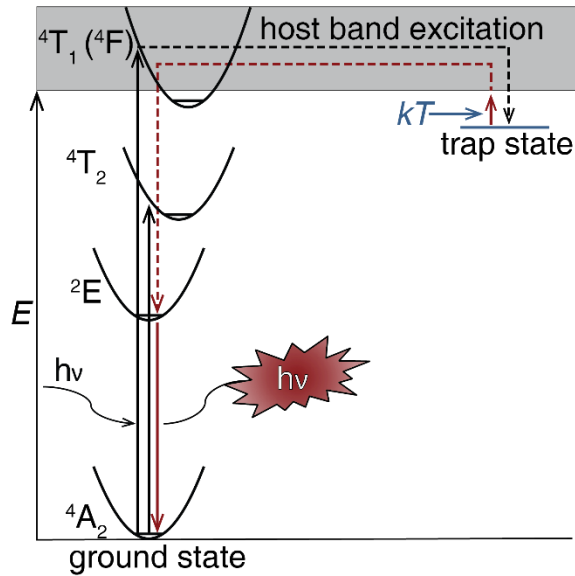


Figure 1.11 A general proposed model of the persistent luminescent mechanism of ZnGa₂O₄:Cr³⁺. An electron is excited from ${}^4A_2 \rightarrow {}^4T_1({}^4F)$, it is trapped in a trap state, thermal energy (kT) releases it, and the ${}^2E \rightarrow {}^4A_2$ transition releases a photon. Excitation and trapping black arrows, relaxation and detrapping are red arrows.

A secondary trapping mechanism can arise when an electron is excited to the lower energy excited state (4T_2). The possible mechanism is shown in Figure 1.12. These trap states are considered to be closer to the excited electron-hole pair and therefore require less energy to populate and depopulate the trap.^{62,65}

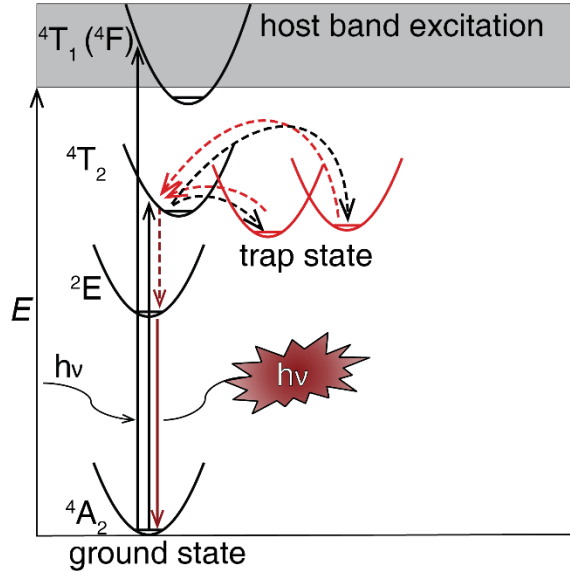


Figure 1.12 A proposed secondary model of the persistent luminescence mechanism in $\text{ZnGa}_2\text{O}_4:\text{Cr}^{3+}$. An electron is excited from ${}^4\text{A}_2 \rightarrow {}^4\text{T}_2$ (${}^4\text{F}$), it is trapped in a trap state, and the ${}^2\text{E} \rightarrow {}^4\text{A}_2$ transition releases a photon. Excitation and trapping black arrows, relaxation and detrapping are red arrows.

It is generally agreed that, for Cr^{3+} , PersL arises from lattice defects; however, the influence of co-dopants in these materials remains to be understood. Interestingly, investigation into the local structure of some spinel-type structures reveal that an increase in lattice defects quench PersL in Cr^{3+} PLPs, which is contrary to the findings in Eu^{2+} substituted PLPs. Thus, a robust investigation of local structure environments of these PLPs will provide valuable insight into the properties that drive PersL.

1.4 Trap States

1.4.1 Types of Trap States Giving Rise to Persistent Luminescence A persistent luminescent phosphor's ability to produce its unique long luminescent lifetime revolves around a charge carrier, *i.e.*, electron, hole, or electron-hole pair, to be "trapped" in a so-called trap state.^{1,26} The relationship between the trap state and a host structure's

conduction band becomes a critical pathway for depopulation of the trap states at room temperature.⁷⁶ Depopulation of a trap state is induced by an activation energy (E_A), or trap depth, available at room temperature. A trap should ideally lie ≥ 0.4 eV to ≤ 1.0 eV with respect to the bottom of the conduction band, or the conduction band minimum (CBM), with an ideal trap depth of 0.65 eV.^{76,77} Thus, shallow traps, those < 0.4 eV, will depopulate immediately at room temperature, whereas those > 1.0 eV require more energy than is available and will remain trapped.⁷⁶ Therefore, the extensive effort has gone into investigating the source of trap states and the ability to control their position since the discovery of PLPs. Classically, the origin of trap states have been described in two ways: firstly, lattice defects in the host crystal structure, and second, unpopulated orbitals from a co-dopant.^{26,28,40,76,78-80}

The long luminescent lifetimes of PLPs with a single luminescent center, i.e., Eu^{2+} or Cr^{3+} , has been observed in common PLPs such as, $\text{SrAl}_2\text{O}_4:\text{Eu}^{2+}$, $\text{Sr}_2\text{MgSi}_2\text{O}_7:\text{Eu}^{2+}$, and $\text{ZnGa}_2\text{O}_4:\text{Cr}^{3+}$.^{25,31,52,55} Thermoluminescence measurements reveal trap depths lying within the established range needed to produce PersL for each of the three examples. This evidence supports the notion that lattice defects present in the crystal structure give rise to the observable long luminescent lifetimes. Lattice defects present in PLPs have been identified to be vacancies, or point defects; these defects can be classified as either as Schottky defects, which are unoccupied anion or cation sites, Frenkel defects, which are a displaced atom onto an interstitial site, or anti-site defects, where two atoms of different types change positions.^{42,43,81} Efforts to establish the type of lattice defects were carried out using computational methods for $\text{SrAl}_2\text{O}_4:\text{Eu}^{2+}$ and $\text{CaAl}_2\text{O}_4:\text{Eu}^{2+}$. In both studies, formation energies of anion and cation vacancies in the form of Schottky defects were calculated and revealed not only favorable conditions for the formation of

anion vacancies, but also their relative E_A to the CBM.^{42,43} Furthermore, it was shown that $\text{ZnGa}_2\text{O}_4:\text{C}$ is composed of anti-site defects, an inversion of the Zn and Ga sites, as well as Frenkel defects of the Zn atoms paired with Schottky defects of the oxygen atoms.⁸¹ The favorable energy formation of these defects in $\text{ZnGa}_2\text{O}_4:\text{Cr}^{3+}$ rely on their proximity to the $[\text{CrO}_6]$ polyhedron, suggesting trap states that form closer to the Cr^{3+} are likely to be populated and depopulated more easily, and those further from the Cr^{3+} require more energy to be populated and depopulated, leading to longer luminescent lifetimes.^{65,81} Although lattice defects have been shown to act as trap states and produce PersL, the intrinsic nature of their formation is still a matter in need of investigation.

In addition to the presence of lattice defects, substituting a co-dopant, which is usually a second or even third luminescent center, can act as both a charge donor and a trap state.^{28,40} Co-dopants are normally a trivalent rare earth ions, e.g. Dy^{3+} or Nd^{3+} ; however, transition metals like Cr^{3+} have been shown to be effective as well.^{7,52,82,83} In the case of $\text{SrAl}_2\text{O}_4:\text{Eu}^{2+}$, when boric acid (H_3BO_3) is used as a flux to aid in the synthesis of a pure phase product, B^{3+} has also been shown to induce trap states.⁸⁴ Identifying the most appropriate co-dopant that improves luminescent lifetimes has been achieved by determining the relationship between the ground state energy levels of the $4f$ -orbitals of the rare earth elements (RE^{2+} is red and RE^{3+} is black) and their trap depths (blue), (Figure 1.13).⁵² Here, the ground state energies are with respect to the VBM and the trap depths are with respect to the CBM in $\text{Sr}_2\text{MgSi}_2\text{O}_7:\text{Eu}^{2+}, \text{RE}^{3+}$. In this study, the main trap depths were determined to be from lattice defects, *i.e.*, anion vacancies, and follow a similar trend in energy formation as the $4f$ -orbitals of rare earth elements. The conclusion postulated that the addition of a co-dopant would enhance the long

luminescent lifetime by providing charge carriers to populate the trap states created by the anion vacancies instead of the creation new trap states.⁵²

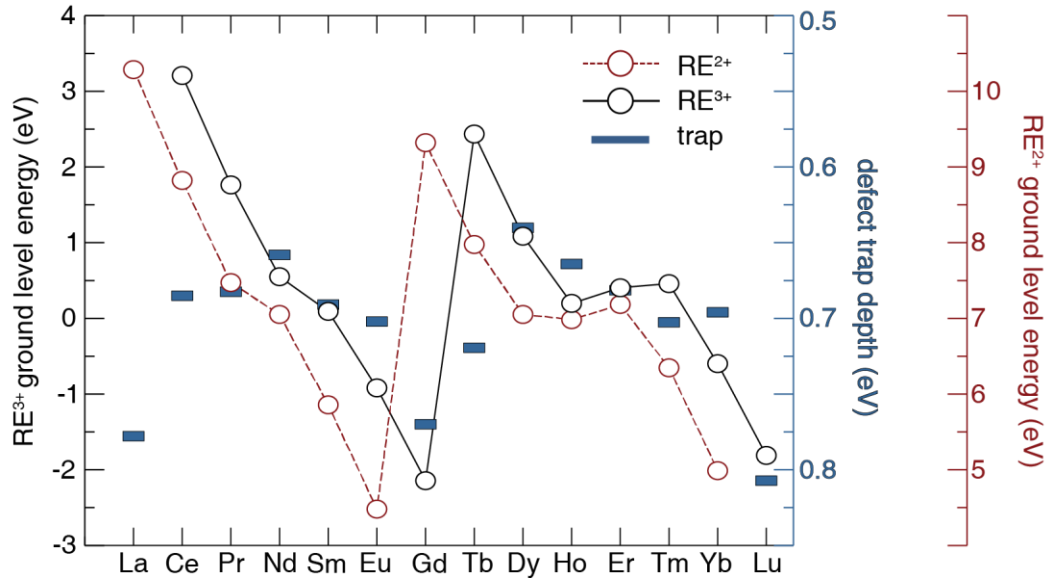


Figure 1.13 Energy scheme of $\text{Sr}_2\text{MgSi}_2\text{O}_7:\text{Eu}^{2+}, \text{RE}^{3+}$ depicting the relationship between defect driven trap states (solid blue dashed) and the rare earth ions (RE^{2+} red circles and RE^{3+} blue circles) in their ground states ($4f$ -orbitals). Defect and RE^{2+} energy levels are with respect to the bottom of the CB. RE^{3+} energy levels are with respect to the top of the VB.

However, TL of $\text{CaAl}_2\text{O}_4:\text{Eu}^{2+}, \text{RE}^{3+}$ ($\text{RE}^{3+} = \text{La}, \text{Ce}, \text{Pr}, \text{Nd}, \text{Sm}, \text{Gd}, \text{Tb}, \text{Dy}, \text{Ho}, \text{Er}, \text{Tm}, \text{Yb}, \text{Lu}, \text{Y}$) indicated the development of additional trap states upon incorporation of a co-dopant.⁸² Nevertheless, the overarching conclusion made from studies with co-dopants is their ability to improve the quality of the PersL observed in PLPs.

1.4.2 Thermoluminescence and Quantifying Trap States The most efficient and reliable method to determine the number of trap states and their E_A or depth from the CBM is the use of TL.^{76,85} TL, also called “heat experiments” at the time of their discovery, was a simple experiment consisting of observing the photoluminescence of two different samples, one at room temperature and one placed in boiling water. The results showed

the sample in boiling water “parted with light” more quickly.⁴ The more formal method of observing visible light emission when applying heat began in the early 20th century and was predominantly used by geologists as a dating technique or radiation dosimetry.^{26,85} Presently, it has become a widely used characterization technique in the study of persistent luminescence.

Today, the TL technique involves placing a sample in a temperature controlled environment followed by ensuring all trap states are emptied by either placing the sample in complete darkness for periods ≥ 12 h or heating the sample to a sufficiently high temperature.^{26,85} The sample is then cooled with the use of liquid nitrogen to the desired starting temperature, often ≈ 80 K – 100 K, and excited with an energy source, typically UV-Vis light, for set period of time. The excitation source is then terminated and after a short delay, the temperature is increased at a rate of β (K/s). This causes trapped electrons or electron-holes to be released and produce a photoemission at a wavelength appropriate for the sample being studied. The resulting curve is called a TL spectra, or “glow-curve,” and is plotted as a function of temperature.^{76,85}

Due to the nature of the TL spectra often being asymmetrical with more than one peak, proper analysis must be done with great care. In the early development of TL, this phenomenon was thought to stem from an inverse relationship with the E_A and the maximum temperature of the TL spectra (T_m); however, is not based on the behavior of charge carriers in trap states.²⁶ Considering the charge carriers in any given PLP is an electron or electron-hole pair, a more appropriate description states the intensity of the TL spectra (I) is proportional to the concentration (n) and frequency factor (s) of the charge carrier being trapped times an exponential that contains the trap depth (Equation 1.1).^{86,87}

$$I \propto sn * e^{(-EA/kT)} \quad (1.1)$$

Expanding Equation 1.1 to include β and T_m leads to Equation 1.2 and is referred to as first order kinetics, although it has been found some PLPs fit better to second order kinetics, where n is squared (n^2). The limitation of this equation is that it considers all charge carriers, *i.e.*, electrons, to recombine with their hole and give off their emission.^{26,76,85}

$$\frac{\beta EA}{kT_m^2} \propto sn * e^{(-EA/kT)} \quad (1.2)$$

In fact it has been found that a “retrapping” mechanism exists, where a charge carrier is released from a trap state, re-excited, and “retrapped.”^{29,87,88} Using the “initial rise” method of analysis, this is taken into account because according to Equation 1.2, the T_m is dependent on β . In this experiment, a sample is heated at varying rates to reveal shifting T_m , so only the “low temperature” side of the TL spectra is evaluated by plotting the spectra as $\ln(T_m^2/\beta)$ versus $(1/T_m)$.⁸⁸ The benefit of using the initial rise method results in an accurate description of trap depth regardless of the order of kinetics; however, isolating and determining the low-temperature side of a peak can be difficult, and assumes only one peak is present.

A second method of analyzing TL spectra is by using the “peak shape method.”⁷⁷ In this method, the order of kinetics is considered general by taking into account the full width at half maximum (ω), low-temperature half maximum, or the high-temperature half maximum. Equation 1.3 shows the resulting equation for ω :

$$E_A = 2kT_m \left(\frac{1.26T_m}{\omega} - 1 \right) \quad (1.3)$$

This approach can be easily modeled by deconvolution of a TL spectra using a Gaussian function and fitting each peak to reveal the necessary variables. It can be estimated that accuracy of this method is within a 5% error of the actual trap depth.^{76,77} Either approach is considered to be an appropriate method for quantifying the approximate trap depth; however, it is difficult to compare results using the two different methods.^{26,29,88,89} As a result, careful consideration of experimental parameters is necessary to evaluate whether the resulting trap depths are accurate.

1.5 Research Goals

The aims of the research presented in this thesis are to investigate the intrinsic properties of persistent luminescent phosphors to understand what drives long luminescent lifetimes. Insight into how chemical composition effects structural changes is an essential fundamental query that will lead to the discovery of new persistent luminescent phosphors. By utilizing control of chemical composition through solid solutions, several key characteristics can be studied. First using Eu^{2+} as the luminescent center, crystal field splitting theory is employed to demonstrate the tunability of emission wavelength without a change to persistent luminescence. Next, using Cr^{3+} as the luminescent center, tuning the optical bandgap is shown to increase the number of lattice defects with increasing band gap energy that has an adverse effect on persistent luminescence. Probing the local structure of Cr^{3+} substituted solid solution will give insight into structural disorder and its role in persistent luminescence. A computational approach to understanding lattice defects in SrAl_2O_4 and $\text{SrAl}_2\text{O}_4:\text{Eu}^{2+}$ establishes that vacancies will occur in favorable energy windows in the optical bandgap as an intrinsic

property. Finally, the development of a novel synthesis approach to size particle size reduction shows how an alternative way to increase lattice defects and improve persistent luminescence by maintaining chemical composition and emission quality. Thus, proving that lattice defects in the form of anion or cation vacancies, anti-site defects, and surface defects are a necessary structural property of persistent luminescent phosphors.

1.6 Organization of the Thesis

Chapter 2 describes both experimental and computational methods explored to conduct in the research presented in this thesis.

Chapter 3 is a detailed investigation into the solid-solution $(\text{Sr}_{1-\delta}\text{Ba}_\delta)_2\text{MgSi}_2\text{O}_7:\text{Eu}^{2+},\text{Dy}^{3+}$ ($\delta = 0, 0.125, 0.25, 0.375$). Here, it is established that the emission wavelength can be tuned without impacting persistent luminescence thus, providing an alternative phosphor for use in point-of-care diagnostics.

[Finley, E.; Cobb, A.; Duke, A.; Paterson, A.; Brgoch, J. Optimizing Blue Persistent Luminescence in $(\text{Sr}_{1-\delta}\text{Ba}_\delta)_2\text{MgSi}_2\text{O}_7:\text{Eu}^{2+},\text{Dy}^{3+}$ via Solid Solution for Use in Point-of-Care Diagnostics. *ACS Appl. Mater. Inter.* **2016**, *8*, 26956-26963.]

Chapter 4 investigates how the substitution of Al^{3+} on to the Ga^{3+} site in ZnGa_2O_4 quenches the persistent luminescence. In this study the change of chemical composition was explored to show how lattice defects impact the observable lifetime in persistent luminescent phosphors.

[Finley, E.; Brgoch, J. Deciphering the Loss of Persistent Red Luminescence in $\text{ZnGa}_2\text{O}_4:\text{Cr}^{3+}$ Upon Al^{3+} Substitution. *J. Mater. Chem. C* **2019**, *7*, 2005-2013.]

Chapter 5 probes the local structure of Cr^{3+} in the solid solution $\text{Zn}(\text{Ga}_{1-\delta}\text{Al}_\delta)_2\text{O}_4:\text{Cr}^{3+}$ with the use of synchrotron X-ray absorption spectroscopy. The results suggest that an

increase in distortion of the Cr³⁺ polyhedron is directly related to the presence of anti-site defects.

Chapter 6 is a computational approach to investigate the intrinsic nature of lattice defects in a persistent luminescent phosphor. Here, DFT calculations were used to determine the formation energy of anion and cation vacancies in SrAl₂O₄ and SrAl₂O₄:Eu²⁺ to establish what drives persistent luminescence.

[Finley, E.; Mansouri Tehrani, A.; Brgoch, J. Intrinsic Defects Drive Persistent Luminescence in Monoclinic SrAl₂O₄:Eu²⁺. *J. Phys. Chem. C* **2018**, *122*, 16309-16314.]

Chapter 7 investigates how to reduce the particle size of SrAl₂O₄:Eu²⁺,Dy³⁺ using a novel solution-based synthetic approach. Here, a reverse-micelle solution-based method was coupled with microwave-assisted heating to reduce the particle size, while maintaining phase purity and optical properties.

[Finley, E.; Paterson, A. S.; Cobb, A.; Willson, R. C.; Brgoch, J. Reducing Particle Size of Persistent Luminescent SrAl₂O₄:Eu²⁺,Dy³⁺ via Microwave-Assisted, Reverse Micelle Synthesis. *Opt. Mat. Express* **2017**, *7*, 2597-2616.]

Chapter 8 features the main points and reviews the conclusions made in this thesis.

1.7 References

1. Xu, J.; Tanabe, S. Persistent Luminescence Instead of Phosphorescence: History, Mechanism, and Perspective. *J. Lumin.* **2018**, *205*, 581-620.
2. Poelman, D.; Avci, N.; Smet, P.F. Measured Luminance and Visual Appearance of Multi-color Persistent Phosphors. *Opt. Express* **2009**, *17*, 358-364.
3. Yen, W.M.; Shinonoya, S.; Yamamoto, H. *Phosphor Handbook*; CRC Press: Boca Raton, FL, 2007.
4. Harvey, E.N. *A History of Luminescence*; Furst Company: Baltimore, Maryland, 1957.
5. Hölsä, J. Persistent Luminescence Beats the Afterglow: 400 Years of Persistent Luminescence. *Electrochem. Soc. Interface* **2009**, *4*, 42-45.
6. Hoogenstraaten, W.; Klasens, H.A. Some Properties of Zinc Sulfide Activated with Copper and Cobalt. *J. Electrochem. Soc.* **1953**, *100*, 366-375.
7. Matsuzawa, T.; Aoki, Y.; Takeuchi, N.; Murayama, Y. A New Long Phosphorescent Phosphor with High Brightness, SrAl₂O₄:Eu²⁺,Dy³⁺. *J. Electrochem. Soc.* **1996**, *143*, 2670-2673.

8. Lécuyer, T.; Teston, E.; Ramirez-Garcia, G.; Maldiney, T.; Viana, B.; Seguin, J.; Mignet, N.; Scherman, D.; Richard, C. Chemically Engineered Persistent Luminescence Nanoprobes for Bioimaging. *Theranostics* **2016**, *6*, 2488-2524.
9. Maldiney, T.; Scherman, D.; Richard, C. *Persistent Luminescence Nanoparticles for Diagnostics and Imaging*; American Chemical Society: Washington, DC, 2012; Vol. 2.
10. Maldiney, T.; Kaikkonen, M.U.; Seguin, J.; le Masne de Chermont, Q.; Bessodes, M.; Airene, K.J.; Ylä-Herttuala, S.; Scherman, D.; Richard, C. In Vitro Targeting of Avidin-Expressing Glioma Cells with Biotinylated Persistent Luminescence Nanoparticles. *Bioconjugate Chem.* **2012**, *23*, 472-478.
11. Maldiney, T.; Bessière, A.; Seguin, J.; Teston, E.; Sharma, S.K.; Viana, B.; Bos, A.J.J.; Dorenbos, P.; Bessodes, M.; Gourier, D.; Scherman, D.; Richard, C. The In Vivo Activation of Persistent Nanophosphors for Optical Imaging of Vascularization, Tumours and Grafted Cells. *Nat. Mater.* **2014**, *13*, 418-426.
12. Paterson, A.S.; Raja, B.; Mandadi, V.; Townsend, B.; Lee, M.; Buell, A.; Vu, B.; Brgoch, J.; Willson, R.C. A Low-Cost Smartphone-Based Platform for Highly Sensitive Point-of-Care Testing with Persistent Luminescent Phosphors. *Lab Chip* **2017**, *17*, 1051-1059.
13. Paterson, A.S.; Raja, B.; Garvey, G.; Kolhatkar, A.; Hagström, A.E.V.; Kourentzi, K.; Lee, T.R.; Willson, R.C. Persistent Luminescence Strontium Aluminate Nanoparticles as Reporters in Lateral Flow Assays. *Anal. Chem.* **2014**, *86*, 9481-9488.
14. le Masne de Chermont, Q.; Chanéac, C.; Seguin, J.; Pellé, F.; Maîtrejean, S.; Jolivet, J.-P.; Gourier, D.; Bessodes, M.; Scherman, D. Nanoprobes with Near-Infrared Persistent Luminescence for In Vivo Imaging. *Proc. Natl. Acad. Sci. U.S.A.* **2007**, *104*, 9266-9271.
15. Maldiney, T.; Richard, C.; Seguin, J.; Wattier, N.; Bessodes, M.; Scherman, D. Effect of Core Diameter, Surface Coating, and PEG Chain Length on the Biodistribution of Persistent Luminescence Nanoparticles in Mice. *ACS Nano* **2011**, *5*, 854-862.
16. Li, J.; Shi, J.; Shen, J.; Man, H.; Wang, M.; Zhang, H. Specific Recognition of Breast Cancer Cells In Vitro Using Near Infrared-Emitting Long-Persistence Luminescent $Zn_3Ga_2Ge_2O_{10}:Cr^{3+}$ Nanoprobes. *Nano-Micro Lett.* **2015**, *7*, 138-145.
17. Shi, J.; Sun, X.; Zhu, J.; Li, J.; Zhang, H. One-Step Synthesis of Amino-Functionalized Ultrasmall Near Infrared-Emitting Persistent Luminescent Nanoparticles for In Vitro and In Vivo Bioimaging. *Nanoscale* **2016**, *8*, 9798-9804.
18. Maldiney, T.; Sraiki, G.; Viana, B.; Gourier, D.; Richard, C.; Scherman, D.; Bessodes, M.; Van den Eeckhout, K.; Poelman, D.; Smet, P.F. In vivo Optical Imaging with Rare Earth Eoped $Ca_2Si_5N_8$ Persistent Luminescence Nanoparticles. *Opt. Mat. Express* **2012**, *2*, 261-268.
19. Sun, M.; Li, Z.-J.; Liu, C.-L.; Fu, H.-X.; Shen, J.-S.; Zhang, H.-W. Persistent Luminescent Nanoparticles for Super-Long Time In Vivo and In Situ Imaging with Repeatable Excitation. *J. Lumin.* **2014**, *145*, 838-842.
20. Luitel, H.N.; Watari, T.; Torikai, T.; Yada, M.; Chand, R.; Xu, C.-N.; Nanoka, K. Highly Water Resistant Surface Coating by Fluoride on Long Persistent $Sr_4Al_{14}O_{25}:Eu^{2+}/Dy^{3+}$ Phosphor. *Appl. Surf. Sci.* **2010**, *256*, 2347-2352.

21. Thompson, N.; Murugaraj, P.; Rix, C.; Mainwaring, D.E. Role of Oxidative Pre-Calcination in Extending Blue Emission of Sr₄Al₁₄O₂₅ Nanophosphors Formed with Microemulsions. *J. Alloys Compd.* **2012**, *537*, 147-153.
22. Abdukayum, A.; Chen, J.-T.; Zhao, Q.; Yan, X.-P. Functional Near Infrared-Emitting Cr³⁺/Pr³⁺ Co-Doped Zinc Gallogermanate Persistent Luminescent Nanoparticles with Superlong Afterglow for In Vivo Targeted Bioimaging. *J. Am. Chem. Soc.* **2013**, *135*, 14125-14133.
23. Srivastava, B.B.; Kuang, A.; Mao, Y. Persistent Luminescent Sub-10 nm Cr Doped ZnGa₂O₄ Nanoparticles by a Biphasic Synthesis Route. *Chem. Commun.* **2015**, *51*, 7372-7375.
24. Finley, E.; Paterson, A.S.; Cobb, A.; Willson, R.C.; Brgoch, J. Reducing Particle Size of Persistent Luminescent SrAl₂O₄:Eu²⁺,Dy³⁺ via Microwave-Assisted, Reverse Micelle Synthesis. *Opt. Mat. Express* **2017**, *7*, 2597-2616.
25. Finley, E.; Cobb, A.; Duke, A.; Paterson, A.; Brgoch, J. Optimizing Blue Persistent Luminescence in (Sr_{1-δ}Ba_δ)₂MgSi₂O₇:Eu²⁺,Dy³⁺ via Solid Solution for Use in Point-of-Care Diagnostics. *ACS Appl. Mater. Inter.* **2016**, *8*, 26956-26963.
26. Van den Eeckhout, K.; Smet, P.F.; Poelman, D. Persistent Luminescence in Eu²⁺-Doped Compounds: A Review. *Materials* **2010**, *3*, 2536.
27. Rojas-Hernandez, R.E.; Rubio-Marcos, F.; Rodriguez, M.Á.; Fernandez, J.F. Long Lasting Phosphors: SrAl₂O₄:Eu, Dy as the Most Studied Material. *Renewable Sustainable Energy Rev.* **2018**, *81*, 2759-2770.
28. Clabau, F.; Rocquefelte, X.; Jobic, S.; Deniard, P.; Whangbo, M.H.; Garcia, A.; Le Mercier, T. Mechanism of Phosphorescence Appropriate for the Long-Lasting Phosphors Eu²⁺-Doped SrAl₂O₄ with Codopants Dy³⁺ and B³⁺. *Chem. Mater.* **2005**, *17*, 3904-3912.
29. Botterman, J.; Joos, J.J.; Smet, P.F. Trapping and Detrapping in SrAl₂O₄:Eu²⁺,Dy³⁺ Persistent Phosphors: Influence of Excitation Wavelength and Temperature. *Phys. Rev. B* **2014**, *90*, 085147.
30. Blasse, G.; Wanmaker, W.L.; ter Vrugt, J.W. Some New Classes of Efficient Eu²⁺-Activated Phosphors. *J. Electrochem. Soc.* **1968**, *115*, 673.
31. Abbruscato, V. Optical and Electrical Properties of SrAl₂O₄:Eu²⁺. *J. Electrochem. Soc.* **1971**, *118*, 930-933.
32. Aitasalo, T.; Hölsä, J.; Jungner, H.; Lastusaari, M.; Niittykoski, J. Sol-Gel Processed Eu²⁺-Doped Alkaline Earth Aluminates. *J. Alloys Compd.* **2002**, *341*, 76-78.
33. Chen, I.-C.; Chen, T.-M. Effect of Host Compositions on the Afterglow Properties of Phosphorescent Strontium Aluminate Phosphors Derived from the Sol-Gel Method. *J. Mater. Res.* **2001**, *16*, 1293-1300.
34. Fu, Z.; Zhou, S.; Yu, Y.; Zhang, S. Combustion Synthesis and Luminescence Properties of Nanocrystalline Monoclinic SrAl₂O₄:Eu²⁺. *Chem. Phys. Lett.* **2004**, *395*, 285-289.
35. Tanaka, H.; Gubarevich, A.V.; Wada, H.; Odawara, O. Process Stages During Solution Combustion Synthesis of Strontium Aluminates. *Int. J. Self-Propag. High-Temp Synth.* **2013**, *22*, 151-156.
36. Xiao, Q.; Xiao, L.; Liu, Y.; Chen, X.; Li, Y. Synthesis and Luminescence Properties of Needle-Like SrAl₂O₄:Eu, Dy Phosphor via a Hydrothermal Co-Precipitation Method. *J. Phys. Chem. Solids* **2010**, *71*, 1026-1030.
37. Rojas-Hernandez, R.E.; Rubio-Marcos, F.; Enriquez, E.; De La Rubia, M.A.; Fernandez, J.F. A Low-Energy Milling Approach to Reduce Particle Size

- Maintains the Luminescence of Strontium Aluminates. *RSC Adv.* **2015**, *5*, 42559-42567.
38. Kandpal, S.K.; Goundie, B.; Wright, J.; Pollock, R.A.; Mason, M.D.; Meulenberg, R.W. Investigation of the Emission Mechanism in Milled SrAl₂O₄: Eu, Dy Using Optical and Synchrotron X-ray Spectroscopy. *ACS Appl. Mater. Inter.* **2011**, *3*, 3482-3486.
 39. Dorenbos, P. 5d-Level Energies of Ce³⁺ and the Crystalline Environment. III. Oxides Containing Ionic Complexes. *Phys. Rev. B* **2001**, *64*, 125117.
 40. Dorenbos, P. Mechanism of Persistent Luminescence in Eu²⁺ and Dy³⁺ Codoped Aluminate and Silicate Compounds. *J. Electrochem. Soc.* **2005**, *152*, H107-H110.
 41. Korthout, K.; Van den Eeckhout, K.; Botterman, J.; Nikitenko, S.; Poelman, D.; Smet, P.F. Luminescence and X-ray Absorption Measurements of Persistent SrAl₂O₄:Eu,Dy Powders: Evidence for Valence State Changes. *Phys. Rev. B* **2011**, *84*, 085140.
 42. Finley, E.; Mansouri Tehrani, A.; Brgoch, J. Intrinsic Defects Drive Persistent Luminescence in Monoclinic SrAl₂O₄:Eu²⁺. *J. Phys. Chem. C* **2018**, *122*, 16309-16314.
 43. Qu, B.; Zhang, B.; Wang, L.; Zhou, R.; Zeng, X.C. Mechanistic Study of the Persistent Luminescence of CaAl₂O₄:Eu,Nd. *Chem. Mater.* **2015**, *27*, 2195-2202.
 44. Lin, Y.; Tang, Z.; Zhang, Z.; Wang, X.; Zhang, J. Preparation of a New Long Afterglow Blue-Emitting Sr₂MgSi₂O₇-Based Photoluminescent Phosphor. *J. Mater. Sci. Lett.* **2001**, *20*, 1505-1506.
 45. Ardit, M.; Dondi, M.; Merlini, M.; Cruciani, G. Melilite-Type and Melilite-Related Compounds: Structural Variations Along the Join Sr_{2-x}Ba_xMgSi₂O₇ (0 ≤ x ≤ 2) and High-Pressure Behavior of the Two End-Members. *Phys. Chem. Miner.* **2012**, *39*, 199-211.
 46. Poort, S.H.M.; Reijnhoudt, H.M.; van der Kuip, H.O.T.; Blasse, G. Luminescence of Eu²⁺ in Silicate Host Lattices with Alkaline Earth Ions in a Row. *J. Alloys Compd.* **1996**, *241*, 75-81.
 47. Tydtgat, C.; Meert, K.W.; Poelman, D.; Smet, P.F. Optically Stimulated Detrapping During Charging of Persistent Phosphors. *Opt. Mat. Express* **2016**, *6*, 844-858.
 48. Liu, B.; Shi, C.; Yin, M.; Dong, L.; Xiao, Z. The Trap States in the Sr₂MgSi₂O₇ and (Sr,Ca)MgSi₂O₇ Long Afterglow Phosphor Activated by Eu²⁺ and Dy³⁺. *J. Alloys Compd.* **2005**, *387*, 65-69.
 49. Carlson, S.; Hölsä, J.; Laamanen, T.; Lastusaari, M.; Malkamäki, M.; Niittykoski, J.; Valtonen, R. X-ray Absorption Study of Rare Earth Ions in Sr₂MgSi₂O₇:Eu²⁺,R³⁺ Persistent Luminescence Materials. *Opt. Mater.* **2009**, *31*, 1877-1879.
 50. Qi, Z.; Shi, C.; Liu, M.; Zhou, D.; Luo, X.; Zhang, J.; Xie, Y. The Valence of Rare Earth ions in R₂MgSi₂O₇:Eu, Dy (R = Ca, Sr) Long-Afterglow Phosphors. *Phys. Status Solidi A* **2004**, *201*, 3109-3112.
 51. Lastusaari, M.; Jungner, H.; Kotlov, A.; Laamanen, T.; Rodrigues Lucas, C.V.; Brito Hermi, F.; Hölsä, J. In *Z. Naturforsch. B* 2014; Vol. 69, p 171.
 52. Brito, H.F.; Hassinen, J.; Hölsä, J.; Jungner, H.; Laamanen, T.; Lastusaari, M.; Malkamäki, M.; Niittykoski, J.; Novák, P.; Rodrigues, L.C.V. Optical Energy Storage Properties of Sr₂MgSi₂O₇:Eu²⁺,R³⁺ Persistent Luminescence Materials. *J. Therm. Anal. Calorim.* **2011**, *105*, 657-662.

53. Zhuang, Y.; Katayama, Y.; Ueda, J.; Tanabe, S. A Brief Review on Red to Near-Infrared Persistent Luminescence in Transition-Metal-Activated Phosphors. *Opt. Mater.* **2014**, *36*, 1907-1912.
54. Van den Eeckhout, K.; Poelman, D.; Smet, P. Persistent Luminescence in Non-Eu²⁺-Doped Compounds: A Review. *Materials* **2013**, *6*, 2789.
55. Bessière, A.; Jacquart, S.; Priolkar, K.; Lecointre, A.; Viana, B.; Gourier, D. ZnGa₂O₄:Cr³⁺: A New Red Long-Lasting Phosphor with High Brightness. *Opt. Express* **2011**, *19*, 10131-10137.
56. Kahan, H.M.; Macfarlane, R.M. Optical and Microwave Spectra of Cr³⁺ in the Spinel ZnGa₂O₄. *J. Chem. Phys.* **1971**, *54*, 5197-5205.
57. Mikenda, W. N-lines in the Luminescence Spectra of Cr³⁺-Doped Spinel (III) Partial Spectra. *J. Lumin.* **1981**, *26*, 85-98.
58. Yixi, Z.; Jumpei, U.; Setsuhisa, T. Enhancement of Red Persistent Luminescence in Cr³⁺-Doped ZnGa₂O₄ Phosphors by Bi₂O₃ Codoping. *Appl. Phys. Express* **2013**, *6*, 052602.
59. Allix, M.; Chenu, S.; Véron, E.; Poumeyrol, T.; Kouadri-Boudjelthia, E.A.; Alahraché, S.; Porcher, F.; Massiot, D.; Fayon, F. Considerable Improvement of Long-Persistent Luminescence in Germanium and Tin Substituted ZnGa₂O₄. *Chem. Mater.* **2013**, *25*, 1600-1606.
60. Sharma, S.K.; Gourier, D.; Teston, E.; Scherman, D.; Richard, C.; Viana, B. Persistent Luminescence Induced by Near Infra-Red Photostimulation in Chromium-Doped Zinc Gallate for In Vivo Optical Imaging. *Opt. Mater.* **2017**, *63*, 51-58.
61. Pan, Z.; Lu, Y.-Y.; Liu, F. Sunlight-Activated Long-Persistent Luminescence in the Near-Infrared from Cr³⁺-Doped Zinc Gallogermanates. *Nat. Mater.* **2011**, *11*, 58.
62. Bessière, A.; Sharma, S.K.; Basavaraju, N.; Priolkar, K.R.; Binet, L.; Viana, B.; Bos, A.J.J.; Maldiney, T.; Richard, C.; Scherman, D.; Gourier, D. Storage of Visible Light for Long-Lasting Phosphorescence in Chromium-Doped Zinc Gallate. *Chem. Mater.* **2014**, *26*, 1365-1373.
63. Basavaraju, N.; Priolkar, K.R.; Gourier, D.; Sharma, S.K.; Bessiere, A.; Viana, B. The Importance of Inversion Disorder in the Visible Light Induced Persistent Luminescence in Cr³⁺ Doped AB₂O₄ (A = Zn or Mg and B = Ga or Al). *Phys. Chem. Chem. Phys.* **2015**, *17*, 1790-1799.
64. Basavaraju, N.; Priolkar, K.R.; Gourier, D.; Bessiere, A.; Viana, B. Order and Disorder Around Cr³⁺ in Chromium Doped Persistent Luminescent AB₂O₄ Spinel. *Phys. Chem. Chem. Phys.* **2015**, *17*, 10993-10999.
65. Gourier, D.; Bessière, A.; Sharma, S.K.; Binet, L.; Viana, B.; Basavaraju, N.; Priolkar, K.R. Origin of the Visible Light Induced Persistent Luminescence of Cr³⁺-Doped Zinc Gallate. *J. Phys. Chem. Solids* **2014**, *75*, 826-837.
66. George, N.C.; Denault, K.A.; Seshadri, R. Phosphors for Solid-State White Lighting. *Annu. Rev. Mater. Res.* **2013**, *43*, 481-501.
67. Kobayashi, T.; Mroczkowski, S.; Owen, J.F.; Brixner, L.H. Fluorescence Lifetime and Quantum Efficiency for 5d → 4f Transitions in Eu²⁺ Doped Chloride and Fluoride Crystals. *J. Lumin.* **1980**, *21*, 247-257.
68. Ying, J.; Lixin, N.; Shangda, X.; Min, Y.; Peter, A.T. Third-Order Contributions to the ⁸S_{7/2} → ⁶P_{7/2}, ⁶P_{5/2} Two-Photon Transitions of Eu²⁺ in KMgF₃. *J. Phys.: Condens. Matter* **2004**, *16*, 2773.

69. Varga, L.P.; Asprey, L.B. Electronic Spectra of Weak-Field Fluoride Complexes of Tetravalent Neodymium. *The Journal of Chemical Physics* **1968**, *49*, 4674-4679.
70. Nakazawa, E.; Mochida, T. Traps in SrAl₂O₄:Eu²⁺ Phosphor with Rare-Earth Ion Doping. *J. Lumin.* **1997**, *72-74*, 236-237.
71. Yuan, H.B.; Jia, W.; Basun, S.A.; Lu, L.; Meltzer, R.S.; Yen, W.M. The Long-Persistent Photoconductivity of SrAl₂O₄:Eu²⁺,Dy³⁺ Single Crystals. *J. Electrochem. Soc.* **2000**, *147*, 3154-3156.
72. Yamamoto, H.; Matsuzawa, T. Mechanism of Long Phosphorescence of SrAl₂O₄:Eu²⁺, Dy³⁺ and CaAl₂O₄:Eu²⁺, Nd³⁺. *J. Lumin.* **1997**, *72-74*, 287-289.
73. Arellano-Tánori, O.; Meléndrez, R.; Pedroza-Montero, M.; Castañeda, B.; Chernov, V.; Yen, W.M.; Barboza-Flores, M. Persistent luminescence dosimetric properties of UV-irradiated SrAl₂O₄:Eu²⁺, Dy³⁺ phosphor. *J. Lumin.* **2008**, *128*, 173-184.
74. Clabau, F.; Rocquefelte, X.; Jobic, S.; Deniard, P.; Whangbo, M.-H.; Garcia, A.; Le Mercier, T. On the Phosphorescence Mechanism in SrAl₂O₄:Eu²⁺ and its Codoped Derivatives. *Solid State Sci.* **2007**, *9*, 608-612.
75. Rojas-Hernandez, R.E.; Rubio-Marcos, F.; Gonçalves, R.H.; Rodriguez, M.Á.; Véron, E.; Allix, M.; Bessada, C.; Fernandez, J.F. Original Synthetic Route To Obtain a SrAl₂O₄ Phosphor by the Molten Salt Method: Insights into the Reaction Mechanism and Enhancement of the Persistent Luminescence. *Inorg. Chem.* **2015**, *54*, 9896-9907.
76. Chen, R.M.S.W.S. *Theory of Thermoluminescence and Related Phenomena*; World Scientific, 1997.
77. Chen, R. Glow Curves with General Order Kinetics. *J. Electrochem. Soc.* **1969**, *116*, 1254-1257.
78. Hölsä, J.; Aitasalo, T.; Jungner, H.; Lastusaari, M.; Niittykoski, J.; Spano, G. Role of Defect States in Persistent Luminescence Materials. *J. Alloys Compd.* **2004**, *374*, 56-59.
79. Aitasalo, T.; Dereń, P.; Hölsä, J.; Jungner, H.; Krupa, J.C.; Lastusaari, M.; Legendziewicz, J.; Niittykoski, J.; Stręk, W. Persistent Luminescence Phenomena in Materials Doped with Rare Earth Ions. *J. Solid State Chem.*, *171*, 114-122.
80. Dorenbos, P. Mechanism of Persistent Luminescence in Sr₂MgSi₂O₇:Eu²⁺,Dy³⁺. *Phys. Status Solidi B* **2005**, *242*, 7-9.
81. De Vos, A.; Lejaeghere, K.; Vanpoucke, D.E.P.; Joos, J.J.; Smet, P.F.; Hemelsoet, K. First-Principles Study of Antisite Defect Configurations in ZnGa₂O₄:Cr Persistent Phosphors. *Inorg. Chem.* **2016**, *55*, 2402-2412.
82. Aitasalo, T.; Hölsä, J.; Jungner, H.; Lastusaari, M.; Niittykoski, J. Thermoluminescence Study of Persistent Luminescence Materials: Eu²⁺- and R³⁺-Doped Calcium Aluminates, CaAl₂O₄:Eu²⁺,R³⁺. *J. Phys. Chem. B* **2006**, *110*, 4589-4598.
83. Ueda, J.; Dorenbos, P.; Bos, A.J.J.; Kuroishi, K.; Tanabe, S. Control of Electron Transfer Between Ce³⁺ and Cr³⁺ in the Y₃Al_{5-x}Ga_xO₁₂ Host via Conduction Band Engineering. *J. Mater. Chem. C* **2015**, *3*, 5642-5651.
84. Nag, A.; Kutty, T.R.N. Role of B₂O₃ on the Phase Stability and Long Phosphorescence of SrAl₂O₄:Eu, Dy. *J. Alloys Compd.* **2003**, *354*, 221-231.
85. McKeever, S.W.S. *Thermoluminescence of Solids*; Cambridge University Press, 1985.

86. Randall John, T.; Wilkins Maurice Hugh, F.; Oliphant Marcus Laurence, E. Phosphorescence and Electron Traps II. The Interpretation of Long-Period Phosphorescence. *Proc. R. Soc. London, Ser. A* **1945**, *184*, 390-407.
87. Randall John, T.; Wilkins Maurice Hugh, F.; Oliphant Marcus Laurence, E. Phosphorescence and Electron Traps - I. The Study of Trap Distributions. *Proc. R. Soc. London, Ser. A* **1945**, *184*, 365-389.
88. Van den Eeckhout, K.; Bos, A.J.J.; Poelman, D.; Smet, P.F. Revealing Trap Depth Distributions in Persistent Phosphors. *Phys. Rev. B* **2013**, *87*, 045126.
89. Smet, P.F.; Van den Eeckhout, K.; Bos, A.J.J.; van der Kolk, E.; Dorenbos, P. Temperature and Wavelength Dependent Trap Filling in $M_2Si_5N_8:Eu$ (M=Ca, Sr, Ba) Persistent Phosphors. *J. Lumin.* **2012**, *132*, 682-689.

Chapter 2

Experimental Procedures and Computational Methods

This chapter serves as an overview of the experimental and computational techniques followed throughout this thesis. Details specific to each chapter are included in the respective experimental methods sections.

2.1 Experimental Synthesis

2.1.1 Starting Reagents Starting materials for all syntheses are listed in Table 2.1 and were used as purchased. Materials were stored in closed containers in the Brgoch Laboratory under ambient conditions unless specified to the contrary. Moisture sensitive materials were stored in a vacuum desiccator in closed containers. Organic materials were stored in appropriate flame resistant cabinets.

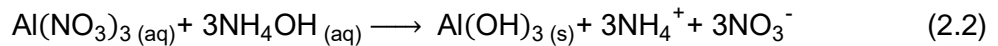
Table 2.1 Starting materials for all synthesis methods

Compound	Source	Purity
Al ₂ O ₃	Sigma-Aldrich	99.99%
	Alfa Aesar	99%
Al(NO ₃) ₃ **	Sigma-Aldrich	≥98%
BaCO ₃	Johnson Matthey	98%
1-butanol**	Sigma-Aldrich	≥98%
C ₇ H ₁₆ **	Sigma-Aldrich	≥98%
C ₁₉ H ₄₂ BrN (CTAB)**	Sigma-Aldrich	≥98%
Cr ₂ O ₃	Alfa Aesar	99%
Dy(NO ₃) ₃ *	Sigma-Aldrich	≥99.9%
Dy ₂ O ₃ *	Sigma-Aldrich	99.99%
Eu(NO ₃) ₃ *	Sigma-Aldrich	≥99.9%
Eu ₂ O ₃ *	Sigma-Aldrich	99.99%
	Materion Advanced Chemicals	99.9%
Ga ₂ O ₃	Alfa Aesar	99.95%
H ₃ BO ₃ *	Sigma-Aldrich,	99.99%
MgO	Sigma-Aldrich	99.99%
(NH ₄) ₂ CO ₃ **	Sigma-Aldrich	≥98%
NH ₄ OH**	Em Science	28%-30%
SiO ₂	Sigma-Aldrich	99.5%
SrCO ₃	Alfa Aesar	99.9%
Sr(NO ₃) ₂ *	Sigma-Aldrich	≥99%
ZnO	Alfa Aesar	99.9%

*indicates storage in desiccator
**indicates storage in Willson Research Group's Laboratory

2.1.2 All Solid-State Method Starting materials were weighed out in stoichiometric ratios and combined in a two-step process of hand grinding in an agate mortar and pestle for ≈30 min followed by mechanical mixing for ≈45 min. For mechanical milling, the starting reagents were placed on a shaker mixer/mill (SPEX 8000M) in polystyrene vials with polystyrene beads (SPEX SamplePrep) as the mixing media. The resulting powders were then pressed into 8 mm pellets and placed in 5 mL alumina crucibles (AdValue) for reaction using a high-temperature tube furnace or microwave-assisted heating.

2.1.3 Reverse Micelle Method This solution-based synthetic route creates a reaction of precursor powders where the elements for the desired final product, in this case $\text{SrAl}_2\text{O}_4:\text{Eu}^{2+},\text{Dy}^{3+}$, are reacted as ions in an aqueous solution and are precipitated to give a homogeneous distribution of the elements. Unlike a sol-gel reaction, where the precipitation is allowed to occur freely throughout the solution, this approach confines the reaction in the micelles, enabling the reduction of particle sizes in the final product. The reactions follow Equations 2.1 and 2.2. Here, precursor particles of $\text{SrAl}_2\text{O}_4:\text{Eu}^{2+},\text{Dy}^{3+}$ were prepared by dissolving the starting metal salts in DI water (Millipore Milli-Q system). Molar concentration of the aqueous metal salt solutions were kept at ≈ 475 mM, with 150.4 mM $\text{Sr}(\text{NO}_3)_2$, 316.7 mM $\text{Al}(\text{NO}_3)_3$, 1.7 mM $\text{Eu}(\text{NO}_3)_3$, and 7.0 mM $\text{Dy}(\text{NO}_3)_3$ to obtain the final nominal stoichiometry of $(\text{Sr}_{0.95}\text{Eu}_{0.01}\text{Dy}_{0.04})\text{Al}_2\text{O}_4$.



The aqueous solution needed for the precipitating agents was then prepared with 170 mM $(\text{NH}_4)_2\text{CO}_3$ dissolved in stock 28%-30% NH_4OH . Two separate flasks containing the organic components for the emulsions were also prepared with 50 wt% n-heptane, 24 wt% 1-butanol, and 26 wt% CTAB.

To prepare the two required microemulsions the following process was followed: one solution was made by pouring the metal salt solution into a flask containing CTAB/n-heptane/1-butanol, and the second by adding the precipitating agent solution to the remaining flask with CTAB/n-heptane/1-butanol.^{1,2} The ratio of the aqueous solution to the organic CTAB/n-heptane/1-butanol mixture that was used to form a stable emulsion was approximately 1:4 by mass, giving an approximate $[\text{H}_2\text{O}]/[\text{CTAB}]$ molar ratio of ≈ 15 .

The two emulsions were stirred separately for ≈ 20 min until no clumps of CTAB remained and each emulsion was a homogenous, transparent solution. The formation of these emulsions is considered to be an endothermic reaction, and placing the suspensions on a hot plate at 37°C helped dissolve the CTAB. Next, the two microemulsions were combined into a single flask, and placed on a magnetic stir plate at room temperature. The mixture gradually turned from transparent to cloudy as the reaction proceeded.

The reaction was allowed to proceed for 24 h. The final solution was poured into a separatory funnel that was subsequently disrupted by the addition of a 50% v/v EtOH/DI H_2O solution at a volume ratio of 1:1 of 50% EtOH to microemulsion solution. Phase separation occurred when the mixture was stirred and allowed to sit for 10 min. The final precursor particles were isolated and washed three times with 50% EtOH/DI H_2O to remove excess NH_4 dissolved salts and any remaining organics. A final wash in acetone was completed, and the product was dried at 100°C for 24 h. Lastly, a 4 wt% H_3BO_3 flux was added to the final precursor powder.

2.1.4 Tube Furnaces Powders prepared via an all solid-state method were reacted in Lindberg/Blue™ programmable furnaces. Two different temperature profiles were used. The first employed a low temperature furnace with a maximum operating temperature of 1200°C , which uses a K-type thermocouple, whereas the second furnace has a maximum operating temperature of 1500°C with an R-type thermocouple. In both cases, SiC heating elements (I Squared R Element Co., Inc.) are the primary source of heating. All reactions employed a heating and cooling rate of $3^{\circ}\text{C}/\text{min}$ in either a reducing atmosphere of industrial grade 95% $\text{N}_2/5\%$ H_2 (Matheson Tri-Gas) or in flowing air.

2.1.5 Microwave Heating An important step in particle size reduction is the choice in sintering method. High-temperature solid-state furnaces often require long reaction times up to 24 h at high-temperatures leading to large, agglomerated particles. An alternative is to employ microwave-based heating to prevent crystal growth and agglomerate formation by quickly reacting starting materials in less than 20 min while still producing phase-pure products.^{3,4}

In this work, a commercial microwave (Panasonic NN-SN651B, 1200 W) produced phase-pure $\text{SrAl}_2\text{O}_4:\text{Eu}^{2+},\text{Dy}^{3+}$ phosphors by using a two-step heating process comprised of an initial heating step at 960 W for 9 min and a second step at 480 W for 5 min. The samples were pressed into 8 mm pellets and loaded into a 5 mL alumina crucible (AdValue Tech). To create the necessary reducing conditions, a 42 mm diameter alumina disk (AdValue Tech) was placed on top of the crucible. The reaction vessel was then centered in a larger 50 mL alumina crucible (AdValue Tech) with 6.5 g of activated carbon (Darco, 12 mesh-20 mesh, Sigma-Aldrich) packed into the annular space. To facilitate proper heating of the reaction vessel, a cylindrical insulation block was prepared by adapting a Thermo Scientific 1" diameter furnace tube adapter for a 1500°C Lindberg/Blue™. A 51 mm diameter hole \approx 48 mm deep was drilled into the middle of the block; a \approx 30 mm x 75 mm deep hole remained in the bottom of the furnace tube adapter which was plugged firebrick (Skyline Components, LLC). To maintain a uniform temperature distribution an insulation lid was constructed out of firebrick, \approx 50 mm thick x 105 mm diameter. The entire set-up is placed in the microwave off-center to promote adequate heat distribution.

2.2 Characterization

2.2.1 X-ray Powder Diffraction To verify phase purity of all samples prepared, powder X-ray diffraction is employed to confirm the crystal structure and phase-purity after concluding the synthesis of all compounds. All final products are ground in an agate mortar and pestle to ensure small homogeneous particles ($\sim 10 \mu\text{m}$) and then placed on a zero-background silicon sample stage. Samples should be flattened but not pressed to avoid the likelihood of preferred orientation, which can result in misidentification of phases. Powder X-ray diffraction is first conducted on a PanAnalytical X'Pert powder diffractometer with Cu K α ($\lambda = 1.54183 \text{ \AA}$), scanning from $10 2\theta$ to $80 2\theta$ over 7 min, to check for phase purity. These powder patterns were manually indexed by comparing the collected diffractograms against known diffractograms from a database in the HighScore software program.⁵

Upon validation of targeted phase, final products were sent to X-ray powder diffraction the 11-BM at the Advanced Photon Source at Argonne National Laboratory via their mail-in service obtain high-resolution synchrotron powder diffractograms.^{6,7} The final diffractograms obtained were analyzed using the General Structure Analysis System (GSAS) by first doing a Le Bail refinement to verify phase purity and acquire accurate lattice parameters and peak shapes.^{8,9} These refinement data are then used to conduct Rietveld refinements to ascertain structural details including atomic positions, atomic displacement parameters, and to detect any statistical atomic mixing. A Chebyshev function was used to fit the background and peak shapes were described using a Pseudo-Voigt function. The resulting crystal structures can be visualized using VESTA.^{10,11}

2.2.2 Inductively Coupled Plasma-Optical Emission Spectrometry (ICP-OES) Analysis of elemental composition in a compound is important to support the results of a desired synthesis. ICP-OES is a flame technique that excites electrons in a range of 6,000 K to 10,000 K from a specific atom or ion, allowing for a quantitative analysis of molar ratios. It is particularly useful for analysis of atoms in a bulk sample. The composition of the reverse micelle precursors was analyzed using ICP-OES (Agilent 725) to determine the exact ratios of Sr to Al in three separate reactions. For this analysis, all samples were prepared by digestion in HF and HNO₃.

2.2.3 Scanning Electron Microscopy (SEM) and Energy Dispersive X-ray Spectroscopy (EDS) SEM-EDS is a powerful tool to analyze a sample's particle size, morphology, and elemental composition when used in combination. An SEM utilizes an electron beam that is scanned across the surface of a sample to produce micrographs down to 1 nm under optimal conditions. Additionally, EDS coupled with the same electron beam of the SEM will excite the inner shell within the sample; this leaves a hole that is filled by an electron in a higher energy shell. The difference between the two energy levels results in a signature X-ray signal unique to each elemental. A JOEL JSM-6330F field emission SEM was used to visualize particle size distribution at 200x magnification with a beam focus and accelerating voltage of 15 eV and an emission current of 12 µA. An AMETEK EDAX Octane Pro established the semi-quantitative compositions of the reverse micelle and solid state materials. Because the samples analyzed in this work are insulators, all powders were first coated with 25 nm of carbon to limit charging in the SEM.

2.2.4 Particle Size Measurements Laser diffraction spectroscopy (Malvern Mastersizer 2000) was used to determine equivalent spherical diameter of particles analyzed in this thesis. This technique was chosen for its ability to measure a wide range of size

distributions from >100 nm to >1 μm by measuring the diffraction patterns of a blue and red laser as they pass through the sample.¹² The angular variation of the diffraction pattern indicates the overall size distribution of the sample by volume/mass.¹² The particle size reported is the diameter volume percentage as either the 10th, 50th, or 90th percentile ($d_{0.1}$, $d_{0.5}$, or $d_{0.9}$).¹² Here, samples were mixed 50 mg of product in 5 mL of ethanol and sonicating for 2 h to fully disperse the particles being analyzed. Measurements were collected five times with a 30 s integration and averaged together to provide the 50% diameter volume percentage ($d_{0.5}$).

2.2.5 Photoluminescence and Long Luminescent Lifetime All samples that were evaluated for their optical properties were prepared by first thoroughly grinding the powder followed by mounting the samples on a quartz slide using two part silicon potting compound (Momentive and United Adhesives). The components of the potting compound were measured out in either a 3:1 ratio (RTV615A:RTV615B) or a 1:1 ratio (OP4036A:OP4036B). Regardless of potting compound used, samples are then weighed out in a 10:1 ratio of silicon to sample and thoroughly mixed to produce a homogenous mixture before drop casting onto the quartz slide. After mounting, the slides were placed in a 150°C oven for 10 – 15 min to cure the mixture and adhere the sample to the slide.

To observe photoemission and excitation spectra and long luminescent lifetime, samples were placed in a steady-state PTI Quanta-Master spectrofluorimeter that is equipped with a 75 W xenon arc lamp. Emission spectra were observed using excitation wavelengths of $\lambda = 365 \text{ nm}$ for Eu^{2+} containing PLPs and $\lambda = 400 \text{ nm}$ for Cr^{3+} containing phosphors. Excitation spectra were collected by using the emission maximum wavelength of each sample.

Room temperature long luminescent lifetimes, also called persistent luminescence lifetimes, were measured by exciting the sample ($\lambda = 365$ nm for Eu^{2+} and $\lambda = 254$ nm for Cr^{3+}) for 10 min. Temperature dependent long luminescent lifetimes were collected by heating samples from 295 K to 500 K with 25 K increments in a Janis cryostat (VPF-100). Samples were excited at $\lambda_{\text{ex}} = 365$ nm for 10 min for each heating increment. The shutter was then manually closed and the emission decay was collected at the emission maximum wavelength of the sample. The signal was collected using the time-dependent option in the FelixGX software. The decays were collected for either 30 min or 1 hour, whichever achieved a zero background decay. All emission decays were fit using a tri-exponential equation to evaluate the time components of each sample (Equation 2.3) where I is the normalized intensity, A_1 , A_2 , and A_3 are pre-exponential constants, τ_1 , τ_2 , and τ_3 are luminescent decays, and t is the time.

$$I = A_1 e^{\frac{-t}{\tau_1}} + A_2 e^{\frac{-t}{\tau_2}} + A_3 e^{\frac{-t}{\tau_3}} \quad (2.3)$$

To achieve a proper fit, the data was first normalized to the maximum intensity. The fitting parameters were set to a bi-exponential with a fitting criterion of 500 iterations and a tolerance of 1×10^{-15} where the fit was allowed to run until converged. The resulting fit was evaluated for goodness of fit by visually inspecting the fit with the observed data in addition to examining the adjusted- R^2 (R^2_{adj}) and standard error for each variable. Since a bi-exponential rarely accounted for the fastest time component, τ_1 , which resulted in $R^2_{\text{adj}} < 0.95$, a third exponential was added. The fit was again set to the same fitting criterion and allowed to converge. The fitting parameters, A_3 and τ_3 , were examined to ensure they did not fall within the standard error of A_2 and τ_2 , an indication the data was over fit and a bi-exponential was appropriate. After the initial determination of the

appropriate number of exponential equations for each dataset, the data was truncated to eliminate over fitting due to high signal to noise ratios. Once $R^2_{adj} \geq 0.98$ was achieved and the residual plot was evenly distributed over the zero line, the data was fit to both the bi-exponential and tri-exponential equations to re-evaluate which equation was most accurate. All standard errors for τ_1 , τ_2 , and τ_3 fit to be statistically relevant and $R^2_{adj} \geq 0.98$ to be considered a reasonable fit.

2.2.6 Thermoluminescence To quantify the position of an electron trap, thermoluminescence spectroscopy is employed. For these measurements, samples were placed in the fluorimeter (PTI instruments) using the same cryostat (Janis VPF-100) as in long luminescent lifetime measurements. Each sample was kept in total darkness for a period >12 h to ensure all traps are emptied. The samples were then cooled with liquid nitrogen (LN2) to 100 K and irradiated for 10 min with $\lambda_{ex} = 365$ nm for Eu^{2+} and $\lambda_{ex} = 254$ nm for Cr^{3+} . Irradiation was then terminated by manually closing the excitation shutter. Heating before heating was started after a delay of ~ 5 min. Samples were subsequently heated with a ramp rate of 5 K/min from 100 K to either 500 K (Eu^{2+}) or 600 K (Cr^{3+}). The resulting thermoluminescence spectra were collect at the maximum wavelength of the emission spectra for each sample using the time-dependent option in FelixGX. For example, the maximum emission observed in $\text{SrAl}_2\text{O}_4:\text{Eu}^{2+}$ is $\lambda_{em-max} = 520$ nm; thus, the thermoluminescence spectra was collected at this wavelength. The resulting spectra were “smoothed” using the function provided in FelixGX to improve the signal to noise ratio.

The “peak shape method” was used to analyze the thermoluminescence spectra and determine the trap depth.^{13,14} Each spectrum was deconvoluted using a Gaussian

function to reveal the number of electron traps present. The Peak Analyzer-Fit Peaks Pro option in Origin 8.6 was used to deconvolute the TL spectra. Peaks were selected manually and fit using a fitting criterion of 500 iterations and a tolerance of 1×10^{-15} . Peaks are added until an $R^2_{adj} \geq 0.95$ was reached and the residual plot was evenly distributed over the zero line. To prevent overfitting of the data, the peaks were evaluated and compared to results reported in literature. To evaluate each resulting peak, Equation 2.4 and 2.5 were employed, where E_A is the activation energy (trap depth), T_m is the maximum temperature of the peak, ω is the full width at half maximum (FWHM), k_B is the Boltzmann constant 8.617×10^{-5} eV/K, μ_g is a geometric factor. μ_g is calculated using the FWHM and $\sigma = T_m - T_2$, where T_2 is the low temperature half maximum. In a Gaussian peak, $\mu_g = 0.50$ assuming second order kinetics.¹³

$$E_A = [2.52 + 10.2(\mu_g - 0.42)] \left(\frac{k_B T_m^2}{\omega} \right) - (2k_B T_m) \quad (2.4)$$

$$\mu_g = \frac{\sigma}{\omega} \quad (2.5)$$

For new phosphors not previously reported, TL spectra should also be collected at varying ramp rates: 1K/min, 3K/min, 5K/min, and 10K/min. In this case, each spectrum should result in an equal number of trap states and trap depths that are nearly identical, for example $\text{SrAl}_2\text{O}_4:\text{Eu}^{2+}$ shown in Figure 2.1. A standard error of 5% is applied because a beneficial result of utilizing the peak shape method has been determined to result in trap depths that are within this margin of error of the real trap depth.^{13,15,16} In this example, each ramp rate produced five trap states that are at a similar T_m and calculated

E_A are in reasonable agreement, such that there are three shallow traps (<2.5 eV) and two deeper traps (> 3.5 eV).

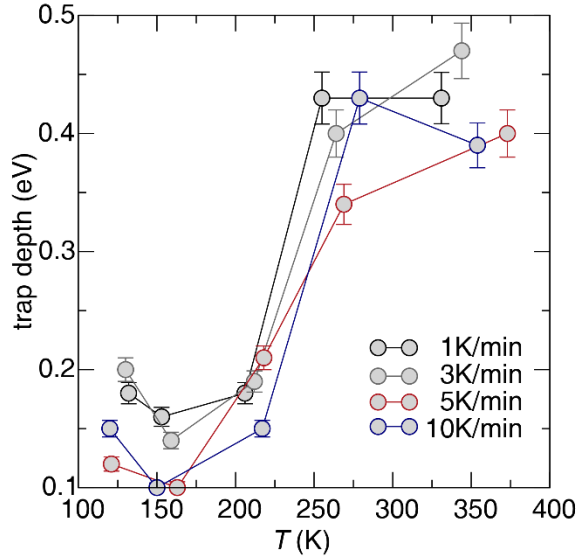


Figure 2.1 Calculated trap depths as a function of T_m of $\text{SrAl}_2\text{O}_4:\text{Eu}^{2+}$ from varying ramp rates resulting from TL.

2.2.7 Diffuse Reflectance The optical bandgap of a persistent luminescent phosphor was experimentally observed using diffuse reflectance. The measurements were completed using an Agilent Technologies Cary 5000 with a diffuse reflectance attachment. Teflon pucks were used to measure the background in the range of 200 nm to 2000 nm prior to measuring the targeted samples. After determining the background, powder samples (~2.0 g) were pressed into a 6.5 cm (2.5 in) sample holder and were placed in the instrument along with a Teflon reference. The measurements were completed in the reduced slit mode between 200 nm and 2000 nm. The resulting spectra were then transformed using the Kubelka-Munk function shown in Equation 2.6 where R_∞ is the absolute reflectance, K is the absorption coefficient, and S is the scattering coefficient.¹⁷

$$F(R_{\infty}) = \frac{(1 - R_{\infty})^2}{2R_{\infty}} = \frac{K}{S} \quad (2.6)$$

The resulting spectra are then used to create a Tauc which determines the estimated optical bandgap for either a direct or indirect bandgap material. After converting the data from wavelength, as collected, to electron volts (eV), Equation 2.7 can be used. Here $F(R_{\infty})$ is the measured absorbance, h is Plank's constant, ν is the photon frequency, n is equal to either $\frac{1}{2}$ for a direct allowed transition or 2 for an indirect allowed transition, and A is a proportional constant.¹⁸

$$(h\nu F(R_{\infty}))^{1/n} = A(h\nu - E_g) \quad (2.7)$$

2.2.8 X-ray Absorption Spectroscopy The local structure of an atom or ion can be probed using X-ray absorption spectroscopy (XAS). The XAS experiment consists of an X-ray that is used to excite a core electron (1s or 2s electron) and is promoted to a higher energy unoccupied orbital, leaving behind its electron-hole.¹⁹ The hole is then filled by an electron from a higher energy that decays into its place, emitting a photon. The resulting XAS spectrum has two regions, X-ray absorption near edge structure (XANES) and the extended X-ray absorption fine structure (EXAFS).¹⁹ XANES is a measurement near the absorption edge, while EXAFS is the oscillatory data beyond the absorption edge. XANES provides information about the oxidation state and structural disorder of the ion of interest. EXAFS, on the other hand, gives details about coordination environment, interatomic distances, and site occupancies.¹⁹

XAS experiments require high-energy X-rays, usually synchrotron radiation. The research presented here employed the Materials Research Collaborative Access Team (MRCAT) at the Advanced Photon Source, Argonne National Laboratory on the 10-BM

A,B beamline.^{20,21} Sample preparation was done by finely grinding and sieving bulk powders to a –325 mesh (Cole Palmer). It is important to note that ensuring bulk powders consisting of small homogenous particles will result in higher signal-to-noise ratios, making it easier to analyze the data.¹⁹ The powders were then spread in a thin even layer over Kapton Tape™.

Data collection for the Cr *K* edge (5989 eV) was done in fluorescence mode due to the low concentration of Cr³⁺ (≤0.005 moles) in the samples.^{20,21} Data analysis was then conducted using the Demeter software suite and its components Athena and Artemis.²² Scattering paths are calculated by *FEFF6* within the Artemis software.²² To calculate the *FEFF*, an optimized crystallographic information file (.cif) was loaded using the “Feff calculations” tab. Within the *FEFF* under the “Atoms” tab all the atoms in the unit cell are listed, selecting an atom from this list calculates the scattering paths for that atom.²² For the Cr *K* edge presented in this work, Cr was manually added in place of a cation in the desired coordination environment and chosen as the core atom. Athena was used to calibrate the data to the second derivative.²² The data is then normalized and background subtracted to E_0 (absorption edge) equal to 5989 eV. The resulting XANES spectra are then plotted for analysis. Artemis is used to employ the EXAFS equation (Equation 2.8).^{19,22}

$$\chi(k) = \sum_j \frac{N_j f_j(k) \exp[-2k^2 \sigma_j^2] \exp[-\frac{2R_j}{\lambda}]}{k R_j^2} \sin[2kR_j + \delta_j(k)] \quad (2.8)$$

The variables used to describe the data are: N_j , degeneracy (coordination number) of the neighboring ion, R_j , the interatomic distance with the neighboring atoms, and σ^2 , the Debye-Waller factor, or the disorder in the scattering path. The remaining terms, $f_j(k)$

and $\delta(k)$, are the amplitude and phase shift of the spectrum.^{19,22} The data was fit using the Fourier transform of the equation into frequency space; this plots the spectra into the most likely distance of the nearest-neighbors. An accurately described fit results in values of $0.002 \text{ \AA}^2 \geq \sigma^2 \leq 0.03 \text{ \AA}^2$, $\Delta R - 1 \geq 1$, and a reduced $\chi^2 \leq 0.05$. Fourier transform was performed using a Hanning window and the parameters are listed in Table 2.2.^{19,22}

Table 2.2 Fourier transform parameters. The first near neighbor was used for phase correction and $\epsilon(k) = 0$.

	min	max	step
Forward (k -range)	3.0 \AA^{-1}	10.0 \AA^{-1}	1.0
Reverse (r -range)	1.0 \AA	4.0 \AA	0.5

2.3 Density Functional Theory (DFT) Calculations

2.3.1 The Vienna *ab initio* Simulation Package (VASP) To account for multi-electron systems unmanageable by analytically solving the Schrödinger equation, DFT suggests valence electrons, primarily responsible for bonding, and core electrons, combined with the nucleus compose an inert core, can be treated as two independent densities by following the Hohenberg-Kohn theorems.²³ Therefore, the wave functions can be approximated by reducing the number of variables from $3N$ (N = number of electrons in a system) to 3, or the x , y , and z directions, thereby making the calculation computationally cheaper while maintaining accuracy.²⁴

VASP is a computer program used to implement DFT utilizes pseudopotentials to model exchanges and correlations between the valence electrons and the inert core.^{25,26} The plane wave basis set with an energy cutoff and projector augmented wave (PAW)

pseudopotentials were used to improve calculation efficiency and maintain an accurate description of the valence electrons enabling easier convergence.²⁶⁻²⁸ Additionally, the exchange-correlation energy was characterized using the generalized gradient approximation (GGA) by way of Perdew-Burke-Ernzerhof (PBE), which improves the accuracy of the calculation by taking into account the electron-electron interactions.²⁹ Implementing this method allows for structure optimizations to determine electronic properties, including bandgap (E_g), density of states (DOS), and total formation energy (E). Notably, the highly correlated 4f-orbitals are also not correctly modeled by DFT when using only the PBE functional due to the on-site Coulomb interactions of the localized 4f orbitals. Therefore, these calculations also require the functional requires manual input of the Hubbard parameter (U) and the exchange parameter (J).³⁰ Moreover, the GGA-PBE functional is also known for underestimating the E_g of a system by ~40% when compared to most experimental values.³¹ This underestimation is due to incorrectly modelling the Coulomb self-repulsion.^{31,32} To overcome this, Hartree-Fock exchange terms were included creating a screened-hybrid DFT functional (HSE06).³³⁻³⁵

2.3.2 Formation Energy Calculations for Point Defects To calculate a point defect in a system, a supercell with dimensions 2 x 1 x 1 (56 atoms) in a defect free structure was generated and optimized first by implementing GGA-PBE or PBE + U (for rare-earth substituted systems). Then, a screened-hybrid exchange-correlation functional (HSE06) functional was used to calculate the total energy.^{29,34} Following sufficient structure optimization, a point defect was created by manually removing one atom from each of the crystallographically independent anion and cation sites. These structures were then optimized using the same optimization parameters as the defect free structure. The total

energies (E) calculated by HSE06 were used to determine the formation energy, $\Delta E(\alpha, q)$, of a point defect in a crystalline lattice can be determined using Equation 2.9.

$$\Delta E_{vac}(\alpha, q) = E_{V_{\alpha, q}} - E_{perfect} + \mu_{\alpha} + q[E_{VBM(perfect)} \pm \Delta V + E_F] \quad (2.9)$$

Here, α is either a cation or an anion, q is the charge of the defect, $E_{V_{\alpha, q}}$ is the total energy of defect-containing supercell at a given charge state, $E_{perfect}$ is the total energy of the defect-free supercell, $E_{VBM(perfect)}$ is the valence band maximum of the perfect structure, and ΔV is used to align the VBM of the charged defect structure to the perfect structure. The band alignment, ΔV , is accomplished by taking the energy difference of between the 1s core-electron of the cation furthest from the defect site in the neutrally charged system and the 1s core electron from the cation furthest from the defect site in the charged system.³⁶ To determine the 1s electron the “ICORELEVEL” tag is set equal to 1 and the HSE06 is run one time.²⁵ The result is the chemical potential μ_{α} of atom α , and E_F the Fermi energy with reference to VBM.³⁷ The chemical potential can be treated by determining its minimum and maximum values based on extreme experimental conditions, e.g. oxygen-poor and oxygen-rich, and thermodynamic stability. Elemental components of the phase being studied first undergo electronic and structural relaxation using GGA+PBE, and then HSE06 is implemented to calculate the total energy per atom. The thermodynamic stability of μ_{α} was then bound to avoid the formation of the binary components, e.g., binary oxides, or the decomposition into the elemental components. The boundary conditions for a ternary phase, AB_2O_4 , composed of oxide reactants, AO and B_2O_3 , can be set using Equations 2.10a, 2.10b, and 2.10c.³⁶⁻³⁸

$$\Delta H_{(AB_2O_4)} = \mu_A + 2\mu_B + 4\mu_O \quad (2.10a)$$

$$\mu_A + \mu_O \leq \Delta H_{(AO)} \quad (2.10b)$$

$$2\mu_B + 3\mu_O \leq \Delta H_{B_2O_3} \quad (2.10c)$$

The enthalpy (ΔH) values are calculated from DFT and the ranges of the chemical potentials are derived and plotted accordingly, and the stability range of the AB_2O_4 is determined based on the chemical potentials.

2.4 References

1. Thompson, N., RMIT University, 2012.
2. Thompson, N.; Murugaraj, P.; Rix, C.; Mainwaring, D. E. Role of Oxidative Pre-Calcination in Extending Blue Emission of $Sr_4Al_{14}O_{25}$ Nanophosphors Formed with Microemulsions. *J. Alloys Compd.* **2012**, *537*, 147-153.
3. Birkel, A.; Denault, K. A.; George, N. C.; Doll, C. E.; Héry, B.; Mikhailovsky, A. A.; Birkel, C. S.; Hong, B.-C.; Seshadri, R. Rapid Microwave Preparation of Highly Efficient Ce^{3+} -Substituted Garnet Phosphors for Solid State White Lighting. *Chem. Mater.* **2012**, *24*, 1198-1204.
4. Brgoch, J.; Kloß, S. D.; Denault, K. A.; Seshadri, R. Accessing $(Ba_{1-x}Sr_x)Al_2Si_2O_8:Eu$ Phosphors for Solid State White Lighting via Microwave-assisted Preparation: Tuning Emission Color by Coordination Environment. *Z. Anorg. Allg. Chem.* **2014**, *640*, 1182-1189.
5. Degen, T.; Sadki, M.; Bron, E.; König, U.; Nénert, G. The HighScore Suite. *Powder Diffr.* **2014**, *29*, S13-S18.
6. Lee, P. L.; Shu, D.; Ramanathan, M.; Preissner, C.; Wang, J.; Beno, M. A.; Von Dreele, R. B.; Ribaud, L.; Kurtz, C.; Antao, S. M.; Jiao, X.; Toby, B. H. A Twelve-Analyzer Detector System for High-Resolution Powder Diffraction. *J. Synchrotron Radiat.* **2008**, *15*, 427-432.
7. Wang, J.; Toby, B. H.; Lee, P. L.; Ribaud, L.; Antao, S. M.; Kurtz, C.; Ramanathan, M.; Dreele, R. B. V.; Beno, M. A. A Dedicated Powder Diffraction Beamline at the Advanced Photon Source: Commissioning and Early Operational Results. *Rev. Sci. Instrum.* **2008**, *79*, 085105.
8. Toby, B. H. EXPGUI, A Graphical User Interface for GSAS. *J. Appl. Crystallogr.* **2001**, *34*, 210.
9. Le Bail, A. Whole Powder Pattern Decomposition Methods and Applications: A Retrospection. *Powder Diffr.* **2012**, *20*, 316-326.
10. Momma, K.; Izumi, F. VESTA 3 for Three-Dimensional Visualization of Crystal, Volumetric and Morphology Data. *J. Appl. Crystallogr.* **2011**, *44*, 1272-1276.
11. McCusker, L. B.; Von Dreele, R. B.; Cox, D. E.; Louer, D.; Scardi, P. Rietveld Refinement Guidelines. *J. Appl. Crystallogr.* **1999**, *32*, 36-50.
12. A Basic Guide to Particle Size Characterization. malvern.com (accessed 2016).

13. Chen, R. Glow Curves with General Order Kinetics. *J. Electrochem. Soc.* **1969**, *116*, 1254-1257.
14. Chen, R.; McKeever, S. W. S. *Theory of Thermoluminescence and Related Phenomena*; World Scientific, 1997.
15. Chen, R. M. S. W. S. *Theory of Thermoluminescence and Related Phenomena*; World Scientific, 1997.
16. McKeever, S. W. S. *Thermoluminescence of Solids*; Cambridge University Press, 1985.
17. Tandon, S. P.; Gupta, J. P. Measurement of Forbidden Energy Gap of Semiconductors by Diffuse Reflectance Technique. *physica status solidi (b)* **1970**, *38*, 363-367.
18. J., T.; R., G.; A., V. Optical Properties and Electronic Structure of Amorphous Germanium. *Phys. Status Solidi B* **1966**, *15*, 627-637.
19. Calvin, S. *EXAFS for Everyone*; CRC Press: Boca Raton, FL, 2013.
20. Segre, C. U.; Leyarovska, N. E.; Chapman, L. D.; Lavender, W. M.; Plag, P. W.; King, A. S.; Kropf, A. J.; Bunker, B. A.; Kemner, K. M.; Dutta, P.; Duran, R. S.; Kaduk, J. The MRCAT Insertion Device Beamline at the Advanced Photon Source. *AIP Conf. Proc.* **2000**, *521*, 419-422.
21. Kropf, A. J.; Katsoudas, J.; Chattopadhyay, S.; Shibata, T.; Lang, E. A.; Zyryanov, V. N.; Ravel, B.; Mclvor, K.; Kemner, K. M.; Scheckel, K. G.; Bare, S. R.; Terry, J.; Kelly, S. D.; Bunker, B. A.; Segre, C. U. The New MRCAT (Sector 10) Bending Magnet Beamline at the Advanced Photon Source. *AIP Conf. Proc.* **2010**, *1234*, 299-302.
22. Ravel, B.; Newville, M. ATHENA, ARTEMIS, HEPHAESTUS: Data Analysis for X-ray Absorption Spectroscopy Using IFEFFIT. *J. Synchrotron Radiat.* **2005**, *12*, 537-541.
23. Seminario, J. M. In *Theoretical and Computational Chemistry*; Seminario, J. M., Politzer, P., Eds.; Elsevier: 1995; Vol. 2, p 1-27.
24. *A Primer in Density Functional Theory*; Springer-Verlag Berlin Heidelberg: New York, 2003.
25. Hafner, J. Ab-initio Simulations of Materials Using VASP: Density-Functional Theory and Beyond. *J. Comput. Chem.* **2008**, *29*, 2044-2078.
26. Kresse, G.; Joubert, D. From Ultrasoft Pseudopotentials to the Projector Augmented-Wave Method. *Phys. Rev. B* **1999**, *59*, 1758.
27. Kresse, G.; Furthmüller, J. Efficient Iterative Schemes for Ab Initio Total-Energy Calculations Using a Plane-Wave Basis Set. *Phys. Rev. B* **1996**, *54*, 11169.
28. Blöchl, P. E. Projector Augmented-Wave Method. *Phys. Rev. B* **1994**, *50*, 17953-17979.
29. Perdew, J. P.; Burke, K.; Ernzerhof, M. Generalized Gradient Approximation Made Simple. *Phys. Rev. Lett.* **1996**, *77*, 3865-3868.
30. Hölsä, J.; Laamanen, T.; Lastusaari, M.; Niittykoski, J.; Novák, P. Electronic Structure of the SrAl₂O₄:Eu²⁺ Persistent Luminescence Material. *J. Rare Earths* **2009**, *27*, 550-554.
31. Perdew, J. P.; Levy, M. Physical Content of the Exact Kohn-Sham Orbital Energies: Band Gaps and Derivative Discontinuities. *Phys. Rev. Lett.* **1983**, *51*, 1884-1887.
32. Mori-Sánchez, P.; Cohen, A. J.; Yang, W. Localization and Delocalization Errors in Density Functional Theory and Implications for Band-Gap Prediction. *Phys. Rev. Lett.* **2008**, *100*, 146401.

33. Crowley, J. M.; Tahir-Kheli, J.; Goddard, W. A. Resolution of the Band Gap Prediction Problem for Materials Design. *J. Phys. Chem. Lett.* **2016**, *7*, 1198-1203.
34. Heyd, J. S., G. E.; Ernzerhof, M. Hybrid functionals based on a screened Coulomb potential. *The Journal of Chemical Physics* **2003**, *118*, 8207-8215.
35. Xiao, H.; Tahir-Kheli, J.; Goddard, W. A. Accurate Band Gaps for Semiconductors from Density Functional Theory. *J. Phys. Chem. Lett.* **2011**, *2*, 212-217.
36. Finley, E.; Mansouri Tehrani, A.; Brgoch, J. Intrinsic Defects Drive Persistent Luminescence in Monoclinic SrAl₂O₄:Eu²⁺. *J. Phys. Chem. C* **2018**, *122*, 16309-16314.
37. Kang, J.; Wang, L.-W. High Defect Tolerance in Lead Halide Perovskite CsPbBr₃. *J. Phys. Chem. Lett.* **2017**, *8*, 489-493.
38. Murat, A.; Medvedeva, J. E. Composition-dependent oxygen vacancy formation in multicomponent wide-band-gap oxides. *Phys. Rev. B* **2012**, *86*, 085123.

CHAPTER 3

Optimizing Blue Persistent Luminescence in $(\text{Sr}_{1-\delta}\text{Ba}_\delta)_2\text{MgSi}_2\text{O}_7:\text{Eu}^{2+},\text{Dy}^{3+}$ via Solid Solution for Use in Point-of-Care Diagnostics

Reproduced with permission from *Journal of Applied Materials and Interfaces*
(*ACS Applied Materials & Interfaces* **2016** 8 (40), 26956-26963)
©2016 American Chemical Society
DOI: 10.1021/acsami.6b10303

Erin Finley¹, Angelica Cobb¹, Anna Duke¹, Andrew Paterson^{2,3}, and Jakoah Brgoch^{1*}
¹Department of Chemistry, University of Houston, Houston, Texas 77204-5003, United States
²Luminostics Inc., Houston, Texas 77204
³Department of Chemical and Biomolecular Engineering, University of Houston, Houston, Texas 77204

3.1 Introduction

Persistent luminescence has been studied at great length to understand the mechanism in which a material is excited with a high energy light source followed by photon emission that can last for seconds to hours.¹ Because the emission after excitation arises from a trapping and detrapping, the lifetimes of persistent luminescence materials are often orders of magnitude longer than the spin-forbidden transitions in phosphorescent molecules and metal-chelate compounds.² In fact, materials such as alkaline earth aluminates produce an emission bright enough for detection by eye up to 10 hours after excitation.²⁻⁴ Currently, the primary application for persistent luminescence materials are in safety signs, emergency displays, and luminescent paints, with green emitting $\text{SrAl}_2\text{O}_4:\text{Eu}^{2+},\text{Dy}^{3+}$ the most widely used compound.^{1,4-7}

Inorganic persistent phosphors have also been applied as optical reports in a lateral flow assay (LFA) as an alternative to traditional organic fluorophores or gold nanoparticles.⁸ Smartphone-based bio-sensing technology has since been developed with the use of persistent phosphors allowing more sensitive point-of-care diagnostics.⁹

These devices use $\text{SrAl}_2\text{O}_4:\text{Eu}^{2+},\text{Dy}^{3+}$ as the reporter because its luminescent lifetime and intensity enable excellent detection limits with a smartphone camera. However, alkaline earth aluminates tend to degrade in aqueous environments¹⁰ and require encapsulation of particles in a water-resistant barrier prior to use in most bio-sensing applications.⁸ The development of alternative persistent phosphors may not only allow the replacement $\text{SrAl}_2\text{O}_4:\text{Eu}^{2+},\text{Dy}^{3+}$ in some applications but if the emission color is sufficiently distinct it may also provide a pathway for creating multiplexed assays. Dual reporter systems are increasingly used in diagnostics for several reasons including enabling healthcare providers to better diagnose diseases that manifest with similar symptoms, decreasing sampling error, and lowering cost by detecting multiple analytes in parallel in a single test.¹¹

Alkaline earth silicates are one category of persistent luminescent materials that have the added advantage of chemical stability that is lacking in the alkaline earth aluminates.^{10,12-15} The series of silicates, $\text{AE}_2\text{MgSi}_2\text{O}_7:\text{Eu}^{2+}$ ($\text{AE} = \text{Ca}, \text{Sr}, \text{Ba}$) that crystallize in the Åkermanite-type structure have all been reported as efficient phosphors.^{16,17} The Ba^{2+} forms in the monoclinic space group $\text{C2}/c$ (no. 15)^{16,18-20} while the Ca^{2+} and Sr^{2+} analogues are isostructural and form in tetragonal space group $\text{P}\bar{4}2_1m$ (no. 113).^{12,16,17,21-23} The most prominent compositions out of these phases for persistent luminescence are $\text{Ca}_2\text{MgSi}_2\text{O}_7:\text{Eu}^{2+}$ and $\text{Sr}_2\text{MgSi}_2\text{O}_7:\text{Eu}^{2+}$, which produce respective emissions in the blue (470 nm) and green (535 nm) regions of the visible spectrum.¹⁷ Preparing a solid solution between Ca^{2+} and Sr^{2+} shows that the emission wavelength is tunable and the persistent luminescent lifetimes (PersL) can be enhanced when co-substituted with Dy^{3+} .^{17,18,23} $\text{Sr}_2\text{MgSi}_2\text{O}_7:\text{Eu}^{2+},\text{Dy}^{3+}$ has since been optimized to push the persistent luminescent lifetime in excess of 10 hours.^{1,12,18,24} $\text{Ca}_2\text{MgSi}_2\text{O}_7:\text{Eu}^{2+},\text{Tb}^{3+}$ and

$\text{Ba}_2\text{MgSi}_2\text{O}_7:\text{Eu}^{2+},\text{Tm}^{3+}$ also show PersL with a reported lifetime greater than 5 hours.¹ Considering the long lifetimes and blue-green emission, these disilicate compounds are ideal targets as alternative persistent luminescent materials.

In this work, $\text{Sr}_2\text{MgSi}_2\text{O}_7:\text{Eu}^{2+}$ was specifically selected for investigation as a potential optical reporter because the crystal structure contains only one crystallographically independent position for Sr^{2+} , and, therefore, produces a narrow emission when substituted with Eu^{2+} .^{15,25} Replacing the broad spectrum emission from $\text{SrAl}_2\text{O}_4:\text{Eu}^{2+},\text{Dy}^{3+}$ with this narrower blue-green emitting PersL phosphor should allow improved spectral resolution. Moreover, substituting the larger Ba^{2+} onto the smaller Sr^{2+} site is a viable route to blue-shift the emission wavelength by modifying the crystal field splitting. The solid solution $(\text{Sr}_{1-\delta}\text{Ba}_\delta)_2\text{MgSi}_2\text{O}_7:\text{Eu}^{2+}$ ($\delta = 0, 0.125, 0.250, 0.375$) and its Dy^{3+} co-substituted analogue are thus investigated here blue-shifting the emission with minimal effect to its PersL. Limiting the green component of this phosphor series will allow the development of a multiplexing LFA by combining $(\text{Sr}_{1-\delta}\text{Ba}_\delta)_2\text{MgSi}_2\text{O}_7:\text{Eu}^{2+}$ with $\text{SrAl}_2\text{O}_4:\text{Eu}^{2+},\text{Dy}^{3+}$ for smartphone-based time-gated imaging. The results show the PersL emission can be easily measured using smartphone-based diagnostics and that the different compositions can be readily discriminated based on their optical signature allowing the potential for future multiplexing LFA studies.

3.2 Experimental

3.2.1 Sample Preparation Polycrystalline powders with the nominal compositions $[(\text{Sr}_{1-\delta}\text{Ba}_\delta)_{1.99}\text{Eu}_{0.01}]\text{MgSi}_2\text{O}_7$ and $[(\text{Sr}_{1-\delta}\text{Ba}_\delta)_{1.96}\text{Eu}_{0.01}\text{Dy}_{0.03}]\text{MgSi}_2\text{O}_7$ ($\delta = 0, 0.125, 0.250, 0.375$) were synthesized *via* high-temperature solid state synthesis using the starting reagents: SrCO_3 (Alfa Aesar 98%), BaCO_3 (Johnson Matthey 98%), MgO (Sigma-Aldrich

99.99%), SiO₂ (Sigma-Aldrich 99.5%), Eu₂O₃ (Materion Advanced Chemicals 99.9%), and Dy₂O₃ (Sigma-Aldrich 99.99%). Additionally, a 5wt% of boric acid (Sigma-Aldrich 99.98%) was incorporated as a flux. All powders were first ground with an agate mortar and pestle for approximately 30 minutes then placed in a shaker mill (Spex 8000M) for 30 min. The mixtures were heated in a reducing atmosphere of 5% H₂/95% N₂ at 1150°C for 6 hours with heating and cooling ramp rates of 3°C/min. They were subsequently ground and annealed at 1000°C for 4 hours with the same reducing atmosphere and ramp rates as the initial heating.

3.2.2 X-ray Diffraction Phase pure samples were confirmed using high-resolution synchrotron X-ray powder diffraction at room temperature with a calibrated wavelength of $\lambda = 0.414221 \text{ \AA}$ using beamline 11-BM at the Advanced Photon Source, Argonne National Laboratory. Crystallographic data were determined by Rietveld refinements using the general structural analysis system (GSAS).^{26,27} A shifted Chebyshev function was used to calculate the background, while a pseudo-Voigt function was used for determining peak shape.

3.2.3 Optical Characterization Emission and excitation spectra and persistent luminescence (PersL) lifetimes were measured at room temperature with 75 W xenon arc lamp steady state fluorimeter (PTI Instruments). For the PersL lifetimes, samples were heated to 150°C and cooled to room temperature in the dark followed by irradiation with an excitation wavelength of 365 nm for 10 min followed by a 30 s delay after the excitation source was turned off. Upon opening the shutter, the samples were measured with an emission wavelength of 460 nm for one hour. PersL lifetimes were determined from an average of three independent sample measurements.

Thermoluminescence was conducted by placing samples in a Janis cryostat (VPF-100) to control the temperature between 100 K and 500 K. The samples were isolated in total darkness for a minimum of 12 hours and initially heated to 500 K to ensure all trap states were emptied then allowed to cool to room temperature. The cryostat was then cooled to 100 K and then the sample was irradiated for 10 minutes at 365 nm using a Xe arc lamp. Upon turning off the lamp, a 30 s delay was used before the cryostat was ramped to 500 K with a ramp rate of 5 K/min. The thermoluminescence emission was measured at 465 nm.

3.2.4 Time-gated Smartphone Imaging A software application developed for the iOS 9 smartphone platform was used to image the samples.⁹ An Apple iPhone 5 was used with camera settings of ISO 2000, an irradiation time of 3.3 seconds followed by an \approx 100 millisecond delay. Five images were captured in a cycle and averaged together. Image processing tools in MATLAB 2015a and an in-house developed script were used to evaluate the red, green, and blue channel intensity profiles of each sample.

3.3 Results and Discussion

3.3.1 Structure Solution for $(\text{Sr}_{1-\delta}\text{Ba}_\delta)_2\text{MgSi}_2\text{O}_7$ ($\delta = 0, 0.125, 0.25, 0.375$) Strontium magnesium disilicate crystallizes in tetragonal space group $P\bar{4}2_1m$ (no. 113)¹⁶, with the Åkermanite structure type. Substituting Ba^{2+} for Sr^{2+} in the crystal structure forms a solid solution following $(\text{Sr}_{1-\delta}\text{Ba}_\delta)_2\text{MgSi}_2\text{O}_7:\text{Eu}^{2+}$ ($\delta = 0, 0.125, 0.25, 0.375$), which can be achieved *via* solid state synthesis. Synchrotron X-ray powder diffraction, shown in Figure 3.1a, confirms the entire solid solution is phase pure with the exception of an unidentified, minor impurity in the $\delta = 0.25$ sample. The crystal structure is maintained across this range with the expected shift in the lattice parameters to smaller Q-spacing

following the larger unit cell volume with increasing Ba^{2+} concentration. Previous reports of this solid solution suggest the crystal structure will maintain the tetragonal space group up to 80% Ba^{2+} substitution before converting to the monoclinic space group.¹⁹⁻²¹ Samples with 50% and 75% Ba^{2+} were also synthesized here; the sample with 50% Ba^{2+} formed the tetragonal space group as expected although subsequent photoluminescence measurements showed an anomalous broad emission peak with a specific increase in the green portion of the visible spectrum while the 75% Ba concentration did not form the tetragonal space group.¹⁹⁻²¹ Thus, the composition range of the samples examined in this study was limited to $0 \leq \delta \leq 0.375$.

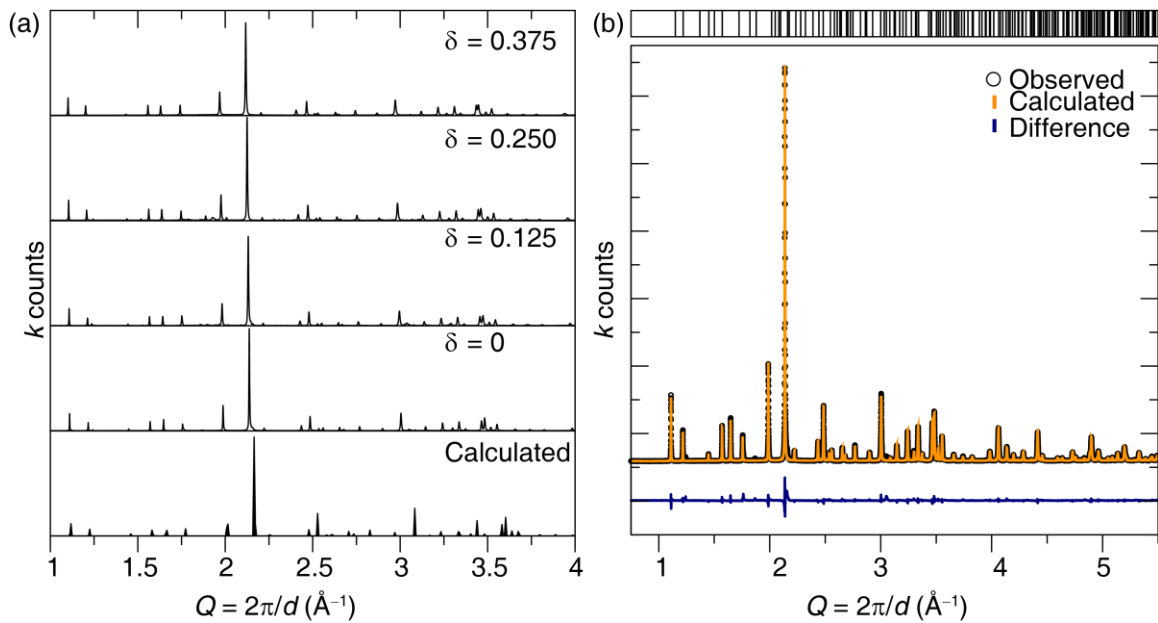


Figure 3.1. (a) Synchrotron X-ray powder diffraction data ($\text{Sr}_{1-\delta}\text{Ba}_{\delta}$) $_2\text{MgSi}_2\text{O}_7$ ($\delta = 0, 0.125, 0.250, 0.375$) shows the solid solution can be prepared phase pure. The calculated pattern was determined from [16]. (b) Rietveld refinement shown for $\delta = 0$. Experimental data is black, refinement is orange, and the difference is blue. The rare-earth ions were excluded in the refinement due to their low substitution concentration.

Table 3.1. Rietveld Refinement Data of Sr₂MgSi₂O₇ Using 11-BM Synchrotron Radiation. The rare-earth ions were excluded in the refinement due to their low substitution concentration.

Formula	Sr ₂ MgSi ₂ O ₇
Radiation type; λ (Å)	11-BM; 0.414221
2θ range (deg)	0.5-49.95
Temperature (K)	295
Space group; Z	<i>P</i> $\bar{4}$ 2 ₁ <i>m</i> (No. 113); 2
Lattice parameters	
<i>a</i> (Å)	8.0071(1)
<i>c</i> (Å)	5.1674(2)
Volume (Å ³)	331.30(1)
Calculated Density (g cm ⁻³)	3.686
Formula weight (g mol ⁻¹)	735.420
R _p	0.0829
R _{wp}	0.1179
χ ²	4.453

Table 3.2. Atomic Coordinates and Isotropic Displacement Parameters of Sr₂MgSi₂O₇:Eu²⁺ as Determined by Rietveld Refinement of 11-BM Synchrotron X-ray Diffraction Data. The rare-earth ions were excluded in the refinement due to their low substitution concentration.

Atom	Wyck. site	<i>x</i>	<i>y</i>	<i>z</i>	U _{iso} (Å ²)
Sr	4 <i>e</i>	0.3345(3)	0.1655(3)	0.5078(9)	0.0087(6)
Mg	2 <i>a</i>	0	0	0	0.006(3)
Si	4 <i>e</i>	0.1381(9)	0.3620(9)	0.943(2)	0.011(3)
O(1)	2 <i>c</i>	1/2	0	0.156(7)	0.013(1)
O(2)	4 <i>e</i>	0.140(2)	0.360(2)	0.255(4)	0.020(7)
O(3)	8 <i>f</i>	0.079(2)	0.188(2)	0.7978(4)	0.010(4)

Rietveld refinement of all phases prepared produces the crystallographic parameters with the Sr₂MgSi₂O₇:Eu²⁺ results listed in Table 3.1 and Table 3.2 and the refinement plotted in Figure 3.1b. The data for the remaining compositions are provided in the Supporting Information. All of the refinements are in excellent agreement with the previously reported crystal structure.¹⁶ The unit cell, shown in Figure 3.2, contains

alternating $[\text{SiO}_4]$ tetrahedra and $[\text{MgO}_4]$ tetrahedra that are corner connected to form layers of five-membered rings. These layers stack along the c -direction creating two dimensional sheets of polyhedral units.¹⁵ The structure also contains only one crystallographic site for Sr^{2+} that sits between the $[\text{SiO}_4]$ and $[\text{MgO}_4]$ layers and is coordinated by 8 oxygens atoms, three of which are crystallographically independent on Wyckoff site 4e. The presence of only one alkaline-earth cation site in the crystal structure is ideal for phosphors because it tends to produce a narrow spectral emission. Moreover, this crystal structure and coordination environment provides an adequate setting for substitution of Ba^{2+} on to the Sr^{2+} site.

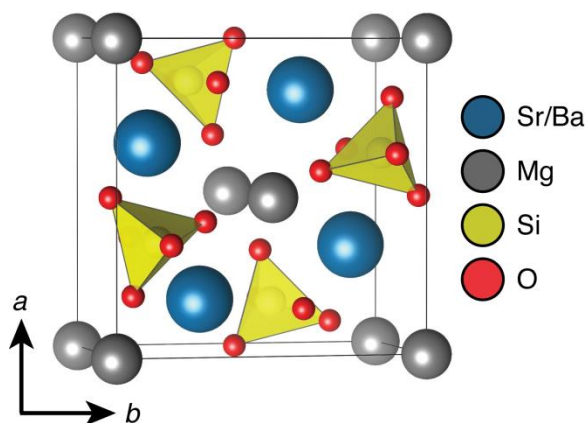


Figure 3.2. Crystal structure of $(\text{Sr}_{1-x}\text{Ba}_x)_2\text{MgSi}_2\text{O}_7$ by Rietveld refinement with $[\text{SiO}_4]$ tetrahedra highlighted.

The unit cell volume of the solid solution follows Végard's law (Figure 3.3a) with the lattice parameters and cell volume increasing linearly as the larger Ba^{2+} ($r_{8\text{-coord}} = 1.42\text{Å}$) is substituted onto the smaller Sr^{2+} site ($r_{8\text{-coord}} = 1.26\text{Å}$).²⁸ The most significant change in the crystal structure arises in the polyhedral volume of the $\text{Sr}^{2+}/\text{Ba}^{2+}$ cation site. As shown in Figure 3.3b, the unit cell volume increase is dictated entirely by the substitution

of the larger Ba^{2+} cation in the $[\text{SrO}_8]$ polyhedra while the $[\text{SiO}_4]$ and $[\text{MgO}_4]$ polyhedral units remain constant regardless of δ . The increase in average (Sr/Ba)–O bond length from $\delta = 0$ to $\delta = 0.375$ is 2.12%, which is comparable to the change in unit cell volume. The largest increase occurs for the (Sr/Ba)–O(3) bond with a 3% increase across the substitution range, while the smallest change in bond length is the (Sr/Ba)–O(2) contact. This increase in bond length with the addition of Ba^{2+} will affect crystal field splitting and ultimately change the luminescent properties of Eu^{2+} in the crystal structure.

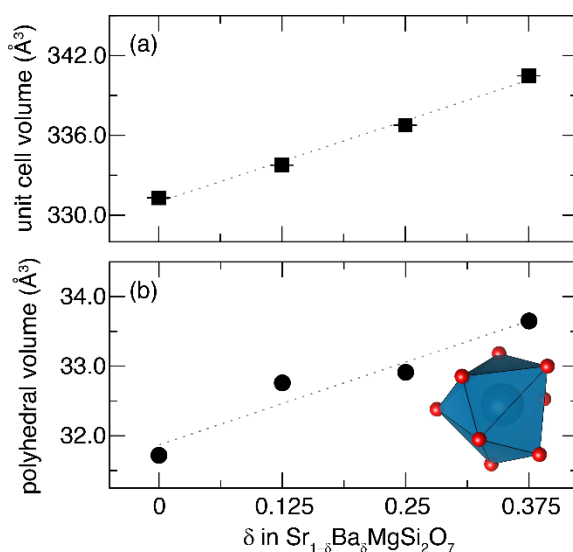


Figure 3.3. (a) Unit cell volume and (b) polyhedral volume increase linearly with in Ba^{2+} concentration. The (Sr/Ba)–O coordination environment is shown.

3.3.2 Photoluminescence The substitution of Eu^{2+} for $\text{Sr}^{2+}/\text{Ba}^{2+}$ as the luminescent center is ideal in this crystal system to induce optical properties because the atoms are isovalent and similar in ionic size.^{28,29} Incorporating Eu^{2+} as the luminescent center in $\text{Sr}_2\text{MgSi}_2\text{O}_7:\text{Eu}^{2+}$ produces an excitation maximum wavelength (λ_{ex}) at approximately 365 nm that in turn generates an efficient photon emission with a maximum wavelength (λ_{em}) at 470 nm. Figure 3.4a shows the excitation spectra of the solid solution changes

minimally upon the addition of Ba^{2+} while Figure 3.4b shows that when excited with a $\lambda_{\text{ex}} = 365 \text{ nm}$ there is an observable blue shift in the emission wavelength from $\lambda_{\text{em}} = 472 \text{ nm}$ ($\delta = 0$) to $\lambda_{\text{em}} = 460 \text{ nm}$ ($\delta = 0.375$). The emission corresponds to the relaxation from the $\text{Eu}^{2+} 5d$ excited state to the $4f$ ground state (${}^2D_j \rightarrow {}^8S_{7/2}$) of a single luminescent center. Plotting the color points of this solid solution on a 1931 Commission Internationale de l'Eclairage (CIE) diagram, Figure 3.4c, further supports the significant blue-shift with the addition of Ba^{2+} . Because Ba^{2+} is larger than Sr^{2+} there will be an increase in bond lengths around the luminescent center. This increase leads to a decrease in the crystal field splitting of the $\text{Eu}^{2+} 5d$ -orbitals producing a greater separation of these states from the $4f$ -orbitals. Consequently, this change causes a greater energy difference between the excited state and the ground state, which gives rise to the observed shift in the emission spectra.^{29,30}

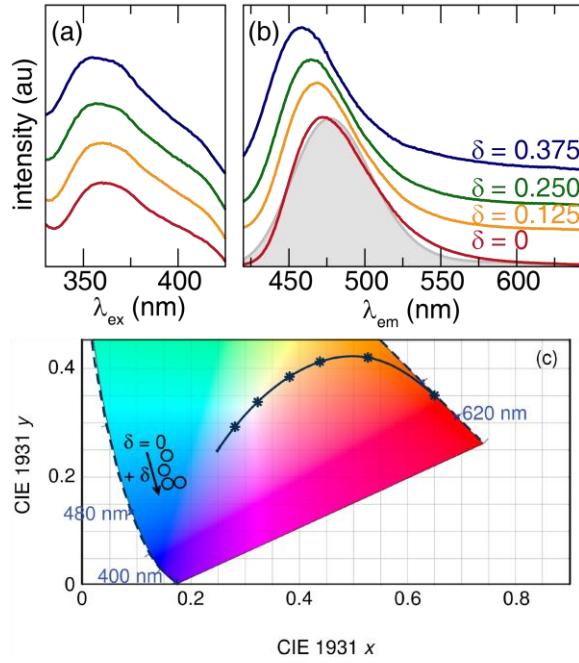


Figure 3.4. The (a) excitation, (b) emission spectra for $(\text{Sr}_{1-\delta}\text{Ba}_\delta)_{2-x}\text{MgSi}_2\text{O}_7:\text{Eu}^{2+}$ ($\delta = 0, 0.125, 0.250, 0.375$). Emission spectra were collected at $\lambda = 365$ nm and the excitation spectra were collected at the λ_{max} of emission spectrum for each sample. The Gaussian fit is solid gray (c) CIE 1931 diagram showing blue shift and reduction in green emission.

Considering these compounds are known to show PersL,^{12,14} the effect of solid solution formation on the photon emission lifetime was also examined. The (long lifetime) decay curves for the solid solutions, shown in Figure 3.5, are analyzed according to Equation 3.1,²⁴ where I is the normalized intensity; A_1 , A_2 , and A_3 are pre-exponential constants; τ_1 , τ_2 , and τ_3 are luminescent decays and t is the time.

$$I = A_1 e^{-\frac{t}{\tau_1}} + A_2 e^{-\frac{t}{\tau_2}} + A_3 e^{-\frac{t}{\tau_3}} \quad (3.1)$$

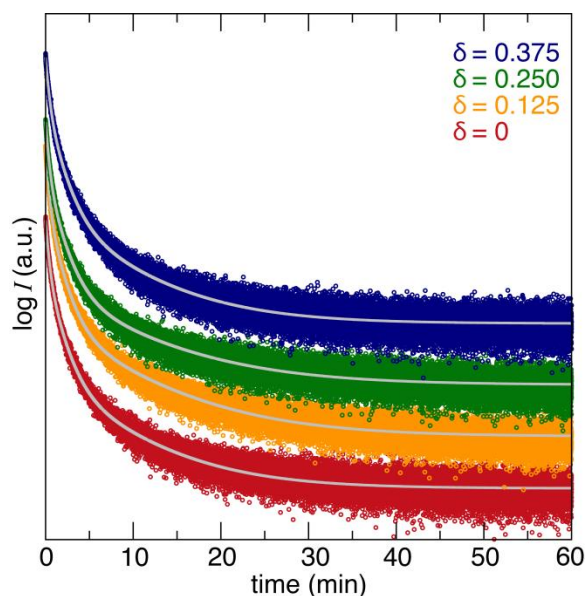


Figure 3.5. PersL of $(\text{Sr}_{1-\delta}\text{Ba}_\delta)_2\text{MgSi}_2\text{O}_7:\text{Eu}^{2+}$ ($\delta = 0, 0.125, 0.250, 0.375$) fit to a triple exponential. Circles indicate raw data and solid gray line is the fit.

Fitting to a tri-exponential provided the best agreement across the entire range of data collected; thus, three different long lifetimes are present in these compounds. Table 3.3 shows the decay times of τ_1 , τ_2 , and τ_3 (in minutes) as the average taken from three measurements on each sample. There is very little variation in time throughout the solid solution suggesting the substitution of Ba^{2+} has little effect on the PersL. These data reveal that it is possible to modify the emission color of this series of phosphors through the preparation of a solid solution without losing any of the PersL qualities.

Table 3.3. Average long lifetime decay times of $(\text{Sr}_{1-\delta}\text{Ba}_\delta)_2\text{MgSi}_2\text{O}_7:\text{Eu}^{2+}$.

δ	τ_1 (min)	τ_2 (min)	τ_3 (min)
0	0.37(1)	1.49(5)	9.2(8)
0.125	0.36(1)	1.51(6)	9.4(8)
0.250	0.38(1)	1.62(1)	10.0(2)
0.375	0.39(1)	1.68(5)	10(1)

Although the PersL lifetimes occur within a desirable range for use in LFA bio-sensing applications, the intensity of the photon emission is also a factor. Therefore, to enhance the emission intensity the addition of a rare-earth co-dopant was explored. The use of co-dopants is often employed to enhance the optical properties and lifetimes of PersL phosphors, specifically the incorporation of Ce^{3+} , Nd^{3+} and Dy^{3+} .^{15,31} In this work, Dy^{3+} was selected for co-substitution with Eu^{2+} because it was determined to have a longer lifetime when compared to Ce^{3+} or Nd^{3+} .¹⁵ To ensure the presence of the trivalent rare-earth ion did not alter the optical properties relative to the Eu^{2+} -only compounds, the emission and excitation spectra of the $\text{Eu}^{2+},\text{Dy}^{3+}$ co-substituted samples were also collected, shown in Figure 3.6a and Figure 3.6b. The excitation spectra of all compositions are comparable to the Eu^{2+} -only compounds and there are no additional peaks in the emission spectra. Likewise, the blue shift in the emission spectra is also observed as the concentration of Ba^{2+} is increased. Plotting the color points for the solid solution on a CIE diagram in Figure 3.6c shows that increasing Ba^{2+} again causes a blue-shift in the emission spectrum.

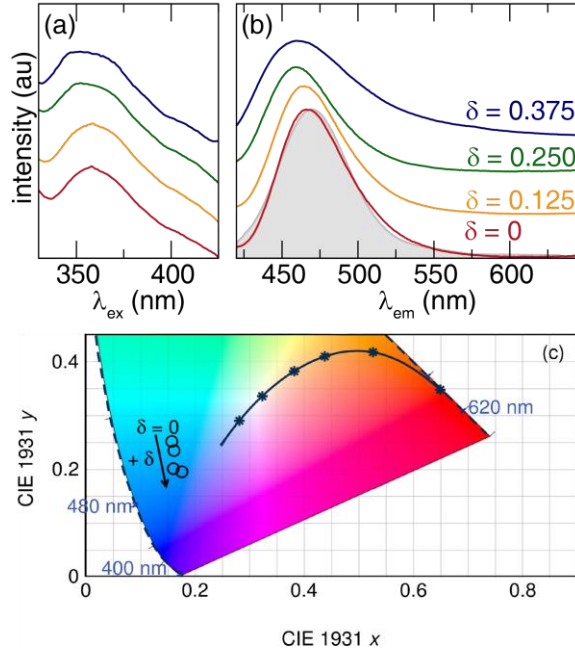


Figure 3.6. (a) excitation, (b) emission spectra for $(\text{Sr}_{1-\delta}\text{Ba}_\delta)_2\text{MgSi}_2\text{O}_7:\text{Eu}^{2+},\text{Dy}^{3+}$ ($\delta = 0, 0.125, 0.250, 0.375$) Emission spectra were collected at $\lambda = 365$ nm and the excitation spectra were collected at the λ_{max} of emission spectrum for each sample. The Gaussian fit is solid gray. (c) CIE diagram showing blue shift across the solid solution.

The PersL for the solid solution was also fit to Equation 3.1 with the results shown in Figure 3.7 and lifetimes given in Table 3.4. The presence of Dy^{3+} indeed contributes to the PersL of this material as previously reported with the average long lifetimes occurring for 3 minutes longer than the Eu^{2+} -only samples.^{15,31} Incorporating the trivalent rare-earth ion in the structure induces additional defect states that can act as luminescent trapping centers, thus increasing the long lifetime as well as the emission intensity of these materials.

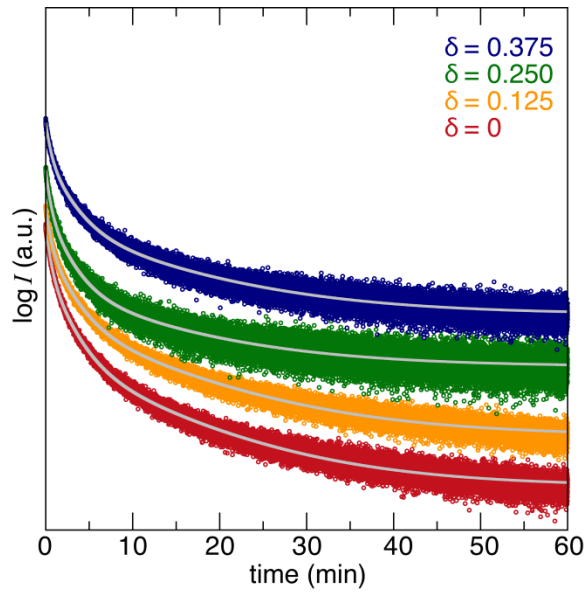


Figure 3.7 . PersL of $(\text{Sr}_{1-\delta}\text{Ba}_\delta)_{2-x}\text{MgSi}_2\text{O}_7:\text{Eu}_x^{2+}$ ($\delta = 0, 0.125, 0.250, 0.375$) fit to a triple exponential. Circles indicate raw data and solid gray line is the fit.

Table 3.4. Average lifetime decay of $(\text{Sr}_{1-\delta}\text{Ba}_\delta)_{2-x}\text{MgSi}_2\text{O}_7:\text{Eu}^{2+}, \text{Dy}^{3+}$ ($\delta = 0, 0.125, 0.250, 0.375$) of each sample measured three times

δ	τ_1 (min)	τ_2 (min)	τ_3 (min)
0	0.50(2)	2.37(5)	12.8(1)
0.125	0.48(3)	2.2(2)	12.7(7)
0.250	0.45(8)	2.3(2)	12.3(8)
0.375	0.49(2)	2.3(1)	12.8(7)

3.3.3 Thermoluminescence To investigate the origin of the persistent luminescent lifetime, thermoluminescence (TL) measurements were conducted on the solid solutions of the Eu^{2+} -only and $\text{Eu}^{2+}, \text{Dy}^{3+}$ co-substituted samples. The presence of trap states is evident when a luminescent emission peak appears as a sample is heated at a constant rate even without concurrent excitation.³² The location, intensity, and shape of the peak is dependent on the heating rate, the wavelength of

irradiation, and the delay between terminating the irradiation and initiating heating.³³ To observe PersL, a trap depth should be greater than 0.4 eV at room temperature because traps shallower than this energy will detrapp (empty) at lower temperatures.^{32,34} Alternatively, traps greater than 1 eV are considered too far below the conduction band for thermal release at room temperature. Therefore, the optimal trap depth reported for PersL at room temperature is often considered to occur at ≈ 0.65 eV.^{2,33} Here, the “peak shape method” of analysis was used to quantify the trap depths from the TL peaks by deconvolution of the data using a Gaussian function ensuring the trap depths are within 5% of the actual trap depth.³⁴

The location of the trap depths are determined by solving for the activation energy (E_A) as shown in Equation 3.2.^{14,15,35} Second order kinetics are expected; however, value of the coefficient (c_ω) is more accurately determined when using the geometric factor, μ_g . In this case, $\mu_g = 0.5$ which is found by Equation 3.3, where $\sigma = T_2 - T_m$ and ω the full width at half maximum of the TL spectrum. T_2 is the low-temperature half maximum, T_m is the maximum temperature and k_B is the Boltzmann constant.³⁵⁻³⁷ Here, ω is used because it is provided by the deconvolution of the experimentally measured peaks. The full deconvolutions of all compounds prepared here are provided in Supporting Information.

$$E_A = [2.52 + 10(\mu_g - 0.42)] \left(\frac{k_B T_m^2}{\omega} \right) - (2k_B T_m) \quad (3.2)$$

$$\mu_g = \frac{\sigma}{\omega} \quad (3.3)$$

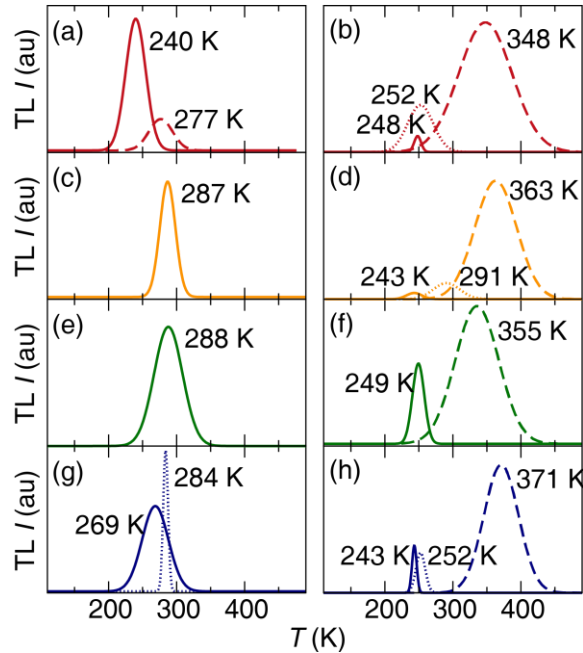


Figure 3.8. Thermoluminescence peaks and the corresponding temperatures for $(\text{Sr}_{1-\delta}\text{Ba}_\delta)_{2-x}\text{MgSi}_2\text{O}_7$ ($\delta = 0, 0.125, 0.250, 0.375$). Eu^{2+} only is shown for plots a, c, e, and g while $\text{Eu}^{2+}, \text{Dy}^{3+}$ is shown as plots b, d, f, and h.

Figure 3.8 shows the presence of TL peaks occurring between 240 K and 371 K, which supports that trap states are present in all of these phases and is likely the origin of PersL. The trap depths calculated from these peaks are presented in Table 3.5. In the Eu^{2+} -only samples, the presence of TL peaks are likely due to intrinsic defects occurring in the crystal structure that give rise to trap states. The solid solution co-substituted with Dy^{3+} has an additional peak above 300 K arising from the inclusion of Dy^{3+} and is consistent with previous reports of $\text{Sr}_2\text{MgSi}_2\text{O}_7:\text{Eu}^{2+}, \text{Dy}^{3+}$.^{12,19} All of the phases regardless of composition produce trap depths between 0.40 eV and 0.89 eV, which is near the ideal value of ≈ 0.65 eV for PersL to occur at room temperature. Interestingly, when $\delta = 0.375$ there are also very deep traps present, >1 eV. These should only weakly contribute to the observed PersL because the activation energy required to empty these traps is not sufficient at room temperature. Nevertheless, peak location and trap depth

vary only slightly across the solid solution supporting the minor changes in PersL lifetimes with the substitution of Ba²⁺ for Sr²⁺. The combination of tunable emission wavelength and only minor variations in the luminescence lifetimes allows the emission color to be optimized as the optical reporter in an LFA.

Table 3.5. TL peaks and their corresponding trap depths for (Sr_{1- δ} Ba _{δ})_{2-x}MgSi₂O₇ (δ = 0, 0.125, 0.250, 0.375). Eu²⁺ only is shown for plots a, c, e, and g, while Eu²⁺,Dy³⁺ is shown as plots b, d, f, and h

Plot	Temperature (K)	Trap Depth (eV)
a	240	0.44
	277	0.49
	247	1.28
b	251	0.40
	364	0.45
c	287	0.83
	243	0.59
d	291	0.48
	363	0.46
e	288	0.43
	249	0.82
f	355	0.42
	269	0.41
g	284	2.69
	243	2.05
	252	1.10
h	371	0.60

3.3.4 Smartphone-Based Time-Gated Imaging For the incorporation of PersL phosphors as optical reporters in this point-of-care diagnostic testing format, it is essential the materials can be excited using a smartphone flash (usually a blue LED-based package) and that the smartphone camera can detect the PersL phosphor emission. This analysis can be completed using smartphone-based time-gated imaging which allows a predetermined and controlled delay between the excitation of a reporter and the detection of the emission intensity.⁹ The short delay offers the ability to excite the

reporter while providing adequate time for background from scattered excitation light and autofluorescence to fade before capturing the image of the reporter's luminescence. A software application designed for smartphones has been developed that sets the delay to approximately 100 ms. $\text{SrAl}_2\text{O}_4:\text{Eu}^{2+},\text{Dy}^{3+}$ has already been demonstrated as a successful reporter in this format and show that images captured by smartphone-based time-gated imaging require significant emission intensity at approximately one second after termination of the excitation source (the smartphone flashlight).^{8,9}

The long lifetimes measured for both of the solid solutions prepared in this study indicate the emission intensity should be sufficient for detection by the smartphone-based time-gated imaging application. Measuring the photon emission with an iPhone 5 (iOS 9) produced the images shown in Figure 3.9. The smartphone images can then be described using an RGB color model to determine the intensity profiles of the red, blue, and green channels present during the emission. The intensity profiles of the blue and green channels of the solid solutions are plotted in Figure 3.9. The red channel has a minimal intensity in these phases and is omitted for clarity. When only Eu^{2+} is substituted in the crystal structure; the green channel intensity decreases with an increase in the Ba^{2+} concentration, while the blue channel retains its intensity. This is in agreement with the blue-shift in the luminescence spectrum upon incorporation of the larger Ba^{2+} cation. Interestingly, the samples co-substituted with $\text{Eu}^{2+},\text{Dy}^{3+}$ also maintain the intensity of the blue channel regardless of δ ; however, the decline in the green channel is only observed when $\delta = 0.375$.

The images collected by the smartphone application for each of the powder samples show the effect of reducing the green-component on the overall intensity. The compounds containing both blue and green components appear significantly brighter as

the smartphone camera's spectral sensitivity varies across the visible spectrum. Consequently, replacing the bright green PersL phosphor $\text{SrAl}_2\text{O}_4:\text{Eu}^{2+},\text{Dy}^{3+}$ would require the bright blue-green emitting Dy^{3+} co-substituted samples due to their similar spectral response and equivalent brightness. However, if the desired application is multiplexing, the intensity of the green channel of the co-substituted samples may be too bright to distinguish the disilicate from $\text{SrAl}_2\text{O}_4:\text{Eu}^{2+},\text{Dy}^{3+}$; thus, differentiating these two compounds in a multiplexed assay may prove difficult. This is best illustrated through a direct comparison between $\text{SrAl}_2\text{O}_4:\text{Eu}^{2+},\text{Dy}^{3+}$ and $(\text{Sr}_{0.625}\text{Ba}_{0.375})_2\text{MgSi}_2\text{O}_7:\text{Eu}^{2+}$ as well as $\text{SrAl}_2\text{O}_4:\text{Eu}^{2+},\text{Dy}^{3+}$ and $(\text{Sr}_{0.625}\text{Ba}_{0.375})_2\text{MgSi}_2\text{O}_7:\text{Eu}^{2+},\text{Dy}^{3+}$ in a single point-of-care diagnostic test.

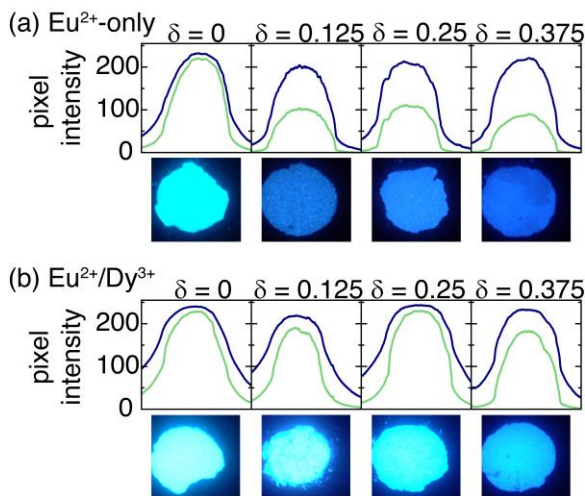


Figure 3.9. Time-gated luminescence imaging acquired with a smartphone-based bio-sensing platform and intensity profile scan. (a) $\text{Sr}_{1-\delta}\text{Ba}_\delta)_2\text{-xMgSi}_2\text{O}_7:\text{Eu}^{2+}$ and (b) $\text{Sr}_{1-\delta}\text{Ba}_\delta)_2\text{-xMgSi}_2\text{O}_7:\text{Eu}^{2+},\text{Dy}^{3+}$. Blue line represents the blue channel intensity and green line is the green channel intensity.

Simultaneously imaging $\text{SrAl}_2\text{O}_4:\text{Eu}^{2+},\text{Dy}^{3+}$ and $(\text{Sr}_{0.625}\text{Ba}_{0.375})_2\text{MgSi}_2\text{O}_7:\text{Eu}^{2+}$ (Figure 3.10a) as well as $\text{SrAl}_2\text{O}_4:\text{Eu}^{2+},\text{Dy}^{3+}$ and $(\text{Sr}_{0.625}\text{Ba}_{0.375})_2\text{MgSi}_2\text{O}_7:\text{Eu}^{2+},\text{Dy}^{3+}$ (Figure 3.10b) shows that the different optical properties of the two PersL phosphors can be resolved

using the color profile collected by the smartphone-based time-gated imaging. $\text{SrAl}_2\text{O}_4:\text{Eu}^{2+},\text{Dy}^{3+}$ has a more intense green channel whereas $(\text{Sr}_{0.625}\text{Ba}_{0.375})_2\text{MgSi}_2\text{O}_7:\text{Eu}^{2+}$ and the co-substituted analogues have a more intense blue channel. In the case of the co-substituted samples, a significant green component remains in the emission that could make partitioning these two signals difficult. Conversely, even though the $(\text{Sr}_{0.625}\text{Ba}_{0.375})_2\text{MgSi}_2\text{O}_7:\text{Eu}^{2+}$ has less of a green component its overall lower intensity may limit detectability at the low concentrations of PersL phosphors used in LFAs.⁸ Nevertheless, these images and color profile scans substantiate the possibility of combining multiple phosphors in point-of-care assays adapted for use in the smartphone-based bio-sensing application.

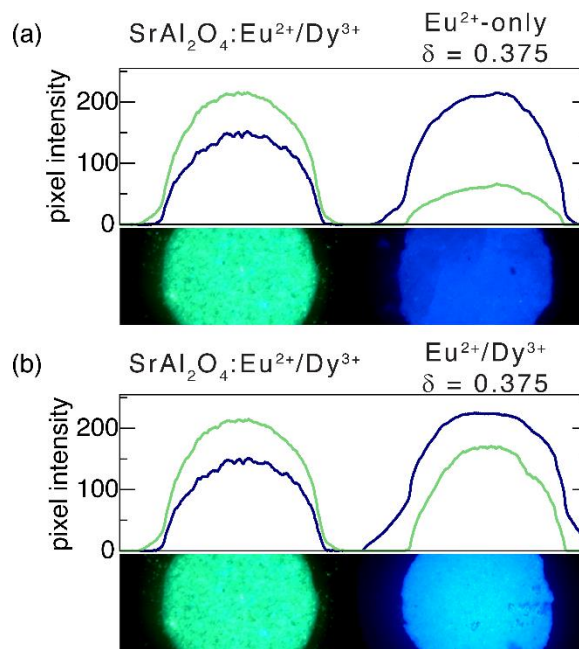


Figure 3.10. Comparison of spectral response between $\text{SrAl}_2\text{O}_4:\text{Eu}^{2+},\text{Dy}^{3+}$ and (a) $(\text{Sr}_{1-\delta}\text{Ba}_\delta)_2\text{MgSi}_2\text{O}_7:\text{Eu}^{2+}$ and (b) $(\text{Sr}_{1-\delta}\text{Ba}_\delta)_2\text{MgSi}_2\text{O}_7:\text{Eu}^{2+},\text{Dy}^{3+}$ using time-gated luminescence. The images were acquired with a smartphone-based bio-sensing platform.

3.4 Conclusions

The solid solutions $(\text{Sr}_{1-\delta}\text{Ba}_\delta)_2\text{MgSi}_2\text{O}_7:\text{Eu}^{2+}$ and $(\text{Sr}_{1-\delta}\text{Ba}_\delta)_2\text{MgSi}_2\text{O}_7:\text{Eu}^{2+},\text{Dy}^{3+}$ ($\delta = 0, 0.125, 0.250, 0.375$) were made *via* solid state synthesis as pure phase polycrystalline powders. Synchrotron X-ray diffraction showed a linear increase in the lattice parameters as well as in the cell volume with the increasing substitution of Ba^{2+} for Sr^{2+} . Photoluminescent measurements supported that changes in coordination environment around the $\text{Sr}^{2+}/\text{Ba}^{2+}$ cations follow crystal field splitting with a blue-shift as the Ba^{2+} concentration is increased. Persistent luminescent lifetimes showed little change across the solid solution due to the consistent position of the traps as determined by thermoluminescence. This supports that it is possible to tune the color of a PersL compound *via* crystal field splitting without any major effect on its lifetime properties.

Integrating these PersL phosphors with a smartphone-based bio-sensing application showed that it is possible to capture images of all compositions prepared using a combination of the smartphone flash for excitation and the smartphone camera. The resulting image analysis showed that $(\text{Sr}_{1-\delta}\text{Ba}_\delta)_2\text{MgSi}_2\text{O}_7:\text{Eu}^{2+}$ has a substantial decrease in the emission intensity of the green channel with increasing Ba^{2+} concentration. A comparison between $\text{SrAl}_2\text{O}_4:\text{Eu}^{2+},\text{Dy}^{3+}$ and $(\text{Sr}_{0.625}\text{Ba}_{0.375})_2\text{MgSi}_2\text{O}_7:\text{Eu}^{2+}$ and $(\text{Sr}_{0.625}\text{Ba}_{0.375})_2\text{MgSi}_2\text{O}_7:\text{Eu}^{2+},\text{Dy}^{3+}$ reinforced the ability to detect the disilicate phases even in the presence of a the well-known green-emitting PersL phosphor. Although the particles sizes produced using the high-temperature route tend to be large, this simple synthetic approach allowed a quick comparison that was necessary to confirm $\text{Sr}_2\text{MgSi}_2\text{O}_7:\text{Eu}^{2+}$ is a suitable alternative to $\text{SrAl}_2\text{O}_4:\text{Eu}^{2+},\text{Dy}^{3+}$ while $(\text{Sr}_{0.625}\text{Ba}_{0.375})_2\text{MgSi}_2\text{O}_7:\text{Eu}^{2+}$ is viable option in multiplexed assays. Transitioning to a soft

chemical synthetic method is now required to produce nanosized persistent luminescence materials for their direct incorporation in any biosensing format.

3.5 Acknowledgments

The authors thank the Department of Chemistry at the University of Houston for providing generous startup funds and the R. A. Welch Foundation through the TcSUH Robert A. Welch Professorship in High Temperature Superconducting (HTSg) and Chemical Materials (E-0001). Use of the Advanced Photon Source at Argonne National Laboratory was supported by the U.S. Department of Energy, Office of Science, Office of Basic Energy Sciences, under Contract DE-AC02-06CH11357.

3.6 References

1. Van den Eeckhout, K.; Smet, P. F.; Poelman, D. Persistent Luminescence in Eu^{2+} -Doped Compounds: A Review. *Materials* **2010**, *3*, 2536.
2. Matsuzawa, T.; Aoki, Y.; Takeuchi, N.; Murayama, Y. A New Long Phosphorescent Phosphor with High Brightness, $\text{SrAl}_2\text{O}_4 : \text{Eu}^{2+}, \text{Dy}^{3+}$. *J. Electrochem. Soc.* **1996**, *143*, 2670-2673.
3. Aitasalo, T.; Hölsä, J.; Jungner, H.; Lastusaari, M.; Niittykoski, J. Thermoluminescence Study of Persistent Luminescence Materials: Eu^{2+} - and R^{3+} -Doped Calcium Aluminates, $\text{CaAl}_2\text{O}_4 : \text{Eu}^{2+}, \text{R}^{3+}$. *J. Phys. Chem. B* **2006**, *110*, 4589-4598.
4. Botterman, J.; Joos, J. J.; Smet, P. F. Trapping and Detrapping in $\text{SrAl}_2\text{O}_4 : \text{Eu}^{2+}, \text{Dy}^{3+}$ Persistent Phosphors: Influence of Excitation Wavelength and Temperature. *Phys. Rev. B* **2014**, *90*, 085147.
5. Aitasalo, T.; Dereń, P.; Hölsä, J.; Jungner, H.; Krupa, J. C.; Lastusaari, M.; Legendziewicz, J.; Niittykoski, J.; Stręk, W. Persistent Luminescence Phenomena in Materials Doped with Rare Earth Ions. *J. Solid State Chem.*, *171*, 114-122.
6. Clabau, F.; Rocquefelte, X.; Jobic, S.; Deniard, P.; Whangbo, M. H.; Garcia, A.; Le Mercier, T. Mechanism of Phosphorescence Appropriate for the Long-Lasting Phosphors Eu^{2+} -Doped SrAl_2O_4 with Co-Dopants Dy^{3+} and B^{3+} . *Chem. Mater.* **2005**, *17*, 3904-3912.
7. Dorenbos, P. Mechanism of Persistent Luminescence in Eu^{2+} and Dy^{3+} Co-doped Aluminate and Silicate Compounds. *J. Electrochem. Soc.* **2005**, *152*, H107-H110.
8. Paterson, A. S.; Raja, B.; Garvey, G.; Kolhatkar, A.; Hagström, A. E. V.; Kourentzi, K.; Lee, T. R.; Willson, R. C. Persistent Luminescence Strontium

- Aluminate Nanoparticles as Reporters in Lateral Flow Assays. *Anal. Chem.* **2014**, *86*, 9481-9488.
9. Willson, R.; Paterson, A.; Phosphorescent reporters, US20150105284 A1, 2015
 10. Denault, K. A.; Brgoch, J.; Kloß, S. D.; Gaultois, M. W.; Siewenie, J.; Page, K.; Seshadri, R. Average and Local Structure, Debye Temperature, and Structural Rigidity in Some Oxide Compounds Related to Phosphor Hosts. *ACS Appl. Mater. Inter.* **2015**, *7*, 7264-7272.
 11. Goldman, E. R.; Clapp, A. R.; Anderson, G. P.; Uyeda, H. T.; Mauro, J. M.; Medintz, I. L.; Mattoussi, H. Multiplexed Toxin Analysis Using Four Colors of Quantum Dot Fluororeagents. *Anal. Chem.* **2004**, *76*, 684-688.
 12. Liu, B.; Shi, C.; Yin, M.; Dong, L.; Xiao, Z. The Trap States in the Sr₂MgSi₂O₇ and (Sr,Ca)MgSi₂O₇ Long Afterglow Phosphor Activated by Eu²⁺ and Dy³⁺. *J. Alloys Compd.* **2005**, *387*, 65-69.
 13. Carlson, S.; Hölsä, J.; Laamanen, T.; Lastusaari, M.; Malkamäki, M.; Niittykoski, J.; Valtonen, R. X-ray Absorption Study of Rare Earth Ions in Sr₂MgSi₂O₇:Eu²⁺, R³⁺ Persistent Luminescence Materials. *Opt. Mater.* **2009**, *31*, 1877-1879.
 14. Sahu, I. P.; Bisen, D. P.; Brahme, N.; Tamrakar, R. K. Enhanced luminescence performance of Sr₂MgSi₂O₇:Eu²⁺ blue long persistence phosphor by co-doping with Ce³⁺ ions. *J. Mater. Sci. - Mater. Electron.* **2016**, *27*, 554-569.
 15. Lastusaari, M.; Jungner, H.; Kotlov, A.; Laamanen, T.; Rodrigues Lucas, C. V.; Brito Hermi, F.; Hölsä, J. In *Z. Naturforsch. B* 2014; Vol. 69, p 171.
 16. Ardit, M.; Dondi, M.; Merlini, M.; Cruciani, G. Melilite-Type and Melilite-Related Compounds: Structural Variations Along the Join Sr_{2-x}Ba_xMgSi₂O₇ (0 ≤ x ≤ 2) and High-Pressure Behavior of the Two End-Members. *Phys. Chem. Miner.* **2012**, *39*, 199-211.
 17. Poort, S. H. M.; Reijnhoudt, H. M.; van der Kuip, H. O. T.; Blasse, G. Luminescence of Eu²⁺ in Silicate Host Lattices with Alkaline Earth Ions in a Row. *J. Alloys Compd.* **1996**, *241*, 75-81.
 18. Lin, Y.; Nan, C.-W.; Zhou, X.; Wu, J.; Wang, H.; Chen, D.; Xu, S. Preparation and characterization of long afterglow M₂MgSi₂O₇-based (M: Ca, Sr, Ba) photoluminescent phosphors. *Mater. Chem. Phys.* **2003**, *82*, 860-863.
 19. Wu, H.; Hu, Y.; Zeng, B.; Mou, Z.; Deng, L. Tunable luminescent properties by adjusting the Sr/Ba ratio in Sr_{1.97-x}Ba_xMgSi₂O₇:Eu^{2+0.01}, Dy^{3+0.02} phosphors. *J. Phys. Chem. Solids* **2011**, *72*, 1284-1289.
 20. Zhang, C.; Gong, X.; Deng, C. The phase transition of color-tunable long afterglow phosphors Sr_{1.94-x}Ba_xMgSi₂O₇. *J. Alloys Compd.* **2016**, *657*, 436-442.
 21. Kim, T.; Kim, Y.; Kang, S. Luminescence properties of Eu²⁺ in M₂MgSi₂O₇ (M=Ca, Sr, and Ba) phosphors. *Appl. Phys. B* **2012**, *106*, 1009-1013.
 22. Zhang, M.; Wang, J.; Ding, W.; Zhang, Q.; Su, Q. Luminescence properties of M₂MgSi₂O₇:Eu²⁺ (M = Ca, Sr) phosphors and their effects on yellow and blue LEDs for solid-state lighting. *Opt. Mater.* **2007**, *30*, 571-578.
 23. Kwon, K. H.; Im, W. B.; Jeon, D. Y. Energy Transfer in Sr₂MgSi₂O₇: Eu²⁺ Phosphors in Nano Scale and Their Application to Solid State Lighting with Excellent Color Rendering. *J. Nanosci. Nanotechnol.* **2013**, *13*, 4079-4083.
 24. Lin, Y.; Tang, Z.; Zhang, Z.; Wang, X.; Zhang, J. Preparation of a New Long Afterglow Blue-Emitting Sr₂MgSi₂O₇-Based Photoluminescent Phosphor. *J. Mater. Sci. Lett.* **2001**, *20*, 1505-1506.

25. Tydtgat, C.; Meert, K. W.; Poelman, D.; Smet, P. F. Optically Stimulated Detrapping During Charging of Persistent Phosphors. *Opt. Mat. Express* **2016**, *6*, 844-858.
26. Larson, A. C. Von. Dreele., R.B. General Structure Analysis System (GSAS). **2004**.
27. Toby, B. H. EXPGUI, A Graphical User Interface for GSAS. *J. Appl. Crystallogr.* **2001**, *34*, 210.
28. Shannon, R. D. Revised Effective Ion Radii and Systematic Studies of Interatomic Distances in Halides and Chalcogenides. *Acta Crystallogr. Sect. A: Found. Crystallogr.* **1976**, *32*, 751-767.
29. George, N. C.; Denault, K. A.; Seshadri, R. Phosphors for Solid-State White Lighting. *Annu. Rev. Mater. Res.* **2013**, *43*, 481-501.
30. Wu, J. L.; Gundiah, G.; Cheetham, A. K. Structure–property correlations in Ce-doped garnet phosphors for use in solid state lighting. *Chem. Phys. Lett.* **2007**, *441*, 250-254.
31. Holsa, J. P.; Niittykoski, J.; Kirm, M.; Laamanen, T.; Lastusaari, M.; Novak, P.; Raud, J. Synchrotron Radiation Study of the $M_2MgSi_2O_7:Eu^{2+}$ Persistent Luminescence Materials. *ECS Transactions* **2008**, *6*, 1-10.
32. Chen, R.; McKeever, S. W. S. *Theory of Thermoluminescence and Related Phenomena*; World Scientific, 1997.
33. Van den Eeckhout, K.; Bos, A. J. J.; Poelman, D.; Smet, P. F. Revealing Trap Depth Distributions in Persistent Phosphors. *Phys. Rev. B* **2013**, *87*, 045126.
34. McKeever, S. W. S. *Thermoluminescence of Solids*; Cambridge University Press, 1985.
35. Brito, H. F.; Hassinen, J.; Hölsä, J.; Jungner, H.; Laamanen, T.; Lastusaari, M.; Malkamäki, M.; Niittykoski, J.; Novák, P.; Rodrigues, L. C. V. Optical Energy Storage Properties of $Sr_2MgSi_2O_7:Eu^{2+},R^{3+}$ Persistent Luminescence Materials. *J. Therm. Anal. Calorim.* **2011**, *105*, 657-662.
36. Chen, R. Glow Curves with General Order Kinetics. *J. Electrochem. Soc.* **1969**, *116*, 1254-1257.
37. Sahu, I. P.; Bisen, D. P.; Brahme, N.; Tamrakar, R. K.; Shrivastava, R. Luminescence studies of dysprosium doped strontium aluminate white light emitting phosphor by combustion route. *J. Mater. Sci. - Mater. Electron.* **2015**, *26*, 8824-8839.

3.7 Supporting Information

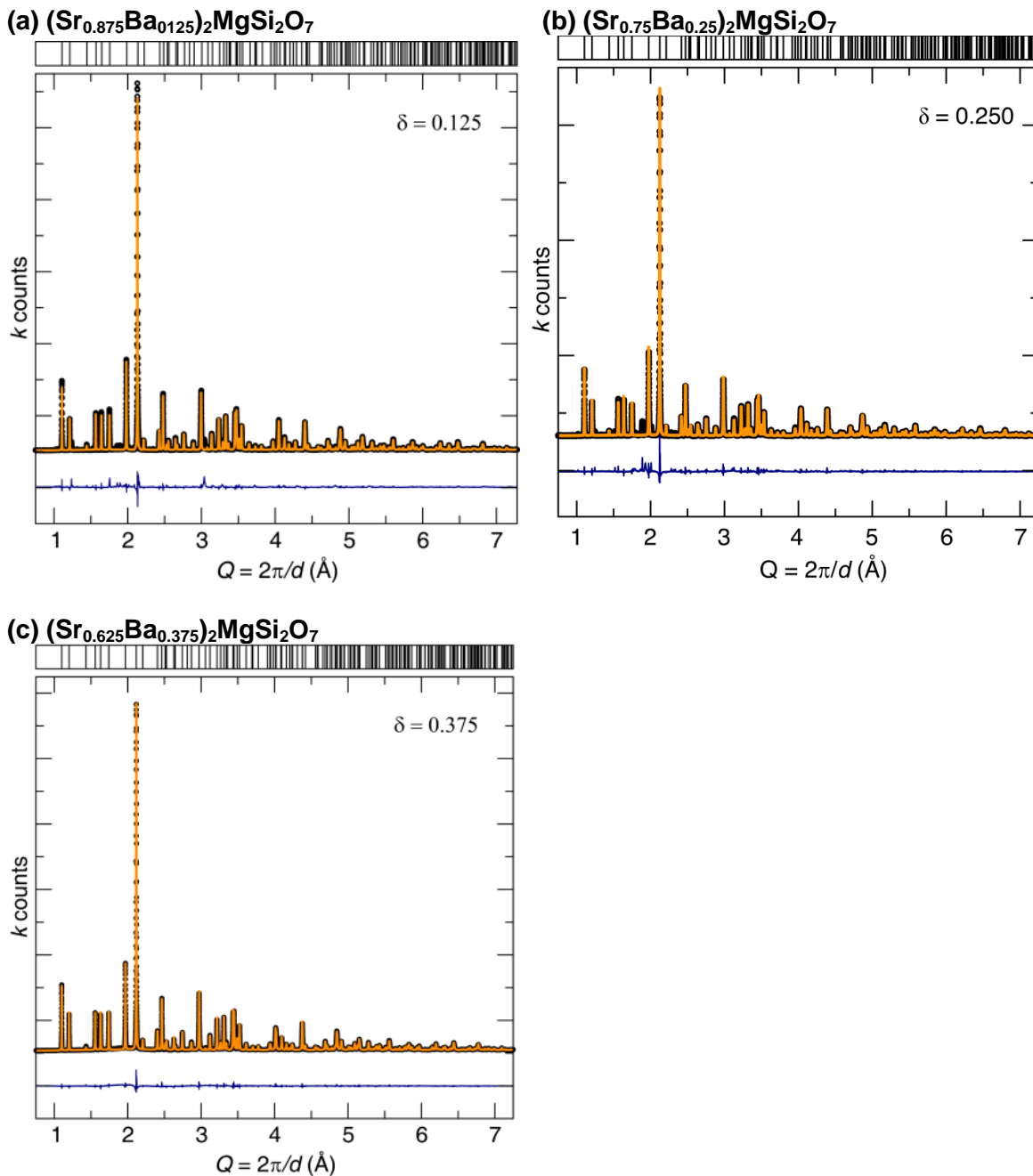


Figure 3.S1. Rietveld refinement shown for $\delta = 0.125, 0.25, 0.375$. Experimental data is black, refinement is orange, and the difference is blue. All are in excellent agreement with the calculated pattern.

Table 3.S1. Rietveld Refinement of $(\text{Sr}_{1-\delta}\text{Ba}_\delta)_2\text{MgSi}_2\text{O}_7$ ($\delta = 0.125, 0.25, 0.375$) Using Synchrotron Radiation

Formula	$(\text{Sr}_{0.875}\text{Ba}_{0.125})_2\text{MgSi}_2\text{O}_7$	$(\text{Sr}_{0.75}\text{Ba}_{0.25})_2\text{MgSi}_2\text{O}_7$	$(\text{Sr}_{0.625}\text{Ba}_{0.375})_2\text{MgSi}_2\text{O}_7$
Radiation type, λ (Å)		11-BM 0.414221	
2θ range (deg)		0.5-50	
Temperature (K)		295	
Space group; Z		$P\bar{4}2_1m$ (No. 113), 2	
Lattice parameters			
a (Å)	8.0249(4)	8.0447(2)	8.0687(1)
c (Å)	5.1831(3)	5.2037(3)	5.2296(2)
Volume (Å ³)	333.79(2)	336.77(2)	340.47(1)
Calculated Density (g cm ⁻³)	3.785	3.827	3.929
Formula weight (g mol ⁻¹)	760.90	776.063	805.601
R_p	0.0974	0.1110	0.0703
R_{wp}	0.1520	0.1538	0.0917
χ^2	7.967	4.911	3.311

Table 3.S2. Atomic Coordinates, Isotropic Displacement Parameters, and Occupancies as Determined by Rietveld Refinement of 11-BM Synchrotron X-ray Diffraction Data

(a) $(\text{Sr}_{0.875}\text{Ba}_{0.125})_2\text{MgSi}_2\text{O}_7$						
Atom	Wyckoff position	x	y	z	Occupancy	$U_{\text{iso}} (\text{\AA}^2)$
Sr	4e	0.3344(4)	0.1656(4)	0.5089(1)	0.872(2)	0.0058(8)
Ba	4e	0.3344(4)	0.1656(4)	0.5089(1)	0.128(2)	0.0441(8)
Mg	2a	0	0	0	1	0.0070(5)
Si	4e	0.1368(1)	0.3632(1)	0.9420(3)	1	0.0123(4)
O(1)	2c	1/2	0	0.142(1)	1	0.025(2)
O(2)	4e	0.1415(4)	0.3585(4)	0.2470(7)	1	0.029(1)
O(3)	8f	0.0784(3)	0.1855(3)	0.7975(5)	1	0.011(6)

(b) $(\text{Sr}_{0.75}\text{Ba}_{0.25})_2\text{MgSi}_2\text{O}_7$						
Atom	Wyckoff position	x	y	z	Occupancy	$U_{\text{iso}} (\text{\AA}^2)$
Sr	4e	0.3346(4)	0.1645(4)	0.5087(1)	0.796(6)	0.00810(9)
Ba	4e	0.3346(4)	0.1645(4)	0.5087(1)	0.204(6)	0.00810(9)
Mg	2a	0	0	0	1	0.0067(6)
Si	4e	0.1368(1)	0.3632(1)	0.9450(3)	1	0.0066(5)
O(1)	2c	1/2	0	0.150(1)	1	0.014(2)
O(2)	4e	0.1380(3)	0.3620(3)	0.2553(6)	1	0.010(1)
O(3)	8f	0.0804(3)	0.1885(3)	0.8096(5)	1	0.0108(7)

(c) $(\text{Sr}_{0.625}\text{Ba}_{0.375})_2\text{MgSi}_2\text{O}_7$						
Atom	Wyckoff position	x	y	z	Occupancy	$U_{\text{iso}} (\text{\AA}^2)$
Sr	4e	0.3342(2)	0.1657(2)	0.5091(8)	0.655(4)	0.00850(6)
Ba	4e	0.3342(2)	0.1657(2)	0.5091(8)	0.345(4)	0.00850(6)
Mg	2a	0	0	0	1	0.0049(3)
Si	4e	0.1368(1)	0.3630(9)	0.9477(2)	1	0.0086(3)
O(1)	2c	1/2	0	0.1498(6)	1	0.0078(9)
O(2)	4e	0.1381(2)	0.3619(2)	0.2466(4)	1	0.0155(8)
O(3)	8f	0.0776(2)	0.1915(2)	0.8128(3)	1	0.0137(5)

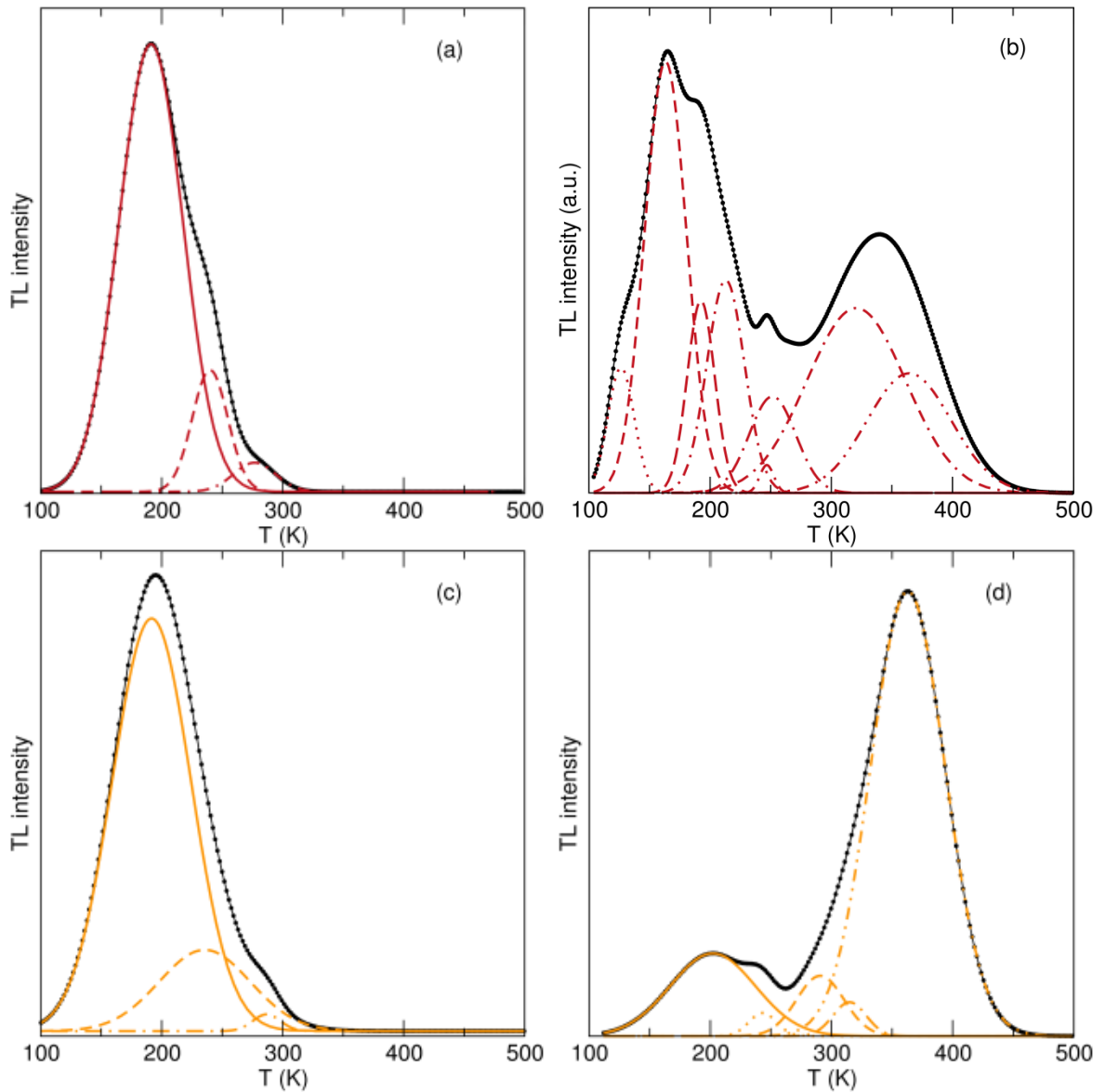


Figure 3.S2. Thermoluminescence spectra showing the deconvolution of the trap states $(\text{Sr}_{1-\delta}\text{Ba}_\delta)_{2-x}\text{MgSi}_2\text{O}_7$ ($\delta = 0, 0.125, 0.250, 0.375$). Eu^{2+} only is shown for plots a, c, e, and g while $\text{Eu}^{2+}, \text{Dy}^{3+}$ is shown as plots b, d, f, and h.

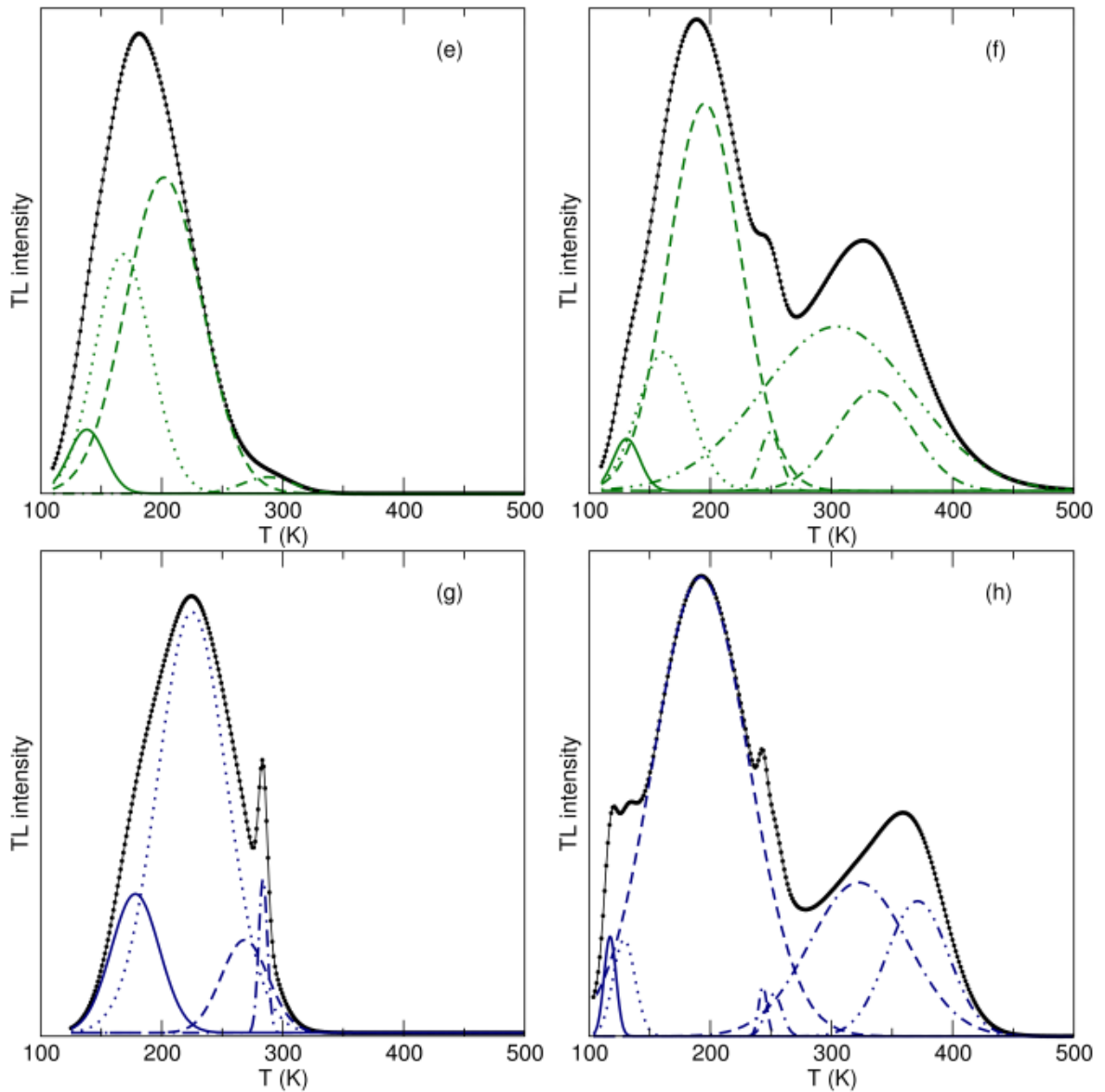


Figure 3.S2. (cont) Thermoluminescence spectra showing the deconvolution of the trap states $(\text{Sr}_{1-\delta}\text{Ba}_{\delta})_{2-x}\text{MgSi}_2\text{O}_7$ ($\delta = 0, 0.125, 0.250, 0.375$). Eu^{2+} only is shown for plots a, c, e, and g while $\text{Eu}^{2+}, \text{Dy}^{3+}$ is shown as plots b, d, f, and h.

CHAPTER 4

Deciphering the Loss of Persistent Red Luminescence in $\text{ZnGa}_2\text{O}_4:\text{Cr}^{3+}$ Upon Al^{3+} Substitution

Reproduced with permission from *Journal of Materials Chemistry C*
(*RSC Journal of Materials Chemistry C* 2019)

©Royal Society of Chemistry

DOI: 10.1039/c8tc06373g.

Erin Finley and Jakoah Brgoch*

Department of Chemistry, University of Houston, Houston, TX 77204

4.1. Introduction

The interest in persistent luminescent phosphors has grown significantly due to impressively long luminescent lifetimes enabling their use in a growing number of applications such as *in-vivo* imaging,¹ bioanalytical assays,^{2,3} emergency signage, and children's toys. The expansion of these materials to new applications is possible with improvements to the long luminescent lifetime, improved intensity of the visible emission, and the discovery of new persistent luminescent phosphors. The research in this area has generally centered on expanding their potential uses as well as enhancing the luminescent lifetimes by synthesizing submicron sized particles,^{4,5} utilizing solid-solutions,^{6,7} and the addition of co-dopants, e.g, Dy^{3+} , to modify the optical properties.⁸⁻¹⁰ A majority of these efforts have focused explicitly on the green-emitting $\text{SrAl}_2\text{O}_4:\text{Eu}^{2+},\text{Dy}^{3+}$, which is the most widely employed persistent luminescent phosphor,¹¹ as well as the red emitting $\text{ZnGa}_2\text{O}_4:\text{Cr}^{3+}$,¹² and the blue-emitting $\text{Sr}_2\text{MgSi}_2\text{O}_7:\text{Eu}^{2+},\text{Dy}^{3+}$, among others.¹³ Although improvements to the long luminescence lifetimes of these materials have all been investigated through these various synthesis approaches, the “design” of new persistent phosphors remains limited by a lack of understanding of what drives persistent luminescence.

The currently accepted mechanism of persistent luminescence involves the presence of trap states in a host crystal structure.¹⁴⁻¹⁶ In a host structure, the substitution of a cation ion with a luminescent center, e.g, Eu^{2+} or Cr^{3+} , induces an emission in the visible wavelengths when excited by light energy.^{17,18} The continued excitation of the luminescent center promotes an electron into the conduction band via photoionization.¹⁷ The photoionized electron is then held by the trap states.^{8,17} These trap states have been suggested to arise from defects, like anion vacancies, or the presence of d -orbitals from a co-dopant.^{6,13,19} The relationship between the existence of defects and their location from the bottom of the conduction band has been proven using both experimental and computational methods.²⁰⁻²³ First principle calculations on monoclinic $\text{SrAl}_2\text{O}_4:\text{Eu}^{2+}$ have shown these defects stem from anion vacancies, which are likely to form as an intrinsic property of the material.¹⁹ Further, experimental results from electron paramagnetic resonance (EPR) spectroscopy and computational studies further indicate persistent luminescence in the spinel-type structure of the red-emitting $\text{ZnGa}_2\text{O}_4:\text{Cr}^{3+}$ stem from anti-site defects that act as trap states.^{7,24-26}

The subsequent thermally induced release of the trapped electron from a trap state leads to the observed long luminescent lifetimes. The ability for persistent phosphors to trap and then release (depopulate) an electron or an electron-hole pair is not only dependent on the presence of trap states but also on their energetic position with respect to the bottom of the host structure's conduction band.^{14,27,28} Therefore, there is a close relationship between the position of the conduction band and the position of the trap states. This is best illustrated through bandgap engineering studies, which have suggested that an increase in Ga^{3+} in $\text{Y}_3\text{Al}_{5-x}\text{Ga}_x\text{O}_{12}:\text{Ce}^{3+},\text{Cr}^{3+}$ ($x = 0-5$) would decrease the bandgap (E_g) resulting in a longer persistent luminescent lifetime.²⁹ This research

showed the trap states were attributed to the presence of the Cr^{3+} 3d-orbitals while thermoluminescence measurements revealed the position of the 3d-orbitals within the bandgap remained in a constant energy window across the entire solid solution, even though the optical bandgap changed.²⁹ Additionally, the experimental and computational analysis of garnets, $\text{Lu}_3(\text{Ga}_x\text{Al}_{1-x})_5\text{O}_{12}$ ($x = 0-1$), $\text{Y}_3\text{Al}_2\text{Ga}_3\text{O}_{12}$, and $\text{Y}_3\text{Ga}_5\text{O}_{12}$, substituted with a single luminescent center (Pr^{3+} or Ce^{3+}) have also found relationships between defects and the E_g .³⁰⁻³² The *ab initio* investigation of $\text{Lu}_3\text{Al}_{5-x}\text{Ga}_x\text{O}_{12}:\text{Ce}^{3+}$, established that anti-site defects of Lu_{Al} could be buried in the conduction band with the substitution of Ga^{3+} onto the Al^{3+} by decreasing the E_g . This is contrary to a thermoluminescence study of $\text{Lu}_3\text{Al}_{5-x}\text{Ga}_x\text{O}_{12}:\text{Pr}^{3+}$ that found a decrease in the number of trap states with Ga^{3+} substitution.^{31,33} The basis of this finding was that the formation energy of the anti-site defects decreased with increasing Ga^{3+} substitution and therefore an observable increase in defects should have been measured.³³ However, photoconductivity experiments of $\text{Y}_3\text{Al}_5\text{O}_{12}:\text{Ce}^{3+}$, $\text{Y}_3\text{Al}_2\text{Ga}_3\text{O}_{12}:\text{Ce}^{3+}$, and $\text{Y}_3\text{Ga}_5\text{O}_{12}:\text{Ce}^{3+}$ discovered defects that can act as trap states remain in the same energy window with respect to the bottom of the conduction band regardless of composition.³² Consequently, in the search for new materials, understanding defect formation and the relationship with E_g will provide valuable insight into persistent luminescent phosphors.

The spinel-type crystal structures provide an ample opportunity to study persistent luminescence because there is a large diversity of compositions allowing a systematic study of the optical properties as a function of composition.¹² This wide range of compositions has led to the discovery of multiple persistent luminescent phosphors.¹² When a transition metal, like Cr^{3+} or Mn^{2+} , is used as a luminescent center long luminescent lifetimes have been observed.¹² For example, $\text{MgAl}_2\text{O}_4:\text{Cr}^{3+}$ has a reported

long lifetime of two hours while $\text{Mg}_2\text{SnO}_4:\text{Mn}^{2+}$ achieved an observable lifetime of five hours.^{30,34} In both cases, the long luminescent lifetimes were attributed to the presence of anti-site defects that act as trap states.^{30,34}

Although more than one spinel has been reported to show persistent luminescence, not all spinel structures show the same response. In ZnAl_2O_4 , when Cr^{3+} is substituted for Al^{3+} , the compound does not exhibit persistent luminescence.²⁵ This lack of persistent luminescence is possibly due to an absence of anti-site defects, that unlike isostructural $\text{ZnGa}_2\text{O}_4:\text{Cr}^{3+}$ contains an estimated 3% inversion of the Zn and Ga sites and shows persistent luminescence.^{7,25,35} Here, this relationship between the presence of defects and the observation of persistent luminescence is systematically probed by preparing a solid solution between $\text{ZnGa}_2\text{O}_4:\text{Cr}^{3+}$ and $\text{ZnAl}_2\text{O}_4:\text{Cr}^{3+}$. $\text{Zn}(\text{Ga}_{1-\delta}\text{Al}_\delta)_2\text{O}_4:\text{Cr}^{3+}$ ($\delta = 0, 0.25, 0.50, 0.75, 1$) crystallizes in the cubic space group, $Fd\bar{3}m$, across the entire range of δ , which allows a systematic study of the change in optical properties as a function of composition. It can be shown that increasing the aluminum content increases the number of defects; however, it does not necessarily lengthen long luminescent lifetime. An examination of the relationship between the defects and E_g shows trap states induced by defects that participate in persistent luminescence become shallower with an increase in Al^{3+} concentration. The presence of shallower trap states, therefore, could be responsible for the quenching of persistent luminescence with increasing Al^{3+} across the solid solution.

4.2. Experimental

4.2.1 Sample Preparation Pure phase, polycrystalline samples, with the nominal compositions $\text{Zn}(\text{Ga}_{1-\delta}\text{Al}_\delta)_{2-x}\text{O}_4:\text{Cr}^{3+}$ ($\delta = 0, 0.25, 0.50, 0.75, 1; x = 0.005$) were prepared via high-temperature solid-state synthesis. The starting materials were weighed out in

stoichiometric ratios using the following reagents: ZnO (Alfa Aesar 99.9%), Ga₂O₃ (Alfa Aesar 99.95%), Al₂O₃ (Alfa Aesar 99%), Cr₂O₃ (Alfa Aesar 99%), and 4 wt% boric acid (Sigma Aldrich 99.98%) as a flux. The starting powders were mixed thoroughly using a shaker mill (Spex 8000M) in a polystyrene vial with 9.5 mm methacrylate balls as grinding media for 45 min. The starting powders were then pressed into 8 mm pellets and heated in air for 10 h at 1300°C with heating and cooling rates of 3°C/min. The products were subsequently ground into fine powders using an agate mortar and pestle.

4.2.2 X-ray Diffraction The purity of the final products was confirmed first using a PanAnalytical X'Pert powder diffractometer using Cu K α radiation (1.54183 Å). Next, high-resolution synchrotron X-ray powder diffraction measurements (11-BM, Advanced Photon Source, Argonne National Lab) were collected at room temperature with a calibrated wavelength of $\lambda = 0.4126760$ Å. Rietveld refinements of the synchrotron data were completed on all samples to confirm the crystal structures using the general structural analysis system (GSAS).^{36,37} Peak shape was determined with a pseudo-Voigt function, and the background was calculated from a shifted Chebyshev function.⁶

4.2.3 Optical Characterization The optical bandgap was experimentally determined *via* diffuse reflectance using an Agilent Technologies Cary 5000 with a diffuse reflectance accessory. The diffuse reflectance data were converted following Kubelka-Munk to $F(R_{\infty})$. The optical bandgap was then estimated using a Tauc plot for either a direct or indirect bandgap depending on composition. A 75 W xenon arc lamp steady-state fluorimeter (PTI Instruments) was used to measure the photoluminescence emission and excitation spectra in addition to the persistent luminescence at room temperature. Persistent luminescent lifetime measurements were collected by first isolating each sample in total darkness for a period of 12 h to ensure depopulation of any trap states.

The samples were then irradiated for 10 min with an excitation wavelength of $\lambda_{\text{ex}} = 254$ nm followed by a 10 s delay after the excitation source was turned off. The lifetime decay was then collected at an emission wavelength of $\lambda_{\text{em}} = 695$ nm for 30 min.

Thermoluminescence was obtained using a Janis cryostat (VPF-100) to control temperatures between 100 and 600 K. Again; the samples were isolated in total darkness for ≥ 12 h to ensure all trap states were depopulated. The cryostat was then cooled to 100 K and subsequently irradiated with an excitation wavelength of $\lambda_{\text{ex}} = 254$ nm for 10 min followed by a 5 min delay after turning off the excitation source. The thermoluminescence spectra were collected at an emission wavelength of $\lambda_{\text{em}} = 695$ nm with a ramp rate of 5 K/min.

4.3. Results and Discussion

4.3.1 Synthesis and Characterization of the Solid Solution $\text{Zn}(\text{Ga}_{1-\delta}\text{Al}_\delta)_2\text{O}_4$ ($\delta = 0, 0.25, 0.50, 0.75, 1$) The solid solution $\text{Zn}(\text{Ga}_{1-\delta}\text{Al}_\delta)_2\text{O}_4$ ($\delta = 0, 0.25, 0.50, 0.75, 1$) was produced using high-temperature solid-state synthesis by combining oxide powders and heating at 1300°C for 10 h in air. Phase purity was confirmed first with laboratory powder X-diffraction followed by synchrotron X-ray powder diffraction (shown in Figure 4.1a). Rietveld refinements of each composition prepared (Figure 4.S1) show the crystal structure always adopts the spinel-type structure crystallizing in the cubic space group $Fd\bar{3}m$ (no. 227).^{38,39} The diffraction peaks shift to higher Q-spacing indicating smaller lattice parameters with increasing aluminum concentration, as expected based on the smaller ionic radii of Al^{3+} ($r_{6\text{-coord}} = 0.535 \text{ \AA}$) compared to Ga^{3+} ($r_{6\text{-coord}} = 0.620 \text{ \AA}$).⁴⁰ The subsequent crystallographic parameters, which were extracted from the Rietveld refinements are listed in Table 4.1 and Table 4.2 for ZnGa_2O_4 and ZnAl_2O_4 .^{38,39} The

crystallographic information for the intermediate values of δ can be found in supporting information Table 4.S1 and 4.S2.

$$a_o^n = a_1^n(X) + a_2^n(1 - X) \quad (4.1)$$

To validate the incorporation of aluminum, Vegard's law was analyzed and states that in a cubic system the lattice parameters will vary linearly with continuous substitution in a solid solution according to Equation 4.1, where a_o^n is the lattice parameter of the system, a_1^n is the lattice parameter of Al, a_2^n is the lattice parameter for Ga, X is the mole fraction of Al and n is a power to describe variance in the system.⁴¹⁻⁴³ When $n = 3$, Retger's rule of additive volumes can be used to describe linearity of a solid solution's unit cell volume.^{42,44} Thus, looking at Figure 4.1b and 4.1c there is a clear linear relationship, which can be attributed to the substitution of the smaller ionic radii of Al^{3+} compared to Ga^{3+} , in both the unit cell volume (Figure 4.1b) and volume of the $[\text{GaO}_6/\text{AlO}_6]$ polyhedron (Figure 4.1c). Interestingly, the Zn-O bond lengths also change with increasing Al^{3+} content; for example, when $\delta = 0.50$ there is a 1.7% decrease in length compared to $\delta = 0$ that becomes an even larger difference of 2.5% when $\delta = 1$. The change in the $[\text{ZnO}_4]$ tetrahedra is even more notable with a 5.2% difference in $\delta = 0.50$ and a 5.5% difference in $\delta = 1$. These significant changes in polyhedral volume and bond length should lead to an increase in the optical bandgap as well as changes in the crystal field splitting that should be observable by photoluminescence spectroscopy.⁴⁵

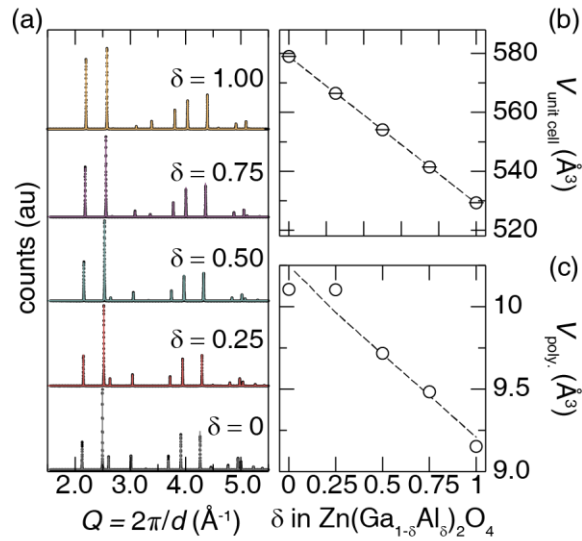


Figure 4.1. (a) Rietveld refinement of synchrotron X-ray powder diffraction data for the solid solution $\text{Zn}(\text{Ga}_{1-\delta}\text{Al}_\delta)_2\text{O}_4$ ($\delta = 0, 0.25, 0.50, 0.75, 1$) the solid line is the fit, and the circles are the observed data. A decreasing linear regression of the (b) unit cell volume and (c) $[\text{GaO}_6/\text{AlO}_6]$ polyhedron volume is shown as a function of Al^{3+} .

Table 4.1. Rietveld Refinement Data for the End Members of Solid Solution from 11-BM Synchrotron X-Ray Diffraction

Formula	ZnGa_2O_4	ZnAl_2O_4
Radiation type, λ (\AA)	11-BM, 0.4126760	
2θ range ($^\circ$)	0.5-50	
Temperature (K)	295	
Space group; Z	$Fd\bar{3}m$ (No. 227); 8	
Lattice parameter, a (\AA)	8.334655(2)	8.089110(3)
Volume (\AA^3)	578.979(1)	529.300(1)
Calculated Density (g cm^{-3})	6.6168	4.601
Formula weight (g mol^{-1})	2150.528	1466.720
R_p	0.1039	0.0838
R_{wp}	0.1299	0.1160
χ^2	3.703	6.926

Table 4.2 (a) Crystallographic Data of ZnGa₂O₄ from Rietveld Refinement Resulting from 11-BM Synchrotron X-ray Diffraction Data, (b) Crystallographic Data of ZnAl₂O₄ from Rietveld Refinement Resulting from 11-BM Synchrotron X-ray Diffraction Data

Atom	Wyck. site	x	y	z	U _{iso} (Å ²)
(a)					
Zn	8a	1/8	1/8	1/8	0.009(5)
Ga	16d	1/2	1/2	1/2	0.009(3)
O	32e	0.26357(7)	0.26357(7)	0.26357(7)	0.00116(2)
(b)					
Zn	8a	1/8	1/8	1/8	0.00258(3)
Al	16d	1/2	1/2	1/2	0.00107(5)
O	32e	0.26332(4)	0.26332(4)	0.26332(4)	0.00170(1)

The refined unit cells of ZnGa₂O₄ and ZnAl₂O₄ are visualized in Figure 4.2. Spinel-type structures, which have the general formula AB₂O₄ (A = divalent metal, B = trivalent metal), form a cubic closed packed structure with eight tetrahedrally coordinated A sites and sixteen octahedrally coordinated B sites. This packing creates 64 tetrahedral and 32 octahedral interstitial voids for the anions to occupy. This is in contrast to the inverse spinel where the B sites will occupy the tetrahedrally coordinated positions and eight A and eight B sites uniformly occupy the sixteen octahedrally coordinated positions. In the crystal structures studied here, the Zn atoms occupy the tetrahedral site [ZnO₄], and Ga or Al atoms occupy the octahedral site [GaO₆/AlO₆]; thus, these compounds are both normal spinels.

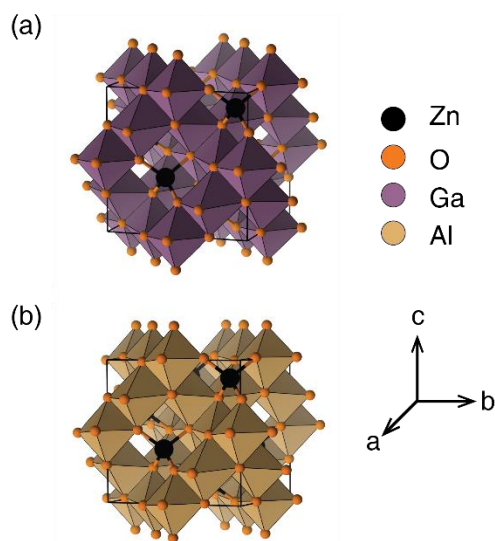


Figure 4.2. The crystal structure for (a) ZnGa₂O₄ and (b) ZnAl₂O₄ as determined by Rietveld refinement with either Ga or Al octahedral sites highlighted

4.3.2 Optical Properties The substitution of Al³⁺ onto the Ga³⁺ is known to increase E_g because of the change in bond lengths^{45,46} To establish this change, and how it may ultimately impact the optical properties of these materials, diffuse reflectance measurements were conducted on the solid solution. Previous experimental reports of the change in E_g with Al³⁺ substitution have suggested that both the ZnGa₂O₄ and ZnAl₂O₄ are direct bandgap materials.^{45,46} However, a computational study on these two end-member compounds found that ZnGa₂O₄ has an indirect bandgap whereas ZnAl₂O₄ has a direct bandgap.^{47,48} The experimental E_g was, therefore, determined from a Tauc plot after applying the Kubelka-Munk transformation following Equation 4.2.

$$(h\nu F(R_\infty))^{1/n} = A(h\nu - E_g) \quad (4.2)$$

Here, h is Plank's constant, ν is the photon frequency, $F(R_\infty)$ is the measured absorbance, n is equal to either $\frac{1}{2}$ for a direct allowed transition or 2 for an indirect

allowed transition, and A is a proportional constant.⁴⁹ The bandgaps were then determined by considering both $n = 1/2$ and $n = 2$ for each composition. The resulting data, plotted in Figure 4.3, show that $\delta = 0, 0.25, 0.50,$ and 0.75 are best fit by $n = 2$ and E_g increases as the Al^{3+} concentration is increased. The ZnAl_2O_4 ($\delta = 1$) is best described as a direct bandgap ($n = 1/2$), which is in agreement with the computational models. The E_g determined by fitting the Tauc plot are provided in Table 4.3.⁴⁶ The observed increase in E_g and decreasing polyhedral volume (Figure 4.1c) follows the inverse relationship between bond length and E_g .⁴⁵

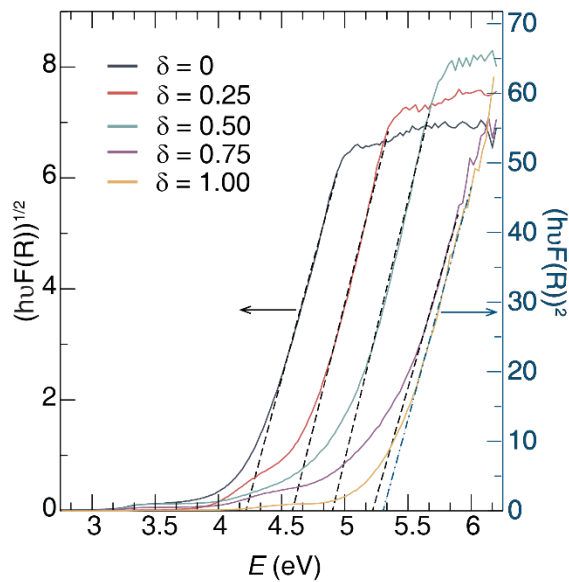


Figure 4.3. Diffuse reflectance of the optical bandgap (E_g) for $\text{Zn}(\text{Ga}_{1-\delta}\text{Al}_\delta)_2\text{O}_4$ ($\delta = 0 - 0.75$) $n = 2$ black dashed lines and black y -axis and ZnAl_2O_4 $n = 1/2$ blue dashed line and blue y -axis.

Table 4.3. Bandgap values across the solid solution determined from diffuse reflectance measurements

δ	E_g (eV)
0	4.2
0.25	4.6
0.50	4.8
0.75	5.2
1.00	5.3

The substitution of Cr^{3+} onto the $\text{Ga}^{3+}/\text{Al}^{3+}$ site in $\text{Zn}(\text{Ga}_{1-\delta}\text{Al}_\delta)_2\text{O}_4:\text{Cr}^{3+}$ ($\delta = 0, 0.25, 0.50, 0.75, 1$) yields excitation spectra with two broad peaks when collected at an emission wavelength of $\lambda_{\text{em}} = 695$ nm (Figure. 4.4a) The optical properties arising from the Cr^{3+} substitution can be described by the Tanabe-Sugano diagram in a $3d^3 O_h$ coordination environment.^{28,50} The two peaks can be assigned to the spin-allowed electronic transitions of ${}^4A_2 \rightarrow {}^4T_1$ (4F) ($\lambda_{\text{ex}} \approx 436$ nm) and ${}^4A_2 \rightarrow {}^4T_2$ (4F) ($\lambda_{\text{ex}} \approx 552$ nm).⁴⁵ Moreover, examining the excitation spectra with increasing Al^{3+} concentration shows there is a blue shift, suggesting an increase in the crystal field strength around the Cr^{3+} .⁴⁵ This is due to a larger energy gap between the ground state (4A_2) and the excited states (4T_1 and 4T_2).

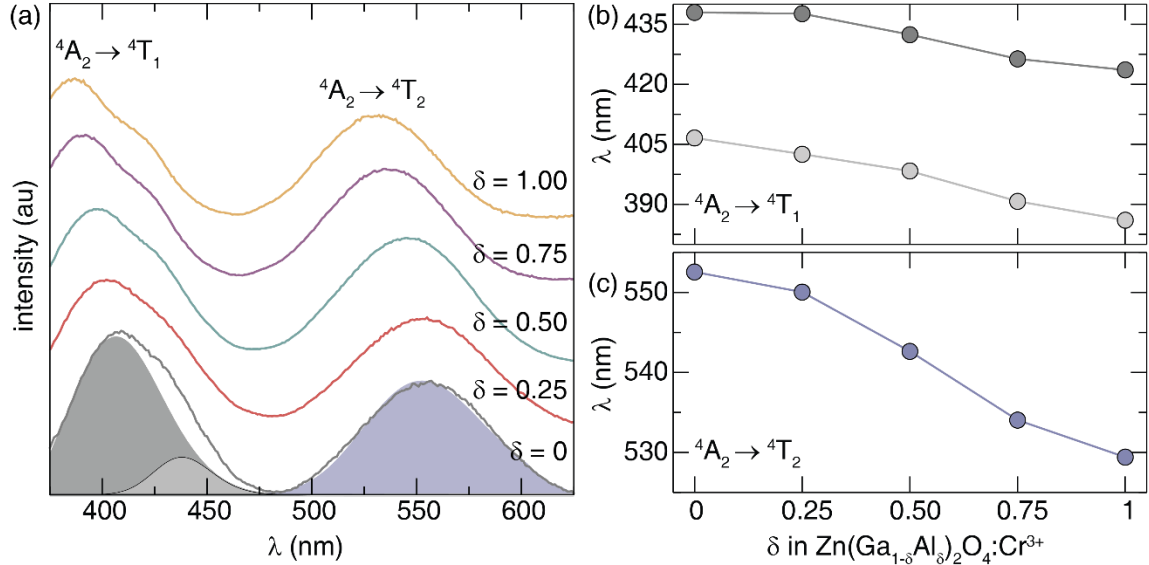


Figure 4.4. (a) Excitation spectra of the solid solution Zn(Ga_{1-δ}Al_δ)₂O₄:Cr³⁺; δ = 0 gray, δ = 0.25 orange, δ = 0.50 green, δ = 0.75 purple, δ = 1 yellow. The deconvoluted peaks are the filled excitation curves for δ = 0. (b) Linear trend of the deconvoluted peaks with increasing Al³⁺ concentration showing a decrease in energy for ⁴A₂ → ⁴T₁ (c) Linear trend for ⁴A₂ → ⁴T₂.

To support the change in the crystal field upon atomic substitution, the Racah parameter (*B*) is calculated using Equation 4.3, 4.4, and 4.5 and solving for 10Dq/*B* (Table 4.4). Across the solid solution there is an overall linear decrease in the value, which further supports a stronger crystal field.⁴⁵ However, this assumes perfect *O_h* symmetry in the Cr³⁺ polyhedra. Upon closer inspection of the data, this is clearly not the case considering a shoulder is visible in ⁴A₂ → ⁴T₁ transition. Deconvoluting the peak reveals two peaks separated by ≈30 nm (δ = 0). Figure 4.4b shows a linear decrease in wavelength with increasing aluminum for both peaks starting at λ_{ex} ≈ 406 nm (filled dark gray) and 436 nm (filled light gray). This additional peak likely arises from a splitting of the ⁴F transition due to a slight trigonal distortion around the Cr³⁺ polyhedron, which is *D_{3d}* symmetry and not *O_h*.^{45,51,52} Therefore, increasing crystal field strength increases the trigonal distortion.^{25,45} The distortion of the [CrO₆] is also believed to be the reason for

the complex emission spectrum that gives rise to several characteristic peaks.^{28,50} Finally, fitting the third peak assigned to ${}^4A_2 \rightarrow {}^4T_2$ (Figure 4.4c) exhibits the same decrease in wavelength with increasing aluminum concentration beginning at $\lambda_{\text{ex}} \approx 552$ nm.

$$10Dq = E({}^2T_2) - E({}^4A_2) \quad (4.3)$$

$$\frac{Dq}{B} = \frac{15(x-8)}{x^2-10x} \quad (4.4)$$

$$x = \frac{E({}^4A_2 \rightarrow {}^4T_1) - E({}^4A_2 \rightarrow {}^4T_2)}{Dq} \quad (4.5)$$

Table 4.4. Calculated Racah Parameter (B) And Crystal Field Strength ($10Dq/B$) for $\text{Zn}(\text{Ga}_{1-\delta}\text{Al}_\delta)_2\text{O}_4$ ($\delta = 0, 0.25, 0.50, 0.75, 1$)

δ	B (cm^{-1})	$10Dq/B$ (cm^{-1})
0	629.54	28.75
0.25	648.58	28.02
0.50	648.53	28.42
0.75	668.83	28.00
1.00	685.80	27.54

Although there is a shift in excitation wavelength upon Al^{3+} substitution, the emission spectra across the solid solution remains nearly constant because the energy gap between 2E and 4A_2 is not influenced by the change in crystal field strength, despite a shift in excitation energy upon Al^{3+} substitution.⁴⁵ In Figure 4.5, several emission peaks are observed, in agreement with previous reports of Cr^{3+} substituted in ZnGa_2O_4 and ZnAl_2O_4 .^{10,35,50,53} The emission peaks on either side of the R- and N-lines are the phonon sidebands (PSB) that lie between 650 nm - 675 nm and 710 nm - 730 nm called the anti-

Stokes are Stokes PSB, respectfully.⁵⁴ The spin forbidden Cr³⁺ electronic transition of the ²E → ⁴A₂ is split into two R-lines, R₁ and R₂, that are observed at λ_{em} ≈ 685 nm and 690 nm.^{45,54} This splitting of the R-lines is attributed to the trigonal distortion of the Cr³⁺ polyhedron in an ideal unperturbed environment.⁵⁴ Interestingly, the emission peak at λ_{em} ≈ 695 nm is associated with the long luminescent lifetime and is known as the N-line; it is due to Cr³⁺ in a perturbed environment arising from lattice defects surrounding Cr³⁺.²⁵ The peak width of the N-line has been associated with the presence of lattice defects and lattice disorder.^{25,50,55} Moreover, the relative intensity of the N-line compared to the R-line is also an indicator of lattice defects, where an observed increase in the intensity of the N-line suggests more anti-site defects.^{25,35} Indeed, a study of MgGa₂O₄:Cr³⁺, ZnGa₂O₄:Cr³⁺, and ZnAl₂O₄:Cr³⁺ revealed that the N-line became more intense in the more disordered samples.²⁵ To this extent, because the N-line is responsible for persistent luminescence, an intense and broad N-line relative to the R-line would produce a long luminescent lifetime. This is observed in δ = 0. To examine this relationship more closely the intensity ratio of the R- and N-line was determined as well as the full width at half maximum (FWHM) of the N-line. These data are shown in Table 4.5.

Table 4.5. The intensity ratio of the R and N-lines and the change in peak width of the N-line for Zn(Ga_{1-δ}Al_δ)₂O₄ (δ = 0, 0.25, 0.50, 0.75, 1)

δ	FWHM (cm ⁻¹)	N/(R+N)
0	80.30	0.51
0.25	90.57	0.43
0.50	151.64	0.36
0.75	106.00	0.38
1	64.16	0.50

A closer look at these emission peaks as a function of composition reveals that going from $\delta = 0$ to $\delta = 0.50$, the N-line broadens and then narrows with continued Al^{3+} substitution. Additionally, when $\delta = 0$ and 1 the intensities of the R and N-lines are nearly the same; however, the FWHM for $\delta = 0$ is broader whereas for the intermediate compositions ($\delta = 0.25, 0.50,$ and 0.75) have a significantly more intense R-line compared to the N-line. The FWHM broadens with increasing δ up to $\delta = 0.50$ and then begins to narrow. In combination, these data suggest there is more disorder in the compounds that contain a partial substitution of Al^{3+} for Ga^{3+} . Thus, it is likely that there will be a change in the persistent luminescence as a function of composition.

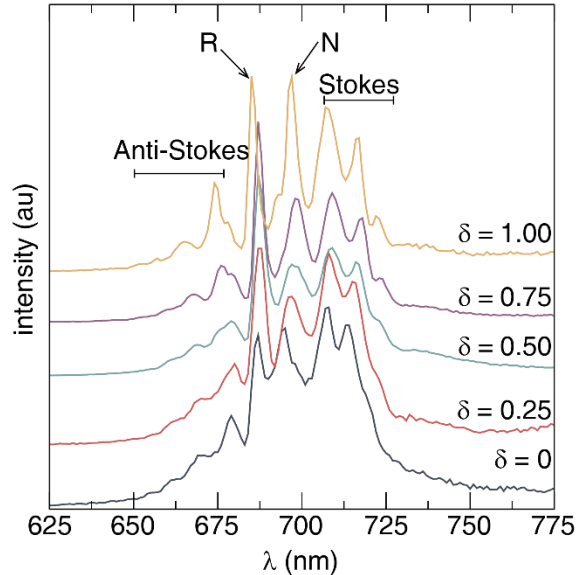
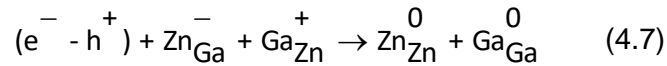
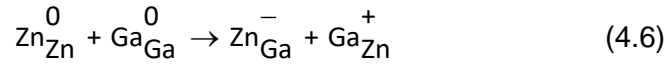


Figure 4.5. Emission spectra of $\text{Zn}(\text{Ga}_{1-\delta}\text{Al}_{\delta})_2\text{O}_4:\text{Cr}^{3+}$ ($\delta = 0, 0.25, 0.50, 0.75, 1$) with an excitation wavelength of $\lambda_{\text{ex}} = 400$ nm. R-lines are highlighted and are assigned to the spin-forbidden transition of ${}^2\text{E} \rightarrow {}^4\text{A}_2$, and the N is highlighted and is responsible for long luminescent lifetimes.

The presence of defects creates trap states, whereupon continuously excited electrons will travel through the conduction band and become trapped leading to persistent luminescence.¹² In $\text{ZnGa}_2\text{O}_4:\text{Cr}^{3+}$, these traps stem from anti-site defects of the cation

ions (Zn_{Ga}^- and Ga_{Zn}^+) that occur with approximately 3% of Ga^{3+} occupying the $[\text{ZnO}_4]$ tetrahedra.^{7,24,25,35} When Cr^{3+} is substituted on the Ga^{3+} site, and an electron is excited it forms an electron-hole pair.²⁸ This pair is then trapped by the anti-site defect according to Equations 4.6 and 4.7.²⁸



The subsequent thermally induced release of these electrons from the trap states gives rise to persistent luminescence.¹² Measuring the long luminescent lifetime decay curves, shown in Figure 4.6, of the N-line ($\lambda_{\text{em}} = 695 \text{ nm}$) was successful for $\delta = 0, 0.25,$ and 0.5 while the Al^{3+} compositions of $\delta = 0.75$ and 1 did not exhibit a measurable persistent luminescence. Thus, the first three compositions were fit to a tri-exponential equation (Equation 4.8) where I is the normalized intensity, A_1, A_2, A_3 are pre-exponential constants, t is time, and τ_1, τ_2, τ_3 are luminescent decay times in minutes.

$$I = A_1 e^{-\frac{t}{\tau_1}} + A_2 e^{-\frac{t}{\tau_2}} + A_3 e^{-\frac{t}{\tau_3}} \quad (4.8)$$

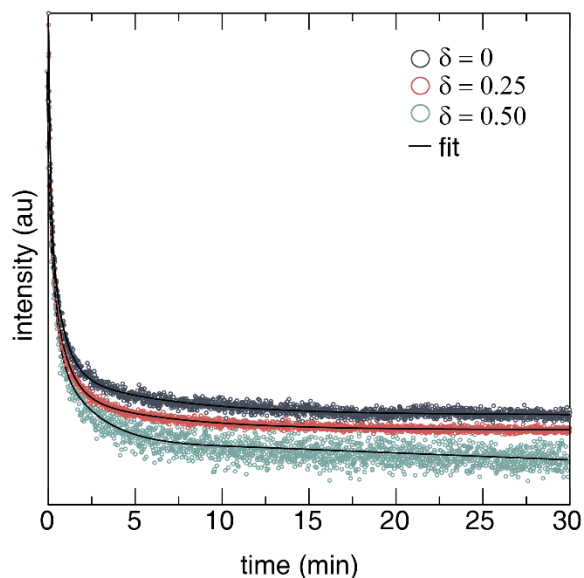


Figure 4.6 Samples were excited by $\lambda_{\text{ex}} = 254$ nm for 10 min. Circles are the observed data, and the black lines are the fit.

The results of the three fits are shown in Table 4.6. It can be seen that as the Al^{3+} concentration is increased, there is a decrease in the long lifetime. Interestingly, this is in contrast with the increase in the disorder predicted from the luminescence spectra. There is very little change going from $\delta = 0$ to $\delta = 0.25$; however, when aluminum is $\delta = 0.50$ there is a significant decrease in the persistent lifetime. This quenching of the lifetime may stem from changes in the concentration of lattice defects. A similar observation was made in the case of the isostructural $\text{Zn}_{1-x}\text{Mg}_x\text{Ga}_2\text{O}_4:\text{Cr}^{3+}$ ($x = 0.1 - 0.5$) system, where with increasing Mg^{2+} concentration the long lifetime was decreased. Here, it was also shown that with increasing Mg^{2+} concentration there was an increase in lattice defects present, which is in agreement with the observations of this research.⁵⁶ Additionally, $\text{MgGa}_2\text{O}_4:\text{Cr}^{3+}$ has a reported 44% inversion of the Mg and Ga sites and also shows a significant loss of persistent luminescence.^{25,57} Therefore, it can be concluded that the increase in lattice defects across the $\text{Zn}(\text{Ga}_{1-\delta}\text{Al}_\delta)_2\text{O}_4:\text{Cr}^{3+}$ solid

solution acts as a quenching mechanism, hindering persistent luminescence. A further increase in anti-site defects prevents persistent luminescence as observed in $\delta = 0.75$. Much like in the case of $\text{MgGa}_2\text{O}_4:\text{Cr}^{3+}$, this inhibits persistent luminescence entirely.^{25,57} Unfortunately, directly studying the concentration of anti-site defects in ZnGa_2O_4 using the crystal structure data available here is not possible because of the similar X-ray scattering power of Zn and Ga.

Table 4.6. Long Luminescent Lifetimes of $\text{Zn}(\text{Ga}_{1-\delta}\text{Al}_\delta)_2\text{O}_4:\text{Cr}^{3+}$ ($\delta = 0, 0.25, 0.50$). No long lifetimes were measured for $\delta = 0.75$ and $\delta = 1$

δ	τ_1 (min)	τ_2 (min)	τ_3 (min)
0	0.118(5)	0.72(2)	6.0(2)
0.25	0.135(3)	0.81(2)	5.7(2)
0.50	0.06(3)	0.37(5)	2.4(2)

To further understand why the long luminescent lifetime changes as a function of aluminum concentration, thermoluminescence (TL) measurements were conducted. The thermoluminescence spectra are measured as a function of temperature and describe the location of the trap states, which arise from defects, with respect to the bottom of the conduction band. Trap states that lead to long lifetimes are defined as lying >0.40 eV but <1.0 eV below the bottom of the conduction band; the ideal depth is 0.65 eV.^{58,59} The position of the trap states can be extracted from the thermoluminescence data by deconvoluting the spectra using a Gaussian function; the resulting trap state energies are within 5% of the actual trap depths when employing the “peak shape method”.⁵⁸⁻⁶⁰

Following Equation 4.9, the trap depths can be quantified by an activation energy (E_A) using μ_g as the geometric factor, k_B as the Boltzmann constant, and T_m as the maximum

temperature of the TL emission. μ_g can be found with, $\sigma = T_2 - T_m$; T_2 is the low temperature half maximum, and ω is the FWHM of the TL emission (Equation 4.10).

$$E_A = [2.52 + 10(\mu_g - 0.42)] \left(\frac{k_B T_m^2}{\omega} \right) - (2k_B T_m) \quad (4.9)$$

$$\mu_g = \frac{\sigma}{\omega} \quad (4.10)$$

ZnGa₂O₄:Cr³⁺ has previously been reported to have two traps with depths of 0.49 eV and 0.91 eV.⁶¹ A separate report using the initial rise method for a Bi³⁺ co-doped sample for Zn(Ga_{1-x}Al_x)₂O₄:Cr³⁺,Bi³⁺ ($x = 0, 0.02, \text{ and } 0.04$) estimated three traps with depths of 0.46 eV, 0.48 eV, and 0.50 eV.⁵³

Figure 4.7 shows the trap states contributing to the long luminescence lifetimes observed for $\delta = 0$, $\delta = 0.25$, and $\delta = 0.50$. The peaks located at 323 K ($\delta = 0$), 413 K ($\delta = 0.25$), and 421 K ($\delta = 0.50$) have trap depths that are in reasonable agreement with previous reports, and are produced in Table 4.7. Increasing aluminum concentration shifts the peaks to slightly higher temperatures, also consistent with literature, which reported values of 333 K ($x = 0$), 348 K ($x = 0.02$) and 363 K ($x = 0.04$).⁵³ The presence of additional peaks in $\delta = 0.25$ and $\delta = 0.50$ can be attributed to the increase in the aluminum concentration and is consistent with the widening of the emission peak at $\lambda_{em} = 695$ nm observed in Figure 4.6. Typically, the long lifetime of a persistent luminescent phosphors increases with increasing number of traps and deepening of the traps; however, this is not the case for this system. Therefore, the combination of additional trap states and the loss of persistent luminescence with increasing Al³⁺ are consistent with the optical properties observed in Zn_{1-x}Mg_xGa₂O₄:Cr³⁺ and MgGa₂O₄:Cr³⁺.^{56,57} However, the relationship to the change in E_g need to be considered. The fully

deconvoluted thermoluminescence spectrum for each sample is shown in the supporting information, Figure 4.S2.

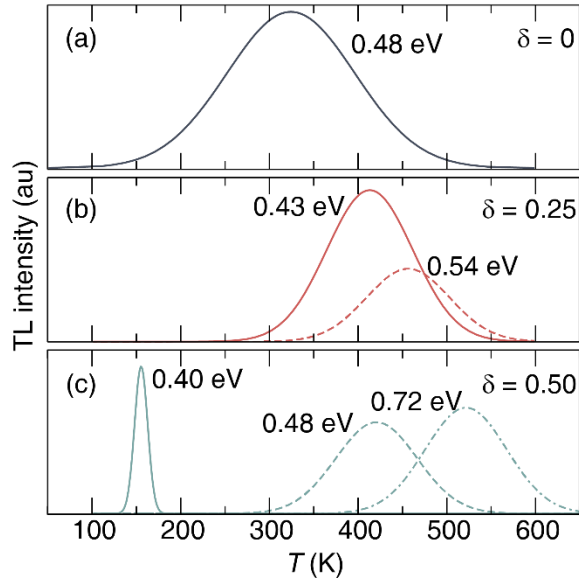


Figure 4.7. Thermoluminescence (TL) spectra of peaks contributing the long lifetimes for $\text{Zn}(\text{Ga}_{1-\delta}\text{Al}_{\delta})_2\text{O}_4:\text{Cr}^{3+}$ (a) $\delta = 0$, (b) $\delta = 0.25$, and (c) $\delta = 0.50$.

Table 4.7. TL Peaks and Corresponding Trap Depths for $\text{Zn}(\text{Ga}_{1-\delta}\text{Al}_{\delta})_2\text{O}_4:\text{Cr}^{3+}$ ($\delta = 0, 0.25, 0.50$)

δ	T (K)	trap depth (eV)
0	323	0.48
	324	0.18
0.25	123	0.19
	145	0.11
	365	0.22
	413	0.43
	456	0.54
0.50	132	0.16
	155	0.40
	169	0.19
	205	0.19
	421	0.48
	522	0.72

4.3.3 Relating Bandgap to Trap Depth The E_g and the location of trap states in $\text{Zn}(\text{Ga}_{1-\delta}\text{Al}_\delta)_2\text{O}_4:\text{Cr}^{3+}$ ($\delta = 0, 0.25, 0.50$) can be visualized in Figure 4.8. As previously stated, increasing the Al^{3+} concentration increases the E_g energy due to the shortening of bond lengths from the smaller Al^{3+} ionic radii. Plotting the change in E_g along with the positions of the trap states in Figure 4.7 demonstrates that with increasing Al^{3+} concentration the traps become more shallow, *i.e.*, closer to the conduction band. This change in trap state position is likely the cause of the decrease in persistent luminescence because it is more energetically favorable to trapping and de-trapping of an electron.

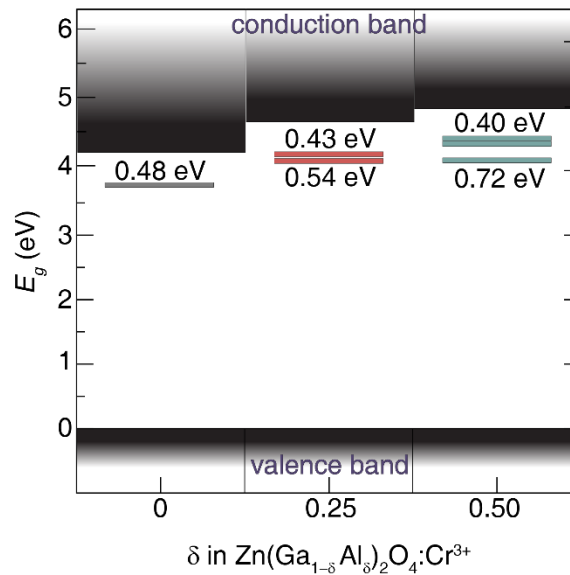


Figure 4.8. Trap depths that are participating in persistent luminescence with respect to the bottom of the conduction band for $\delta = 0, 0.25$ and 0.50 .

In fact, in the previously reported study of $\text{Zn}_{1-x}\text{Mg}_x\text{Ga}_2\text{O}_4:\text{Cr}^{3+}$ and $\text{MgGa}_2\text{O}_4:\text{Cr}^{3+}$, the loss of long luminescent lifetime was also observed with increasing lattice defects. That work postulated the quenching of the lifetime is due to a direct recombination pathway of the electron-hole pair; however, there is no experimental evidence to support the claim.

Nevertheless, the findings in this study are consistent with observations of the previous work in that there is a dependence on lattice defects to induce persistent luminescence, but when they become too numerous a quenching of the lifetime will be observed. In the case of $\text{Zn}(\text{Ga}_{1-\delta}\text{Al}_\delta)_2\text{O}_4:\text{Cr}^{3+}$ when $\delta = 1$ there is no experimentally observed inversion of cation ion site according to Rietveld refinements and thermoluminescence, hence, the lack of persistent luminescence.^{25,35} This is also likely the case for $\delta = 0.75$ because there was no measurable long luminescence lifetime or thermoluminescence to support an increase in lattice defects.

4.4 Conclusion

A solid solution $\text{Zn}(\text{Ga}_{1-\delta}\text{Al}_\delta)_2\text{O}_4:\text{Cr}^{3+}$ ($\delta = 0, 0.25, 0.50, 0.75, 1$) was prepared using high-temperature solid state synthesis. Rietveld refinements from synchrotron X-ray powder diffraction data show that both Vegard's law and Retger's law were followed with increasing substitution of Al^{3+} onto the Ga^{3+} site. This substitution also showed an increase in the optical bandgap which was determined from diffuse reflectance. Moreover, a blue shift in the photoluminescence excitation spectra is observed. Fitting the excitation spectra and determining the crystal field strength shows an overall decrease in $10Dq/B$, suggesting more aluminum creates a stronger crystal field environment. The emission spectra for the whole solid solution indicate a change in the N-line ($\lambda_{\text{em}} = 695 \text{ nm}$) that broadens going from $\delta = 0$ to $\delta = 0.50$ signifying a change in the lattice defects.

The change in relative intensity between the R and N-lines is also an indication of an increase in lattice defects with the intensity of the N-line in $\delta = 0.25, 0.50$ decreasing with the increase in Al^{3+} concentration. Measuring the long luminescent lifetimes revealed a

decrease in the emission decay with increasing aluminum concentrations with $\delta = 0.75$ and 1 exhibiting no long luminescent lifetime. To investigate the quenching of the long luminescence lifetimes, thermoluminescence was conducted to measure the trap states of the materials and determine their location with respect to the bottom of the conduction band. The measured trap depths of $\delta = 0$ were consistent with previous reports, as was a shift in the TL emission spectra with increasing Al^{3+} concentration. Furthermore, there was an increase in the number of trap states going from $\delta = 0$ to $\delta = 0.50$ indicating an increase in the number of lattice defects. Combining this result with the long lifetimes supports the claim that with increasing lattice defects there will be a loss of persistent luminescence. Therefore, it reasonable to conclude that although defects are necessary to induce persistent luminescence, there is a threshold to the number before they begin to have a reverse effect.

4.5. Acknowledgments

The authors would like to thank the Advanced Photon Source, an Office of Science User Facility operated for the U.S. Department of Energy (DOE) Office of Science by Argonne National Laboratory, was supported by the U.S. DOE under Contract No. DE-AC02-06CH11357, for the use of the 11-BM beamline and the collection of the powder X-ray diffraction data. The authors would also like to thank the University of Houston Division of Research for the generous funds provided by the Grants to Enhance and Advance Research (GEAR).

4.6 References

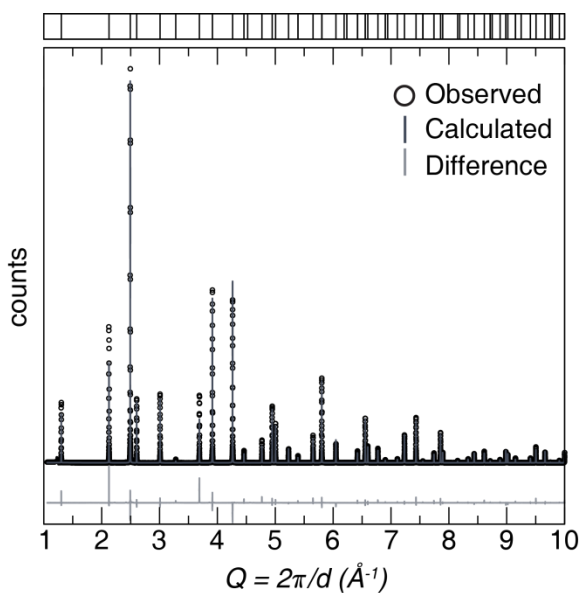
1. Maldiney, T.; Bessière, A.; Seguin, J.; Teston, E.; Sharma, S.K.; Viana, B.; Bos, A.J.J.; Dorenbos, P.; Bessodes, M.; Gourier, D.; Scherman, D.; Richard, C. The In Vivo Activation of Persistent Nanophosphors for Optical Imaging of Vascularization, Tumours and Grafted Cells. *Nat. Mater.* **2014**, *13*, 418-426.
2. Paterson, A.S.; Raja, B.; Garvey, G.; Kolhatkar, A.; Hagström, A.E.V.; Kourrentzi, K.; Lee, T.R.; Willson, R.C. Persistent Luminescence Strontium Aluminate Nanoparticles as Reporters in Lateral Flow Assays. *Anal. Chem.* **2014**, *86*, 9481-9488.
3. Paterson, A.S.; Raja, B.; Mandadi, V.; Townsend, B.; Lee, M.; Buell, A.; Vu, B.; Brgoch, J.; Willson, R.C. A Low-Cost Smartphone-Based Platform for Highly Sensitive Point-of-Care Testing with Persistent Luminescent Phosphors. *Lab Chip* **2017**, *17*, 1051-1059.
4. Maldiney, T.; Scherman, D.; Richard, C. *Persistent Luminescence Nanoparticles for Diagnostics and Imaging*; American Chemical Society: Washington, DC, 2012; Vol. 2.
5. Rojas-Hernandez, R.E.; Rodriguez, M.A.; Rubio-Marcos, F.; Serrano, A.; Fernandez, J.F. Designing Nanostructured Strontium Aluminate Particles with High Luminescence Properties. *J. Mater. Chem. C* **2015**, *3*, 1268-1276.
6. Finley, E.; Cobb, A.; Duke, A.; Paterson, A.; Brgoch, J. Optimizing Blue Persistent Luminescence in $(\text{Sr}_{1-x}\text{Ba}_x)_2\text{MgSi}_2\text{O}_7:\text{Eu}^{2+},\text{Dy}^{3+}$ via Solid Solution for Use in Point-of-Care Diagnostics. *ACS Appl. Mater. Inter.* **2016**, *8*, 26956-26963.
7. Allix, M.; Chenu, S.; Véron, E.; Pomeyrol, T.; Kouadri-Boudjelthia, E.A.; Alahraché, S.; Porcher, F.; Massiot, D.; Fayon, F. Considerable Improvement of Long-Persistent Luminescence in Germanium and Tin Substituted ZnGa_2O_4 . *Chem. Mater.* **2013**, *25*, 1600-1606.
8. Matsuzawa, T.; Aoki, Y.; Takeuchi, N.; Murayama, Y. A New Long Phosphorescent Phosphor with High Brightness, $\text{SrAl}_2\text{O}_4:\text{Eu}^{2+},\text{Dy}^{3+}$. *J. Electrochem. Soc.* **1996**, *143*, 2670-2673.
9. Abd McKayum, A.; Chen, J.-T.; Zhao, Q.; Yan, X.-P. Functional Near Infrared-Emitting $\text{Cr}^{3+}/\text{Pr}^{3+}$ Co-Doped Zinc Gallogermanate Persistent Luminescent Nanoparticles with Superlong Afterglow for In Vivo Targeted Bioimaging. *J. Am. Chem. Soc.* **2013**, *135*, 14125-14133.
10. Yixi, Z.; Jumpei, U.; Setsuhisa, T. Enhancement of Red Persistent Luminescence in Cr^{3+} -Doped ZnGa_2O_4 Phosphors by Bi_2O_3 Codoping. *Appl. Phys. Express* **2013**, *6*, 052602.
11. Rojas-Hernandez, R.E.; Rubio-Marcos, F.; Rodriguez, M.Á.; Fernandez, J.F. Long Lasting Phosphors: $\text{SrAl}_2\text{O}_4:\text{Eu}, \text{Dy}$ as the Most Studied Material. *Renewable Sustainable Energy Rev.* **2018**, *81*, 2759-2770.
12. Van den Eeckhout, K.; Poelman, D.; Smet, P. Persistent Luminescence in Non- Eu^{2+} -Doped Compounds: A Review. *Materials* **2013**, *6*, 2789.
13. Van den Eeckhout, K.; Smet, P.F.; Poelman, D. Persistent Luminescence in Eu^{2+} -Doped Compounds: A Review. *Materials* **2010**, *3*, 2536.
14. Botterman, J.; Joos, J.J.; Smet, P.F. Trapping and Detrapping in $\text{SrAl}_2\text{O}_4:\text{Eu}^{2+},\text{Dy}^{3+}$ Persistent Phosphors: Influence of Excitation Wavelength and Temperature. *Phys. Rev. B* **2014**, *90*, 085147.

15. Van den Eeckhout, K.; Bos, A.J.J.; Poelman, D.; Smet, P.F. Revealing Trap Depth Distributions in Persistent Phosphors. *Phys. Rev. B* **2013**, *87*, 045126.
16. Dorenbos, P. Mechanism of Persistent Luminescence in $\text{Sr}_2\text{MgSi}_2\text{O}_7:\text{Eu}^{2+},\text{Dy}^{3+}$. *Phys. Status Solidi B* **2005**, *242*, R7-r9.
17. Clabau, F.; Rocquefelte, X.; Jolic, S.; Deniard, P.; Whangbo, M.H.; Garcia, A.; Le Mercier, T. Mechanism of Phosphorescence Appropriate for the Long-Lasting Phosphors Eu^{2+} -Doped SrAl_2O_4 with Codopants Dy^{3+} and B^{3+} . *Chem. Mater.* **2005**, *17*, 3904-3912.
18. George, N.C.; Denault, K.A.; Seshadri, R. Phosphors for Solid-State White Lighting. *Annu. Rev. Mater. Res.* **2013**, *43*, 481-501.
19. Finley, E.; Mansouri Tehrani, A.; Brgoch, J. Intrinsic Defects Drive Persistent Luminescence in Monoclinic $\text{SrAl}_2\text{O}_4:\text{Eu}^{2+}$. *J. Phys. Chem. C* **2018**, *122*, 16309-16314.
20. Hölsä, J.; Aitasalo, T.; Jungner, H.; Lastusaari, M.; Niittykoski, J.; Spano, G. Role of Defect States in Persistent Luminescence Materials. *J. Alloys Compd.* **2004**, *374*, 56-59.
21. Hölsä, J.; Laamanen, T.; Lastusaari, M.; Niittykoski, J.; Novák, P. Electronic Structure of the $\text{SrAl}_2\text{O}_4:\text{Eu}^{2+}$ Persistent Luminescence Material. *J. Rare Earths* **2009**, *27*, 550-554.
22. Abbruscato, V. Optical and Electrical Properties of $\text{SrAl}_2\text{O}_4:\text{Eu}^{2+}$. *J. Electrochem. Soc.* **1971**, *118*, 930-933.
23. Qu, B.; Zhang, B.; Wang, L.; Zhou, R.; Zeng, X.C. Mechanistic Study of the Persistent Luminescence of $\text{CaAl}_2\text{O}_4:\text{Eu},\text{Nd}$. *Chem. Mater.* **2015**, *27*, 2195-2202.
24. De Vos, A.; Lejaeghere, K.; Vanpoucke, D.E.P.; Joos, J.J.; Smet, P.F.; Hemelsoet, K. First-Principles Study of Antisite Defect Configurations in $\text{ZnGa}_2\text{O}_4:\text{Cr}$ Persistent Phosphors. *Inorg. Chem.* **2016**, *55*, 2402-2412.
25. Basavaraju, N.; Priolkar, K.R.; Gourier, D.; Sharma, S.K.; Bessiere, A.; Viana, B. The Importance of Inversion Disorder in the Visible Light Induced Persistent Luminescence in Cr^{3+} Doped AB_2O_4 ($\text{A} = \text{Zn}$ or Mg and $\text{B} = \text{Ga}$ or Al). *Phys. Chem. Chem. Phys.* **2015**, *17*, 1790-1799.
26. Gourier, D.; Bessière, A.; Sharma, S.K.; Binet, L.; Viana, B.; Basavaraju, N.; Priolkar, K.R. Origin of the Visible Light Induced Persistent Luminescence of Cr^{3+} -Doped Zinc Gallate. *J. Phys. Chem. Solids* **2014**, *75*, 826-837.
27. Dorenbos, P. Mechanism of Persistent Luminescence in Eu^{2+} and Dy^{3+} Codoped Aluminate and Silicate Compounds. *J. Electrochem. Soc.* **2005**, *152*, H107-H110.
28. Bessière, A.; Sharma, S.K.; Basavaraju, N.; Priolkar, K.R.; Binet, L.; Viana, B.; Bos, A.J.J.; Maldiney, T.; Richard, C.; Scherman, D.; Gourier, D. Storage of Visible Light for Long-Lasting Phosphorescence in Chromium-Doped Zinc Gallate. *Chem. Mater.* **2014**, *26*, 1365-1373.
29. Ueda, J.; Dorenbos, P.; Bos, A.J.J.; Kuroishi, K.; Tanabe, S. Control of Electron Transfer Between Ce^{3+} and Cr^{3+} in the $\text{Y}_3\text{Al}_{5-x}\text{Ga}_x\text{O}_{12}$ Host via Conduction Band Engineering. *J. Mater. Chem. C* **2015**, *3*, 5642-5651.
30. Lorincz, A.; Puma, M.; James, F.J., Jr., J.H.C. Thermally Stimulated Processes Involving Defects in γ - and x -Irradiated Spinel (MgAl_2O_4). *J. Appl. Phys.* **1982**, *53*, 927-932.
31. Nikl, M.; Pejchal, J.; Mihokova, E.; Mares, J.A.; Ogino, H.; Yoshikawa, A.; Fukuda, T.; Vedda, A.; D'Ambrosio, C. Antisite Defect-Free $\text{Lu}_3(\text{Ga}_x\text{Al}_{1-x})_5\text{O}_{12}:\text{Pr}$ Scintillator. *Appl. Phys. Lett.* **2006**, *88*, 141916.

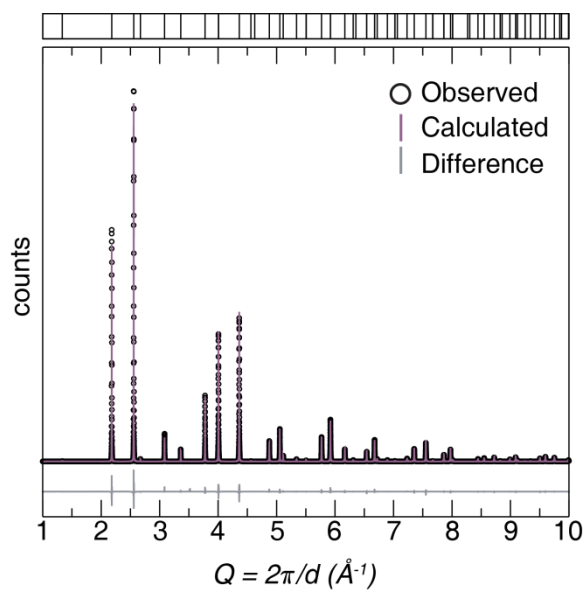
32. Ueda, J.; Tanabe, S.; Nakanishi, T. Analysis of Ce³⁺ Luminescence Quenching in Solid Solutions Between Y₃Al₅O₁₂ and Y₃Ga₅O₁₂ by Temperature Dependence of Photoconductivity Measurement. *J. Appl. Phys.* **2011**, *110*, 053102.
33. Fasoli, M.; Vedda, A.; Nikl, M.; Jiang, C.; Uberuaga, B.P.; Andersson, D.A.; McClellan, K.J.; Stanek, C.R. Band-Gap Engineering for Removing Shallow Traps in Rare-Earth Lu₃Al₅O₁₂ Garnet Scintillators Using Ga³⁺Doping. *Phys. Rev. B* **2011**, *84*, 081102.
34. Lei, B.; Li, B.; Wang, X.; Li, W. Green Emitting Long Lasting Phosphorescence (LLP) Properties of Mg₂SnO₄:Mn²⁺ Phosphor. *J. Lumin.* **2006**, *118*, 173-178.
35. Basavaraju, N.; Priolkar, K.R.; Gourier, D.; Bessiere, A.; Viana, B. Order and Disorder Around Cr³⁺ in Chromium Doped Persistent Luminescent AB₂O₄ Spinel. *Phys. Chem. Chem. Phys.* **2015**, *17*, 10993-10999.
36. Larson, A.C.VonDreele, Robert.B. General Structure Analysis System (GSAS). **1994**.
37. Toby, B.H. EXPGUI, A Graphical User Interface for GSAS. *J. Appl. Crystallogr.* **2001**, *34*, 210.
38. Levy, D.P., A.; Sani, A.; Pischedda, V. Structure and Compressibility of Synthetic ZnAl₂O₄ (Gahnite) Under High-Pressure Conditions, from Synchrotron X-ray Powder Diffraction. *Phys. Chem. Miner.* **2001**, *28*, 612-618.
39. Hornstra, J.K., E. The Oxygen Parameter of the Spinel ZnGa₂O₄. *Philips Res. Rep.* **1972**, *27*, 76-81.
40. Shannon, R.D. Revised Effective Ionic Radii and Systematic Studies of Interatomic Distances in Halides and Chalcogenides. *Acta Cryst. A* **1976**, *32*, 751-767.
41. Vegard, L. Die Konstitution der Mischkristalle und die Raumfüllung der Atome. *Z. Phys.* **1921**, *5*, 17-26.
42. Slagle, O.D.; McKinstry, H.A. The Lattice Parameter in the Solid Solution KCl-KBr. *Acta Crystallogr.* **1966**, *21*, 1013.
43. Jacob, K.T.; Raj, S.; Rannesh, L. Vegard's Law: A Fundamental Relation or an Approximation? *Int. J. Mater. Res.* **2007**, *98*, 776-779.
44. Retgers, J.W. In *Z. Phys. Chem.* 1889; Vol. 4U, p 189.
45. Zhang, W.; Zhang, J.; Chen, Z.; Wang, T.; Zheng, S. Spectrum Designation and Effect of Al Substitution on the Luminescence of Cr³⁺ Doped ZnGa₂O₄ Nano-sized Phosphors. *J. Lumin.* **2010**, *130*, 1738-1743.
46. Sakoda, K.; Hirano, M. Formation of Complete Solid Solutions, Zn(AI_xGa_{1-x})₂O₄ Spinel Nanocrystals via Hydrothermal Route. *Ceram. Int.* **2014**, *40*, 15841-15848.
47. Dixit, H.T., N.; Cottenier, S.; Saniz, R.; Lamoen, D.; Partoens, B.; Van Speybroek, B.; Waroquier, M. Electronic Structure and Band Gap of Zinc Spinel Oxides Beyond LDA: ZnAl₂O₄, ZnGa₂O₄ and ZnIn₂O₄. *New J. Phys.* **2011**, *13*, 2-10.
48. Pathak, N.; Ghosh, P.S.; Saxena, S.; Dutta, D.; Yadav, A.K.; Bhattacharyya, D.; Jha, S.N.; Kadam, R.M. Exploring Defect-Induced Emission in ZnAl₂O₄: An Exceptional Color-Tunable Phosphor Material with Diverse Lifetimes. *Inorg. Chem.* **2018**, *57*, 3963-3982.
49. Tauc, J.G., R.; Vancu, A. Optical Properties and Electronic Structure of Amorphous Germanium. *Phys. Status Solidi B* **1966**, *15*, 627-637.

50. Bessière, A.; Jacquart, S.; Priolkar, K.; Lecointre, A.; Viana, B.; Gourier, D. ZnGa₂O₄:Cr³⁺: A New Red Long-Lasting Phosphor with High Brightness. *Opt. Express* **2011**, *19*, 10131-10137.
51. Menon, S.G.; Hebbar, D.N.; Kulkarni, S.D.; Choudhari, K.S.; Santhosh, C. Facile Synthesis and Luminescence Studies of Nanocrystalline Red Emitting Cr:ZnAl₂O₄ Phosphor. *Mater. Res. Bull.* **2017**, *86*, 63-71.
52. Kahan, H.M.; Macfarlane, R.M. Optical and Microwave Spectra of Cr³⁺ in the Spinel ZnGa₂O₄. *J. Chem. Phys.* **1971**, *54*, 5197-5205.
53. Yixi, Z.; Jumpei, U.; Tanabe, S. Tunable Trap Depth in Zn(Ga_{1-x}Al_x)₂O₄:Cr,Bi Red Persistent Phosphors: Considerations of High Temperature Persistent Luminescence and Photostimulated Persistent Luminescence. *J. Mater. Chem. C* **2013**, *1*, 7849-7855.
54. Zhang, D.; Guo, Q.; Ren, Y.; Wang, C.; Shi, Q.; Wang, Q.; Xiao, X.; Wang, W.; Fan, Q. Influence of Inversion Defects and Cr–Cr Pairs on the Photoluminescent Performance of ZnAl₂O₄ Crystals. *J. Sol-Gel Sci. Technol.* **2018**, *85*, 121-131.
55. Mikenda, W. N-lines in the Luminescence Spectra of Cr³⁺-Doped Spinel (III) Partial Spectra. *J. Lumin.* **1981**, *26*, 85-98.
56. Basavaraju, N.; Priolkar, K.R.; Bessière, A.; Sharma, S.K.; Gourier, D.; Binet, L.; Viana, B.; Emura, S. Controlling disorder in the ZnGa₂O₄:Cr³⁺ persistent phosphor by Mg²⁺ substitution. *Phys. Chem. Chem. Phys.* **2017**, *19*, 1369-1377.
57. Basavaraju, N.; Sharma, S.; Bessière, A.; Viana, B.; Gourier, D.; Priolkar, K.R. Red Persistent Luminescence in MgGa₂O₄:Cr³⁺; A New Phosphor for In Vivo Imaging. *J. Phys. D: Appl. Phys.* **2013**, *46*, 375401.
58. Chen, R. Glow Curves with General Order Kinetics. *J. Electrochem. Soc.* **1969**, *116*, 1254-1257.
59. Chen, R.; McKeever, S.W.S. *Theory of Thermoluminescence and Related Phenomena*; World Scientific, 1997.
60. McKeever, S.W.S. *Thermoluminescence of Solids*; Cambridge University Press, 1985.
61. Zhihao Zhou, W.Z., Jintao Kong, Yan Liu, Ping Huang, Shanyong Zhou, Zhuo Chen, Jianlin Shi and Xueyuan Chen Rechargeable and LED-Activated ZnGa₂O₄: Cr³⁺ Near-Infrared Persistent Luminescence Nanoprobes for Background-Free Biodetection. *Nanoscale* **2017**, *9*, 6846-6853.

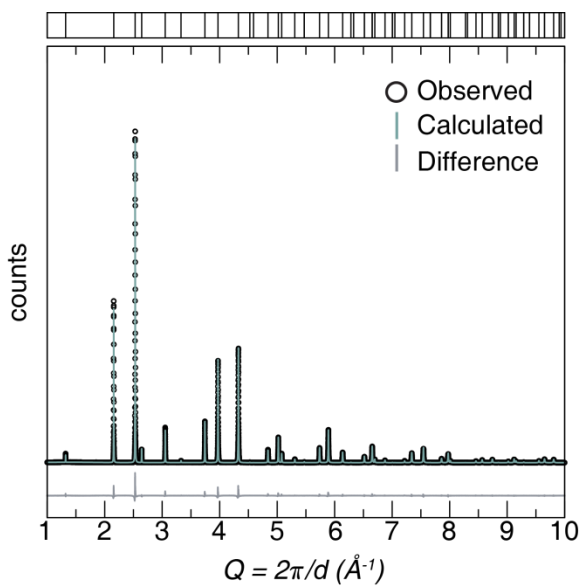
4.7 Supporting Information



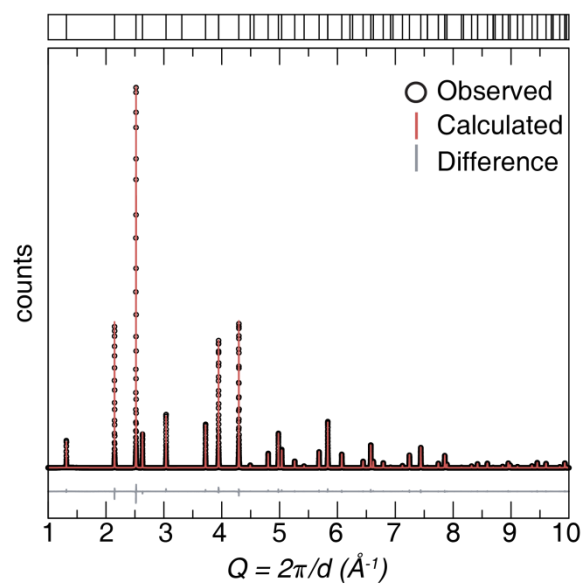
(a) ZnGa₂O₄



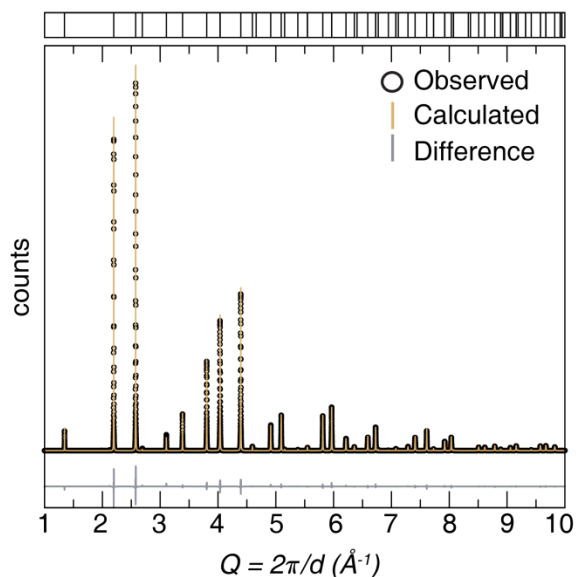
(b) Zn(Ga_{0.740(1)}Al_{0.260(1)})₂O₄



(c) Zn(Ga_{0.497(1)}Al_{0.503(1)})₂O₄



(d) Zn(Ga_{0.238(1)}Al_{0.762(1)})₂O₄



(f) ZnAl₂O₄

Figure 4.S1. Rietveld refinement shown for (a) $\delta = 0$, (b) $\delta = 0.25$, (c) $\delta = 0.50$, (d) $\delta = 0.75$, and (f) $\delta = 1$ Experimental data is indicated by black circles, refinement is the solid color, and the difference is gray. Each refinement is in good agreement with the calculated pattern.

Table 4.S1. Rietveld Refinement of Zn(Ga_{1- δ} Al _{δ})₂O₄ ($\delta = 0.25, 0.50, 0.75$) from 11-BM Synchrotron X-Ray Diffraction

Formula	$\delta = 0.25$	$\delta = 0.50$	$\delta = 0.75$
Radiation type, λ (Å)		11-BM 0.4126760	
2θ range (deg)		0.5-50	
Temperature (K)		295	
Space group; Z		$Fd\bar{3}m$ (No. 227); 8	
Lattice parameters (Å)	$a = 8.274091(2)$	$a = 8.21351(2)$	$a = 8.150408(3)$
Volume (Å ³)	566.449(1)	554.098(3)	541.425(1)
Calculated Density (g cm ⁻³)	5.782	5.413	4.997
Formula weight (g mol ⁻¹)	1972.508	1806.310	1629.164
R_p	0.0604	0.0943	0.0848
R_{wp}	0.0774	0.1480	0.1165
χ^2	2.0214	6.796	6.996

Table 4.S2. Crystallographic Data of $\text{Zn}(\text{Ga}_{1-\delta}\text{Al}_\delta)_2\text{O}_4$ ($\delta = 0.25, 0.50, 0.75$) from Rietveld Refinement Resulting from 11-BM Synchrotron X-ray Diffraction Data

(a) $\text{Zn}(\text{Ga}_{0.740(1)}\text{Al}_{0.260(1)})_2\text{O}_4$						
Atom	Wyck. site	x	y	z	U_{iso} (Å)	Occup.
Zn	8a	1/8	1/8	1/8	0.00407(3)	1
Ga	16d	1/2	1/2	1/2	0.00359(3)	0.740(1)
Al	16d	1/2	1/2	1/2	0.00271(3)	0.260(1)
O	32e	0.26357 (7)	0.26357(7)	0.26357(7)	0.0068(1)	1
(b) $\text{Zn}(\text{Ga}_{0.497(1)}\text{Al}_{0.503(1)})_2\text{O}_4$						
Zn	8a	1/8	1/8	1/8	0.00314(7)	1
Ga	16d	1/2	1/2	1/2	0.00249(7)	0.497(1)
Al	16d	1/2	1/2	1/2	0.00249(7)	0.503(1)
O	32e	0.26323(3)	0.26323(3)	0.26323(3)	0.0039(2)	1
(c) $\text{Zn}(\text{Ga}_{0.238(1)}\text{Al}_{0.762(1)})_2\text{O}_4$						
Zn	8a	1/8	1/8	1/8	0.00289(4)	1
Ga	16d	1/2	1/2	1/2	0.00219(6)	0.238(1)
Al	16d	1/2	1/2	1/2	0.00219(6)	0.762(1)
O	32e	0.26332(4)	0.26332(4)	0.26332(4)	0.0044(1)	1

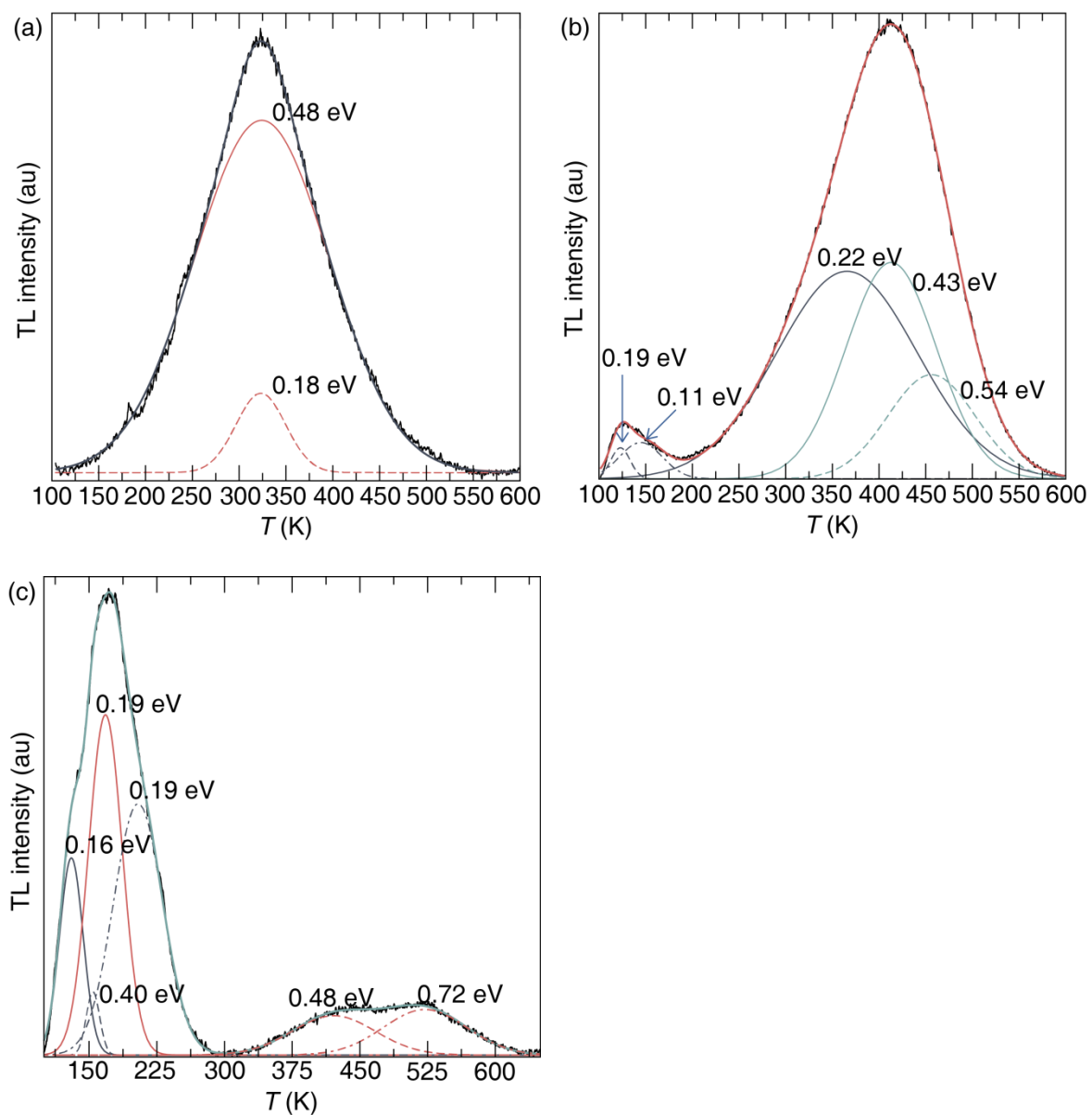


Figure 4.S2. Thermoluminescence spectra showing the deconvolution of the trap states for $\text{Zn}(\text{Ga}_{1-\delta}\text{Al}_{\delta})_2\text{O}_4:\text{Cr}^{3+}$ (a) $\delta = 0$, (b) $\delta = 0.25$, and (c) $\delta = 0.50$.

CHAPTER 5

Exploring the Local Structure in Cr-substituted $\text{Zn}(\text{Ga}_{1.5}\text{Al}_{0.5})_2\text{O}_4$ Persistent Luminescent Phosphors

Erin Finley and Jakoah Brgoch
Department of Chemistry, University of Houston, Houston, TX 77204

5.1 Introduction

Persistent luminescence is a phenomenon observed in inorganic phosphors where a luminescent center, e.g., Cr^{3+} or Eu^{2+} , can emit visible light for minutes to hours after the termination of an excitation source.¹ Due to the extraordinarily long luminescent lifetimes of these materials, a wide range of applications have been developed including emergency signage,² medical diagnostics,³⁻⁷ and novelty items such as wristwatch dials or toys. Their diverse range of functions have led to the discovery of persistent luminescent phosphors with a range of emission colors and lifetimes, chemical compositions, and structure types that most notably include a blue-emitting $\text{Sr}_2\text{MgSi}_2\text{O}_7:\text{Eu}^{2+},\text{Dy}^{3+}$, a green-emitting $\text{SrAl}_2\text{O}_4:\text{Eu}^{2+},\text{Dy}^{3+}$, an orange-emitting $\text{Ca}_2\text{Si}_5\text{N}_8:\text{Eu}^{2+},\text{Tm}^{3+}$, and a near IR-emitting $\text{ZnGa}_2\text{O}_4:\text{Cr}^{3+}$.⁸⁻¹⁰

The mechanism that drives persistent luminescence is widely agreed to include an electron from the luminescent center being photoionized into the conduction band with continued excitation.¹¹⁻¹⁵ The electron is then trapped by a “trap state,” which stems from a defect within the crystal structure or the presence of $5d$ -orbitals from a co-dopant such as Dy^{3+} .¹²⁻¹⁵ When energy (usually thermal) is then applied to the material, the electrons held in the trap states are slowly released leading to longer than expected luminescent lifetimes. Evidence of this mechanism has involved work to understand the relationship between co-dopants and trap states in an attempt to further extend the persistent

luminescence or improve emission intensity.^{11,16,17} Research has also shown the presence lattice defects (anion vacancies or anti-site defects) are essential in the persistent luminescent mechanism has increasingly gained attention.¹⁸⁻²⁰ For example, first principle calculations revealed the presence of anion vacancies were responsible for the observed emission lifetimes in $\text{SrAl}_2\text{O}_4:\text{Eu}^{2+}$, $\text{CaAl}_2\text{O}_4:\text{Eu}^{2+},\text{Nd}^{3+}$ whereas anti-site (Zn/Ga) defects were the reason for the long luminescence lifetimes in $\text{ZnGa}_2\text{O}_4:\text{Cr}^{3+}$.¹⁸⁻²⁰ Experimental investigations have also been central for understanding the relationship between defects and optical properties. In one study, the local structure of Eu^{2+} was analyzed using synchrotron X-ray absorption spectroscopy (XAS)^{21,22} and electron paramagnetic resonance spectroscopy (EPR)²³ to show that oxygen vacancies contributed to the trapping of electrons in $\text{Sr}_2\text{MgSi}_2\text{O}_7:\text{Eu}^{2+},\text{Dy}^{3+}$. Moreover, ^{71}Ga solid-state NMR of $\text{ZnGa}_2\text{O}_4:\text{Cr}^{3+}$ confirmed anti-site defects were present with EPR showing the resulting trap states lie next to the first cationic neighbor with respect to Cr^{3+} .^{24,25}

Interest in Cr^{3+} substituted spinel-type phosphors have become a central research focus with a specific interest on understanding how the local coordination environment around the luminescent ion influences persistent luminescence. Recent work has revealed that the most likely origin is due to the presence of anti-site defects influencing the polyhedron of Cr^{3+} in the structure.^{9,25,26} These spinel structures provide an attractive platform to further study the implications of structural defects around Cr^{3+} because they can be studied as a function of chemical composition.^{24,27,28} The family of normal spinel-type structures, AB_2O_4 (A = divalent cation and B = trivalent cation) form in a cubic closed packed structure, space group $Fd\bar{3}m$ (no. 227), with eight A sites and sixteen B sites whereas an inverse spinel has eight of the trivalent B atoms occupying the eight A sites and the divalent A atoms evenly distributed with the remaining eight B atoms over

the sixteen B sites. Within this family of spinel-type structures, persistent luminescence has been extensively investigated for three compounds: $\text{ZnGa}_2\text{O}_4:\text{Cr}^{3+}$, $\text{ZnAl}_2\text{O}_4:\text{Cr}^{3+}$, and $\text{MgGa}_2\text{O}_4:\text{Cr}^{3+}$.^{25-27,29-32} The compound $\text{ZnGa}_2\text{O}_4:\text{Cr}^{3+}$ exhibits the longest reported lifetime lasting for ≥ 5 h, $\text{MgGa}_2\text{O}_4:\text{Cr}^{3+}$ shows a lifetime of ≤ 15 min, and $\text{ZnAl}_2\text{O}_4:\text{Cr}^{3+}$ does not have a measureable persistent luminescent lifetime.^{27,29-31}

Interestingly, $\text{ZnAl}_2\text{O}_4:\text{Cr}^{3+}$ crystallizes as a nearly perfect normal spinel with Zn almost exclusively occupying the A sites and Al occupying the B sites, which is different from $\text{ZnGa}_2\text{O}_4:\text{Cr}^{3+}$, which has been suggested to contain $\sim 3\%$ Zn/Ga inversion, *i.e.*, anti-site defects.²⁴ This is in contrast to $\text{MgGa}_2\text{O}_4:\text{Cr}^{3+}$, which shows $\sim 44\%$ Mg/Ga inversion.^{30,31} There is an apparent connection between the concentration of the anti-site defects and the luminescent lifetimes; therefore, the relationship between persistent luminescence and anti-site defects should be probed. Recent work using photon emission and thermoluminescence spectroscopies to study $\text{Zn}(\text{Ga}_{1-\delta}\text{Al}_\delta)_2\text{O}_4:\text{Cr}^{3+}$ showed there is, in fact, a dependence on the number of lattice defects stemming from the different concentrations of δ .³³ Additionally, a study of $(\text{Zn}_{1-\delta}\text{Mg}_\delta)\text{Ga}_2\text{O}_4:\text{Cr}^{3+}$ using ERP and XAS, of Cr^{3+} indicated a correlation between anti-site defects and local structure by identifying a decrease in bond length between Cr-O with increasing number of defects.²⁷

The substitution of Cr^{3+} in these spinel-type crystal structures not only induces defects leading to the formation of trap states, but it also causes the normally octahedrally coordinated B site to trigonally distort reducing the point group symmetry from O_h to D_{3d} .³⁴ This distortion can be observed in the photoemission of $\text{ZnGa}_2\text{O}_4:\text{Cr}^{3+}$ and $\text{ZnAl}_2\text{O}_4:\text{Cr}^{3+}$, where assuming O_h symmetry there is a spin-forbidden photon emission, ${}^2E_g \rightarrow {}^4A_{2g}$. Detailed analysis of this photon emission at 77 K revealed a splitting of the emission peak into two distinct peaks confirming a lowering of the symmetry from O_h (2E_g

$\rightarrow {}^4A_{2g}$) to D_{3d} ($E_g \rightarrow {}^4A_{2g}$ and $2A_g \rightarrow {}^4A_{2g}$), where the gallate ($\approx 40 \text{ cm}^{-1}$) had a greater splitting of the E_g and $2A_g$ versus the aluminate ($\approx 6 \text{ cm}^{-1}$).³⁴⁻³⁶ An examination of the relationship between the trigonal distortions of Cr^{3+} in $\text{ZnGa}_2\text{O}_4:\text{Cr}^{3+}$, $\text{ZnAl}_2\text{O}_4:\text{Cr}^{3+}$, and $\text{MgGa}_2\text{O}_4:\text{Cr}^{3+}$ and anti-site defects was subsequently conducted using EPR.³¹ The study revealed that strain broadening, which is an indication of anti-site defects, increased following $\text{MgGa}_2\text{O}_4:\text{Cr}^{3+} > \text{ZnGa}_2\text{O}_4:\text{Cr}^{3+} > \text{ZnAl}_2\text{O}_4:\text{Cr}^{3+}$. This result provided further evidence that was consistent with the known inversion of these materials and the observed splitting of the E_g and $2A_g$ states.^{31,35} The EPR study also showed the zero field splitting of the 4A_2 ground state with $\text{ZnAl}_2\text{O}_4:\text{Cr}^{3+} > \text{MgGa}_2\text{O}_4:\text{Cr}^{3+} > \text{ZnGa}_2\text{O}_4:\text{Cr}^{3+}$ suggesting decreasing trigonal distortion on the C_3 axis.^{31,35} Interestingly, the zero field splitting trend corresponds to the loss of long luminescent lifetimes reported with this family of spinel-type structures such that as zero field splitting increases there is a decrease in lifetime.^{25-27,29-31} The combination of these results suggest that the relationship between the C_3 axial distortion of Cr^{3+} and anti-site defects are linked to the efficiency of persistent luminescence.

In the research presented here, the local structure surrounding the Cr^{3+} ion is investigated across the solid solution $\text{Zn}(\text{Ga}_{1-\delta}\text{Al}_\delta)_2\text{O}_4:\text{Cr}^{3+}$ ($\delta = 0 - 1$) using XAS and its ensuing components: X-ray absorption near edge structure (XANES) and extended X-ray absorption fine structure (EXAFS). The previously reported optical properties of this solid solution revealed there was a significant quenching of the long luminescent lifetime with increasing aluminum concentration from $\delta = 0 - 0.50$, with the persistent luminescence completely quenched at $\delta = 0.75$.³³ The loss of persistent luminescence in this series was indirectly attributed to an increase in the number of lattice defects that became shallower as Al^{3+} concentration increased up to $\delta = 0.50$.³³ The XANES spectra

confirm the main oxidation state of Cr in this system is 3+ and resides in a [CrO₆] octahedron. Moreover, fitting the data reveals changes in peak shape that indicates distortions in the octahedron arising from anti-site defects. Combining these results with additional EXAFS fitting and the aforementioned optical properties indicate that as the Al³⁺ concentration increases to $\delta = 0.50$ there is a [CrO₆] octahedral distortion that is accompanied by an increase in the concentration of lattice defects.

5.2 Experimental

5.2.1 Sample Preparation and Characterization Polycrystalline samples, with the nominal compositions Zn(Ga_{1- δ} Al _{δ})_{2-x}O₄:Cr³⁺ ($\delta = 0, 0.25, 0.50, 0.75, 1; x = 0.005$) were prepared *via* high-temperature solid-state synthesis. The starting materials were weighed out in stoichiometric ratios using the following reagents: ZnO (Alfa Aesar 99.9%), Ga₂O₃ (Alfa Aesar 99.95%), Al₂O₃ (Alfa Aesar 99%), Cr₂O₃ (Alfa Aesar 99%), and 4 wt% boric acid (Sigma Aldrich 99.98%) as a flux. These powders were first mixed using a shaker mill (Spex 8000M) in a polystyrene vial with 9.5 mm methacrylate balls as grinding media for 45 min and then pressed into 8 mm pellets. The pellets were then heated in air for 10 h at 1300°C with heating and cooling rates of 3°C/min. The products were subsequently ground into fine powders using an agate mortar and pestle for characterization.³³ Phase purity of each product was then confirmed by indexing the diffractograms collected using a PanAnalytical X'Pert powder diffractometer equipped with Cu K α radiation (1.54183 Å), shown in Figure 5.1.

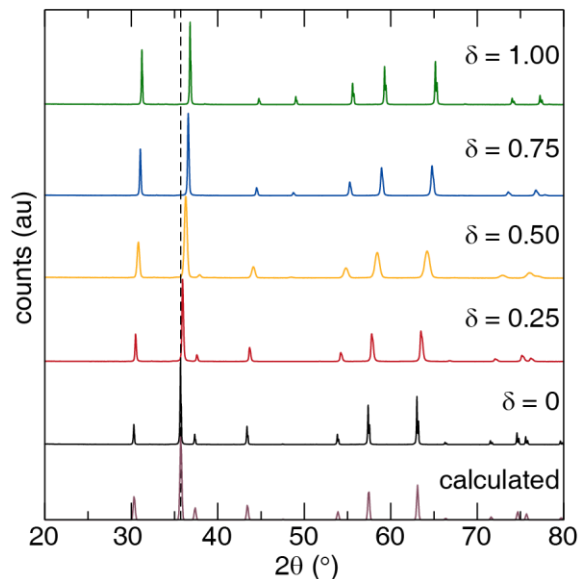


Figure 5.1 Powder X-ray diffraction of $\text{Zn}(\text{Ga}_{1-\delta}\text{Al}_{\delta})_2\text{O}_4:\text{Cr}^{3+}$ ($\delta = 0 - 1$). The whole solid solution forms in the space group $Fd\bar{3}m$ (no. 227) in agreement with the calculated pattern.³⁷ Shift of peaks to higher angle indicate smaller unit cell parameters confirming incorporation of Al^{3+} into the system.

5.2.2 Density Functional Theory Calculations Structure optimization for the full range of δ was conducted using the Vienna *Ab initio* Simulation Package (VASP).³⁸ All calculations employed a plane-wave basis set with projector augmented wave (PAW) potentials.^{39,40} The atomic positions and unit cell volumes were relaxed within the Generalized Gradient Approximation (GGA) and the exchange and correlation described using the Perdew-Burke-Ernzerhof (PBE) functional.⁴¹ Total energy calculations used a plane-wave cutoff energy of 500 eV, convergence condition of 1×10^{-8} eV electronic relaxation, 1×10^{-6} eV structural relaxation, and a $2 \times 2 \times 2$ Γ -centered Monkhorst-Pack k -point mesh. The crystal structures were visualized using Vesta.⁴²

5.2.3 X-ray Absorption Spectroscopy XANES and EXAFS measurements were carried out in conjunction with the research presented here employed the Materials Research Collaborative Access Team (MRCAT) at the Advanced Photon Source, Argonne

National Laboratory on the 10-BM A,B beamline.^{43,44} Samples were finely ground and sieved to a –325 mesh (Cole Palmer) and spread thinly over Kapton Tape™. The data were collected on the Cr *K* edge, 5989 eV in fluorescence mode between 5000 eV – 7000 eV. Analysis was conducted using the Athena and Artemis software packages.⁴⁵

5.3 Results and Discussion

5.3.1 XANES Spectra of the Cr *K* Edge X-ray absorption spectroscopy was conducted using the solid solution $\text{Zn}(\text{Ga}_{1-\delta}\text{Al}_\delta)_2\text{O}_4:\text{Cr}^{3+}$ ($\delta = 0 - 1$) to investigate the local structure environment of Cr^{3+} . Owing to the low concentrations of Cr^{3+} substitution in this crystal structure, refining the specific crystallographic details surrounding the luminescent cation is not easily done using conventional, average structure methods like powder X-ray diffraction. Thus, XAS is a valuable tool for determining structural properties in persistent luminescent materials because these are atom specific measurements.⁴⁶ XAS experiments result in two spectra with distinct features; first, the XANES region provides information about orbital mixing and oxidation state whereas the second, EXAFS region provides details about interatomic distances, site occupancies, and coordination environment.⁴⁵⁻⁴⁷

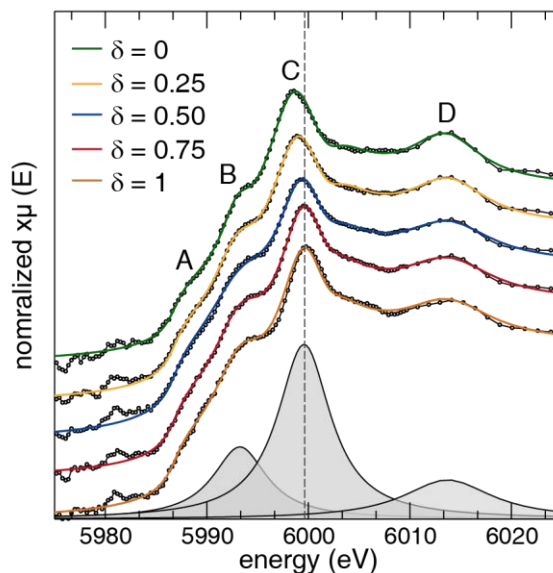


Figure 5.2 Cr K edge XANES spectra for $\text{Zn}(\text{Ga}_{1-\delta}\text{Al}_\delta)_2\text{O}_4:\text{Cr}^{3+}$ ($\delta = 0 - 1$). The four prominent features A-B is the $1s \rightarrow 3d$ transition, C $1s$ -to-continuum, D is the first constructive interference. Lorentzian fitted peaks are grey. The dashed line is a guide for the eye to show the shift in energy of the C peak.

In this work, the XANES spectra were collected for the Cr K edge in $\text{Zn}(\text{Ga}_{1-\delta}\text{Al}_\delta)_2\text{O}_4:\text{Cr}^{3+}$ ($\delta = 0 - 1$), plotted in Figure 5.2. In the pre-edge range, ≤ 5989 eV, there are no intense peaks, which indicate Cr exists primarily in its 3+ oxidation state.^{48,49} A closer analysis indicates there are four prominent features in the XANES data, labeled A, B, C, and D. First is the A (absorption edge at 5989 eV) and B features represent the $1s \rightarrow 3d$ photoelectronic transition of Cr^{3+} .⁵⁰ Next is the C feature and identified is the electronic transition of an electron from the $1s$ -to-continuum and shows a shift to higher energy (eV) with increasing Al^{3+} concentration, which is consistent with an increase in the optical bandgap as Al^{3+} increases.^{33,51,52} Finally, is the D feature which is the first constructive interference with neighboring atoms.³²

To gain qualitative insight into how these features change with varying composition the B, C, and D features were fit using a Lorentzian function and are listed in Table 5.1, resulting in three distinct peaks. The A feature was fit using an arctan step function and

was set to a 5989 eV, the value of the absorption edge, for all values of δ . Firstly, peaks B and D have a constant energy centroid across the whole range of δ , whereas peak C shifts to a higher energy with increasing Al^{3+} concentration. The shift in energy is a result from the increased electronegativity of Al^{3+} compared to Ga^{3+} .⁵⁰

Table 5.1. XANES peak fitting results for $\text{Zn}(\text{Ga}_{1-\delta}\text{Al}_\delta)_2\text{O}_4:\text{Cr}^{3+}$ ($\delta = 0 - 1$)

	Centroid (eV)	Height (E)	Width (E)
(a) B			
0	5993(1)	1.3(3)	3.7(3)
0.25	5993(4)	2(1)	5.3(3)
0.50	5993(5)	5(4)	8.5(3)
0.75	5993(1)	3.6(7)	6.5(2)
1	5993.4(8)	4.0(5)	6.7(2)
(b) C			
0	5998.7(1)	11.1(3)	7.5(3)
0.25	5998.99(9)	10(1)	7.3(6)
0.50	5999.4(1)	8(4)	6.5(7)
0.75	5999.58(9)	8.6(7)	6.4(1)
1	5999.8(1)	8.2(5)	6.1(1)
(c) D			
0	6013.5(4)	3.1(2)	8.4(8)
0.25	6013.8(4)	3.0(2)	9.1(9)
0.50	6013.8(5)	3.0(3)	10(1)
0.75	6013.7(4)	3.2(2)	11(1)
1	6013.8(5)	3.1(2)	11(6)

Next, the height variation in the signal, which arises from changes in valence orbitals, remains constant for peak D, it increases in peak B, and it decreases in peak C. The increase in peak B is due the increasing presence of the lower energy $3p$ -orbitals that stems from the shifting of energy of the C peak.⁵⁰ The decrease in the intensity in peak C is attributed to a decrease in the number of unoccupied orbitals above the Fermi level.⁵⁰ Finally, the peak widths in XANES have been ascribed to distortions in the $[\text{CrO}_6]$ octahedron when comparing $\text{ZnGa}_2\text{O}_4:\text{Cr}^{3+}$ and $\text{ZnAl}_2\text{O}_4:\text{Cr}^{3+}$, where a broader peak for $\text{ZnGa}_2\text{O}_4:\text{Cr}^{3+}$ was reported suggesting the broader the peak the more anti-site defects were present.^{27,32} From these data it is evident that peak B becomes broader up to $\delta = 0.50$ and then narrows going to $\delta = 0.75$ and $\delta = 1$. These observation are consistent

with an increase in the number of lattice defects that were also observed in a thermoluminescence study.³³ Alternatively, Peak C narrows and D widens with increasing Al³⁺ concentration, likely due to a change in the atomic interactions between Cr³⁺ and its neighboring atoms with varying δ . This is similar to the previous report of ZnGa₂O₄:Cr³⁺ and ZnAl₂O₄:Cr³⁺ that reported the changes in peak width and intensity and ascribed the changes to shifts in the Cr–O bond lengths.³² To support these claims, it is essential to investigate the Cr³⁺ local structure by examining the EXAFS region and extract a more precise coordination environment around Cr³⁺.

5.3.2 EXAFS Spectra of Cr K Edge To further explore how the local symmetry distortions observed in the XANES spectra are changing as a function of δ , the EXAFS spectra of the solid solution was investigated. The processed data are plotted in Figure 5.3. Looking closely at the first coordination shell, the first near neighbor is the Cr–O interaction, which is an octahedrally coordinated Cr atom ([CrO₆]), located at ≈ 1.5 Å. The next region is the second and third coordination shells between 2.0 Å and 3.5 Å. They are assigned to the first cationic neighbor, Cr–Ga or Cr–Al, which is the *B* atom in an octahedrally coordinated environment (Cr–[Ga/AlO₆] ≈ 2.6 Å), and the second cationic neighbor, Cr–Zn, the *A* atom in a tetrahedrally coordinated environment (Cr–[ZnO₄] ≈ 3.5 Å).^{46,47,53-55} When $\delta = 0$ there is an intense broad peak centered at ~ 2.6 Å as expected for occupation of [GaO₆] octahedron and [ZnO₄] tetrahedron.^{31,55} Increasing the aluminum concentration decreases this peak's intensity and causes a significant broadening by $\delta = 0.25$. Then the peak becomes noticeably asymmetric at $\delta = 0.50$. Further increasing Al³⁺ to $\delta = 0.75$ shows the EXAFS peak begins to become bimodal, which is an indication of the two distinct coordination environments of the second and third coordination shells. Finally, for $\delta = 1$, there are two independent peaks centered at

~ 2.5 Å and ~ 3.0 Å.³¹ This change in the peak shape is attributed to the site mixing between Ga³⁺ and Al³⁺. This is due to the smaller ionic radii of Al³⁺ ($r_{6\text{-coord}} = 0.535$ Å) compared to Ga³⁺ ($r_{6\text{-coord}} = 0.620$ Å) that results in an overserved shortening of the interatomic distance between Cr–Al.⁵⁶ Noting that because the ionic radii of Zn²⁺ ($r_{6\text{-coord}} = 0.600$ Å) is nearly the same as Ga³⁺ the narrower, more intense peak observed in $\delta = 0$ is seen.⁵⁶ Thus, as the smaller Al³⁺ concentration increases the two shells (second and third) become more resolved as a result of the difference in ionic radii. Moreover, it is consistent with the observations made in the XANES region with the widening of peak D.

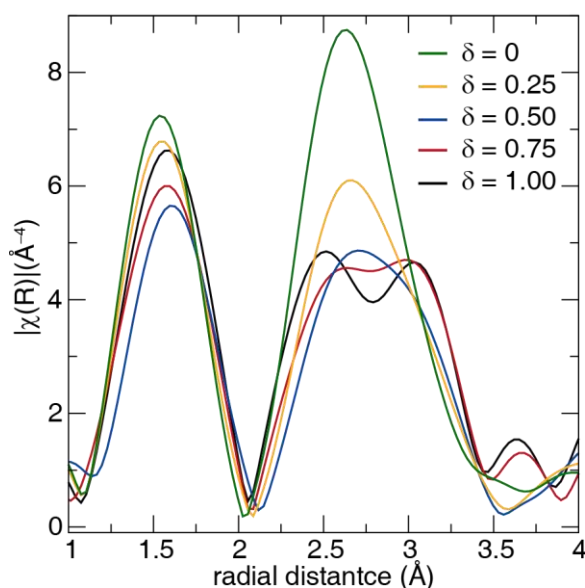


Figure 5.3 EXAFS spectra across the solid solution $\text{Zn}(\text{Ga}_{1-\delta}\text{Al}_\delta)_2\text{O}_4:\text{Cr}^{3+}$ ($\delta = 0 - 1$) with k^3 -weighted Fourier transform of the magnitude.

To determine the interatomic distances of Cr–O, Cr–Ga/Al, and Cr–Zn, the EXAFS data were fit using the *IFEFFIT* software for the R -range (radial distance) of 1 Å to 4 Å using a Hanning window for the full range of δ .⁴⁵ It is straight forward to model the data of the end members of the solid solution; however, modeling statistical atomic mixing using *IFEFFIT* is problematic because it is complicated to generate the complex scattering

paths needed to describe these situations.⁴⁵ The intermediate values of δ in this spinel-type structure, *i.e.*, $\delta = 0.25, 0.50,$ and $0.75,$ all contain statistical mixing of the Ga/Al position (*B* site). As a result, ordered models where the symmetry of the *B* site is reduced must first be created for use as an input, starting structure models for *IFEFIT*. In this work, the ordered models were constructed using the program “Supercell.”⁵⁷ A supercell approach is a classic method for approximating atomic disorder in a material by lowering the point symmetry and reducing Wyckoff multiplicity of each site. The result is a straightforward way to mimic atomic disorder. The “Supercell” program also creates a large number of structures by enumerating all possible combinations of local environments are probed. The ordered crystal structures generated can then be optimized using DFT to determine the lowest energy structure, which is likely the best model for the experimentally observed mixing. For $\text{Zn}(\text{Ga}_{1-\delta}\text{Al}_\delta)_2\text{O}_4$ ($\delta = 0.25, 0.50,$ and 0.75) the lowest total DFT calculated energies are visualized in Figure 5.4. These structures were used to calculate the scattering paths in *IFEFFIT* as a starting point for the EXAFS fitting.

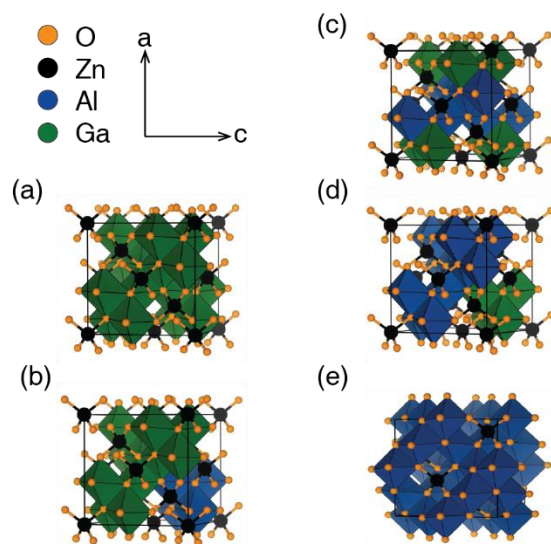


Figure 5.4 Unit cells of the solid-solution from DFT calculations [GaO₆] (green) and [AlO₆] (blue) octahedron are highlighted, Zn²⁺ (black), and O²⁻ (orange). (a) ZnGa₂O₄ (b) Zn(Ga_{0.75}Al_{0.25})₂O₄ (c) Zn(Ga_{0.50}Al_{0.50})₂O₄ (d) Zn(Ga_{0.25}Al_{0.75})₂O₄ and (e) ZnAl₂O₄.

The final EXAFS fits across the full range of δ are presented in Figure 5.5. The resulting fits are in good agreement with the observed data, as well as the previous report of ZnGa₂O₄:Cr³⁺ and ZnAl₂O₄:Cr³⁺.³² The fit parameters including, the degeneracy of the absorbing atom (N), radial distance (R) of the atomic neighbors, the difference in R_{eff} (calculated R) and R (ΔR), and the Debye-Waller factor (σ^2) are provided in Table 5.1. Notably, σ^2 , which measures the disorder in the path, is quite large for Cr-O path in $\delta = 0.50$ supporting the presence of disorder in the crystal structure, as expected. The parameter N , as previously mentioned, is the degeneracy of the absorbing atoms. In other words, it is the number of atoms that are the same. For example, when $N = 6$ for the first near neighbor of Cr³⁺ that means there are six oxygen atoms as the first neighbor. The varying values of N for the first cationic neighbor for $\delta = 0.25$, 0.50 , and 0.75 are a result of site mixing between gallium and aluminum; however, total an $N = 6$ that is consistent with [Ga/AlO₆] octahedron assigned to the second coordination shell.

Likewise, N = 6 for Cr–O and Cr–Zn are consistent with [CrO₆] octahedral and [ZnO₄] tetrahedra.⁵³

Table 5.2 Structural parameters around Cr³⁺ determined by fitting the Cr K edge EXAFS.

	N	R (Å)	ΔR (Å)	σ ² (Å ²)
(a) δ = 0 $\chi_{red}^2 = 53.90$ R-factor = 0.018				
Cr–O	6	1.961	-0.0284(8)	0.001(1)
Cr–Ga	6	2.945	-0.005(8)	0.0017(9)
Cr–Zn	6	3.428	-0.03(1)	0.003(2)
(a) δ = 0.25 $\chi_{red}^2 = 74.96$ R-factor = 0.020				
Cr–O	6	1.966	-0.039(8)	0.000(9)
Cr–Ga	5	2.956	-0.01(2)	0.003(1)
Cr–Al	1	2.814	-0.2(1)	0.003(1)
Cr–Zn	6	3.419	-0.06(3)	0.004(2)
(b) δ = 0.50 $\chi_{red}^2 = 83.55$ R-factor = 0.022				
Cr–O	6	2.009	0.019(9)	0.019(2)
Cr–Ga	2	2.963	0.02(6)	0.002(9)
Cr–Al	4	2.872	-0.07(3)	0.001(7)
Cr–Zn	6	3.459	0.01(2)	0.004(3)
(c) δ = 0.75 $\chi_{red}^2 = 188.61$ R-factor = 0.037				
Cr–O	6	1.997	0.01(1)	0.009(2)
Cr–Ga	2	2.529	-0.4(2)	0.02(2)
Cr–Al	4	2.903	-0.04(3)	0.001(5)
Cr–Zn	6	3.409	-0.04(2)	0.004(3)
(b) δ = 1 $\chi_{red}^2 = 99.04$ R-factor = 0.034				
Cr–O	6	1.988	0.017(1)	0.001(1)
Cr–Al	6	2.899	0.02(2)	0.002(2)
Cr–Zn	6	3.395	0.04(1)	0.004(2)

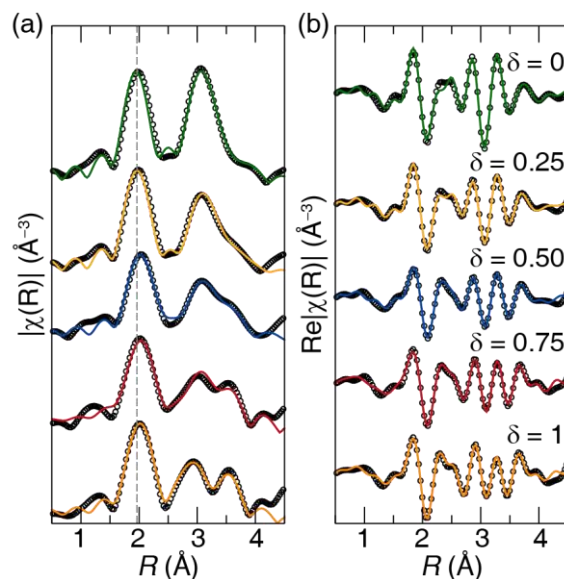


Figure 5.5 Cr K edge EXAFS of for in Fourier transform k^2 -weighted R -space of (a) magnitude and (b) real. Black circles are the observed data, solid line is the fit. Dashed line is a guide for the eye to show the peak shift.

Examining the changes in the radial distance across the solid solution the first near neighbor revealed a particularly interesting change as a function of δ . A closer look at Figure 5.5a reveals that a shift to longer values of R with increasing Al^{3+} concentration is occurs for $\delta = 0.25$ and 0.50 . Once $\delta = 0.75$ there is a small shift to a shorter value of R , and finally another shift to smaller R when $\delta = 1$. This could be an indication of distortion in the polyhedron of Cr–O. Plotting R across the solid solution for the Cr–O bond (first near neighbor or $[\text{CrO}_6]$ octahedron) is shown in Figure 5.6a. The difference in the calculated radial distance (R_{eff}) and the fit radial distance is described by ΔR (Figure 5.6b).⁴⁶ To accurately describe the value of R , ΔR should not be $\geq \pm 0.5 \text{ \AA}$.⁴⁶ The Cr–O bond shows an increase in the R with increasing Al^{3+} up to $\delta = 0.50$ and then decreases for $\delta = 0.75$ and again when $\delta = 1$.

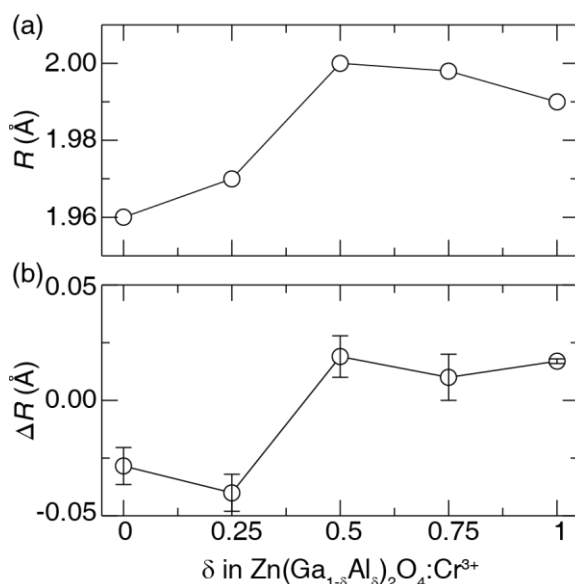


Figure 5.6 (a) Radial distance (R) of Cr–O as a function of δ in $\text{Zn}(\text{Ga}_{1-\delta}\text{Al}_{\delta})_2\text{O}_4:\text{Cr}^{3+}$ ($\delta = 0 - 1$). (b) Difference in the calculated distance and the fit as a function of δ .

Examining the results of the EXAFS fitting presented here suggest that as Al^{3+} increases to $\delta = 0.50$ there will be an increase in the number of lattice defects, presumably anti-site defects, that will distort the $[\text{CrO}_6]$ octahedron lengthening the Cr–O bond. Recalling the thermoluminescence measurements of this solid solution, $\text{Zn}(\text{Ga}_{1-\delta}\text{Al}_{\delta})_2\text{O}_4:\text{Cr}^{3+}$ ($\delta = 0 - 1$), which recently confirmed an increase in the number of trap states for $\delta = 0 < 0.25 < 0.50$, and was also supported by observations made using fluorescence spectroscopy.³³ Additionally, the reported EPR data showing an increase in the zero field splitting along the C_3 axis of $\text{ZnAl}_2\text{O}_4:\text{Cr}^{3+} > \text{MgGa}_2\text{O}_4:\text{Cr}^{3+} > \text{ZnGa}_2\text{O}_4:\text{Cr}^{3+}$ supporting a distortion that corresponds to changes in the observed persistent luminescence.³¹ In combination, the data suggest a correlation between the distortion observed in the local structure of the Cr^{3+} luminescent center and the increase in the number of trap states that lead to the quenching of long luminescent lifetimes.

5.4 Conclusion

The spinel-type structure of the solid solution $\text{Zn}(\text{Ga}_{1-\delta}\text{Al}_\delta)_2\text{O}_4\cdot\text{Cr}^{3+}$ ($\delta = 0 - 1$) was investigated to explore the changes in local structure around the luminescent center, Cr^{3+} . The synthesis of the full solid solution was achieved *via* high-temperature solid-state synthesis at 1300°C in air for 10 h. The final phase pure products were confirmed with PXRD and used to conduct XAS experiments. The XANES spectra show four prominent regions, A, B, C, and D. A and B are the absorption of a $1s \rightarrow 3d$ photoelectron transition consistent with the presence of Cr^{3+} . A distinct peak, labeled C, the $1s$ -to-continuum, shifted to higher energies with increasing Al^{3+} concentration consistent with an increase in the optical bandgap and the increasing electronegativity of aluminum. Fitting three of the prominent features in the XANES region revealed a change in peak intensity of the B peak that increases up to $\delta = 0.50$ then decreases again to $\delta = 1$. Peak C has shift to higher energy that becomes less intense and narrower with increasing Al^{3+} concentration.

Finally, peak D remains constant in both peak location and intensity; however it becomes broader with increasing Al^{3+} concentration. Explicitly examining the first coordination shell shows the Cr–O interaction is centered at $\approx 1.5 \text{ \AA}$, while the second and third shells ($2.5 \text{ \AA} - 3.5 \text{ \AA}$) show a change of peak shape. These peaks decrease in intensity and become increasingly asymmetrical with increasing Al^{3+} until two distinct peaks are observed at $\delta = 0.75$ and 1. Fitting the EXAFS spectra of each composition revealed a trend in the R of Cr–O that is consistent with the change in peak B's intensity from the XANES data. The resulting R values imply that an increase in distortion along the C_3 axis in the $[\text{CrO}_6]$ octahedron occurs up to $\delta = 0.50$, which also supports an

increase in the number of lattice defects present. These results combined with previously reported optical properties support the hypothesis that lattice defects are an essential property to persistent luminescent phosphors and that a distortion in local coordination environment can induce defects. However, when a maximum is reached they will have an adverse effect.

5.5 Acknowledgements

XAS experiments were conducted under the use of the Advanced Photon Source, an Office of Science User Facility operated for the U.S. Department of Energy (DOE) Office of Science by Argonne National Laboratory, was supported by the U.S. DOE under Contract No. DE-AC02-06CH11357. The authors would like to thank the staff scientists at MRCAT for assistance with sample preparation on site and assistance in collecting data. A special thank you to Dr. Michael Gaultois for help with the Demeter software suite and Kush Patel for writing and executing the script used for DFT calculations. Lastly, the authors thank The University of Houston Division of Research and the Grant to Enhance and Advance Research for funding this research.

5.6 References

1. Xu, J.; Tanabe, S. Persistent Luminescence Instead of Phosphorescence: History, Mechanism, and Perspective. *J. Lumin.* **2018**, *205*, 581-620.
2. Yen, W.M.; Shinonoya, S.; Yamamoto, H. *Phosphor Handbook*; CRC Press: Boca Raton, FL, 2007.
3. Maldiney, T.; Sraiki, G.; Viana, B.; Gourier, D.; Richard, C.; Scherman, D.; Bessodes, M.; Van den Eeckhout, K.; Poelman, D.; Smet, P.F. In vivo Optical Imaging with Rare Earth Eoped $\text{Ca}_2\text{Si}_5\text{N}_8$ Persistent Luminescence Nanoparticles. *Opt. Mat. Express* **2012**, *2*, 261-268.
4. le Masne de Chermont, Q.; Chanéac, C.; Seguin, J.; Pellé, F.; Maîtrejean, S.; Jolivet, J.-P.; Gourier, D.; Bessodes, M.; Scherman, D. Nanoprobes with Near-Infrared Persistent Luminescence for In Vivo Imaging. *Proc. Natl. Acad. Sci. U.S.A.* **2007**, *104*, 9266-9271.
5. Abdukayum, A.; Chen, J.-T.; Zhao, Q.; Yan, X.-P. Functional Near Infrared-Emitting $\text{Cr}^{3+}/\text{Pr}^{3+}$ Co-Doped Zinc Gallogermanate Persistent Luminescent

- Nanoparticles with Superlong Afterglow for In Vivo Targeted Bioimaging. *J. Am. Chem. Soc.* **2013**, *135*, 14125-14133.
6. Paterson, A.S.; Raja, B.; Mandadi, V.; Townsend, B.; Lee, M.; Buell, A.; Vu, B.; Brgoch, J.; Willson, R.C. A Low-Cost Smartphone-Based Platform for Highly Sensitive Point-of-Care Testing with Persistent Luminescent Phosphors. *Lab Chip* **2017**, *17*, 1051-1059.
 7. Paterson, A.S.; Raja, B.; Garvey, G.; Kolhatkar, A.; Hagström, A.E.V.; Kourentzi, K.; Lee, T.R.; Willson, R.C. Persistent Luminescence Strontium Aluminate Nanoparticles as Reporters in Lateral Flow Assays. *Anal. Chem.* **2014**, *86*, 9481-9488.
 8. Van den Eeckhout, K.; Smet, P.F.; Poelman, D. Persistent Luminescence in Eu^{2+} -Doped Compounds: A Review. *Materials* **2010**, *3*, 2536.
 9. Van den Eeckhout, K.; Poelman, D.; Smet, P. Persistent Luminescence in Non- Eu^{2+} -Doped Compounds: A Review. *Materials* **2013**, *6*, 2789.
 10. Smet, P.F.; Botterman, J.; Van den Eeckhout, K.; Korthout, K.; Poelman, D. Persistent Luminescence in Nitride and Oxynitride Phosphors: A Review. *Opt. Mater.* **2014**, *36*, 1913-1919.
 11. Botterman, J.; Joos, J.J.; Smet, P.F. Trapping and Detrapping in $\text{SrAl}_2\text{O}_4:\text{Eu}^{2+},\text{Dy}^{3+}$ Persistent Phosphors: Influence of Excitation Wavelength and Temperature. *Phys. Rev. B* **2014**, *90*, 085147.
 12. Aitasalo, T.; Dereń, P.; Hölsä, J.; Jungner, H.; Krupa, J.C.; Lastusaari, M.; Legendziewicz, J.; Niittykoski, J.; Stręk, W. Persistent Luminescence Phenomena in Materials Doped with Rare Earth Ions. *J. Solid State Chem.*, *171*, 114-122.
 13. Clabau, F.; Rocquefelte, X.; Jobic, S.; Deniard, P.; Whangbo, M.H.; Garcia, A.; Le Mercier, T. Mechanism of Phosphorescence Appropriate for the Long-Lasting Phosphors Eu^{2+} -Doped SrAl_2O_4 with Codopants Dy^{3+} and B^{3+} . *Chem. Mater.* **2005**, *17*, 3904-3912.
 14. Dorenbos, P. Mechanism of Persistent Luminescence in Eu^{2+} and Dy^{3+} Codoped Aluminate and Silicate Compounds. *J. Electrochem. Soc.* **2005**, *152*, H107-H110.
 15. Dorenbos, P. Mechanism of Persistent Luminescence in $\text{Sr}_2\text{MgSi}_2\text{O}_7:\text{Eu}^{2+},\text{Dy}^{3+}$. *Phys. Status Solidi B* **2005**, *242*, 7-9.
 16. Yixi, Z.; Jumpei, U.; Setsuhisa, T. Enhancement of Red Persistent Luminescence in Cr^{3+} -Doped ZnGa_2O_4 Phosphors by Bi_2O_3 Codoping. *Appl. Phys. Express* **2013**, *6*, 052602.
 17. Van den Eeckhout, K.; Smet, P.F.; Poelman, D. Luminescent Afterglow Behavior in the $\text{M}_2\text{Si}_5\text{N}_8$: Eu Family (M = Ca, Sr, Ba). *Materials* **2011**, *4*, 980.
 18. Finley, E.; Mansouri Tehrani, A.; Brgoch, J. Intrinsic Defects Drive Persistent Luminescence in Monoclinic $\text{SrAl}_2\text{O}_4:\text{Eu}^{2+}$. *J. Phys. Chem. C* **2018**, *122*, 16309-16314.
 19. Qu, B.; Zhang, B.; Wang, L.; Zhou, R.; Zeng, X.C. Mechanistic Study of the Persistent Luminescence of $\text{CaAl}_2\text{O}_4:\text{Eu},\text{Nd}$. *Chem. Mater.* **2015**, *27*, 2195-2202.
 20. De Vos, A.; Lejaeghere, K.; Vanpoucke, D.E.P.; Joos, J.J.; Smet, P.F.; Hemelsoet, K. First-Principles Study of Antisite Defect Configurations in $\text{ZnGa}_2\text{O}_4:\text{Cr}$ Persistent Phosphors. *Inorg. Chem.* **2016**, *55*, 2402-2412.
 21. Carlson, S.; Hölsä, J.; Laamanen, T.; Lastusaari, M.; Malkamäki, M.; Niittykoski, J.; Valtonen, R. X-ray Absorption Study of Rare Earth Ions in

- Sr₂MgSi₂O₇:Eu²⁺,R³⁺ Persistent Luminescence Materials. *Opt. Mater.* **2009**, *31*, 1877-1879.
22. Korthout, K.; Van den Eeckhout, K.; Botterman, J.; Nikitenko, S.; Poelman, D.; Smet, P.F. Luminescence and X-ray Absorption Measurements of Persistent SrAl₂O₄:Eu,Dy Powders: Evidence for Valence State Changes. *Phys. Rev. B* **2011**, *84*, 085140.
 23. Hölsä, J.; Aitasalo, T.; Jungner, H.; Lastusaari, M.; Niittykoski, J.; Spano, G. Role of Defect States in Persistent Luminescence Materials. *J. Alloys Compd.* **2004**, *374*, 56-59.
 24. Allix, M.; Chenu, S.; Véron, E.; Poumeyrol, T.; Kouadri-Boudjelthia, E.A.; Alahraché, S.; Porcher, F.; Massiot, D.; Fayon, F. Considerable Improvement of Long-Persistent Luminescence in Germanium and Tin Substituted ZnGa₂O₄. *Chem. Mater.* **2013**, *25*, 1600-1606.
 25. Gourier, D.; Bessière, A.; Sharma, S.K.; Binet, L.; Viana, B.; Basavaraju, N.; Priolkar, K.R. Origin of the Visible Light Induced Persistent Luminescence of Cr³⁺-Doped Zinc Gallate. *J. Phys. Chem. Solids* **2014**, *75*, 826-837.
 26. Bessière, A.; Sharma, S.K.; Basavaraju, N.; Priolkar, K.R.; Binet, L.; Viana, B.; Bos, A.J.J.; Maldiney, T.; Richard, C.; Scherman, D.; Gourier, D. Storage of Visible Light for Long-Lasting Phosphorescence in Chromium-Doped Zinc Gallate. *Chem. Mater.* **2014**, *26*, 1365-1373.
 27. Basavaraju, N.; Priolkar, K.R.; Bessière, A.; Sharma, S.K.; Gourier, D.; Binet, L.; Viana, B.; Emura, S. Controlling disorder in the ZnGa₂O₄:Cr³⁺ persistent phosphor by Mg²⁺ substitution. *Phys. Chem. Chem. Phys.* **2017**, *19*, 1369-1377.
 28. Yixi, Z.; Jumpei, U.; Tanabe, S. Tunable Trap Depth in Zn(Ga_{1-x}Al_x)₂O₄:Cr,Bi Red Persistent Phosphors: Considerations of High Temperature Persistent Luminescence and Photostimulated Persistent Luminescence. *J. Mater. Chem. C* **2013**, *1*, 7849-7855.
 29. Bessière, A.; Jacquart, S.; Priolkar, K.; Lecointre, A.; Viana, B.; Gourier, D. ZnGa₂O₄:Cr³⁺: A New Red Long-Lasting Phosphor with High Brightness. *Opt. Express* **2011**, *19*, 10131-10137.
 30. Basavaraju, N.; Sharma, S.; Bessière, A.; Viana, B.; Gourier, D.; Priolkar, K.R. Red Persistent Luminescence in MgGa₂O₄:Cr³⁺; A New Phosphor for In Vivo Imaging. *J. Phys. D: Appl. Phys.* **2013**, *46*, 375401.
 31. Basavaraju, N.; Priolkar, K.R.; Gourier, D.; Sharma, S.K.; Bessiere, A.; Viana, B. The Importance of Inversion Disorder in the Visible Light Induced Persistent Luminescence in Cr³⁺ Doped AB₂O₄ (A = Zn or Mg and B = Ga or Al). *Phys. Chem. Chem. Phys.* **2015**, *17*, 1790-1799.
 32. Basavaraju, N.; Priolkar, K.R.; Gourier, D.; Bessiere, A.; Viana, B. Order and Disorder Around Cr³⁺ in Chromium Doped Persistent Luminescent AB₂O₄ Spinels. *Phys. Chem. Chem. Phys.* **2015**, *17*, 10993-10999.
 33. Finley, E.; Brgoch, J. Deciphering the Loss of Persistent Red Luminescence in ZnGa₂O₄:Cr³⁺ Upon Al³⁺ Substitution. *J. Mater. Chem. C* **2019**, *7*, 2005-2013.
 34. Macfarlane, R.M. Analysis of the Spectrum of d₃ Ions in Trigonal Crystal Fields. *J. Chem. Phys.* **1963**, *39*, 3118-3126.
 35. Kahan, H.M.; Macfarlane, R.M. Optical and Microwave Spectra of Cr³⁺ in the Spinel ZnGa₂O₄. *J. Chem. Phys.* **1971**, *54*, 5197-5205.
 36. Macfarlane, R.M. On the Ground-State Splitting in Ruby. *J. Chem. Phys.* **1965**, *42*, 442-442.

37. Hornstra, J.K., E. The Oxygen Parameter of the Spinel ZnGa₂O₄. *Philips Res. Rep.* **1972**, *27*, 76-81.
38. Hafner, J. Ab-initio Simulations of Materials Using VASP: Density-Functional Theory and Beyond. *J. Comput. Chem.* **2008**, *29*, 2044-2078.
39. Kresse, G.; Joubert, D. From Ultrasoft Pseudopotentials to the Projector Augmented-Wave Method. *Phys. Rev. B* **1999**, *59*, 1758.
40. Kresse, G.; Furthmüller, J. Efficient Iterative Schemes for Ab Initio Total-Energy Calculations Using a Plane-Wave Basis Set. *Phys. Rev. B* **1996**, *54*, 11169.
41. Perdew, J.P.; Burke, K.; Ernzerhof, M. Generalized Gradient Approximation Made Simple. *Phys. Rev. Lett.* **1996**, *77*, 3865-3868.
42. Momma, K.; Izumi, F. VESTA 3 for Three-Dimensional Visualization of Crystal, Volumetric and Morphology Data. *J. Appl. Crystallogr.* **2011**, *44*, 1272-1276.
43. Segre, C.U.; Leyarovska, N.E.; Chapman, L.D.; Lavender, W.M.; Plag, P.W.; King, A.S.; Kropf, A.J.; Bunker, B.A.; Kemner, K.M.; Dutta, P.; Duran, R.S.; Kaduk, J. The MRCAT Insertion Device Beamline at the Advanced Photon Source. *AIP Conf. Proc.* **2000**, *521*, 419-422.
44. Kropf, A.J.; Katsoudas, J.; Chattopadhyay, S.; Shibata, T.; Lang, E.A.; Zyryanov, V.N.; Ravel, B.; Mclvor, K.; Kemner, K.M.; Scheckel, K.G.; Bare, S.R.; Terry, J.; Kelly, S.D.; Bunker, B.A.; Segre, C.U. The New MRCAT (Sector 10) Bending Magnet Beamline at the Advanced Photon Source. *AIP Conf. Proc.* **2010**, *1234*, 299-302.
45. Ravel, B.; Newville, M. ATHENA, ARTEMIS, HEPHAESTUS: Data Analysis for X-ray Absorption Spectroscopy Using IFEFFIT. *J. Synchrotron Radiat.* **2005**, *12*, 537-541.
46. Calvin, S. *EXAFS for Everyone*; CRC Press: Boca Raton, FL, 2013.
47. Calvin, S.; Carpenter, E.E.; Ravel, B.; Harris, V.G.; Morrison, S.A. Multiedge Refinement of Extended X-ray-Absorption Fine Structure of Manganese Zinc Ferrite Nanoparticles. *Phys. Rev. B* **2002**, *66*, 224405.
48. The Materials Research Collaborative Access Team. <http://mrcat.iit.edu/> (accessed 2018).
49. Kaneko, M.; Matsuno, S.; Miki, T.; Nakayama, M.; Ikuta, H.; Uchimoto, Y.; Wakihara, M.; Kawamura, K. Local Structural Studies of LiCr_yMn_{2-y}O₄ Cathode Materials for Li-Ion Batteries. *J. Phys. Chem. B* **2003**, *107*, 1727-1733.
50. Grunes, L.A. Study of the K Edges of 3d Transition Metals in Pure and Oxide Form by X-ray-Absorption Spectroscopy. *Phys. Rev. B* **1983**, *27*, 2111-2131.
51. Zhang, W.; Zhang, J.; Chen, Z.; Wang, T.; Zheng, S. Spectrum Designation and Effect of Al Substitution on the Luminescence of Cr³⁺ Doped ZnGa₂O₄ Nanosized Phosphors. *J. Lumin.* **2010**, *130*, 1738-1743.
52. Dixit, H.T., N., Cottenier, S., Saniz, R., Lamoen, D., Partoens, B., Van Speybroek, B., Waroquier, M. Electronic Structure and Band Gap of Zinc Spinel Oxides Beyond LDA: ZnAl₂O₄, ZnGa₂O₄ and ZnIn₂O₄. *New J. Phys.* **2011**, *13*, 2-10.
53. Harris, V.G.; Koon, N.C.; Williams, C.M.; Zhang, Q.; Abe, M.; Kirkland, J.P.; McKeown, D.A. Direct Measurement of Octahedral and Tetrahedral Site Environments in NiZn-Ferrites. *IEEE Trans. Magn.* **1995**, *31*, 3473-3475.
54. Chinnasamy, C.N.; Narayanasamy, A.; Ponpandian, N.; Chattopadhyay, K.; Shinoda, K.; Jeyadevan, B.; Tohji, K.; Nakatsuka, K.; Furubayashi, T.; Nakatani, I. Mixed Spinel Structure in Nanocrystalline NiFe₂O₄. *Phys. Rev. B* **2001**, *63*, 184108.

55. Wei, C.; Feng, Z.; Scherer, G.G.; Barber, J.; Shao-Horn, Y.; Xu, Z.J. Cations in Octahedral Sites: A Descriptor for Oxygen Electrocatalysis on Transition-Metal Spinels. *Adv. Mater.* **2017**, *29*, 1606800.
56. Shannon, R.D. Revised Effective Ionic Radii and Systematic Studies of Interatomic Distances in Halides and Chalcogenides. *Acta Cryst. A* **1976**, *32*, 751-767.
57. Okhotnikov, K.; Charpentier, T.; Cadars, S. Supercell Program: A Combinatorial Structure-Generation Approach for the Local-Level Modeling of Atomic Substitutions and Partial Occupancies in Crystals. *J. Cheminf.* **2016**, *8*, 1-15.

CHAPTER 6

Intrinsic Defects Drive Persistent Luminescence in Monoclinic $\text{SrAl}_2\text{O}_4:\text{Eu}^{2+}$

Reproduced with permission from *Journal of Physical Chemistry C*
(*J. Phys. Chem. C* **2018**, 122, 16309-16314.)
©2018 American Chemical Society
DOI: 10.1021/acs.jpcc.8b04378

Erin Finley, Aria Mansouri Tehrani, Jakoah Brgoch*
Department of Chemistry, University of Houston, Houston, TX 77204

6.1 Introduction

The signature long luminescent lifetimes of persistent luminescent phosphors (PLPs) are critical for an array of applications spanning chemistry, engineering, and even design. They have found use in deep tissue *in vivo* imaging,¹ point-of-care diagnostics,^{2,3} luminous paint,² emergency signage,⁴ and novelty items such as watch dial faces and children's toys. PLPs produce a range of colors from orange emitting $\text{Ca}_2\text{Si}_5\text{N}_8:\text{Eu}^{2+}, \text{Tm}^{3+}$ to blue emitting $\text{CaAl}_2\text{O}_4:\text{Eu}^{2+}, \text{Nd}^{3+}$ and $\text{Sr}_2\text{MgSi}_2\text{O}_7:\text{Eu}^{2+}, \text{Dy}^{3+}$.⁵ Among them, however, $\text{SrAl}_2\text{O}_4:\text{Eu}^{2+}, \text{Dy}^{3+}$ is the most widely used due to its impressive long luminescent lifetime of ≈ 70 min⁶ when substituted with Eu^{2+} , while the addition of the co-dopant Dy^{3+} pushes the lifetime reportedly to 30 hours.⁷

The origin of the long luminescent lifetimes in PLPs is the subject of extensive research focusing specifically on the mechanism that produces this optical phenomenon, often in an effort to find pathways that further extend their lifetimes.^{5,8} It is widely accepted that the persistent luminescent mechanism involves the excitation of an electron from its ground state to an excited state, which is further photoionized into the conduction band through continued excitation.⁸ This excited state electron is subsequently "trapped" by a defect in the crystal structure that is alleged to arise due to vacancies or the presence of

d-orbitals from a rare-earth co-dopant such as Dy³⁺. The trapped electrons are then slowly released by applying energy to the system, typically thermal energy, leading to photoemission and the observed long luminescent lifetimes.^{9,10}

Investigations into the source of these traps have largely focused on the presence of *d*-orbitals from the trivalent rare-earth co-dopant based on experimental studies^{8,11} or *ab initio* calculations.¹² However, as noted, SrAl₂O₄:Eu²⁺ surprisingly exhibits a long luminescent lifetime even in the absence of Dy³⁺,⁶ as do other well-known PLPs including Sr₂MgSi₂O₇:Eu²⁺.¹³ This suggests that the observation of persistent luminescence is independent of the co-dopant's *d*-orbitals, and that Eu²⁺ alone is sufficient to generate the long emission lifetime.^{13,14} Considering the persistent luminescence mechanism is undoubtedly related to the presence of trap states, alternative defects unrelated to the rare-earth co-dopant must be present in these crystal structures to produce the observed optical properties. This hypothesis is supported in particular by the recent implementation of an empirical fitting method to show that defects are likely to form in monoclinic SrAl₂O₄ even in the absence of a rare-earth luminescent center, like Eu²⁺,¹⁵ and is also supported by electron paramagnetic resonance data.^{16,17} Based on these reports, it is reasonable to conclude the formation of defects are intrinsic in PLP materials like SrAl₂O₄. However, to better understand the relationship between persistent luminescence and point defects, it is imperative to computationally study the formation energy and trap depth of vacancies in SrAl₂O₄ and SrAl₂O₄:Eu²⁺.

6.2 Computational Details

Full structure optimizations and total energy calculations employed the Vienna *ab initio* simulation package (VASP) within the DFT framework.¹⁸ The plane wave basis set and projector augmented wave (PAW) potentials were used to define the electronic wave functions.¹⁹ A supercell with dimensions of 2 x 1 x 1 (56 atoms) was first optimized using the Perdew-Burke-Ernzerhof (PBE) exchange and correlation functional.²⁰ A larger 2 x 2 x 1 (112 atoms) supercell was also tested and found there to be less than a 3% formation energy difference, indicating the supercell size effect was negligible. Therefore, the 2 x 1 x 1 was selected as a compromise between computational cost and accuracy. Further, PBE+U method was used for the description of highly correlated Eu 4*f* electrons in SrAl₂O₄:Eu²⁺, with $U = 7.62$ and $J = 0.68$.¹² Full structural optimizations were performed with the electronic convergence criteria set to 1×10^{-8} eV while the ionic relaxation was set to 1×10^{-2} eV/Å. A cutoff energy of 500 eV was used and the integration of the first Brillouin zone was carried out using a Monkhorst-Pack *k*-point grid of 2 x 2 x 2.

The resulting optimized crystal structure of the monoclinic SrAl₂O₄, shown in Figure 6.1a, contains two crystallographically independent cation ion sites that sit in the middle of a three-dimensional network of [AlO₄] tetrahedra formed by eight crystallographically independent oxygen atoms.⁷ The HSE06 functional was then implemented to correct for the significant underestimation of the PBE band gap ($E_g = 4.21$ eV) compared to the experimental value ($E_g = 6.5$ eV).¹² A reasonable calculated band gap value of 6.02 eV (Figure 6.1b) is achieved by implementing the 75%:25% mixture of PBE:Hartree-Fock and is maintained upon the substitution of Eu²⁺ into the system (Figure 6.1c).²¹

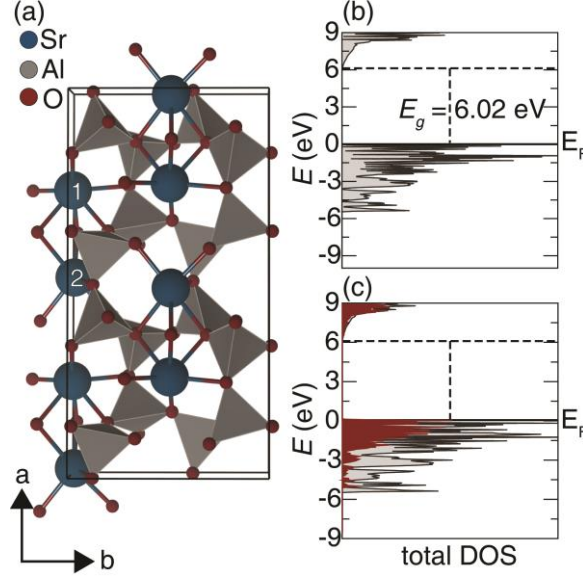


Figure 6.1. (a) Optimized $2 \times 1 \times 1$ supercell showing the two independent crystallographic sites for Sr^{2+} (blue) and the $[\text{AlO}_4]$ tetrahedra highlighted in gray. (b) Total density of states (DOS) without Eu^{2+} and (c) total DOS with Eu^{2+} f -orbitals outlined in red, as determined by HSE06 with a calculated $E_g = 6.02$ eV.

A defect crystal structure was then created by manually removing one atom at a time from each of the eight crystallographically independent oxygen sites or the two strontium sites, and then re-optimizing the vacancy containing crystal structure. The formation energies, $\Delta E(\alpha, q)$, of the cation and anion ($\alpha = \text{Sr}$ or O) defects at charge q can be calculated using the general equation (Eq. 6.1):

$$\Delta E_{vac}(\alpha, q) = E_{V_{\alpha, q}} - E_{perfect} + \mu_{\alpha} + q[E_{VBM(perfect)} \pm \Delta V + E_F] \quad (6.1)$$

Here, $E_{perfect}$ is the total energy of the defect-free supercell, $E_{V_{\alpha, q}}$ is the total energy of defect-containing supercell at a given charge state, $E_{VBM(perfect)}$ is the valence band maximum of the perfect structure, and ΔV is used to align the VBM of the charged defect structure to the perfect structure.¹² The band alignment is accomplished by taking the energy difference between the 1s core-electron of the Sr atom that is furthest from the defect site in the neutral system and the 1s core-electron of the Sr atom that is furthest

from the defect site in the charged system.²² The terms μ_α and E_F are defined as the chemical potential of atom α and the Fermi energy with reference to VBM (chemical potential of electron) respectively. These chemical potentials are determined by assuming an equilibrium between the crystal structure and a reservoir where atoms and electrons can be freely exchanged. The Fermi level is a variable bound to the values within the band gap. Moreover, since the determination of chemical potential is not trivial and depends on the experimental condition, it is also treated as a variable in these defect calculations.

One way to treat the chemical potential is to determine its minimum and maximum values based on extreme experimental conditions and thermodynamic stability considerations. Here, μ_α is bound to avoid the formation of the binary oxides (Al_2O_3 and SrO) or decomposition into the elements, Al ($Fd\bar{3}m$), Sr ($Fd\bar{3}m$), and $\text{O}_{2(g)}$, thus, the boundary conditions are defined using Equations 6.2a, 6.2b, 6.2c.

$$\Delta H_{(\text{SrAl}_2\text{O}_4)} = \mu_{\text{Sr}} + 2\mu_{\text{Al}} + 4\mu_{\text{O}} = -22.24 \text{ eV} \quad (6.2a)$$

$$\mu_{\text{Sr}} + \mu_{\text{O}} \leq \Delta H_{(\text{SrO})} = -5.18 \text{ eV} \quad (6.2b)$$

$$2\mu_{\text{Al}} + 3\mu_{\text{O}} \leq \Delta H_{(\text{Al}_2\text{O}_3)} = -16.03 \text{ eV} \quad (6.2c)$$

Therefore, the vacancy formations energies are determined based on chemical potentials derived considering oxygen-rich (strontium-poor) atmosphere, $\mu_{\text{O}} = 0$ and an oxygen-poor (strontium-rich), $\mu_{\text{Sr}} = 0$. The thermodynamic phase stability regions of Sr, Al, and O are shown in Figure 6.2 with the green region highlighting the stability boundary of SrAl_2O_4 . The two black dots (Figure 6.2) represent the oxygen-rich and oxygen-poor conditions where $\mu_{\text{O-rich}} = -6.98 \text{ eV}$ and $\mu_{\text{O-poor}} = -12.72 \text{ eV}$ respectfully.

Similarly, the strontium-poor regime is calculated to be, $\mu_{Sr-poor} = -7.79$ eV and strontium-rich regime is, $\mu_{Sr-rich} = -2.05$ eV.

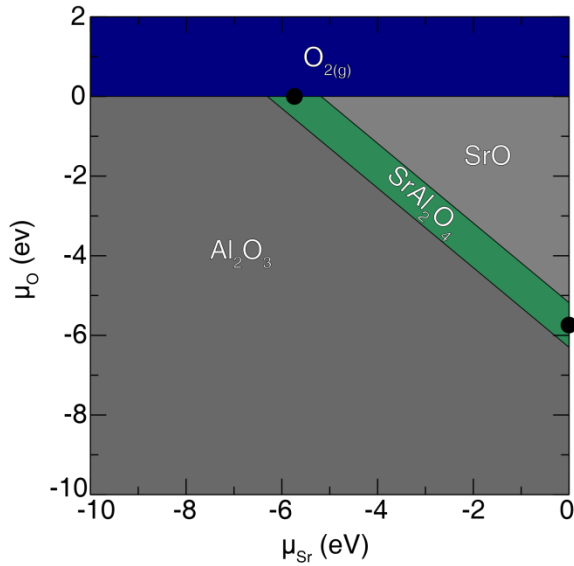


Figure 6.2. Chemical stability regime of Sr-O-Al phase space. The chemical potential ($\mu_{O_{2(g)}}$) is set to zero. Stability regime of $SrAl_2O_4$ is highlighted in green with the oxygen rich and poor limits indicated by black dots.

6.3 Results and Discussion

The role of defects in $SrAl_2O_4:Eu^{2+}$ that lead to persistent luminescence is not well understood. Experimental observations from thermoluminescence and electron paramagnetic resonance data support the presence of either cation or anion vacancies.^{16,17,23} However, the extent to which they contribute to the mechanism which leads to the notable long lifetimes in $SrAl_2O_4:Eu^{2+}$ can be investigated using computational methods by investigating the energetics of these potential atomic vacancies. Moreover, to further understand the formation of these vacancies considering strontium aluminate in the presence and absence of Eu^{2+} is necessary. Due to the computational cost, an initial screening of the most energetically favorable neutral defect ($q = 0$) in strontium aluminate was first conducted using the PBE functional for $SrAl_2O_4$

and $\text{SrAl}_2\text{O}_4:\text{Eu}^{2+}$ using PBE+U (Table 6.1) based on the chemical potential models in Figure 6.2. The vacancy formation energies are determined using Eq. 6.1.

Table 6.1. Formation energies, ΔE_{vac} (eV) of potential vacancy sites in SrAl_2O_4 and $\text{SrAl}_2\text{O}_4:\text{Eu}^{2+}$ as determined by α -rich ($\alpha = \text{Sr}$ or O for the respective vacancy) conditions by PBE and PBE+U

Vacancy	SrAl_2O_4	$\text{SrAl}_2\text{O}_4:\text{Eu}^{2+}$
Sr(1)	9.603	8.111
Sr(2)	9.520	8.084
O(1)	6.024	6.029
O(2)	6.006	6.007
O(3)	6.023	6.024
O(4)	6.034	6.033
O(5)	6.097	6.098
O(6)	6.096	6.096
O(7)	6.123	6.136
O(8)	6.094	6.095

It is clear based on the PBE vacancy formation energies that the strontium vacancies (V_{Sr}) produce a larger ΔE_{vac} than any of the oxygen vacancies (V_{O}), with $V_{\text{Sr}(1)}$ being larger than $V_{\text{Sr}(2)}$. Looking closer, the oxygen vacancies show that the formation energies are separated into two groups, with vacancies $V_{\text{O}(1)}$ through $V_{\text{O}(4)}$ forming at lower energies than $V_{\text{O}(5)}$ through $V_{\text{O}(8)}$ regardless of Eu^{2+} substitution. As a result of the discernable energy differences, all further hybrid calculations (HSE06) and analysis are focused specifically on the $V_{\text{Sr}(1)}$ and $V_{\text{Sr}(2)}$ vacancies as well as the $V_{\text{O}(1)}$ through $V_{\text{O}(4)}$ vacancies.

Initially, the vacancy formation energies of the host in the absence of Eu^{2+} are considered in order to identify the most favorable vacancy sites. The vacancy formation energies of $V_{\text{Sr}(1)}$, $V_{\text{Sr}(2)}$, $V_{\text{O}(1)}$, $V_{\text{O}(2)}$, $V_{\text{O}(3)}$, and $V_{\text{O}(4)}$ in SrAl_2O_4 are determined at the oxygen-poor and oxygen-rich conditions using the HSE06 functional are shown in Table 6.2. The vacancy formation energy for V_{Sr} is the most favorable under an oxygen-rich regime compared to the formation of V_{O} . Conversely, in an oxygen-poor regime the

formation energy of V_O decreases considerably compared to the V_{Sr} . Considering the common synthesis method of the rare-earth substituted PLPs employs high-temperature solid state synthesis including a reducing atmosphere,²⁴ usually 5% $H_2/95\% N_2$, to reduce the oxidation state of the Eu_2O_3 starting materials from Eu^{3+} to Eu^{2+} , this implies that anion vacancies and not cation vacancies are the favorable defect in any persistent luminescent phosphor that is prepared.

Table 6.2. Formation energies of potential vacancy sites in $SrAl_2O_4$ as determined by HSE06 at the μ_α limits.

Vacancy	ΔE_{vac} (eV) O-rich/Sr-poor	ΔE_{vac} (eV) O-poor/Sr-rich
$V_{Sr(1)}$	4.45	10.02
$V_{Sr(2)}$	4.57	10.03
$V_{O(1)}$	6.34	0.60
$V_{O(2)}$	6.33	0.58
$V_{O(3)}$	6.31	0.56
$V_{O(4)}$	6.27	0.53

Given that anion defects are expected in strontium aluminate prepared under reducing conditions, identifying the energetic position of these defect levels will provide insight into the nature of the trap states. To determine these energetic positions, Equation 6.3 is employed to determine the Fermi level where the transition between different charge states (q) occur at equilibrium, and are called the thermodynamic transition levels ($\epsilon(q/q')$; $q = 0$ or ± 1 and $q' = \pm 1$ or ± 2).

$$\epsilon(q/q') = [\Delta E_{vac}(\alpha, q) - \Delta E_{vac}(\alpha, q') + (q - q')(E_{VBM} + \Delta V)] / (q' - q) \quad (5.3)$$

The resulting positions for the different calculated transition levels are illustrated in Figure 6.3.¹⁵ Often, these transition levels are defined by their proximity to the CBM or the VBM such that a deep $\epsilon(q/q')$ lies in the middle of the E_g whereas a shallow $\epsilon(q/q')$ lies either near the CBM or the VBM.^{22,25,26} In the case of persistent luminescence, the

position of the thermodynamic transition levels that can act as “trap states” and contribute to the long lifetimes must lie between 0.4 eV and 1 eV below the CBM.^{25,27} The position is critical because if a trap state is too shallow (<0.4 eV from the CBM) the electron in this trap can be readily depopulated at room temperature preventing persistent luminescence. Conversely, a trap that is too deep (>1 eV from the CBM) will not allow the electron to be released with the thermal energy available at room temperature.²⁸ An ideal trap has been established to occur ≈ 0.65 eV below the conduction band edge because it is deep enough to trap an electron effectively but not too deep to prevent slow release at room temperature.^{5,29} Thus, the calculated $\epsilon(q/q')$ is expected to be at or around 0.65 eV based on the experimental observation of persistent luminescence in $\text{SrAl}_2\text{O}_4:\text{Eu}^{2+}$.²³

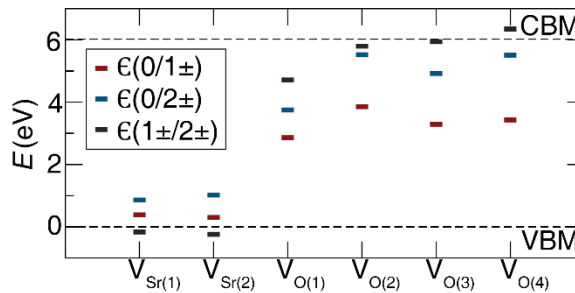


Figure 6.3. Thermodynamic transition levels, $\epsilon(q/q')$, of energetically favorable vacancies. The strontium vacancies (V_{Sr}) form at $E_{\text{F}} < 1$ eV and oxygen (V_{O}) from at $E_{\text{F}} > 2$ eV.

Looking at the $V_{\text{Sr}(1)}$ and $V_{\text{Sr}(2)}$ in Figure 6.3, it is clear these trap states are close to the VBM and cannot act as electron trap states, but rather act as potential electron hole traps. Although these hole traps are in an energy window (<1 eV from the valence band) that could contribute to persistent luminescence, there is little evidence to support the role of hole traps in SrAl_2O_4 .^{10,15,30} Instead, the calculated position of the anion

vacancies, specifically the $E(0/2+)$ thermodynamic transition levels for the $V_{O(2)}$ and $V_{O(4)}$ defects, each fall ≈ 0.50 eV below the CBM. These are in a nearly ideal position to act as an electron traps leading to persistent luminescence. All other $E(q/q')$ values indicate they are either too deep or too shallow to participate in the accepted persistent luminescence mechanism. These results are in excellent agreement with a computational examination of the $\text{CaAl}_2\text{O}_4:\text{Eu}^{2+},\text{Nd}^{3+}$ persistent luminescence mechanism that revealed that the cation vacancy was also positioned just above the VBM whereas the anion vacancy was closer to the CBM.⁹

These thermodynamic transition level calculations provide information on the energetic position of the trap states; however, this does not consider the chemical potential, which can indicate favorability of formation of a specific vacancy charge state, e.g., neutral or 2+, based on the synthesis conditions. The calculated formation energies of the different charge states were accordingly calculated as a function of Fermi level at the oxygen-poor limit to mimic the most probable experimental conditions for rare-earth substituted persistent phosphors. As plotted in Figure 6.4, the most energetically favorable vacancy charge state is either a 2+ charged vacancy (V_{O}^{2+}) (solid blue line) or a neutral vacancy (V_{O}^0) (solid gray line) for all four types of anion defects. The 1+ charge states (dashed red line) are never energetically favorable. Examining the energy window close to the valence band shows that all of the oxygen vacancies should have a 2+ charge, whereas the vacancies near the conduction band are likely to be neutral ($q = 0$) vacancies. Noting, the negative formation energies determined close to the valence band, for 1+ and 2+ vacancies, are an indication that the vacancies are either not favorable or the extreme oxygen-poor limit used here for chemical potential is not feasible experimentally

as it leads to spontaneous formation of vacancies or destabilizing the formation of strontium aluminate.³¹

Since these vacancies must be charged to accept electrons and act as a trap state, it is necessary for the positively charged vacancy to be the most favorable between ≈ 0.4 eV and 1.0 eV below the CBM. Based on these requirements, $V_{O(2)}^{2+}$ (Figure 6.4b) and $V_{O(4)}^{2+}$ (Figure 6.4d) meet the criteria with formation energies of ≈ 5.5 eV (or ≈ 0.5 eV below the CBM) for the 2+ charged vacancies. Additionally, $V_{O(3)}^{2+}$ is ≈ 5.0 eV (≈ 1.0 eV below the CBM) indicating it too is likely to form at a favorable energy for trapping electrons. The $V_{O(1)}^{2+}$ is energetically favorable until ≈ 4.0 eV (≈ 2.0 eV from the CBM) making it too deep to act as trap states in the assumed persistent luminescence mechanism. Thus, it is reasonable to surmise that in unsubstituted SrAl_2O_4 , anion vacancies will form under reducing conditions at energetically favorable depths that would allow them to act as trap states.

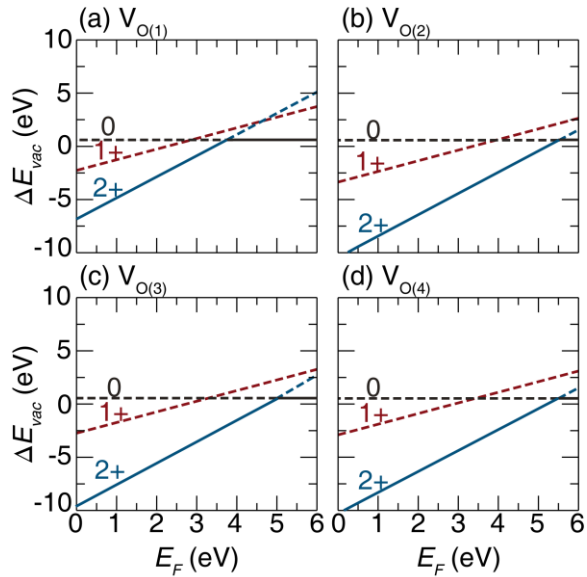


Figure 6.4. Formation energies of (a) $V_{O(1)}$, (b) $V_{O(2)}$, (c) $V_{O(3)}$, and (d) $V_{O(4)}$ in $SrAl_2O_4$ charged point defects at the oxygen-poor bounds. The solid lines show point charge that is favorable at a given E_F within E_g . Dashed lines show unfavorable point charge.

In light of the favorable $\epsilon(0/2+)$ of $V_{O(2)}^{2+}$ and $V_{O(4)}^{2+}$ in unsubstituted $SrAl_2O_4$, the effect of Eu^{2+} substitution on the Sr^{2+} site of $SrAl_2O_4$ was also examined. Because the signature blue-green emission of $SrAl_2O_4:Eu^{2+}$ visible at room temperature is known to stem only from Eu^{2+} occupying the $Sr(1)^{2+}$ site, this is the only substitution site that was considered.⁸ Thus, the influence of the rare-earth in the crystal structure on the formation energy and $\epsilon(q/q')$ of the four V_O was also studied using the HSE06 functional on the optimized crystal structures. The formation energies of the four anion vacancy sites ($V_{O(1)}$, $V_{O(2)}$, $V_{O(3)}$, and $V_{O(4)}$) upon addition of Eu^{2+} are nearly identical to the unsubstituted system (Table 6.3).

Table 6.3. Formation energies of (a) $V_{O(1)}$, (b) $V_{O(2)}$, (c) $V_{O(3)}$, and (d) $V_{O(4)}$ in $SrAl_2O_4$ charged point defects at the oxygen-poor bounds. The solid lines show point charge that is favorable at a given E_F within E_g . Dashed lines show unfavorable point charge.

Vacancy	ΔE_{vac} (eV)
O(1)	0.60
O(2)	0.58
O(3)	0.57
O(4)	0.53

However, the effect on the $\epsilon(q/q')$ (Figure 6.5) exhibits changes to the location of the trap states for three of the vacancies; $V_{O(1)}$, $V_{O(3)}$, and $V_{O(4)}$. Nevertheless, $V_{O(2)}$ has a thermodynamic transition level, $\epsilon(0/2+)$, of 0.52 eV, which is approximately the same as the unsubstituted example, suggesting this defect will form at an applicable trap depth regardless of the presence of Eu^{2+} . More notably, $V_{O(1)}$ creates a $\epsilon(0/2+)$ trap at nearly the ideal trap depth of 0.67 eV upon addition of Eu^{2+} . Remarkably, the formation of these two traps are experimentally supported by thermoluminescence measurements, which show traps at 0.55 eV, 0.60 eV, and 0.65 eV in $SrAl_2O_4:Eu^{2+}$.³⁰

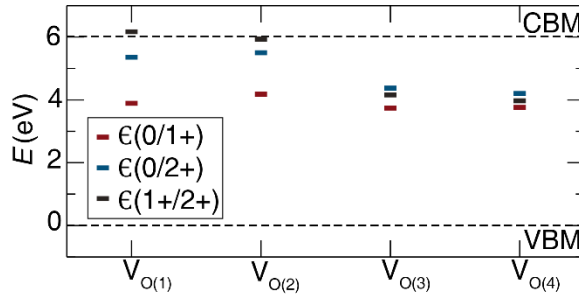


Figure 6.5. The thermodynamic transition levels, $\epsilon(q/q')$, for each vacancy does increase, placing $\epsilon(0/2+)$ in an ideal location to be a trap state participating in Persistent luminescence.

As with the unsubstituted system, the formation energy for each charge state must be considered as a function of Fermi level at the oxygen-poor limit. In each of the four vacancies a 1+ charged vacancy (red dashed line) is never favorable, while the V_O^{2+}

(blue line) is favorable close to the VBM and a V_O^0 (gray line) charge is favorable close to the CBM. These results are consistent with the observed formation energies in Figure 6.4 of the unsubstituted system.

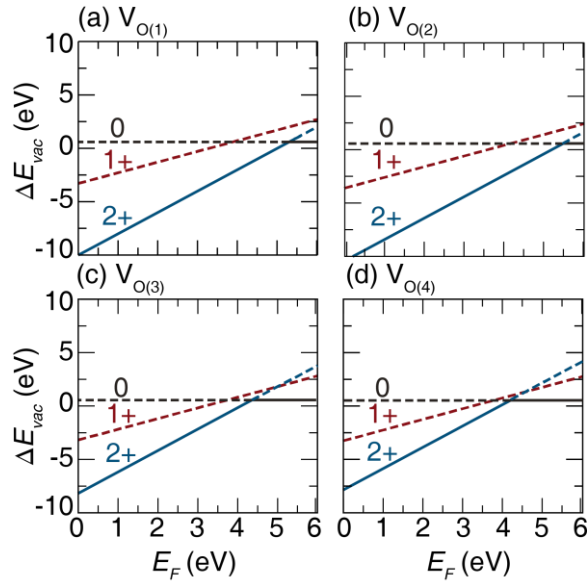


Figure 6.6. Formation energies of (a) $V_{O(1)}$, (b) $V_{O(2)}$, (c) $V_{O(3)}$, and (d) $V_{O(4)}$ in $SrAl_2O_4:Eu^{2+}$ charged point defects at the oxygen-poor bounds. The solid lines show point charge that is favorable at a given E_F within E_g . Dashed lines show unfavorable point charge.

However, the vacancy sites with charged vacancies in the “trap state energy window” of >0.4 eV to <1.0 eV changes from the unsubstituted system. Upon addition of Eu^{2+} , $V_{O(4)}^{2+}$ (Figure 6.6d) is favorable until ≈ 4.0 eV (2.0 eV from the CBM) which is too deep to be a viable vacancy for thermal release at room temperature. The same observation can be made for $V_{O(3)}^{2+}$ (Figure 6.6c) which changes to $V_{O(3)}^0$ at ≈ 4.5 eV (1.5 eV from the CBM). Examining $V_{O(1)}^{2+}$ (Figure 6.6a) and $V_{O(2)}^{2+}$ (Figure 6.6b) this charged state is favorable until ≈ 5.5 eV (0.5 eV from the CBM) suggesting either of these two charge vacancies are suitable for trapping electrons that can be thermally released at room temperature. Due to these favorable formation energy of a 2+ for $V_{O(2)}$ it can be concluded this vacancy is likely to form in the absence of Eu^{2+} and remains in a favorable energy window upon the

addition of the rare-earth ion. Additionally, a vacancy, in this case $V_{O(1)}$, is influenced by the addition of Eu^{2+} to become favorable to trapping electrons that will lead to the observable long lifetimes in $\text{SrAl}_2\text{O}_4:\text{Eu}^{2+}$.

6.4 Conclusion

In summary, first principle calculations were conducted on monoclinic SrAl_2O_4 and $\text{SrAl}_2\text{O}_4:\text{Eu}^{2+}$ to explore the presence of point defects due to cation and anion vacancies and their potential relationship to persistent luminescence. The calculations show the thermodynamic transition level, $\epsilon(0/2+)$, for the $V_{O(2)}$ and $V_{O(4)}$ are at a nearly ideal trap depth of ≈ 0.50 eV below the CBM, while all other V_{O} and V_{Sr} are either too shallow or too deep to be efficient for persistent luminescence in unsubstituted SrAl_2O_4 . Furthermore, analysis of charged vacancies at the oxygen-poor limit indicate that V_{O}^{2+} is more energetically favorable until ≈ 5.5 eV for both $V_{O(2)}$ and $V_{O(4)}$. Substituting Eu^{2+} in the crystal structure shows that the position of $V_{O(2)}$ remains constant while $V_{O(1)}$ moves to only 0.67 eV below the CBM when in an oxygen-poor environment. Thus, the addition of Eu^{2+} shifts the location of trap depths into an energy window where they can contribute to producing long luminescent lifetimes. Combining the results of the calculations on SrAl_2O_4 and $\text{SrAl}_2\text{O}_4:\text{Eu}^{2+}$ establish that anion vacancies are present in both compositions, indicating these defects are favorable and likely intrinsic in the crystal structure. Moreover, when Eu^{2+} is present in the crystal structure the trap depths shift to favorable energetic positions that are responsible for strontium aluminates exceptional luminescent lifetime.

6.5 Acknowledgements

The authors would like to thank the University of Houston, Department of Chemistry and the Division of Research for the generous startup funds and the Grants to Enhance and Advance Research (GEAR) at the University of Houston. This work was conducted by the resources provided by the Maxwell and Opuntia Clusters at the University of Houston and the Center for Advanced Computing and Data Systems and the uHPC cluster at the University of Houston provided by NSF Award Number 15-31814. We also thank Kush Patel for his valuable contribution in the chemical potential analysis.

6.6 References

1. Maldiney, T.; Richard, C.; Seguin, J.; Wattier, N.; Bessodes, M.; Scherman, D. Effect of Core Diameter, Surface Coating, and PEG Chain Length on the Biodistribution of Persistent Luminescence Nanoparticles in Mice. *ACS Nano* **2011**, *5*, 854-862.
2. Paterson, A. S.; Raja, B.; Garvey, G.; Kolhatkar, A.; Hagström, A. E. V.; Kourentzi, K.; Lee, T. R.; Willson, R. C. Persistent Luminescence Strontium Aluminate Nanoparticles as Reporters in Lateral Flow Assays. *Anal. Chem.* **2014**, *86*, 9481-9488.
3. Paterson, A. S.; Raja, B.; Mandadi, V.; Townsend, B.; Lee, M.; Buell, A.; Vu, B.; Brgoch, J.; Willson, R. C. A Low-Cost Smartphone-Based Platform for Highly Sensitive Point-of-Care Testing with Persistent Luminescent Phosphors. *Lab Chip* **2017**, *17*, 1051-1059.
4. Yen, W. M.; Shinonoya, S.; Yamamoto, H. *Phosphor Handbook*; CRC Press: Boca Raton, FL, 2007.
5. Van den Eeckhout, K.; Smet, P. F.; Poelman, D. Persistent Luminescence in Eu^{2+} -Doped Compounds: A Review. *Materials* **2010**, *3*, 2536.
6. Katsumata, T.; Nabaie, T.; Sasajima, K.; Komuro, S.; Morikawa, T. Effects of Composition on the Long Phosphorescent $\text{SrAl}_2\text{O}_4:\text{Eu}^{2+}, \text{Dy}^{3+}$ Phosphor Crystals. *J. Electrochem. Soc.* **1997**, *144*, L243-L245.
7. Finley, E.; Paterson, A. S.; Cobb, A.; Willson, R. C.; Brgoch, J. Reducing Particle Size of Persistent Luminescent $\text{SrAl}_2\text{O}_4:\text{Eu}^{2+}, \text{Dy}^{3+}$ via Microwave-Assisted, Reverse Micelle Synthesis. *Opt. Mat. Express* **2017**, *7*, 2597-2616.
8. Botterman, J.; Joos, J. J.; Smet, P. F. Trapping and Detrapping in $\text{SrAl}_2\text{O}_4:\text{Eu}^{2+}, \text{Dy}^{3+}$ Persistent Phosphors: Influence of Excitation Wavelength and Temperature. *Phys. Rev. B* **2014**, *90*, 085147.
9. Clabau, F.; Rocquefelte, X.; Jolic, S.; Deniard, P.; Whangbo, M. H.; Garcia, A.; Le Mercier, T. Mechanism of Phosphorescence Appropriate for the Long-Lasting Phosphors Eu^{2+} -Doped SrAl_2O_4 with Codopants Dy^{3+} and B^{3+} . *Chem. Mater.* **2005**, *17*, 3904-3912.

10. Dorenbos, P. Mechanism of Persistent Luminescence in Eu^{2+} and Dy^{3+} Codoped Aluminate and Silicate Compounds. *J. Electrochem. Soc.* **2005**, *152*, H107-H110.
11. Maldiney, T.; Lecointre, A.; Viana, B.; Bessière, A.; Bessodes, M.; Gourier, D.; Richard, C.; Scherman, D. Controlling Electron Trap Depth To Enhance Optical Properties of Persistent Luminescence Nanoparticles for *in vivo* Imaging. *J. Am. Chem. Soc.* **2011**, *133*, 11810-11815.
12. Hölsä, J.; Laamanen, T.; Lastusaari, M.; Niittykoski, J.; Novák, P. Electronic Structure of the $\text{SrAl}_2\text{O}_4:\text{Eu}^{2+}$ Persistent Luminescence Material. *J. Rare Earths* **2009**, *27*, 550-554.
13. Finley, E.; Cobb, A.; Duke, A.; Paterson, A.; Brgoch, J. Optimizing Blue Persistent Luminescence in $(\text{Sr}_{1-\delta}\text{Ba}_\delta)_2\text{MgSi}_2\text{O}_7:\text{Eu}^{2+},\text{Dy}^{3+}$ via Solid Solution for Use in Point-of-Care Diagnostics. *ACS Appl. Mater. Inter.* **2016**, *8*, 26956-26963.
14. Abbruscato, V. Optical and Electrical Properties of $\text{SrAl}_2\text{O}_4:\text{Eu}^{2+}$. *J. Electrochem. Soc.* **1971**, *118*, 930-933.
15. Qu, B.; Zhang, B.; Wang, L.; Zhou, R.; Zeng, X. C. Mechanistic Study of the Persistent Luminescence of $\text{CaAl}_2\text{O}_4:\text{Eu},\text{Nd}$. *Chem. Mater.* **2015**, *27*, 2195-2202.
16. Schweizer, S.; Henke, B.; Rogulis, U.; Yen, W. M. Recombination Processes in Rare-Earth Doped MAl_2O_4 ($\text{M} = \text{Ca}, \text{Sr}$) Persistent Phosphors Investigated by Optically-Detected Magnetic Resonance. *Phys. Status Solidi A* **2007**, *204*, 677-682.
17. Hölsä, J.; Aitasalo, T.; Jungner, H.; Lastusaari, M.; Niittykoski, J.; Spano, G. Role of Defect States in Persistent Luminescence Materials. *J. Alloys Compd.* **2004**, *374*, 56-59.
18. Hafner, J. Ab-initio Simulations of Materials Using VASP: Density-Functional Theory and Beyond. *J. Comput. Chem.* **2008**, *29*, 2044-2078.
19. Kresse, G.; Furthmüller, J. Efficient Iterative Schemes for *ab initio* Total-Energy Calculations Using a Plane-Wave Basis Set. *Phys. Rev. B* **1996**, *54*, 11169.
20. Blöchl, P. E. Projector Augmented-Wave Method. *Phys. Rev. B* **1994**, *50*, 17953-17979.
21. Perdew, J. P.; Burke, K.; Ernzerhof, M. Generalized Gradient Approximation Made Simple. *Phys. Rev. Lett.* **1996**, *77*, 3865-3868.
22. Kang, J.; Wang, L.-W. High Defect Tolerance in Lead Halide Perovskite CsPbBr_3 . *J. Phys. Chem. Lett.* **2017**, *8*, 489-493.
23. Matsuzawa, T.; Aoki, Y.; Takeuchi, N.; Murayama, Y. A New Long Phosphorescent Phosphor with High Brightness, $\text{SrAl}_2\text{O}_4:\text{Eu}^{2+},\text{Dy}^{3+}$. *J. Electrochem. Soc.* **1996**, *143*, 2670-2673.
24. Poort, S. H. M.; Blokpoel, W. P.; Blasse, G. Luminescence of Eu^{2+} in Barium and Strontium Aluminate and Gallate. *Chem. Mater.* **1995**, *7*, 1547-1551.
25. Van de Walle, C. G.; Neugebauer, J. First-Principles Calculations for Defects and Impurities: Applications to III-Nitrides. *J. Appl. Phys.* **2004**, *95*, 3851-3879.
26. Lany, S.; Zunger, A. Assessment of Correction Methods for the Band-Gap Problem and for Finite-Size Effects in Supercell Defect Calculations: Case studies for ZnO and GaAs. *Phys. Rev. B* **2008**, *78*, 235104.
27. Chen, R.; McKeever, S. W. S. *Theory of Thermoluminescence and Related Phenomena*; World Scientific, 1997.
28. Chen, R. Glow Curves with General Order Kinetics. *J. Electrochem. Soc.* **1969**, *116*, 1254-1257.

29. McKeever, S. W. S. *Thermoluminescence of Solids*; Cambridge University Press, 1985.
30. Aitasalo, T.; Hölsä, J.; Jungner, H.; Krupa, J.-C.; Lastusaari, M.; Legendziewicz, J.; Niittykoski, J. Effect of Temperature on the Luminescence Processes of $\text{SrAl}_2\text{O}_4:\text{Eu}^{2+}$. *Radiat. Meas.* **2004**, *38*, 727-730.
31. Jhi, S.-H.; Louie, S. G.; Cohen, M. L.; Ihm, J. Vacancy Hardening and Softening in Transition Metal Carbides and Nitrides. *Phys. Rev. Lett.* **2001**, *86*, 3348-3351.

CHAPTER 7

Reducing Particle Size of Persistent Luminescent $\text{SrAl}_2\text{O}_4:\text{Eu}^{2+},\text{Dy}^{3+}$ via Microwave-Assisted, Reverse Micelle Synthesis

Reproduced with permission from *Optical Materials Express*
(*Optical Materials Express* **2017** 7 (7), 2597-2616)
©2017 Optical Materials Society
DOI: 10.1364/OME.7.002597

Erin Finley,¹ Andrew S. Paterson,^{2,3} Angelica Cobb,¹ Richard C. Willson,^{3,4,5} Jakoah Brgoch^{1*}

¹Department of Chemistry, University of Houston, Houston, Texas 77204, USA

²Department of Chemical and Biomolecular Engineering, University of Houston, Houston, Texas 77204, USA

³Luminostic, Inc., Houston, Texas 77204

⁴Department of Biology and Biochemistry, University of Houston, Houston, Texas 77204, USA

⁵Centro de Biotecnología FEMSA, Tecnológico de Monterrey, Campus Monterrey, Monterrey, Nuevo León 64849, Mexico

7.1. Introduction

Monoclinic $\text{SrAl}_2\text{O}_4:\text{Eu}^{2+},\text{Dy}^{3+}$, is a persistent luminescent phosphor that was primarily developed for applications such as safety signs or emergency displays and luminescent paints.¹ The commercial production of strontium aluminate is generally done in bulk, using conventional solid state synthesis that involves combining metal oxide reagents, typically in the presence of a flux like boric acid, and heating the mixture to high temperatures (1300°C to 1500°C) for several hours in a mildly reducing atmosphere.² These long reaction times and high temperatures tend to produce highly agglomerated, relatively large (20 μm to 100 μm)³, and polydispersed particles. Size reduction by milling and sieving is then required to obtain smaller particles, although does not often results in a monodisperse product. Additionally, the mechanical milling is shown to negatively impact the phosphor's optical properties by oxidizing Eu^{2+} to Eu^{3+} as well as the possibility of amorphous phases, which both change influence the optical properties.⁴

Recent research suggests that if monoclinic $\text{SrAl}_2\text{O}_4:\text{Eu}^{2+},\text{Dy}^{3+}$ can be prepared as submicron particles, it may be of use for bioanalytical applications such as *in vitro* diagnostics.^{5,6} These applications require a small particle size to minimize gravitational sedimentation⁷ and an increase in surface-area-to-volume ratio for optimal binding of the recognition molecules.^{8,9} Moreover, a small particle size allows effective transport through porous media¹⁰ like membranes in lateral-flow assays,¹¹ dipstick tests, and flow-through assays,¹² all of which could use monoclinic $\text{SrAl}_2\text{O}_4:\text{Eu}^{2+},\text{Dy}^{3+}$ as an optical reporter for analyte detection.⁶ As a result, a process for targeting small particles of $\text{SrAl}_2\text{O}_4:\text{Eu}^{2+},\text{Dy}^{3+}$ is extremely desirable.⁵

Various synthetic strategies have been investigated for producing alkaline earth aluminate persistent phosphors with particle sizes less than 10 μm . Solution based synthesis methods like; sol-gel,¹³⁻¹⁵ reverse micelle,^{2,16,17} solvothermal,^{18,19} combustion,^{3,20-24}, spray pyrolysis,²⁵⁻²⁷ and molten salt methods,²⁸ are often studied because these methods provide a considerable reduction in particle size of the phosphor precursor materials and a significant decrease in the required reaction temperature, both of which can limit particle size. Laser synthesis has also been shown to reduce particle size by limiting reaction time.²⁹ Sol-gel³⁰ and co-precipitation³¹ methods, in combination with microwave-assisted heating, limit crystal growth by using lower reaction temperatures and decreased reaction time. Unfortunately, many of these methods yield significant impurities of hexagonal $\text{SrAl}_2\text{O}_4:\text{Eu}^{2+},\text{Dy}^{3+}$ and $\text{Sr}_4\text{Al}_{14}\text{O}_{25}:\text{Eu}^{2+},\text{Dy}^{3+}$ in the final products.²⁶ Furthermore, it remains unclear if particles prepared using these alternative synthetic routes have comparable optical properties to the materials made by the more common high-temperature solid state methods.

Here, a process is reported that combines reverse micelle synthesis with microwave-assisted heating to achieve nearly phase-pure monoclinic $\text{SrAl}_2\text{O}_4:\text{Eu}^{2+},\text{Dy}^{3+}$. This route establishes a solution-based method to prepare persistent luminescent materials where the rapid microwave-based heating and reverse micelle precursors facilitates the reaction of the starting materials to desired product in less than 20 min while also limiting particle size. Comparing the photon excitation and photon emission spectra, the time-gated luminescence, and the thermoluminescence of the solution-based persistent phosphors to an all solid state route indicates only minor changes to the optical properties. Finally, this report highlights the capability of using a low-cost consumer microwave oven that can be adapted to virtually any laboratory enabling the broader adoption of $\text{SrAl}_2\text{O}_4:\text{Eu}^{2+},\text{Dy}^{3+}$ or other persistent phosphors as reporter compounds in laboratories that may not otherwise have access to high-temperature solid state synthesis equipment.

7.2. Experimental

7.2.1 Precursor Synthesis

7.2.1.1 Reverse Micelle Preparation The reverse micelle synthesis used europium (III) nitrate pentahydrate (99.9%), dysprosium (III) nitrate hydrate (99.9%), strontium nitrate ($\geq 99\%$), aluminum nitrate nonahydrate ($\geq 98\%$), hexadecyltrimethylammonium bromide (CTAB; $\geq 98\%$), heptane, anhydrous 1-butanol, ammonium carbonate, and acetone were purchased from Sigma-Aldrich. Ammonium hydroxide (28%-30%) was obtained from EM Science (Gibbstown, N.J.), and 200 proof anhydrous ethanol from PHARMCO-AAPER. Deionized (DI) water was obtained from a Millipore Milli-Q system.

The precursor particles were prepared with a nominal stoichiometry of $(\text{Sr}_{0.95}\text{Eu}_{0.01}\text{Dy}_{0.04})\text{Al}_2\text{O}_4$ by dissolving the starting material salts in DI water.² The total molar concentration of the aqueous metal salt solution was kept at ≈ 475 mM, with 150.4 mM $\text{Sr}(\text{NO}_3)_2$, 316.7 mM $\text{Al}(\text{NO}_3)_3$, 1.7 mM $\text{Eu}(\text{NO}_3)_3$, and 7.0 mM $\text{Dy}(\text{NO}_3)_3$. An aqueous solution of precipitating agents was prepared with 170 mM ammonium carbonate dissolved in stock 28% to 30% ammonium hydroxide. Two different flasks containing the organic components for the emulsions (n-heptane, CTAB, and 1-butanol) were prepared with weight percentages of 50% n-heptane, 24% 1-butanol, and 26% CTAB.

Two separate microemulsions were then prepared: one by pouring the metal salt solution into a flask containing CTAB/n-heptane/1-butanol, and the other by adding the precipitating agent solution to the remaining flask with CTAB/n-heptane/1-butanol.^{2,17} The ratio of the aqueous solution to the organic CTAB/n-heptane/1-butanol mixture that was used to form a stable emulsion was approximately 1:4 by mass, giving an approximate $[\text{H}_2\text{O}]/[\text{CTAB}]$ molar ratio of ≈ 15 . The two different emulsions were stirred for at least 20 min until no clumps of CTAB remained and each emulsion appeared to be a homogenous, transparent solution. Formation of these emulsions is apparently endothermic, and placing the suspensions on a hot plate at 37°C helped dissolve the CTAB. The metal salt emulsion and precipitating agent emulsion were combined into a single flask and placed on a magnetic stir plate at room temperature. The solution gradually turned from transparent to cloudy as the reaction proceeded.

After reacting for 24 h, the solution was poured into a separatory funnel. The microemulsion was disrupted by addition of a 50% v/v ethanol/water solution at a volume ratio of 1:1 of 50% ethanol to microemulsion solution. The contents of the separatory funnel was stirred and allowed to sit for at least 10 min to allow phase separation to

occur. After isolating the precursor particles, they were washed at least three times with 50% ethanol/water to remove excess ammonia, dissolved salts, and organics. The particles were washed a final time in acetone, and dried at 100°C for 24 h. Before reaction of the precursor powders in the microwave, a 4 wt% boric acid (Sigma-Aldrich, 99.99%) flux was added to the starting material.¹⁷

7.2.1.2 All Solid-State Preparation For comparison, homogeneous polycrystalline powders were synthesized *via* an all solid state synthesis with starting reagents of SrCO₃ (Alfa Aesar, 99.9%), Al₂O₃ (Sigma-Aldrich, 99.99%), Eu₂O₃ (Sigma-Aldrich, 99.99%), and Dy₂O₃ (Sigma-Aldrich, 99.99%) and ground thoroughly with an agate mortar and pestle for approximately 30 min. A 4 wt% flux of boric acid (Sigma-Aldrich, 99.99%) was added prior to heating.

7.2.2 Synthesis Procedure

7.2.2.1 Microwave-Assisted Heating The reverse micelle and all solid state starting materials were both reacted using microwave-assisted heating. The samples were loaded into a 5 mL alumina crucible (AdValue Tech) that was centered in a larger 50 mL alumina crucible (AdValue Tech) with 6.5 g of activated carbon (Darco, 12 mesh-20 mesh, Sigma-Aldrich) packed into the annular space and covered by an alumina disk (AdValue Tech) to maintain a reducing atmosphere produced by the hot carbon. Heating by a commercial microwave (Panasonic NN-SN651B, 1200 W) produced phase-pure materials with optimal luminescence intensity by using a two-step heating process comprised of an initial heating step at 960 W for 9 min and a second step at 480 W for 5 min. The resulting phosphor powders were first ground by hand with an agate mortar

and pestle and then sieved using a 3 in. sieve shaker to a 325 mesh size (Cole-Parmer; Performer III) to break up any agglomerates prior to characterization.

7.2.2.2 High-Temperature Furnace Heating A series of different compounds were prepared using the traditional high-temperature furnace heating route as a standard. Separate samples that used started materials from the reverse micelle preparation as well as from the all solid state preparation were heated at 1300°C for 5 hours with a heating and cooling ramp rate of 3°C/min in a reducing atmosphere of 5% H₂/95% N₂. The resulting phosphor powders were first ground by hand with an agate mortar and pestle and then sieved using a 3 in. sieve shaker to a 325 mesh size (Cole-Parmer; Performer III) to break up any agglomerates prior to characterization.

7.2.3 Characterization The composition of the reverse micelle precursors was analyzed prior to the microwave-assisted reaction using Inductively Coupled Plasma-Optical Emission Spectroscopy (Agilent 725 ICP-OES) to determine the exact ratios of Sr to Al. Samples were prepared by digestion in HF and HNO₃ for analysis. The phase purity of the reacted powders was verified *via* powder X-ray diffraction using a PANalytical X'Pert PRO diffractometer at room temperature with an average wavelength of $\lambda = 1.5406 \text{ \AA}$. Phase purity and crystallographic information were determined by Rietveld refinement, which was completed using the General Structure Analysis System (GSAS).^{32,33} Particle size analysis was carried out by mixing 50 mg of sample in 5 mL of ethanol and sonicating for 2 h; laser diffraction spectroscopy (Malvern Mastersizer 2000) was used to determine equivalent spherical diameter. Measurements were collected five times with a 30 s integration and averaged together to provide the 50% diameter volume percentage ($d_{0.5}$). A JOEL JSM-6330F field emission Scanning Electron Microscope (SEM) was used to visualize particle size distribution at 200x magnification with a beam focus and

accelerating voltage of 15 eV and an emission current of 12 μ A. An AMETEK EDAX Octane Pro energy dispersive X-ray spectroscopy (EDS) established the semi-quantitative compositions of the reverse micelle and solid state materials. Samples were coated with 25 nm of carbon to limit charging in the SEM. All crystal structure drawings were created using VESTA.³⁴

7.2.4 Optical Properties Photon excitation and emission spectra were collected using a PTI QuantaMaster 400 equipped with a 75 W Xe steady state lamp (PTI Instruments). Temperature dependent photoluminescence, luminescence lifetime decays, and thermoluminescence (TL) were carried out using a Janis cryostat (VPF-100) to control the temperature measurements. Temperature dependent photoluminescence was measured between 80 K and 500 K in 30 K intervals. Temperature dependent luminescence lifetime decays were measured by first irradiating the sample for 10 min at 365 nm followed by a 15 sec delay after shutting off irradiation. TL measurements between 100 K to 500 K. Samples were first heated to 500 K and then cooled to 100 K prior to being irradiated for 10 min at 365 nm using the Xe lamp. A 3 min delay was employed after turning off the lamp before the temperature of the cryostat was ramped at a rate of 5 K/min. The TL emission was collected at $\lambda_{em} = 520$ nm.

7.3. Results and Discussion

7.3.1. Microwave-Assisted, Reverse Micelle Synthesis of Persistent Phosphors

Reverse micelle synthesis affords the advantages of a sol-gel route where the elements for the phosphor host and the luminescent centers start as ions in aqueous solution and are then precipitated to give a precursor material with a more homogenous distribution of the component elements at small scales. Instead of allowing precipitation to occur freely throughout the solution, as in a conventional sol-gel approach, the reverse micelle synthesis continues to confine the reactions within aqueous nanodroplets formed by micelles.^{24,35} The reaction works by preparing two separate emulsions. One solution is an aqueous solution of dissolved metal salts of the elements needed for the phosphor host. A separate solution is prepared containing an aqueous solution of precipitating agents such as ammonium carbonate or ammonium hydroxide. After combining the emulsions, the micelles collide in solution and exchange reactants, causing precipitation. The precipitation reactions used for preparing strontium carbonate and aluminum hydroxide as precursors for the strontium aluminate host are given by Equation 7.1 and Equation 7.2. Figure S7.1 shows the resulting X-ray diffraction pattern confirming the formation of SrCO₃.



A significant volume of work has been published on synthesizing materials and inorganic nanoparticles with reverse micelles,³⁵ examining the effect of surfactants and co-surfactants on the resulting particle size distribution, and modeling the complexities of the reaction kinetics and dynamics. Reverse micelle synthesis of nanoparticles has also

been demonstrated to be highly scalable with the successful scale-up of manganese zinc ferrite nanoparticle synthesis from a bench-top setup to a 30 L pilot plant.³⁶ One established system for reverse micelle synthesis is the use of cetyltrimethylammonium bromide (CTAB) as a surfactant with 1-butanol as a co-surfactant, and an organic such as n-heptane or a similar solvent for the organic component.^{24,37,38} The CTAB/butanol/heptane system was previously described for the synthesis of $\text{Sr}_4\text{Al}_{14}\text{O}_{25}$ and other strontium aluminates with a reaction temperature of 1200°C .^{2,17} Another study reported the synthesis of nano-sized $\text{SrAl}_2\text{O}_4:\text{Eu}^{2+},\text{Dy}^{3+}$ using a related microemulsion route and high-temperature (1000°C) calcination to obtain a mixture of polymorphs, *i.e.*, the product contained both hexagonal and monoclinic space groups.¹⁶

One limitation of these solution-based synthetic methods is that the stoichiometric ratio of metals in the final precursor material is determined by the extent of precipitation of the metal salts, and so it is not necessarily equal to the initial molar concentration of the metal salts in solution. Therefore, measuring the molar concentrations of Sr and Al in the resulting precipitates (precursor powders) is essential to ensure that the reverse micelle protocol results in the correct stoichiometry for SrAl_2O_4 . Analysis by ICP-OES (Table 7.1) revealed that there was an excess amount of Al present in the precursor material when the initial metal salt solution started with an exact 1:2 mole ratio of Sr to Al salts. Hence, two additional solutions were prepared with excess $\text{Sr}(\text{NO}_3)_2$ to account for the presence of the additional Al. As shown in Table 7.1, using 5% excess $\text{Sr}(\text{NO}_3)_2$ in the reverse micelle synthesis improved the molar ratio while 10% excess $\text{Sr}(\text{NO}_3)_2$ produced the exact, desired stoichiometry. Therefore, all subsequent reactions used samples that started with 10% excess $\text{Sr}(\text{NO}_3)_2$ to ensure the formation of the stoichiometric $\text{SrAl}_2\text{O}_4:\text{Eu}^{2+},\text{Dy}^{3+}$.

Table 7.1. ICP-OES of reverse micelle precursors establishing the amount of excess $\text{Sr}(\text{NO}_3)_2$ required to produce the desired stoichiometric ratios of Sr:Al.

sample	Sr ($\mu\text{g/g}$)	Al ($\mu\text{g/g}$)	Sr:Al mole ratio
0% excess $\text{Sr}(\text{NO}_3)_2$	9.1	6.3	1:2.3
5% excess $\text{Sr}(\text{NO}_3)_2$	9.5	6.3	1:2.1
10% excess $\text{Sr}(\text{NO}_3)_2$	10.2	6.4	1:2

Once the starting reverse micelle precursor powders are prepared, they must be reacted to achieve the final product. The most common method for reaction is to perform high-temperature calcination or sintering (1300 °C to 1500 °C) under a reducing atmosphere (5% H_2 /95% N_2). This heating environment can require reaction times up to 24 hours and may produce large crystal growth and particle agglomeration. Instead, rapid microwave-assisted heating has also been shown as an effective method to produce high quality inorganic phosphors.²³ The advantage of microwave heating is that the time required to produce a pure phase product can be reduced to less than 20 minutes, limiting crystal growth and agglomerate formation. In this approach, microwave heating programs must first be optimized to ensure ideal distribution of heat throughout the material. A program that is too long may melt the starting materials, while heating for too little time will produce inhomogeneous, impure products. Once a program is determined, in this case, a two-step process with an initial heating step and then a holding step as described in the experimental section, numerous batches from the same starting precursors can be prepared with identical results.

To illustrate the reliability and consistency of the microwave-assisted heating, five batches, each consisting of ≈ 50 mg of the reverse micelle precursor, were reacted and examined *via* powder X-ray diffraction. Figure 7.1 shows the phase forms in the desired monoclinic space group $P2_1$ (No. 4), and was produced as a major phase with a minor Al_2O_3 impurity, likely from the alumina crucible. This impurity can be disregarded

because it lacks optical properties that could have an impact on the optical properties of strontium aluminate. The diffraction patterns show that the microwave-assisted synthetic route is consistent in converting the precursor material to the desired product repeatedly, without any indication of hexagonal $\text{SrAl}_2\text{O}_4:\text{Eu}^{2+},\text{Dy}^{3+}$ or other related strontium aluminates.

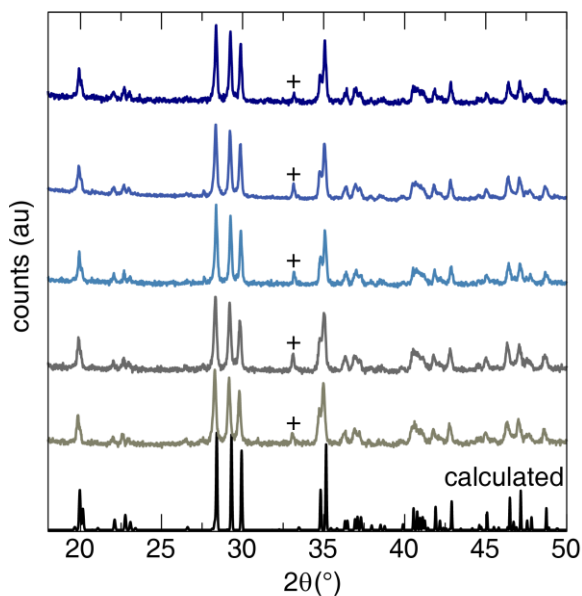


Figure 7.1. XRD patterns of microwave-assisted reverse micelle $\text{SrAl}_2\text{O}_4:\text{Eu}^{2+},\text{Dy}^{3+}$ showing batch-to-batch consistency of the microwave heating process. Black is the calculated pattern.³⁹ “+” is an Al_2O_3 impurity.

To compare the reverse micelle synthesis pathway with conventionally prepared materials, a sample was also made using the all solid state method by weighing out stoichiometric amounts of the respective oxide reagents and mixing them by hand grinding with a mortar and pestle. This all solid state sample was reacted following the same microwave-assisted heating protocol as the reverse micelle sample to also yield nearly phase-pure material. Elemental composition was analyzed by SEM-EDS to determine that no elemental impurities were present in either product. A semi-

quantitative EDS analysis of the reverse micelle sample estimates the mole ratio between Sr and Al to be approximately 1:2.6 while the solid state sample is 1:2.3. The excess Al measured in the EDS is likely from the Al_2O_3 impurity also detected in the X-ray powder diffraction.

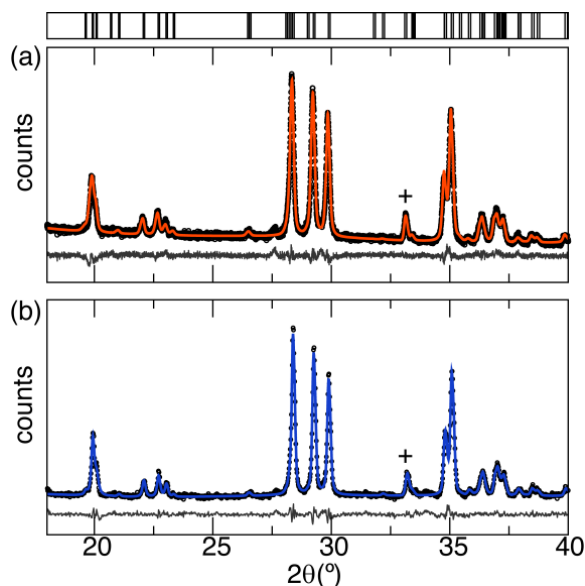


Figure 7.2. (a) Reverse micelle and (b) solid state synthesis Rietveld refinements show the reverse micelle is comparable to the traditional solid state synthesis. Black circles are for observed data, solid lines are the refined pattern, and “+” is the Al_2O_3 impurity.

Because impurities like hexagonal SrAl_2O_4 and $\text{Sr}_4\text{Al}_{14}\text{O}_{25}$ are often present in the products of these solution based methods, Rietveld refinements of the reverse micelle (Figure 7.2a) and the all solid state (Figure 7.2b) prepared materials *via* microwave-assisted heating were conducted. The refinement data and associated crystallographic parameters are listed in Table 7.2 and Table 7.3. The refinements show excellent agreement with the observed data, supporting there are no impurities beyond Al_2O_3 .

$\text{SrAl}_2\text{O}_4:\text{Eu}^{2+},\text{Dy}^{3+}$ crystallizes in monoclinic space group $P2_1$ with two independent crystallographic Sr^{2+} sites, both at Wyckoff position 2a, that are 7-coordinated to oxygen (six of which are crystallographically independent).⁴⁰ There are also four

crystallographically independent Al^{3+} forming $[\text{AlO}_4]$ tetrahedra connected in a three-dimensional, corner-sharing framework.⁴⁰ The refined unit cell of the reverse micelle product is visualized in Figure 7.3 with the $[\text{AlO}_4]$ tetrahedra and the two crystallographically independent $[\text{SrO}_7]$ polyhedral highlighted.

The similarity between the crystal structures is confirmed by comparing the refined unit cell parameters and atomic positions, which are nearly identical regardless of synthesis method. Further, the two synthesis methods produce nearly identical polyhedral unit volumes indicating a consistent local composition. In fact, the difference in polyhedral volumes between the two synthetic pathways for $[\text{Sr}(1)\text{O}_7]$ is only $\approx 0.348 \text{ \AA}^3$ with the reverse micelle being slightly larger whereas the polyhedral volumes of $[\text{Sr}(2)\text{O}_7]$ is even closer, differing by only 0.017 \AA^3 . Combining the information obtained from ICP-OES, SEM-EDS, and powder X-ray diffraction, it can be concluded that the reverse micelle synthesis produces a nearly (structurally) identical monoclinic $\text{SrAl}_2\text{O}_4:\text{Eu}^{2+},\text{Dy}^{3+}$. Finally, to substantiate that microwave heating generates equivalent samples to conventionally prepared products, a separate set of compounds were reacted using high-temperature furnace heating and analyzed using the same techniques (presented in the Supporting Information). These data reveal that the traditionally prepared samples are in excellent agreement with the compounds prepared using microwave-assisted heating.

Table 7.2. Rietveld refinement results for reverse micelle and solid state synthesis of $\text{SrAl}_2\text{O}_4:\text{Eu}^{2+},\text{Dy}^{3+}$ using powder X-ray diffraction.

Formula: $\text{SrAl}_2\text{O}_4:\text{Eu}^{2+},\text{Dy}^{3+}$	Reverse micelle	Solid state
radiation type, λ (Å)	Cu, 1.5406 Å	
2θ range (°)	18-60	
temperature (K)	295	
space group; Z	$P2_1$ (No. 4); 2	
a (Å)	8.4455(1)	8.4458(2)
b (Å)	8.8252(1)	8.8248(2)
c (Å)	5.15884(7)	5.1570(1)
β (°)	93.381(1)	93.349(2)
V (Å ³)	383.834(6)	383.71(1)
calculated density (g cm ⁻³)	3.558	3.559
formula weight (g mol ⁻¹)	822.320	822.320
R_p	0.0234	0.0301
R_{wp}	0.0304	0.0387
χ^2	1.173	1.328

Table 7.3. Crystallographic results as determined by Rietveld refinement of powder X-ray diffraction.

(a) Reverse micelle

Atom	Wyck.	<i>x</i>	<i>y</i>	<i>z</i>	$U_{iso}(\text{\AA}^2)$
Sr(1)	2 <i>a</i>	0.4923(4)	0.0046(9)	0.2552(6)	0.039(1)
Sr(2)	2 <i>a</i>	0.0278(3)	0.9968(9)	0.2053(5)	0.052(2)
Al(1)	2 <i>a</i>	0.179(2)	0.843(2)	0.742(2)	0.047(2)
Al(2)	2 <i>a</i>	0.802(2)	0.859(2)	0.742(2)	0.047(2)
Al(3)	2 <i>a</i>	0.698(2)	0.688(2)	0.221(2)	0.047(2)
Al(4)	2 <i>a</i>	0.696(2)	0.186(2)	0.797(2)	0.047(2)
O(1)	2 <i>a</i>	0.264(2)	0.160(2)	0.356(3)	0.013(1)
O(2)	2 <i>a</i>	0.747(2)	0.326(2)	0.516(4)	0.013(1)
O(3)	2 <i>a</i>	0.333(1)	0.489(2)	0.345(2)	0.013(1)
O(4)	2 <i>a</i>	0.272(1)	0.957(2)	0.878(2)	0.013(1)
O(5)	2 <i>a</i>	0.163(2)	0.279(2)	0.960(3)	0.013(1)
O(6)	2 <i>a</i>	0.208(2)	0.672(2)	0.911(3)	0.013(1)
O(7)	2 <i>a</i>	0.485(1)	0.227(1)	0.881(1)	0.013(1)
O(8)	2 <i>a</i>	0.997(1)	0.9029(9)	0.652(2)	0.013(1)

(b) Solid state

Atom	Wyck.	<i>x</i>	<i>y</i>	<i>z</i>	$U_{iso}(\text{\AA}^2)$
Sr(1)	2 <i>a</i>	0.4937(7)	0.001(2)	0.251(1)	0.023(2)
Sr(2)	2 <i>a</i>	0.0286(7)	0.993(2)	0.201(1)	0.041(3)
Al(1)	2 <i>a</i>	0.196(3)	0.825(3)	0.738(4)	0.025(3)
Al(2)	2 <i>a</i>	0.799(3)	0.850(3)	0.747(3)	0.025(3)
Al(3)	2 <i>a</i>	0.694(4)	0.664(3)	0.246(5)	0.025(3)
Al(4)	2 <i>a</i>	0.691(3)	0.182(3)	0.785(5)	0.025(3)
O(1)	2 <i>a</i>	0.273(4)	0.191(4)	0.425(8)	0.004(3)
O(2)	2 <i>a</i>	0.737(7)	0.334(4)	0.564(8)	0.004(3)
O(3)	2 <i>a</i>	0.331(3)	0.466(4)	0.364(4)	0.004(3)
O(4)	2 <i>a</i>	0.259(3)	1.020(6)	0.883(4)	0.004(3)
O(5)	2 <i>a</i>	0.168(3)	0.301(3)	0.940(6)	0.004(3)
O(6)	2 <i>a</i>	0.223(3)	0.675(3)	0.884(6)	0.004(3)
O(7)	2 <i>a</i>	0.491(4)	0.236(3)	0.894(4)	0.004(3)
O(8)	2 <i>a</i>	1.005(5)	0.871(3)	0.688(5)	0.004(3)

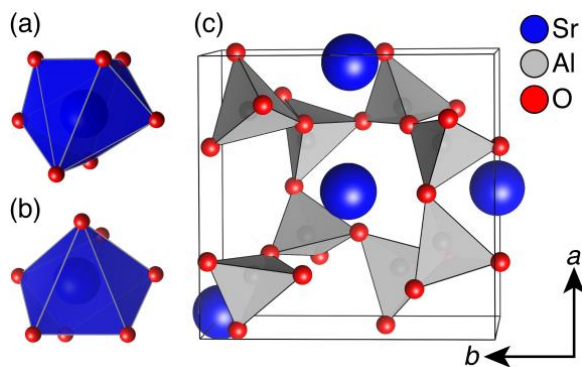


Figure 7.3. The 2 independent polyhedra (a) $[\text{Sr}(1)\text{O}_7]$ and (b) $[\text{Sr}(2)\text{O}_7]$ are shown to the left of the unit cell (c) of SrAl_2O_4 in the monoclinic space group $P2_1$ with the $[\text{AlO}_4]$ tetrahedra highlighted.

7.3.2 Particle Size Analysis The use of solution-based routes can generate nano-sized precursor powders and allow shorter reaction times leading to a decrease in product's particle size.⁴¹ This is advantageous for materials used in bioanalytical applications where particle sizes <500 nm are often targeted because of the increased surface-to-volume ratios.⁵ Therefore, targeting particles with a diameter between 250 nm and $1\mu\text{m}$ is of scientific importance. To achieve this size range in $\text{SrAl}_2\text{O}_4:\text{Eu}^{2+},\text{Dy}^{3+}$, extensive post processing is often required, which can cause changes in the optical properties due to the oxidation of Eu^{2+} to Eu^{3+} .⁴ Therefore, it is necessary to identify a procedure for preventing destructive post processing. Here, SEM micrographs of the samples synthesized using both approaches were collected at 200x magnification to demonstrate the difference in overall particle size between the two routes. The reverse micelle method (Figure 7.4a) clearly produced significantly smaller particles than the all solid state synthesis method (Figure 7.4b); both remain relatively polydispered.

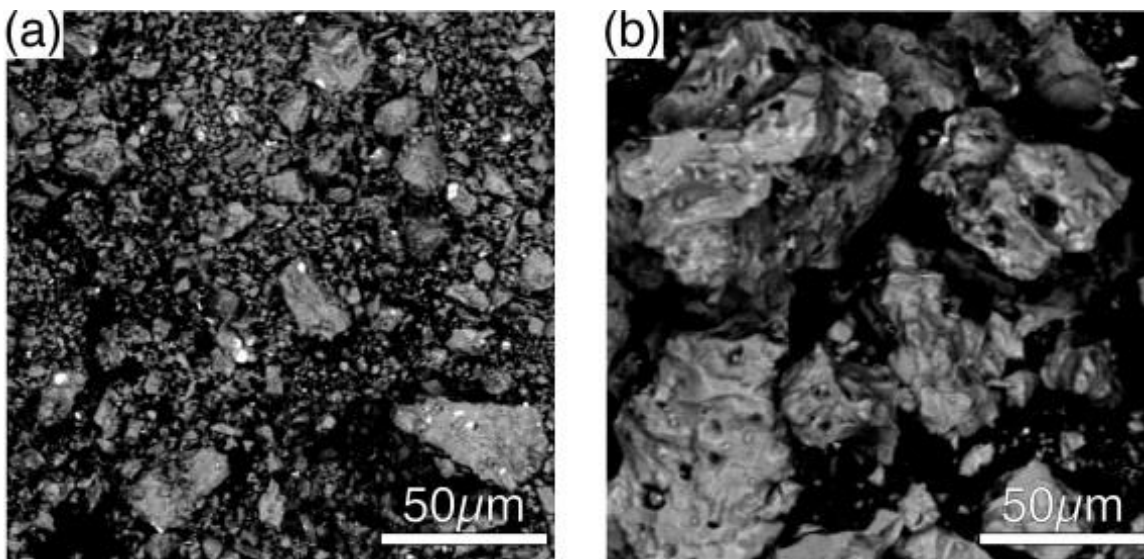


Figure 7.4. SEM with a 200 \times magnification and the scale bar is 50 μm . (a) Reverse micelle synthesis visualizes the overall particle sizes are much smaller than the (b) solid state synthesis. Both starting materials were reacted using microwave-assisted heating.

Because the SEM micrographs revealed a significant difference in particle size, laser diffraction spectroscopy was used to measure the distribution of particle volume/mass of all particles in a sample. The equivalent sphere diameter is reported for the 50th-percentile ($d_{0.5}$), or the percentage of particle sizes at or below that diameter. As shown in Figure 7.5a, the reverse micelle synthesis produces a much greater fraction of small particles compared to the solid state synthesis (Figure 7.5b). In fact, combining the microwave-assisted heating with the reverse micelle route leads to a nearly 70% decrease in the particle size relative to the all solid state powders reacted in the microwave. Comparing these data to the samples prepared *via* high-temperature furnace shows that conventional heating produces significantly larger particles for both the reverse micelle starting materials ($d_{0.5} = 14.3 \mu\text{m}$) and even larger particles ($d_{0.5} = 15.2 \mu\text{m}$) for the all solid state method. Interestingly, the use of reverse micelle powders in conjunction with reacting in a conventional high-temperature furnace shows only a 6% decrease in particle size compared to starting from oxide powders. These data are

shown in Figure SI 7.3. Hence, for $\text{SrAl}_2\text{O}_4:\text{Eu}^{2+},\text{Dy}^{3+}$ the advantage of the solution-based route is only fully realized when coupled with microwave-assisted heating. This substantial decrease in particle size limits the need for extensive mechanical milling to reduce the particle size of $\text{SrAl}_2\text{O}_4:\text{Eu}^{2+},\text{Dy}^{3+}$ powders, which is ideal because the milling process can generate impurities and ultimately the loss of any optical response.⁴²

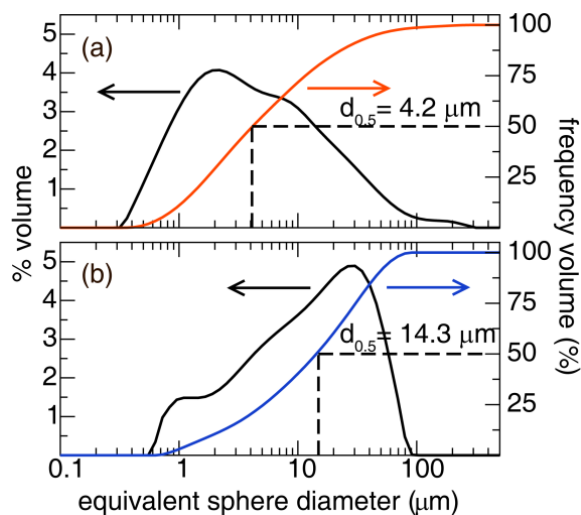


Figure 7.5. Particle size analysis of the (a) reverse micelle synthesis showing that 50% of the equivalent sphere diameters ($d_{0.5}$) are 4.2 μm or smaller and (b) the all solid state synthesis gives a $d_{0.5} = 14.3 \mu\text{m}$.

7.3.3 Optical Characterization In light of the significant decrease in particle size measured for the reverse micelle and all solid state produced *via* microwave-assisted heating method, these two samples are the focus of the ensuing optical property measurements. The excitation spectra of the two syntheses, Figure 7.6a, indicated a nearly identical peak shape. Subsequently exciting the samples at $\lambda_{\text{ex}} = 365 \text{ nm}$ produced identical emission peaks with a $\lambda_{\text{em,max}} = 520 \text{ nm}$. The substitution of Eu^{2+} for the two crystallographically independent positions of Sr^{2+} in SrAl_2O_4 should produce two emission peaks, both of which follow the customary $5d \rightarrow 4f$ transition of Eu^{2+} from the first excited state, ${}^7\text{H}_j$, to the ground state, ${}^8\text{S}_{7/2}$.¹ However, in $\text{SrAl}_2\text{O}_4:\text{Eu}^{2+}$ the second

emission peak at 450 nm is not observed at room temperature.¹ Calculating the color coordinates for the emission spectra using the 1931 Commission Internationale de l'Eclairage (CIE) diagram validated the reverse micelle (0.3218, 0.5605) and solid state routes (0.3107, 0.5552) are nearly identical, further confirming that photon emission is not affected by the synthesis method (Figure 7.6b).

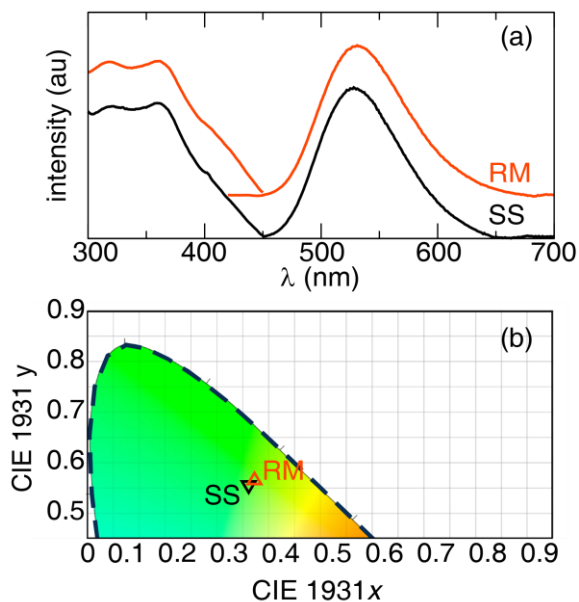


Figure 7.6. (a) Excitation and emission spectra of solid state (SS) and reverse micelle (RM) showing $\lambda_{em,max} = 520$ nm for both synthesis pathways. (b) CIE diagram illustrating the calculated color coordinates have nearly identical visible emission.

Although the observed steady state photoluminescence is nearly identical, further inquiry into potential optical differences was necessary. Typically, temperature-dependent luminescence is conducted on phosphors to determine their ability maintain emission intensity when being heated to high-temperatures.^{43,44} In the case of strontium aluminate, determining quenching temperature gives insight into the thermal stability of persistent lifetime behavior.^{1,45,46} Figure 7.6.7 visualizes the temperature dependence of both the reverse micelle (Figure 7.6.7a) and the all solid state (Figure 7.6.7b). Each

sample was heated to 500 K and subsequently cooled to 80 K to ensure all trap states were emptied prior to beginning the measurement. Emission spectra were then taken every 30 K. Interestingly, the reverse micelle prepared sample exhibits an improved quenching temperature (T_{50}), the temperature at which the emission intensity has reached 50% of the initial intensity, by 68 K. This improved T_{50} could be due to additional trap states being occupied or an increase in the trapping and retrapping of electrons; however, additional research into the origin of this difference is required to identify the exact mechanism. Moreover, the emission seen at approximately $\lambda_{em} = 450$ nm does completely quench prior to room temperature for both the reverse micelle and the all solid state sample.¹

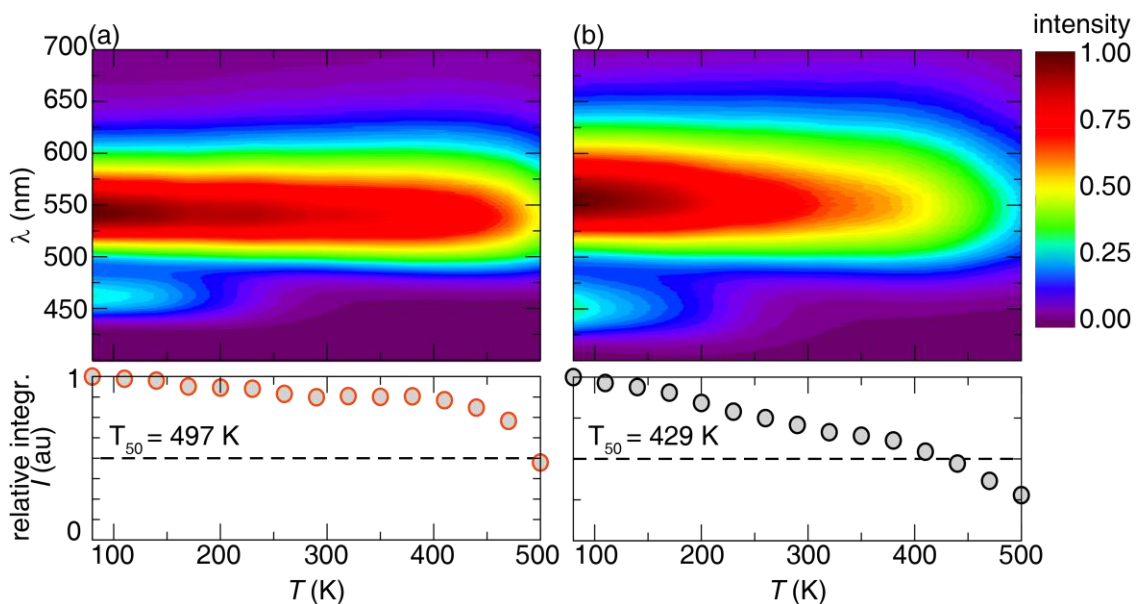


Figure 7.7. Temperature-dependent measurement of (a) RM and (b) SS emission spectra (top) and the relative integrated intensity of the quenching temperature (T_{50}) of the combined emission peaks (bottom).

Additionally, investigating the temperature dependence of the two synthesis pathways was completed by performing temperature-dependent long lifetimes measurements on the reverse micelle sample (Figure 7.6.8a) and the all solid state sample (Figure 7.6.8b).

Each lifetime was measured starting at room temperature and then at 25 K intervals until 423 K with an irradiation time of 10 min and a 15 sec delay before beginning the measurement. This temperature range is of great importance for use in bioanalytical systems, both *in vivo* and *in situ*, because cells need to be maintained at a constant temperature of 310 K.^{47,48} Therefore, maintaining a sufficiently long lifetime at temperatures at or above 310 K is largely desirable. Each sample was prepared by first ensuring all trap states were emptied. The lifetime decay was then collected for one hour (3600 sec). The resulting data was fit to a tri-exponential, Equation 7.3 where; I is the intensity; A_1 , A_2 , and A_3 are pre-exponential values; t is time; and τ_1 , τ_2 , and τ_3 are the lifetime decay components.

$$I = A_1 e^{-\frac{t}{\tau_1}} + A_2 e^{-\frac{t}{\tau_2}} + A_3 e^{-\frac{t}{\tau_3}} \quad (7.3)$$

The three lifetime components are compared to temperature in Figure 7.8c (reverse micelle) and Figure 7.8d (solid state). An increase in lifetime is expected as temperature increases due to the detrapping of deeper traps, and is clearly observed in both samples. However, the reverse micelle exhibits a longer lifetime than the all solid state sample, even at room temperature. Furthermore, the all solid state sample only exhibited two decay components at 423 K, which is consistent with its T_{50} observed in Figure 7.7b. This interesting result indicates that particle size has a slight influence on the long luminescence lifetime of $\text{SrAl}_2\text{O}_4:\text{Eu}^{2+}, \text{Dy}^{3+}$.

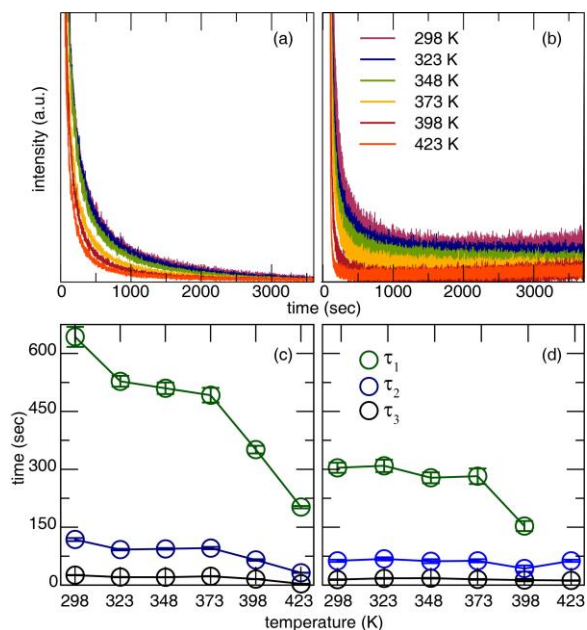


Figure 7.8. Temperature-dependent luminescent decay of the (a) reverse micelle and (b) solid state observed for 3600 seconds. The data fit to a tri-exponential (c) reverse micelle and (d) solid state show the reverse micelle has a longer lifetime than the all solid state sample.

The origin for the change in lifetimes is most reliably determined by conducting TL measurements to identify and quantify the trap depths, which control the long lifetime in persistent phosphors. These measurements are particularly important because a change in TL emission is known to occur with a change in particle size for nanophosphors such as ZnS and $Y_2O_3:Eu^{3+}$.^{49,50} Therefore, the reverse micelle and all solid state samples were examined using TL measurements between 100 K and 500 K. The overall shape of the TL spectra (Figure 7.8a) clearly differ, with a widening of the TL emission spectra and presence of multiple new features in the reverse micelle sample compared to the all solid state sample.

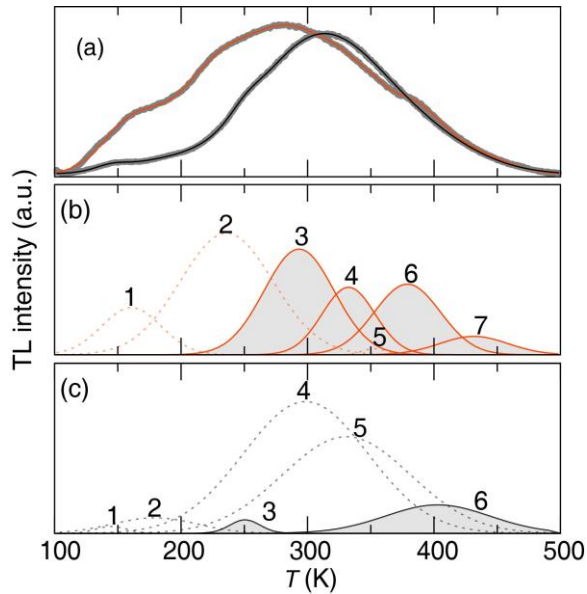


Figure 7.9. (a) TL emission curve cumulative fit of solid state (black) and reverse micelle (red), grey is the observed data. Peaks determined by deconvolution for (b) reverse micelle and (c) solid state. Peaks with traps < 0.4 eV or > 1 eV are dashed lines and peaks between 0.4 eV and 1 eV are solid lines.

Deconvoluting the TL emission spectra with multiple Gaussian functions indicated there is not only one additional peak in the reverse micelle sample (Figure 7.9b) relative to the all solid state sample (Figure 7.9c) but also that the peaks occur in different positions. Each peak location, intensity, and shape is strongly dependent on the irradiation wavelength, heating rate, and time delay between initiating heating and termination of the excitation source.^{1,51} A semi-quantitative comparison between the two materials is best achieved by calculating the trap depth energies (within 5% of the exact trap depth⁵²) using the deconvoluted TL spectra following the “peak shape method”⁵³ (Equation 7.4), where E_A is the activation energy (of the trap) T_m is the temperature maximum of the TL emission, and k_B is the Boltzmann constant. The geometric factor (μ_g) is found according to Equation 7.5, where $\sigma = T_2 - T_m$, T_2 is the low-temperature half maximum and ω is the full width at half maximum of TL emission.^{53,54} Because deconvolution provides ω , it is

directly calculated to be $\mu_g = 0.50$, which is in agreement with second order kinetics as previously reported for monoclinic $\text{SrAl}_2\text{O}_4:\text{Eu}^{2+},\text{Dy}^{3+}$.⁵⁴ The calculated values are provided in Table 7.4.

$$E_A = [2.52 + 10.2(\mu_g - 0.42)] \left(\frac{k_B T_m^2}{\omega} \right) - (2k_B T_m) \quad (7.4)$$

$$\mu_g = \frac{\sigma}{\omega} \quad (7.5)$$

Based on the E_A calculated from the data in Figure 7.8 and reported in Table 7.4, it is possible to determine if these new traps affect the luminescence lifetimes. It is understood that the optimal depth for long persistent lifetime is ≈ 0.65 eV⁵⁵⁻⁵⁷ and that materials with trap depths greater than 1 eV are too deep for electrons to be detrapped at room temperature. Conversely, trap depths < 0.4 eV are too shallow and will instantaneously detrapp at room temperature. Therefore, trap depths calculated to have values $0.4 \text{ eV} < E_A < 1.0 \text{ eV}$ are considered to contribute to a persistent luminescent lifetime.^{51,56}

Table 7.4. Calculated trap depths of reverse micelle and solid state synthesis from deconvolution of TL emission spectra.

peak	Reverse micelle		Solid state	
	T (K)	trap depth (eV)	T (K)	trap depth (eV)
1	161	0.13	144	0.21
2	236	0.19	179	0.12
3	294	0.38	251	0.64
4	333	0.64	299	0.22
5	353	1.58	331	0.26
6	379	0.67	403	0.48
7	432	0.84	---	---

The increase in the number of traps observed likely arises from the presence of surface defects due to the smaller particle size. This new trap has a depth of 0.84 eV should

increase the luminescence lifetime; however, the reverse micelle sample also has a significantly deeper trap (trap 5) than in the solid state sample. Moreover, the changes in trap depth observed at 333 eV (RM) and 331 eV (SS) could be explained by a retrapping and detrapping behavior rather than a deeper trap. It is likely that combination of these changes negate any potential impact on the persistent luminescence lifetimes. Therefore, synthesizing smaller particles using the reverse micelle microwave-assisted synthesis will not affect most applications of monoclinic $\text{SrAl}_2\text{O}_4:\text{Eu}^{2+},\text{Dy}^{3+}$.

7.4. Conclusion

A synthetic approach combining reverse micelle synthesis with microwave-assisted heating was developed to produce small particles of $\text{SrAl}_2\text{O}_4:\text{Eu}^{2+},\text{Dy}^{3+}$. Because this solution-based route does not guarantee the desired starting stoichiometry, ICP-OES was employed to identify that 10% excess $\text{Sr}(\text{NO}_3)_2$ is necessary to acquire the correct Sr:Al stoichiometry for SrAl_2O_4 . Subsequently, reacting multiple batches of these powders using microwave-assisted heating showed excellent reproducibility, which, in combination with the solution-based reverse micelle synthesis, provides an opportunity to scale-up this synthesis for mass production of these materials? Moreover, a direct comparison of the reverse micelle and an all solid state prepared materials show the crystal structures are nearly identical.

The major difference between the two syntheses is in the particle size, with the reverse micelle synthesis producing a 70% decrease in the particle size compared to the all-solid state route. Even with the reduction of the particle size, the observed photon excitation and photon emission spectra were not affected. The temperature dependence of the photoluminescence and long lifetimes were considered and the reverse micelle showed

both an improved thermal quenching temperature and longer lifetimes. Finally, thermoluminescence revealed the reverse micelle pathway created an additional trap state that could contribute to a persistent luminescence, which may be due to surface defects because of the smaller particle size. The combination of these results highlights that future persistent luminescent materials like $\text{SrAl}_2\text{O}_4:\text{Eu}^{2+},\text{Dy}^{3+}$ can be synthesized by employing soft chemical synthetic routes, like the reverse micelle approach demonstrated here, coupled with microwave-assisted heating to reduce particle size with an enhanced overall optical performance.

7.5 Acknowledgements

The authors thank the staff at the Texas Center for Superconductivity at the University of Houston for assistance with EDS and SEM and the staff at the University of Houston ICP Analytical Laboratory and Agilent Facility Center for their assistance in preparing and collecting the ICP-OES data.

7.8 References

1. Botterman, J.; Joos, J.J.; Smet, P.F. Trapping and Detrapping in $\text{SrAl}_2\text{O}_4:\text{Eu}^{2+},\text{Dy}^{3+}$ Persistent Phosphors: Influence of Excitation Wavelength and Temperature. *Phys. Rev. B* **2014**, *90*, 085147.
2. Thompson, N., RMIT University, 2012.
3. Rojas-Hernandez, R.E.; Rodriguez, M.A.; Rubio-Marcos, F.; Serrano, A.; Fernandez, J.F. Designing Nanostructured Strontium Aluminate Particles with High Luminescence Properties. *J. Mater. Chem. C* **2015**, *3*, 1268-1276.
4. Rojas-Hernandez, R.E.; Rubio-Marcos, F.; Enriquez, E.; De La Rubia, M.A.; Fernandez, J.F. A Low-Energy Milling Approach to Reduce Particle Size Maintains the Luminescence of Strontium Aluminates. *RSC Adv.* **2015**, *5*, 42559-42567.
5. Lécuyer, T.; Teston, E.; Ramirez-Garcia, G.; Maldiney, T.; Viana, B.; Seguin, J.; Mignet, N.; Scherman, D.; Richard, C. Chemically Engineered Persistent Luminescence Nanoprobes for Bioimaging. *Theranostics* **2016**, *6*, 2488-2524.
6. Paterson, A.S.; Raja, B.; Garvey, G.; Kolhatkar, A.; Hagström, A.E.V.; Kourentzi, K.; Lee, T.R.; Willson, R.C. Persistent Luminescence Strontium Aluminate Nanoparticles as Reporters in Lateral Flow Assays. *Anal. Chem.* **2014**, *86*, 9481-9488.

7. Hermanson, G.T. In *Bioconjugate Techniques (Second Edition)*; Academic Press: New York, 2008, p 582-626.
8. Riuttamäki, T., *Annales Universitatis Turkuensis*, 2011.
9. Rosi, N.L.; Mirkin, C.A. Nanostructures in Biodiagnostics. *Chem. Rev.* **2005**, *105*, 1547-1562.
10. May, R.; Li, Y. The effects of particle size on the deposition of fluorescent nanoparticles in porous media: Direct observation using laser scanning cytometry. *Colloids and Surfaces A: Physicochemical and Engineering Aspects* **2013**, *418*, 84-91.
11. Posthuma-Trumpie, G.A.; Korf, J.; van Amerongen, A. Lateral Flow (Immuno)assay: Its Strengths, Weaknesses, Opportunities and Threats. A Literature Survey. *Anal. Bioanal. Chem.* **2009**, *393*, 569-582.
12. Yetisen, A.K.; Akram, M.S.; Lowe, C.R. Paper-Based Microfluidic Point-of-Care Diagnostic Devices. *Lab Chip* **2013**, *13*, 2210-2251.
13. Aitasalo, T.; Hölsä, J.; Jungner, H.; Lastusaari, M.; Niittykoski, J. Sol-Gel Processed Eu²⁺-Doped Alkaline Earth Aluminates. *J. Alloys Compd.* **2002**, *341*, 76-78.
14. Zhang, P.; Xu, M.; Zheng, Z.; Liu, L.; Li, L. Synthesis and Characterization of Europium-Doped Sr₃Al₂O₆ Phosphors by Sol–Gel Technique. *J. Sol-Gel Sci. Technol.* **2007**, *43*, 59-64.
15. Chen, I.-C.; Chen, T.-M. Effect of Host Compositions on the Afterglow Properties of Phosphorescent Strontium Aluminate Phosphors Derived from the Sol-Gel Method. *J. Mater. Res.* **2001**, *16*, 1293-1300.
16. Lu, C.-H.; Chen, S.-Y.; Hsu, C.-H. Nanosized strontium aluminate phosphors prepared via a reverse microemulsion route. *Materials Science and Engineering: B* **2007**, *140*, 218-221.
17. Thompson, N.; Murugaraj, P.; Rix, C.; Mainwaring, D.E. Role of Oxidative Pre-Calcination in Extending Blue Emission of Sr₄Al₁₄O₂₅ Nanophosphors Formed with Microemulsions. *J. Alloys Compd.* **2012**, *537*, 147-153.
18. Karmaoui, M.; Willinger, M.-G.; Mafra, L.; Hertrich, T.; Pinna, N. A General Nonaqueous Route to Crystalline Alkaline Earth Aluminate Nanostructures. *Nanoscale* **2009**, *1*, 360-365.
19. Si, D.; Geng, B.; Wang, S. One-Step Synthesis and Morphology Evolution of Luminescent Eu²⁺ Doped Strontium Aluminate Nanostructures. *CrystEngComm* **2010**, *12*, 2722-2727.
20. Song, H.; Chen, D.; Tang, W.; Peng, Y. Synthesis of SrAl₂O₄: Eu²⁺, Dy³⁺, Gd³⁺ Phosphor by Combustion Method and Its Phosphorescence Properties. *Displays* **2008**, *29*, 41-44.
21. Tanaka, H.; Gubarevich, A.V.; Wada, H.; Odawara, O. Process Stages During Solution Combustion Synthesis of Strontium Aluminates. *Int. J. Self-Propag. High-Temp Synth.* **2013**, *22*, 151-156.
22. Zhang, R.; Han, G.; Zhang, L.; Yang, B. Gel Combustion Synthesis and Luminescence Properties of Nanoparticles of Monoclinic SrAl₂O₄: Eu²⁺, Dy³⁺. *Mater. Chem. Phys.* **2009**, *113*, 255-259.
23. Birkel, A.; Denault, K.A.; George, N.C.; Doll, C.E.; Héry, B.; Mikhailovsky, A.A.; Birkel, C.S.; Hong, B.-C.; Seshadri, R. Rapid Microwave Preparation of Highly Efficient Ce³⁺-Substituted Garnet Phosphors for Solid State White Lighting. *Chem. Mater.* **2012**, *24*, 1198-1204.

24. Ranjan, R.; Vaidya, S.; Thaplyal, P.; Qamar, M.; Ahmed, J.; Ganguli, A.K. Controlling the Size, Morphology, and Aspect Ratio of Nanostructures Using Reverse Micelles: A Case Study of Copper Oxalate Monohydrate. *Langmuir* **2009**, *25*, 6469-6475.
25. Li, C.; Imai, Y.; Adachi, Y.; Yamada, H.; Nishikubo, K.; Xu, C.-N. One-Step Synthesis of Luminescent Nanoparticles of Complex Oxide, Strontium Aluminate. *J. Am. Ceram. Soc.* **2007**, *90*, 2273-2275.
26. Shi, W.S.; Yamada, H.; Nishikubo, K.; Kusaba, H.; Xu, C.N. Novel Structural Behavior of Strontium Aluminate Doped with Europium. *J. Electrochem. Soc.* **2004**, *151*, H97-H100.
27. Imai, Y.; Momoda, R.; Adachi, Y.; Nishikubo, K.; Kaida, Y.; Yamada, H.; Xu, C.-N. Water-Resistant Surface-Coating on Europium-Doped Strontium Aluminate Nanoparticles. *J. Electrochem. Soc.* **2007**, *154*, J77-J80.
28. Rojas-Hernandez, R.E.; Rubio-Marcos, F.; Gonçalves, R.H.; Rodriguez, M.Á.; Véron, E.; Allix, M.; Bessada, C.; Fernandez, J.F. Original Synthetic Route To Obtain a SrAl₂O₄ Phosphor by the Molten Salt Method: Insights into the Reaction Mechanism and Enhancement of the Persistent Luminescence. *Inorg. Chem.* **2015**, *54*, 9896-9907.
29. Aroz, R.; Lennikov, V.; Cases, R.; Sanjuán, M.L.; de la Fuente, G.F.; Muñoz, E. Laser Synthesis and Luminescence Properties of SrAl₂O₄:Eu²⁺, Dy³⁺ Phosphors. *J. Eur. Ceram. Soc.* **2012**, *32*, 4363-4369.
30. Wu, S.; Zhang, S.; Yang, J. Influence of Microwave Process on Photoluminescence of Europium-Doped Strontium Aluminate Phosphor Prepared by a Novel Sol-Gel-Microwave Process. *Mater. Chem. Phys.* **2007**, *102*, 80-85.
31. Shan, W.; Wu, L.; Tao, N.; Chen, Y.; Guo, D. Optimization Method for Green SrAl₂O₄:Eu²⁺, Dy³⁺ Phosphors Synthesized via Co-Precipitation Route Assisted by Microwave Irradiation Using Orthogonal Experimental Design. *Ceram. Int.* **2015**, *41*, 15034-15040.
32. Larson, A.C.; Von Dreele, R.B. General Structure Analysis System (GSAS). **1994**.
33. Toby, B.H. EXPGUI, A Graphical User Interface for GSAS. *J. Appl. Crystallogr.* **2001**, *34*, 210.
34. Momma, K.; Izumi, F. VESTA 3 for Three-Dimensional Visualization of Crystal, Volumetric and Morphology Data. *J. Appl. Crystallogr.* **2011**, *44*, 1272-1276.
35. Qi, L. In *Encyclopedia of Surface and Colloid Science*; 2nd ed.; Somasundaran, P., Ed.; Taylor & Francis: 2006; Vol. 8, p 6183-6207.
36. Morrison, S.A.; Cahill, C.L.; Carpenter, E.E.; Harris, V.G. Production Scaleup of Reverse Micelle Synthesis. *Industrial & Engineering Chemistry Research* **2006**, *45*, 1217-1220.
37. López-Quintela, M.A.; Tojo, C.; Blanco, M.C.; García Rio, L.; Leis, J.R. Microemulsion Dynamics and Reactions in Microemulsions. *Curr. Opin. Colloid Interface Sci.* **2004**, *9*, 264-278.
38. Sharma, S.; Ganguli, A.K. Spherical-to-Cylindrical Transformation of Reverse Micelles and their Templating Effect on the Growth of Nanostructures. *The Journal of Physical Chemistry B* **2014**, *118*, 4122-4131.
39. Schulze, A.R.; Buschbaum, H.M. Zur Verbindungsbildung von MeO: M₂O₃. IV. Zur Struktur von Monoklinem SrAl₂O₄. *Z. Anorg. Allg. Chem.* **1981**, *475*, 205-210.
40. Clabau, F.; Rocquefelte, X.; Jobic, S.; Deniard, P.; Whangbo, M.H.; Garcia, A.; Le Mercier, T. Mechanism of Phosphorescence Appropriate for the Long-Lasting

- Phosphors Eu²⁺-Doped SrAl₂O₄ with Codopants Dy³⁺ and B³⁺. *Chem. Mater.* **2005**, *17*, 3904-3912.
41. Srivastava, B.B.; Kuang, A.; Mao, Y. Persistent Luminescent Sub-10 nm Cr Doped ZnGa₂O₄ Nanoparticles by a Biphasic Synthesis Route. *Chem. Commun.* **2015**, *51*, 7372-7375.
 42. Kandpal, S.K.; Goundie, B.; Wright, J.; Pollock, R.A.; Mason, M.D.; Meulenberg, R.W. Investigation of the Emission Mechanism in Milled SrAl₂O₄: Eu²⁺, Dy³⁺ Using Optical and Synchrotron X-ray Spectroscopy. *ACS Appl. Mater. Inter.* **2011**, *3*, 3482-3486.
 43. Smet, P.F.; Parmentier, A.B.; Poelman, D. Selecting Conversion Phosphors for White Light-Emitting Diodes. *J. Electrochem. Soc.* **2011**, *158*, R37-R54.
 44. George, N.C.; Denault, K.A.; Seshadri, R. Phosphors for Solid-State White Lighting. *Annu. Rev. Mater. Res.* **2013**, *43*, 481-501.
 45. Bierwagen, J.; Yoon, S.; Gartmann, N.; Walfort, B.; Hagemann, H. Thermal and Concentration Dependent energy Transfer of Eu²⁺ in SrAl₂O₄. *Opt. Mat. Express* **2016**, *6*, 793-803.
 46. Poort, S.H.M.; Blokpoel, W.P.; Blasse, G. Luminescence of Eu²⁺ in Barium and Strontium Aluminate and Gallate. *Chem. Mater.* **1995**, *7*, 1547-1551.
 47. Maldiney, T.; Kaikkonen, M.U.; Seguin, J.; le Masne de Chermont, Q.; Bessodes, M.; Airene, K.J.; Ylä-Herttuala, S.; Scherman, D.; Richard, C. In Vitro Targeting of Avidin-Expressing Glioma Cells with Biotinylated Persistent Luminescence Nanoparticles. *Bioconjugate Chem.* **2012**, *23*, 472-478.
 48. Sun, M.; Li, Z.-J.; Liu, C.-L.; Fu, H.-X.; Shen, J.-S.; Zhang, H.-W. Persistent Luminescent Nanoparticles for Super-Long Time In Vivo and In Situ Imaging with Repeatable Excitation. *J. Lumin.* **2014**, *145*, 838-842.
 49. Chen, W.; Wang, Z.; Lin, Z.; Lin, L. Thermoluminescence of ZnS Nanoparticles. *Appl. Phys. Lett.* **1997**, *70*, 1465-1467.
 50. Krishna, R.H.; Nagabhushana, B.M.; Nagabhushana, H.; Murthy, N.S.; Sharma, S.C.; Shivakumara, C.; Chakradhar, R.P.S. Effect of Calcination Temperature on Structural, Photoluminescence, and Thermoluminescence Properties of Y₂O₃:Eu³⁺ Nanophosphor. *The Journal of Physical Chemistry C* **2013**, *117*, 1915-1924.
 51. Van den Eeckhout, K.; Bos, A.J.J.; Poelman, D.; Smet, P.F. Revealing Trap Depth Distributions in Persistent Phosphors. *Phys. Rev. B* **2013**, *87*, 045126.
 52. McKeever, S.W.S. *Thermoluminescence of Solids*; Cambridge University Press, 1985.
 53. Chen, R. Glow Curves with General Order Kinetics. *J. Electrochem. Soc.* **1969**, *116*, 1254-1257.
 54. Sahu, I.P.; Bisen, D.P.; Brahme, N.; Tamrakar, R.K.; Shrivastava, R. Luminescence Studies of Dysprosium Doped Strontium Aluminate White Light Emitting Phosphor by Combustion Route. *J. Mater. Sci. - Mater. Electron.* **2015**, *26*, 8824-8839.
 55. Matsuzawa, T.; Aoki, Y.; Takeuchi, N.; Murayama, Y. A New Long Phosphorescent Phosphor with High Brightness, SrAl₂O₄: Eu²⁺, Dy³⁺. *J. Electrochem. Soc.* **1996**, *143*, 2670-2673.
 56. Chen, R.; McKeever, S.W.S. *Theory of Thermoluminescence and Related Phenomena*; World Scientific, 1997.

57. Dorenbos, P. Mechanism of Persistent Luminescence in Eu^{2+} and Dy^{3+} Codoped Aluminate and Silicate Compounds. *J. Electrochem. Soc.* **2005**, *152*, H107-H110.
58. Pannhorst, W.; Löhn, J. In *Z. Kristallogr.* 1970; Vol. 131, p 455.

7.7 Supporting Information

Powder X-ray diffraction of precursors show formation of SrCO_3 as predicted by balanced chemical equations 1 and 2. Rietveld refinements and resulting crystallographic information of the reverse micelle and solid state synthesis for reactions performed via high-temperature furnace heating, Particle size analysis for reactions performed via high-temperature furnace heating for reverse micelle and solid state synthesis routes.

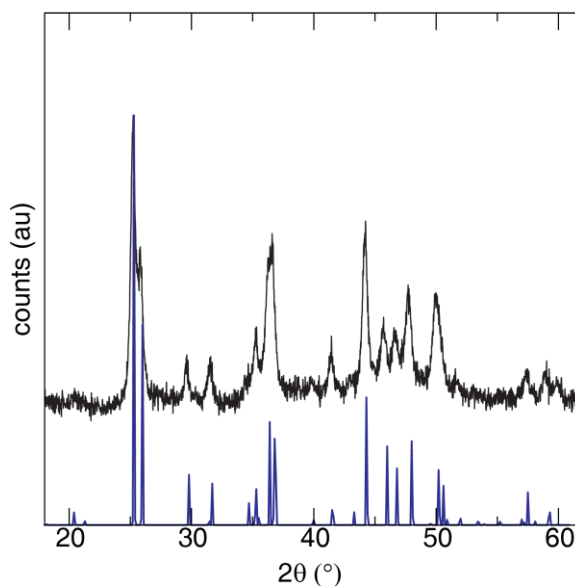


Figure 7.S1. Powder X-ray diffraction of precursor material from reverse micelle synthesis. Black is the observed data and blue is the calculated pattern from ICSD⁵⁸

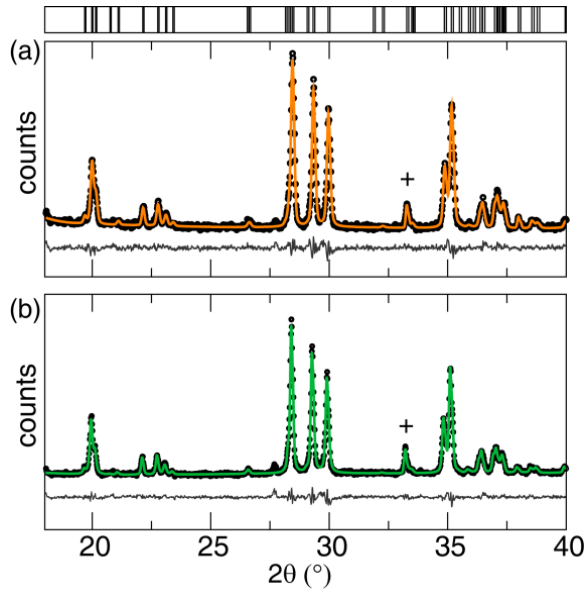


Figure 7.S2. (a) Reverse micelle and (b) solid state synthesis performed by high-temperature furnace heating of Rietveld refinements. Show the reverse micelle is again comparable to the solid state sample. Black circles are for observed data, solid lines are the refined pattern. And “+” is the Al_2O_3 impurity. An additional unidentified impurity.

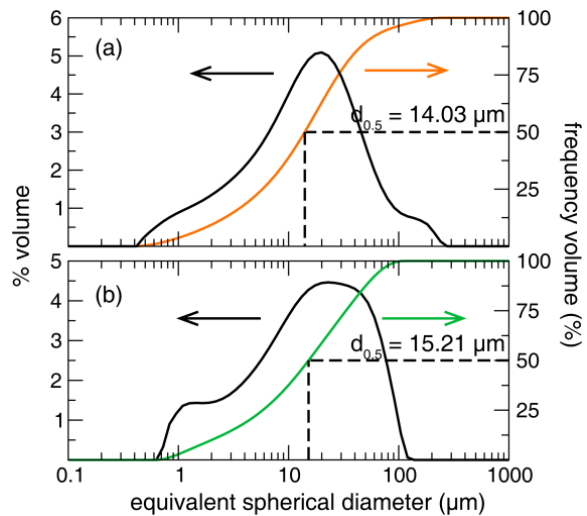


Figure 7.S3. Particle size analysis of samples prepared via high-temperature furnace heating (a) reverse micelle synthesis and (b) solid state synthesis have comparable particle sizes.

Table 7.S1. Rietveld refinement results for reverse micelle and solid state synthesis of $\text{SrAl}_2\text{O}_4:\text{Eu}^{2+},\text{Dy}^{3+}$ using powder X-ray diffraction of synthesis performed using a high-temperature furnace

Formula: $\text{SrAl}_2\text{O}_4:\text{Eu}^{2+},\text{Dy}^{3+}$	Reverse micelle	Solid state
radiation type, λ (Å)	Cu, 1.5406 Å	
2θ range (°)	18-40	
temperature (K)	295	
space group; Z	$P2_1$ (No. 4); 2	
a (Å)	8.4387(2)	8.4486(2)
b (Å)	8.8171(2)	8.8243(2)
c (Å)	5.1545(1)	5.1579(1)
β (°)	93.378(2)	93.344(2)
V (Å ³)	382.86(1)	383.89(1)
calculated density (g cm ⁻³)	3.567	3.557
formula weight (g mol ⁻¹)	822.320	822.320
R_p	0.0389	0.0391
R_{wp}	0.0502	0.519
χ^2	1.263	1.562

Table 7.S2. Crystallographic results as determined by Rietveld refinement of powder X-ray diffraction. The samples were reacted using a high-temperature furnace.

(c) Reverse micelle					
Atom	Wyck.	<i>x</i>	<i>y</i>	<i>z</i>	U_{iso} (Å ²)
Sr(1)	2 <i>a</i>	0.4917(7)	0.012(2)	0.256(1)	0.010(2)
Sr(2)	2 <i>a</i>	0.0309(8)	1.003(2)	0.199(1)	0.048(4)
Al(1)	2 <i>a</i>	0.204(4)	0.837(3)	0.707(5)	0.024(4)
Al(2)	2 <i>a</i>	0.791(4)	0.849(3)	0.727(6)	0.041(4)
Al(3)	2 <i>a</i>	0.677(5)	0.689(4)	0.226(9)	0.080(4)
Al(4)	2 <i>a</i>	0.684(3)	0.172(3)	0.795(5)	0.035(4)
O(1)	2 <i>a</i>	0.267(4)	0.173(4)	0.42(1)	0.01(4)
O(2)	2 <i>a</i>	0.730(5)	0.306(4)	0.58(1)	0.01(4)
O(3)	2 <i>a</i>	0.336(3)	0.489(5)	0.348(5)	0.01(4)
O(4)	2 <i>a</i>	0.262(3)	0.955(4)	0.874(5)	0.01(4)
O(5)	2 <i>a</i>	0.158(4)	0.283(4)	0.909(6)	0.01(4)
O(6)	2 <i>a</i>	0.198(4)	0.648(4)	0.912(6)	0.01(4)
O(7)	2 <i>a</i>	0.500(6)	0.238(3)	0.898(5)	0.01(4)
O(8)	2 <i>a</i>	1.003(4)	0.879(4)	0.650(6)	0.01(4)

(d) Solid state					
Atom	Wyck.	<i>x</i>	<i>y</i>	<i>z</i>	U_{iso} (Å ²)
Sr(1)	2 <i>a</i>	0.490(1)	-0.008(1)	0.253(2)	0.077(6)
Sr(2)	2 <i>a</i>	0.0288(8)	0.980(2)	0.207(1)	0.091(6)
Al(1)	2 <i>a</i>	0.201(3)	0.833(3)	0.722(5)	0.080(7)
Al(2)	2 <i>a</i>	0.780(4)	0.833(4)	0.721(6)	0.080(7)
Al(3)	2 <i>a</i>	0.670(4)	0.695(4)	0.215(6)	0.080(7)
Al(4)	2 <i>a</i>	0.685(4)	0.181(4)	0.799(6)	0.080(7)
O(1)	2 <i>a</i>	0.289(4)	0.171(4)	0.46(1)	0.056(6)
O(2)	2 <i>a</i>	0.751(4)	0.346(5)	0.610(7)	0.056(6)
O(3)	2 <i>a</i>	0.342(3)	0.471(5)	0.337(4)	0.056(6)
O(4)	2 <i>a</i>	0.271(4)	1.052(4)	0.878(6)	0.056(6)
O(5)	2 <i>a</i>	0.172(3)	0.303(4)	0.963(9)	0.056(6)
O(6)	2 <i>a</i>	0.214(4)	0.685(5)	0.909(9)	0.056(6)
O(7)	2 <i>a</i>	0.497(5)	0.246(3)	0.907(6)	0.056(6)
O(8)	2 <i>a</i>	0.984(5)	0.834(4)	0.665(7)	0.056(6)

CHAPTER 8

Conclusions and Direction of Research

The research presented in this thesis focused on investigating the characteristics of persistent luminescent phosphors that give rise to their long luminescent lifetimes. By identifying intrinsic properties such as anion vacancies that produce the desired response and their associated chemical handles, the design of new persistent luminescent phosphors can be realized.

First, crystal field splitting theory was applied to a Eu^{2+} substituted solid solution, $(\text{Sr}_{1-\delta}\text{Ba}_\delta)_2\text{MgSi}_2\text{O}_7:\text{Eu}^{2+}$ ($\delta = 0, 0.125, 0.250, 0.375$). In this case, the controlled substitution of Ba^{2+} onto the Sr^{2+} site established that emission wavelength could be tuned from $\lambda_{\text{em}} = 472 \text{ nm}$ ($\delta = 0$) to $\lambda_{\text{em}} = 460 \text{ nm}$ ($\delta = 0.375$) due to the increase of bond lengths. Conducting persistent luminescent lifetime measurements showed the luminescence lifetimes were maintained across the solid solution. Moreover, thermoluminescence spectroscopy revealed that the trap depths were also consistent. Since the inclusion of a co-dopant is known to improve the quality of the long luminescent lifetime, Dy^{3+} was added to the system. It was found that Dy^{3+} did not alter the emission wavelength of the solid solution; however, long luminescent lifetimes did increase by $\approx 3 \text{ min}$. Further analysis revealed this result arises from the presence of an additional trap state attributed to the unoccupied $5d$ -orbital of Dy^{3+} , which is also consistent across the solid solution. The logical conclusion is that crystal field splitting in Eu^{2+} substituted systems can provide tunable emission wavelengths without negatively affecting persistent luminescence. Likewise, these materials also have a trap state that leads to long

luminescent lifetimes without the presence of a co-dopant, which suggests that lattice defects may be an inherent structural property of the persistent luminescent phosphors.

The next investigation used crystal field splitting theory in a Cr^{3+} substituted solid solution of $\text{Zn}(\text{Ga}_{1-\delta}\text{Al}_\delta)_2\text{O}_4:\text{Cr}^{3+}$ ($\delta = 0-1$) to identify the relationship between persistent luminescence and a material's optical bandgap. Here, the substitution of smaller Al^{3+} onto the Ga^{3+} site caused an increase in the optical bandgap. This change is a direct result of increasing crystal field strength, which arises from the shortening of bonds across the aluminogallate solid solution. There are also distinct changes to peak intensity and peak width are associated with an increase in lattice defects and disorder. Persistent luminescent lifetime measurements revealed an associated a quenching of the observable long luminescent lifetimes with aluminum substitution. Further analysis using thermoluminescence spectroscopy showed an increase in the number of trap states that also became more shallow with increasing Al^{3+} up to $\delta = 0.50$. To better understand the impact of lattice defects on persistent luminescence, the local structure of Cr^{3+} in this solid solution was then investigated. Employing X-ray absorption spectroscopy, the radial distance (R) of the first near neighbor, the Cr-O bond length, increased up to $\delta = 0.50$, indicating a distortion of the polyhedron of Cr^{3+} , which causes an increase in lattice defects near Cr^{3+} substitution site and is consistent with the trends observed in the experimental photoluminescence and thermoluminescence measurements, thus, validating the hypothesis regarding the need for lattice defects and their impact on persistent luminescence.

Lattice defects were shown to be an integral structural component to observe persistent luminescence; however, their inherent nature needed to be determined. To achieve this goal, a computational study of SrAl_2O_4 and $\text{SrAl}_2\text{O}_4:\text{Eu}^{2+}$ was conducted to determine the

formation energies of lattice defects, *e.g.*, cation and anion vacancies. The intrinsic nature of the vacancies was identified by calculating the formation energies at the oxygen-poor limit, revealing that an anion vacancy with a 2+ (V_O^{2+}) would form in an energy window favorable to trapping electrons. Because a V_O^{2+} formed in the absence and presence of Eu^{2+} in favorable energy windows for trapping electrons, it is likely this property is an imperative structural component of persistent luminescent phosphors.

Finally, a novel synthesis method was developed that involved a reverse micelle solution combined with microwave-assisted heating to reduce particle sizes of $SrAl_2O_4:Eu^{2+}, Dy^{3+}$. The ideal particle size for a persistent luminescent phosphor for use in bioanalytical application is <500 nm; however, to achieve phase purity of $SrAl_2O_4:Eu^{2+}, Dy^{3+}$, reaction temperatures >1300°C are often required, leading to large agglomerates >10 μm . Therefore, solution based synthesis methods were chosen owing to the known reduction in reaction time and temperature, which is useful for limiting crystallite growth. Using microwave-assisted heating in combination with a reverse micelle prepared precursors, $SrAl_2O_4:Eu^{2+}, Dy^{3+}$ showed a 70% reduction in particle size compared to an all-solid-state method. Optical property characterization showed an improvement to both the thermal stability of the photoemission and the long luminescent lifetime of the reverse micelle. Examining thermoluminescence revealed that reduction in particle size increased the number of trap states, further supporting the increase in persistent luminescence. This increase in trap states is likely a result of new surface defects that originated from the reduction of the particle size.

In conclusion, the research presented resulted in an enhanced understanding of the role of structural properties, such as, lattice defects, in persistent luminescent phosphors and

their relationship with persistent luminescence. Future work using computational methods, in series such as the solid solution $\text{Zn}(\text{Ga}_{1-\delta}\text{Al}_\delta)_2\text{O}_4:\text{Cr}^{3+}$ ($\delta = 0-1$), will further aid in identifying the type of defects, *e.g.*, anti-site or anion vacancies, that will most likely to induce persistent luminescence. Employing the knowledge generated through this work will allow researchers to target new compounds with a high probability of generating long luminescence lifetimes.